PORTUGALIAE
PHYSICA

PORTUGALIAE PHYSICA

117

FRONTIERS IN NUCLEAR SCIENCE (*)

J. H. HAMILTON

Department of Physics and Astronomy, Vanderbilt University,
Nashville, TN 37235, USA

WALTER GREINER

Institute für Theoretische Physik,
Universität Frankfurt/Main
Frankfurt/Main, West Germany

ABSTRACT — A review is made of some of the frontiers in nuclear research with heavy ions. Recent results from studies of nuclei far from stability, very high spin states and nuclear molecules with $Z = 184$ are given. New applications of nuclear techniques in medicine, positron emission tomography and nuclear magnetic resonance, also are presented.

1 — INTRODUCTION

The last decade has seen the development of exciting new frontiers in basic nuclear science and in the application of nuclear science in important societal problems such as health care and energy. New accelerator facilities which can give beams of heavy ions all the way to uranium with up to 10 and more MeV per nucleon and in some cases over 1 GeV per nucleon are opening up many exciting, new areas in nuclear, atomic and solid state physics, astrophysics, chemistry, materials science, and beyond. From the broad spectrum of basic and applied nuclear science, a few limited examples were selected to illustrate some of the new frontiers and the excitement they are generating. In basic research, examples are drawn from studies of nuclei far from

---

(*) This paper is based on two talks, one delivered and one prepared for the Third National Physics Conference of the Portuguese Physical Society (Coimbra, June 1982).

the stable ones found in nature, nuclei under conditions of high angular momentum, and the properties of atoms with Z up to 188 and tests of quantum electrodynamics of very strong fields. In applied research, there is again a broad range from uses of heavy ions to initiate the fusion of hydrogen into helium in a fusion energy reactor to nuclear medicine. Within the last several years, new applications of nuclear techniques in positron emission tomography and nuclear magnetic resonance offer the promise of revolutionizing diagnostic medicine. Illustrations of the power of these new techniques are given.

Three sections of this paper were prepared from a talk given at the Third Portuguese National Physics Conference. These sections are intended to be only illustrative and not comprehensive as in a regular review article. The fourth section was prepared for the conference but in the absence of the second author presented only briefly by the first. We have given full attention to the exciting developments in the studies of atoms with Z up to 188 in this combined paper.

2 — SHAPE COEXISTENCE AND SUPER DEFORMATION AROUND Z = N = 38

For over two decades after Bohr and Mottelson [1] described collective excitations in nuclei with rotational motions in deformed nuclei and vibrational motions in both spherical and deformed nuclei, the classification of a nucleus as a deformed rotor or spherical vibrator clearly defined its shape and the general features of its structure. Regions of deformation occurred essentially in heavy nuclei where the neutron number is far removed from closed shells. Additional regions of deformation were expected in similar regions labelled one and three (Fig. 1). Near the closed shells or below N = 50 where N and Z were never very far from a magic number, nuclei were considered spherical with only a few exceptions and were described by shell or vibrational models.

The discoveries of the coexistence of overlapping low energy states with well deformed and near spherical shapes in both the light mercury nuclei far off stability [2, 3] and in ^{72}Se (refs. 3-5) helped break down the idea that a given nucleus had one fixed shape. The bands built on the different shapes in $^{184-188}$Hg are shown in Fig. 2. The $2 \rightarrow 0$ energies in the two bands are inversely

2

Portgal. Phys. — Vol. 14, fasc. 1-2, pp. 1-47, 1983
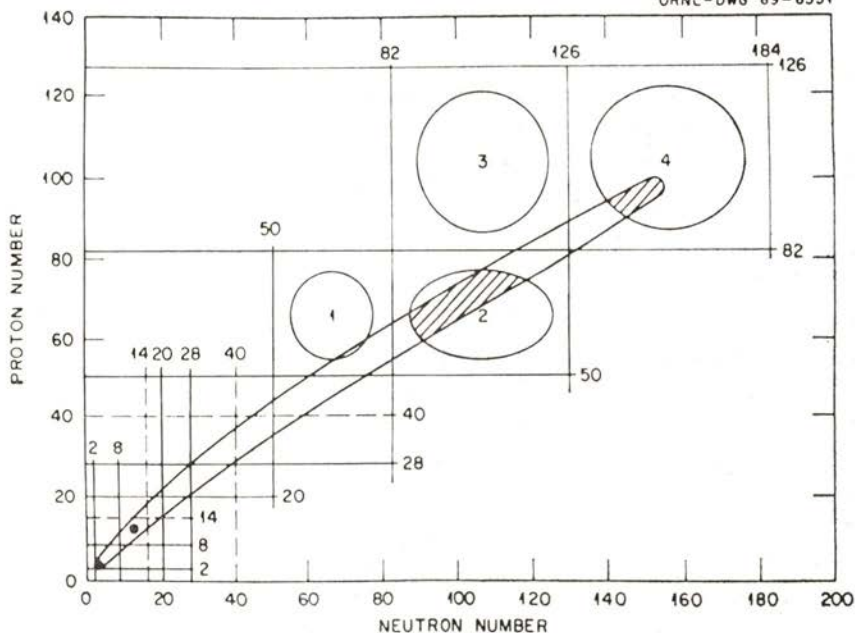
Fig. 1 — An older chart of the nuclides as functions of N and Z with the nuclei in the valley of beta stability inside the ellipse. The closed shells are shown by lines and the known and then predicted new regions of deformation far off stability are identified by circles.
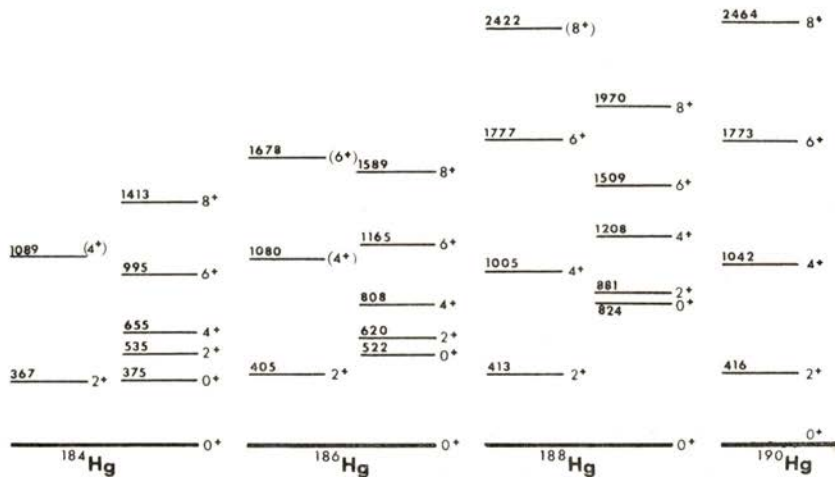

Fig. 2 — Energy levels in $^{184-188}$Hg where coexisting bands of levels built on different shapes are observed [2, 3].

Portgal. Phys. — Vol. 14, fasc. 1-2, pp. 1-47, 1983

3

proportional to the moments of inertia and so show clearly the large differences in deformation in the two bands. Now shape coexistence is reported in many regions of the periodic table including at both low and high spins as can be seen, for example, in numerous papers in the Proceedings of the most recent Conference on Nuclei Far From Stability at Helsingør, 1981.

The A = 60 to 84 region has become an important, new testing ground for many types of nuclear structure models because of the richness of different collective motions and structures which are found in this region and the rapid changes seen in some structures with the addition of only two protons or two neutrons. Some of the variety of different structures and the rapidity of their changes can be seen in an earlier survey of the moments of inertia as a function of the rotational frequency $(\hbar\omega)^2$ for the yrast states in nuclei in this region (Fig. 3). Note the striking difference between ^{68}Ge with its triple forking at 8+ and two back bends of $\mathscr{J}$ as discovered by de Lima et al. [6] and the single band with forward
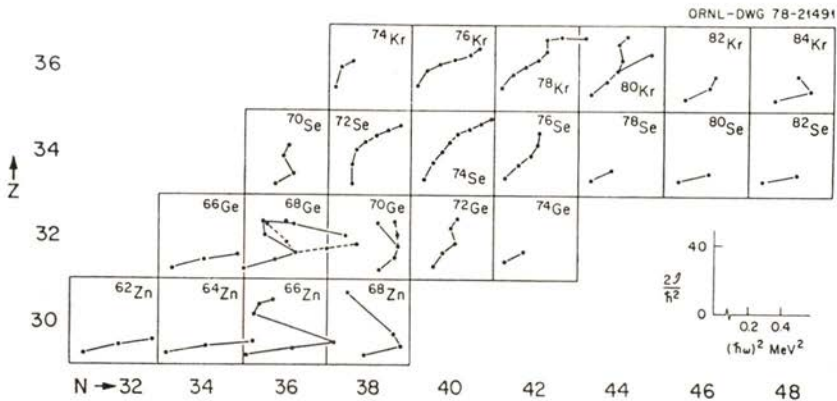

Fig. 3 — Moments of inertia for the yrast cascades in A = 60-80 region [5].

bend in ^{72}Se. The first nucleus studied to high spin was ^{72}Se (ref. 4) and its strong forward bend of $\mathscr{J}$, very like the forward bends of $\mathscr{J}$ seen [2, 3] in $^{184-188}$Hg, was similarly interpreted in terms of shape coexistence [3-5]. While there is definite exper-

imental evidence [7, 8] supported by theoretical calculations [7, 9] that the low lying 0_2^+ states in $^{70, 72}_{32}$Ge indeed have much larger deformations than their ground states as in $^{72, 74}_{34}$Se, they have no well developed rotational bands built on the 0_2^+ states. This was considered by some as a serious problem for the shape coexistence picture.

Recent studies [10] of $^{74, 76}$Kr have illuminated the origin of the shape coexistence in this region and given evidence for super deformation of the ground states where both N and Z are at or near 38. The $2_1^+ \rightarrow 0_1^+$ energy does not indicate super deformation in $^{74}_{36}$Kr$_{38}$. The origin of the masking of the strong deformation now is understood in terms of the interaction of two close lying 0^+ states [10]. A similar masking is now understood to occur in the light Pt isotopes. Simultaneously, Möller and Nix [11] carried out calculations that predicted that nuclei in this region around $N = Z = 38$ should have the strongest ground state deformation of any nuclei, with $\beta \sim 0.4$. Likewise, the recent analysis of the levels of $^{74-80}$Kr in the collective potential energy surface approach of the Frankfurt group [12] indicate shape coexistence and large deformations in $^{74, 76}$Kr. New studies in the Sr nuclei [13, 14, 15] support this conclusion. Indeed, we have found experimentally [10] and independently predicted theoretically [11] a new region of strong deformation. The understanding of the origin of this deformation gives insights into nuclear shape coexistence in a wide range of different masses.

Our studies of the light Kr isotopes provide the clues to understanding this region. The B (E2 ; $2 \rightarrow 0$) for $^{78, 80, 82, 84, 86}$Kr were measured by Sakamoto et al. [16]. They found nearly a factor of 10 increase in B (E2) strength in going from $N = 50$, $^{86}_{36}$Kr , B (E2 ; $2 \rightarrow 0$) = 6.5 spu to ^{78}Kr where it is 51.8 spu. This suggests the onset of large collective effects possibly associated with deformation. However, the $2 \rightarrow 0$ energies (455-617 keV) do not suggest large deformation.

We investigated the levels in ^{76}Kr and our results are shown in Fig. 4 (ref. 10). Note the dominance of rotational-like band structures. We measured the B (E2) strengths of the transitions from the 4^+ to 10^+ levels by Doppler-shift, line-shape analysis [10]. Both singles and concidence spectra line shapes were analized.

Portgal. Phys. — Vol. 14, fasc. 1-2, pp. 1-47, 1983

5

Fig. 4 — Energy levels in ^{76}Kr from in-beam studies [10].

The results are given in Table I along with similar results more recently obtained by Winter et al. [17]. The B(E2)'s show surprisingly large collective strength — the largest of any nucleus in this region. For comparison the B(E2)$_{exp}$/B(E2)$_{sp}$ for the $2 \to 0$ and $4 \to 2$ transitions in $^{68, 72}$Ge are of the order of 10-20. These data provide strong evidence for large collective effects associated with nuclear deformation. From the 2^+ to 10^+ level, the B(E2) values generally follow the gradual increase expected in a rotational model in sharp contrast to the rapid increase in B(E2) in a vibrational model.

Note in ^{76}Kr that the energy of the first excited, 0_2^+, level has continued to drop sharply relative to the 0_1^+ ground state as N decreases analogous to the similar sharp drops seen in Ge and Se nuclei around N = 40. But there is no rotational band built on it as in ^{72}Se. The only feeding to the 0_2^+ level is from a 2^+

6

Portgal. Phys. — Vol. 14, fasc. 1-2, pp. 1-47, 1983

TABLE I — Measured mean lives and extracted B (E2) values [10, 17] for transitions in ^{76}Kr.

$E\gamma$ (keV)	$I_i \to I_f$	τ_{mean} (ps)			B(E2)/B(E2)$_{sp}$
		(ref. 10)	(ref. 17)	Average	
424	$2^+ \to 0^+$	53(7) †	35(3) ††	40(5)	78(9)
611	$4^+ \to 2^+$	5.0(20)	3.5(10)	4.2(10)	120(30)
825	$6^+ \to 4^+$	1.25(12)	0.9(2)	1.12(10)	99(10)
1020	$8^+ \to 6^+$	0.30(3)	0.32(4)	0.31(3)	125(12)
1188	$10^+ \to 8^+$	0.14(2)	0.18(4)	0.15(2)	120(20)
1278	$(12^+) \to 10^+$	0.24(5) *			52(11) *

* Composite state plus feeding lifetime and composite B (E2) compared to single particle values.

† E. NOLTE et al., *Z. Phys.* A268, 267 (1974).

†† J. KEINONEN et al., *Nucl. Phys.* A376, 246 (1982).

level at 1688 keV. Note the $2^+ \to 0_2^+$ energy of 917 keV is more than twice the $2_1^+ \to 0_1^+$ energy of 424 keV. This is in sharp contrast to ^{72}Se where these two energies are the reverse, eg., the $2^+ \to 0_2^+$ energy is low compared to the $2_1^+ \to 0_1^+$ energy. A (2^+) $\to 2^+ \to 0_2^+$ cascade (882-917 keV γ rays) is seen in UNISOR studies [18] of the decay of ^{76}Rb. All these data indicate that something different and unusual is happening in ^{76}Kr.

We carried out a similar study of the energy levels in ^{74}Kr (ref. 10). The moments of inertia for $^{74-80}$Kr are shown in Fig. 5. One can see from Fig. 5 that at low spin, $\mathcal{J}$ of each band becomes larger when going from N = 44 to N = 38, except for ^{74}Kr where the point corresponding to the $2 \to 0$ energy in ^{74}Kr strongly deviates as first noted by Funke et al. [19]. This tendency also is seen in ^{76}Kr to a lesser degree. These nuclei exhibit forward bends in $\mathcal{J}$ above the 2_1^+ states analogous to those in $^{72,\ 74}$Se$_{38,\ 40}$ which were interpreted (refs. 3, 4) in a shape coexistence picture with bands built on the ground and 0_2^+ states of quite different deformations. All the above data led to the suggestion that the ground state of ^{76}Kr is well deformed and the 0_2^+ level is associated with a near-spherical shape [10], in contrast to the reverse situation in $^{72,\ 74}$Se . A similar situation should be occurring in ^{74}Kr .

Portgal. Phys. — Vol. 14, fasc. 1-2, pp. 1-47, 1983

7

How can we understand large ground state deformation but relatively small $\mathcal{J}$'s extracted from the relatively large $2 \to 0$ energies in $^{74\text{-}76}$Kr? The relatively large $2 \to 0$ energies and corresponding small $\mathcal{J}$ in $^{74,\,76}$Kr, which make these nuclei look less deformed than they really are, can arise from an interaction between the 0_1^+ deformed ground states and higher states such as the 0_2^+ states to push down the 0_1^+ energies. Shape coexistence for N ~ 38 nuclei is related to the number of protons which delicately controls whether a deformed shape or near-spherical shape is lowest in this region. Our $^{74,\,76}$Kr data give evidence that their ground states have remarkably large deformation.
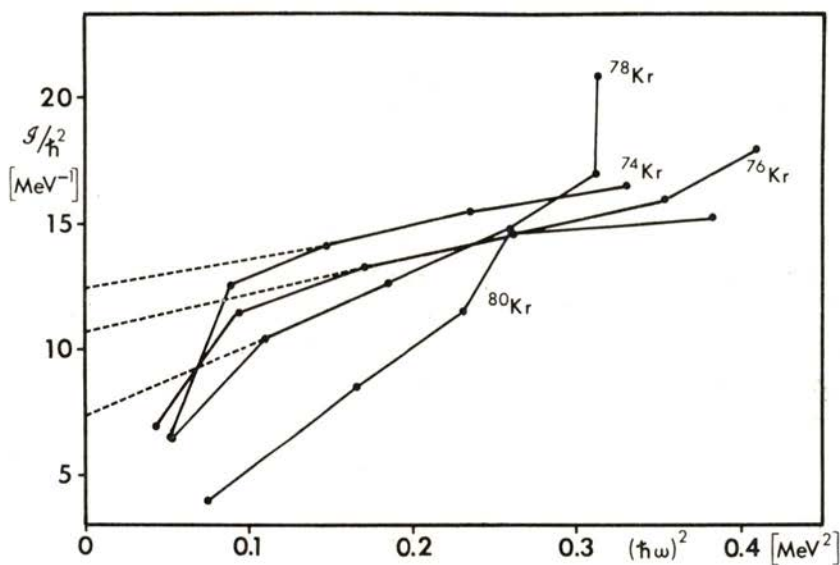

Fig. 5 — The moment of inertia of the yrast cascades are shown. The dashed lines correspond to an extrapolation back to low spin of a Harris parametrization of the states with I = 6 - 10 where $\mathcal{J}$ is linear [10].

The origin of strong deformation and shape coexistence in this region can be attributed to the gaps in the single-particle spectrum seen in Fig. 6 at N (or Z) = 40, δ ~ 0, and N (Z) = 38, δ ~ 0.3, that stabilize the nuclear shape. Evidence for the spherical subshell closure around N = 40 is found when Z is close or equal
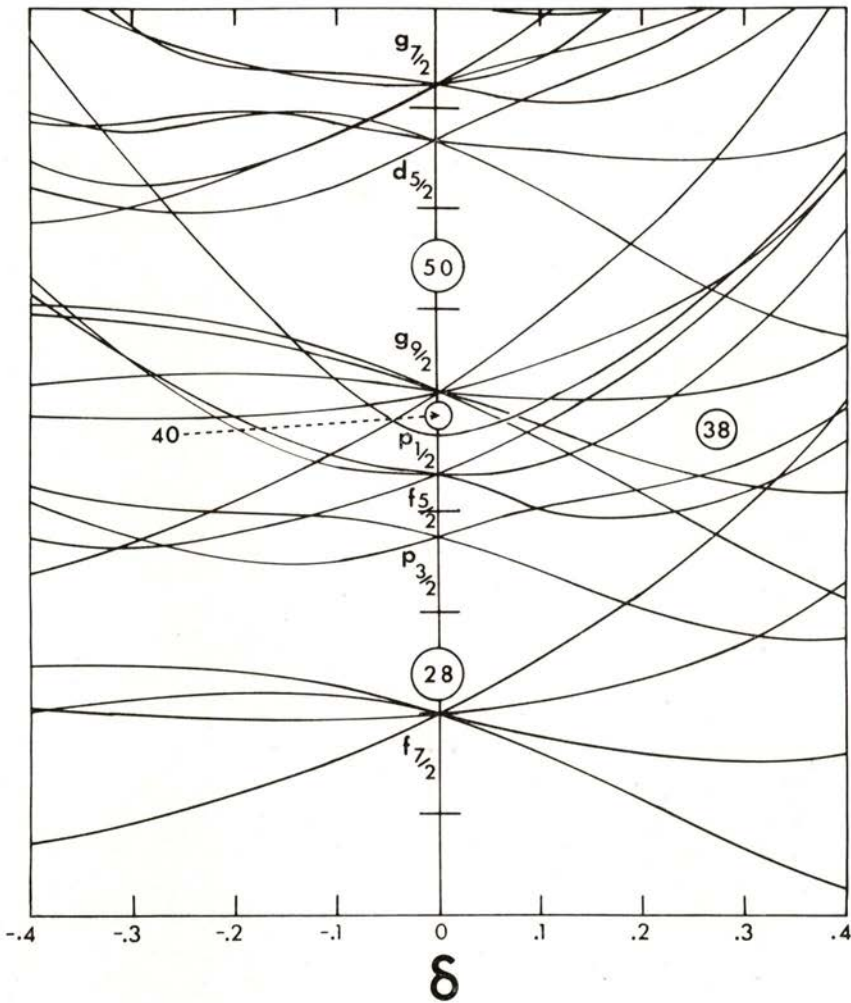
Fig. 6 — The Nilsson single particle spectrum for protons. Note the gap at N = 38 for large deformation. The neutron spectrum is similar.

to 28 or 50, or around Z = 40 when N ~ 28 or 50 because then the protons (neutrons) prefer a spherical shape, as seen for example in $^{66}_{28}\mathrm{Ni}_{38}$ ($^{90}_{40}\mathrm{Zr}_{50}$). However, as Z moves away from 28 or 50 the level density for a spherical shape becomes very high and the minimum of the proton deformation energy moves to deformed shapes and similarly for the neutrons which have almost identical

single-particle levels. Away from $Z(N) = 28$ and 50 closed shells, maximal deformation is expected at $N(Z) \sim 38$. However, the deformed state can coexist with a nearly spherical configuration in a delicate balance. Which one is lower depends on the proton number. For $^{70, 72}_{32}Ge_{38, 40}$ and $^{72, 74}_{34}Se_{38, 40}$ the coexistence of nearly spherical ground states with deformed 0^+_2 states has been reported [3, 5, 7] as noted earlier. In $^{72, 74}Se$, the deformed band becomes yrast at $I \sim 2 - 4$ because of its lower rotational energy. For the Ge isotopes, the bands built on the two different shapes are not well developed and so not seen because of the smaller deformation (two protons less than Se). In the Kr isotopes, the 36 protons favor deformation even more.

To quantify our interpretation, we analyzed [10] the Kr yrast bands in a two-band mixing model. For $I \gtrsim 6\hbar$, where $\mathcal{J}$ is nearly linear, we considered the yrast levels to be purely deformed. The up bends above 8^+- 10^+ (Fig. 5) are related to the alignment of a $g_{9/2}$ proton pair. The position of the unperturbed deformed levels were determined by extrapolating the linear part of $\mathcal{J}(\omega^2)$ down to $\omega = 0$. This corresponds to a Harris or variable moment of inertia (VMI) parametrization of the deformed g bands. The extracted unperturbed $2 \to 0$ energies in the deformed ground bands are 200 and 237 keV in $^{74, 76}Kr$, respectively. By scaling the unperturbed $2 \to 0$ energy by $A^{5/3}$, one may compare the deformation of ^{74}Kr to that of strongly deformed ^{240}Pu with one of the lowest $2 \to 0$ energies known. The 200 keV transition in ^{74}Kr would correspond to 28 keV in ^{240}Pu compared with its actual value of 43 keV (see Fig. 7). This is an unusually large ground-state deformation, slightly larger than the "super deformation" recently reported for ^{100}Sr with its scaled 30 - keV 2^+_1 (Fig. 7) energy [20]. Such interaction of two 0^+ levels and their splitting may have masked strong ground-state deformation in other regions. Indeed, recent analysis indicates that this is clearly happening in the light platinum isotopes, too.

These data extend our understanding of the coexistence of different nuclear shapes first proposed in ^{72}Se. However, in $^{74, 76}Kr$ the roles of the near-spherical and deformed minima are reversed with the ground states well deformed and the excited 0^+_2 states associated probably with near-spherical minima. The present data give evidence for large ground-state deformation in these light Kr isotopes [10]. This interpretation for the $N = 38$ and 40 Kr nuclei

10

Portgal. Phys. — Vol. 14, fasc. 1-2, pp. 1-47, 1983

supports the expectation that at these neutron numbers as the proton number approaches the middle between Z = 28 and 50 closed shells, the protons can drive a nucleus with a pair of $g_{9/2}$ neutrons toward deformation. Recently Möller and Nix [11] calculated nuclear masses and ground state shapes for 4023 nuclei from ^{16}O to ^{279}112 with a Yukawa-Plus-Exponential Macroscopic Model and a folded Yukawa single-particle potential. Their calculations [11] predict that nuclei with both N and Z at or near 38 should be among the most strongly deformed ones in nature, with $\beta \sim 0.4$. The $^{74, 76}$Kr data [10] support their calculations.
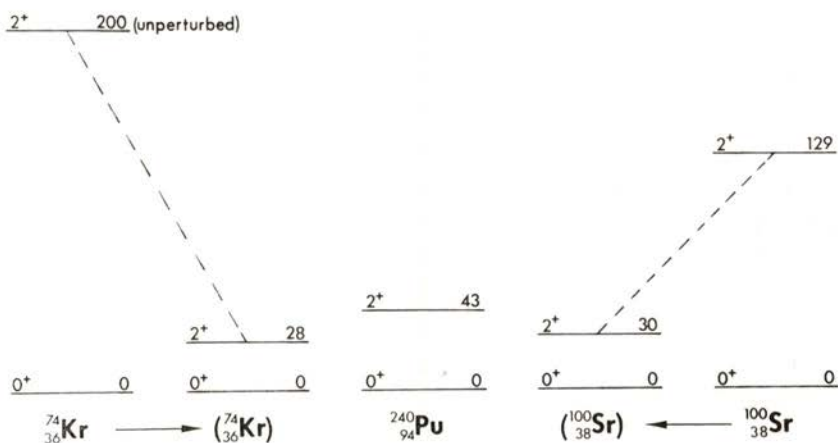

Fig. 7 — Comparison of the $2_1 - 0_1$ energies in $^{74}_{36}$Kr$_{38}$ and $^{100}_{38}$Sr$_{62}$ scaled by $A^{5/3}$ to compare with the very well deformed ^{240}Pu.

Potential energy surfaces have recently been calculated for $^{76-80}$Kr by the Frankfurt group [12]. The ^{76}Kr surface is shown in Fig. 8. Two minima are seen, one at large deformation and one near spherical. There is mixing, but the ground state wave function is centered in the deformed minimum with large β and the 0_2^+ wave function in the near spherical one. The low lying levels and their B(E2)'s are nicely reproduced by the fits. For $^{78, 80}$Kr the surfaces show the nuclei are soft to γ deformation.

Further support for the importance of deformation when N(Z) = 38 and Z(N) is well removed from a closed shell come from the lightest and heaviest Sr nuclei far from stability [13, 14, 15].
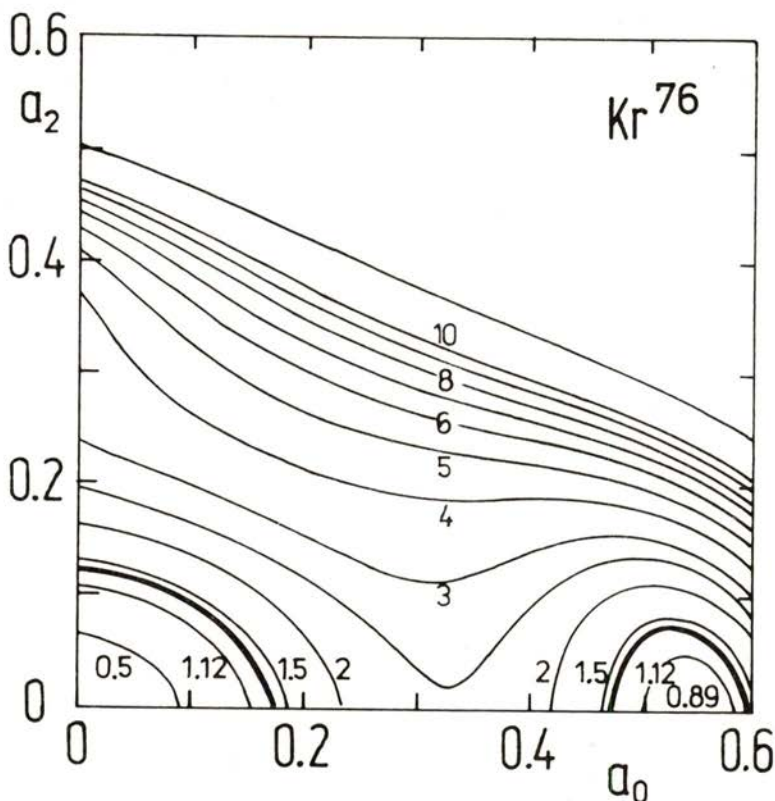
Fig. 8 — Potential energy surface for ^{76}Kr (ref. 12). Note two minima at large deformation and at zero deformation. Note $a_0 \sim \beta$.

In Fig. 9 is shown the yrast levels of $^{80}_{38}Sr_{42}$ obtained from a recent in-beam study (ref. 13) at the new Holifield tandem. The reaction $^{32}S + ^{51}V$ was carried out with terminal voltages of 16-19 MeV. One sees (Fig. 9) that the $2 \to 0$ energy continues to drop to the lowest energy then known for any nucleus in the A = 80 region. This sharp drop in the $2 \to 0$ energies indicates that the Sr nuclei are moving toward large ground-state deformation in $^{76}_{38}Sr_{38}$ as N decreases toward N = 38 with the 38 protons strongly supporting deformation, too. To search for ^{78}Sr, ^{58}Ni was bombarded with ^{24}Mg at the Holifield tandem [14]. A neutron multiplicity technique was used to pick out the (2p, 2n) reaction to ^{78}Sr from other four particle reaction channels. From an initial analysis of only our

(n, γ) spectra, wrong low energy γ rays were assigned as the 0-2-4 cascade. Our (2n, γ) data agree with the independent work of Lister et al. [15] who used neutron and particle detectors to

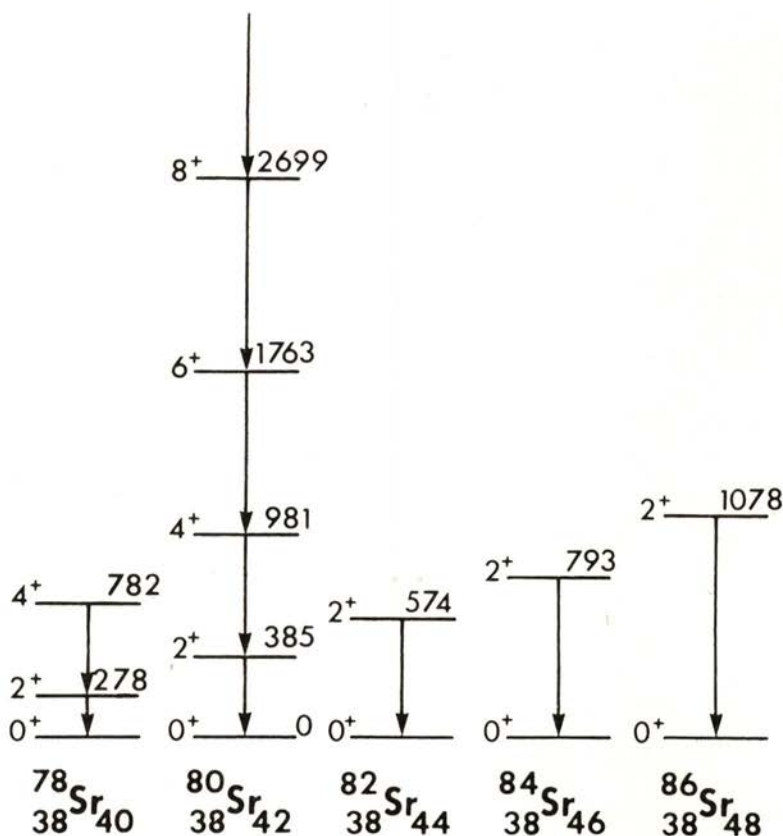Fig. 9 — Levels of ⁸⁰Sr seen in the reaction ³²S + ⁵¹V and of ⁷⁸Sr in the reaction ²⁴Mg + ⁵⁸Ni at the Holifield tandem [13, 14] are compared with the 2 → 0 energies in the heavier nuclei.

identify ⁷⁸Sr for the first time. Their lifetime measurements also confirm the large deformation. Thus, there is a continued increase toward large deformation at N = 38 in the light Sr nuclei.

The sudden onset of strong deformation also has been reported in ⁹⁸Sr (refs. 21, 22) and "super" deformation subsequently in

[100]Sr (ref. 20). The origin of this deformation was related [20] to a gap at $N = 60$ in the neutron Nilsson levels. The potential energy surfaces calculated for the Sr nuclei show minima at large deformation for both prolate and oblate shapes for $N = 60$ and 62, which are not present for $N < 60$ (Fig. 10). The experimental data
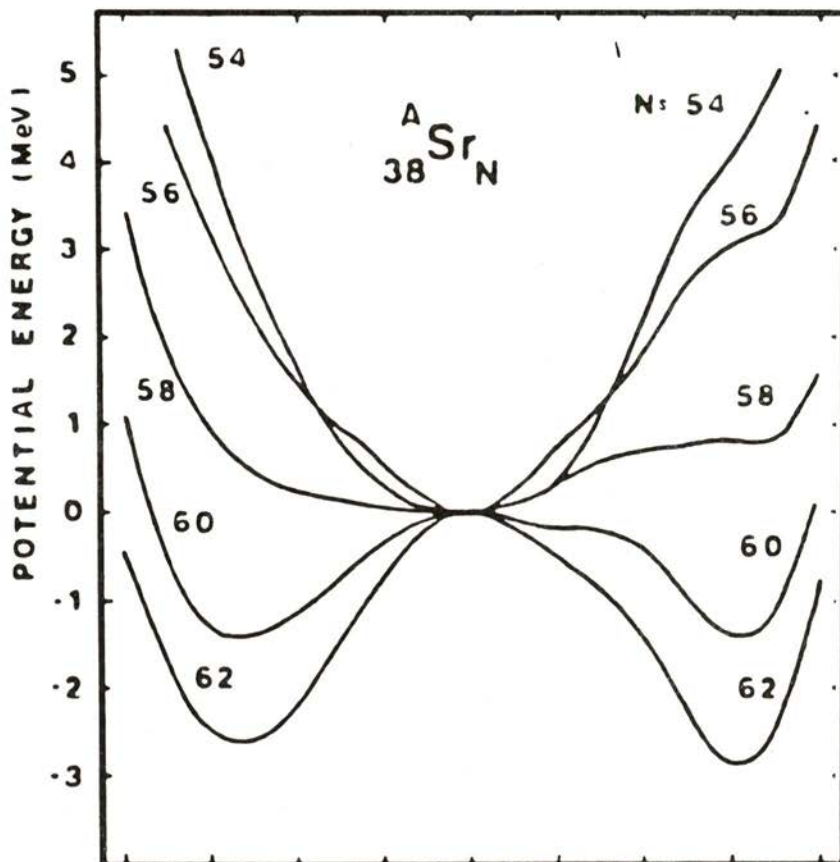

Fig. 10 — Potential energies calculated for Sr nuclei [20].

favor prolate deformation. Now we see this $N = 60$ gap can be strongly reinforced by the gap at $Z = 38$ at large prolate deformation. The reinforcement of these two gaps at similar large

14

prolate deformation is undoubtedly the cause of the sudden large deformation in [98, 100]Sr just as when both N and Z are near 38 they reinforce each other to give unusually large deformation in the [74, 76]Kr ground states. The importance of the gap at $Z = 38$ in deformation in this region is seen in that as one goes away from $Z = 38$ the deformation begins to decrease for the $N = 60$ and 62 nuclei, e.g., the 2_1-0_1 energies are 129.2, 151.9, and 192.2 keV for $N = 62$ $^{100}_{38}$Sr, $^{102}_{40}$Zr, and $^{104}_{42}$Mo (refs. 20, 23, 24).

Thus, we have found experimentally and supported by theoretical calculations two new regions of strong deformation; one around $Z = N = 38$ and the other for $Z = 38$, $N \geq 60$.

3 — NUCLEI UNDER CONDITIONS OF RAPID ROTATION

What happens to a nucleus at high spins is another of the major areas of nuclear structure research today as evidenced by the several recent international conferences in this field. Theoretical work of Bohr and Mottelson [25] developed for the deformed rare earth nuclei, indicates that as the angular momentum of a deformed nucleus becomes high the nucleus can carry angular momentum more efficiently by the alignment of the spins of pairs of nucleons along the rotation axis. At some spin one ends up with a phase transition so that all the angular momentum is carried in this manner by an oblate shaped nucleus. This occurs around 50 $\hbar$ in rare earth nuclei. At still higher angular momentum, the nucleus may go to a super deformed prolate shape before fission. In this paper we present evidence for the importance of collective rotations and alignment of pairs of particles to record energies in relatively light nuclei around $A = 70$ and possible evidence for the break off of the rotations and the phase transition around 50 $\hbar$ in [158]Er.

Here we describe two new approaches to study high spin states — partial fusion reactions and neutron multiplicity experiments. Here we will describe only two recent experiments to illustrate the new insights being gained. Another important, new advancement is the spin ball spectrometers developed at the Holifield Heavy Ion Laboratory and Max Planck Institute, Heidelberg. In these devices one has a large array of 70 or more NaI detectors that cover essentially a 4π solid angle to measure

all the γ-rays emitted. Results are just being reported from these systems [26]. The spin ball with a Ge(Li) detector was used to see discrete states in ^{158}Er to spin 40 $\hbar$ and above [26].

3.1 — *Two Discontinuities of $\mathcal{J}$ at High Spin in ^{74}Kr*

Two discontinuities of the moments of inertia, $\mathcal{J}$, of the yrast cascades in ^{158}Er and ^{160}Yb (refs. 27, 28), and very recently a third and possibly higher discontinuity of $\mathcal{J}$ in ^{158}Er (refs. 26, 29, 30) have provided evidence for the persistence of collective rotations and the alignment of individual pairs of quasiparticles to much higher spins than previously thought for deformed rare earth nuclei. As discussed in the previous section, recent evidence for strong ground state deformation was reported in $^{74, 76}$Kr based on data for states with $I^{\pi} \lesssim 10^{+}$ (ref. 10). With a newly developed neutron multiplicity technique [31] the yrast cascade in ^{74}Kr has been observed [32] to the highest spin reported for a medium-light nucleus, tentatively 20^{+}. Two discontinuities were observed in $\mathcal{J}$ of the yrast cascade in ^{74}Kr.

Backbending of $\mathcal{J}$ has been observed a 8^{+} in ^{68}Ge (ref. 6) and ^{80}Kr (ref. 33) with bands built on three 8^{+} states in ^{68}Ge and two 8^{+} states in ^{80}Kr. These two discontinuities at 8^{+} were interpreted as the crossing of rotation aligned bands built on both proton and neutron $(g_{9/2})^{2}$ configurations in ^{68}Ge. A similar interpretation is made [33] for ^{80}Kr.

The levels of ^{74}Kr were studied via the reaction ^{58}Ni $(^{19}$F, p2n$\gamma)$ ^{74}Kr at 66-68 MeV with $> 99\,\%$ enriched, thick targets. A recently developed neutron-multiplicity-γ coincidence technique [31] was essential to separate the weak neutron evaporation channel to ^{74}Kr from the competing charged particle channels. Four large liquid scintillator neutron detectors especially designed to cover most of the forward 2π solid angle were used to gate the γ-ray spectra. The overall neutron efficiency of about 30 % made it possible to apply this technique not only to (n, γ) and (n, n, γ) coincidences, but also to (n, γ, γ) measurements, angular distributions, and recoil distance lifetime measurements.

The level scheme of ^{74}Kr was known to 8^{+}. In Fig. 11 is shown the levels established on the basis of our n-γ-γ and
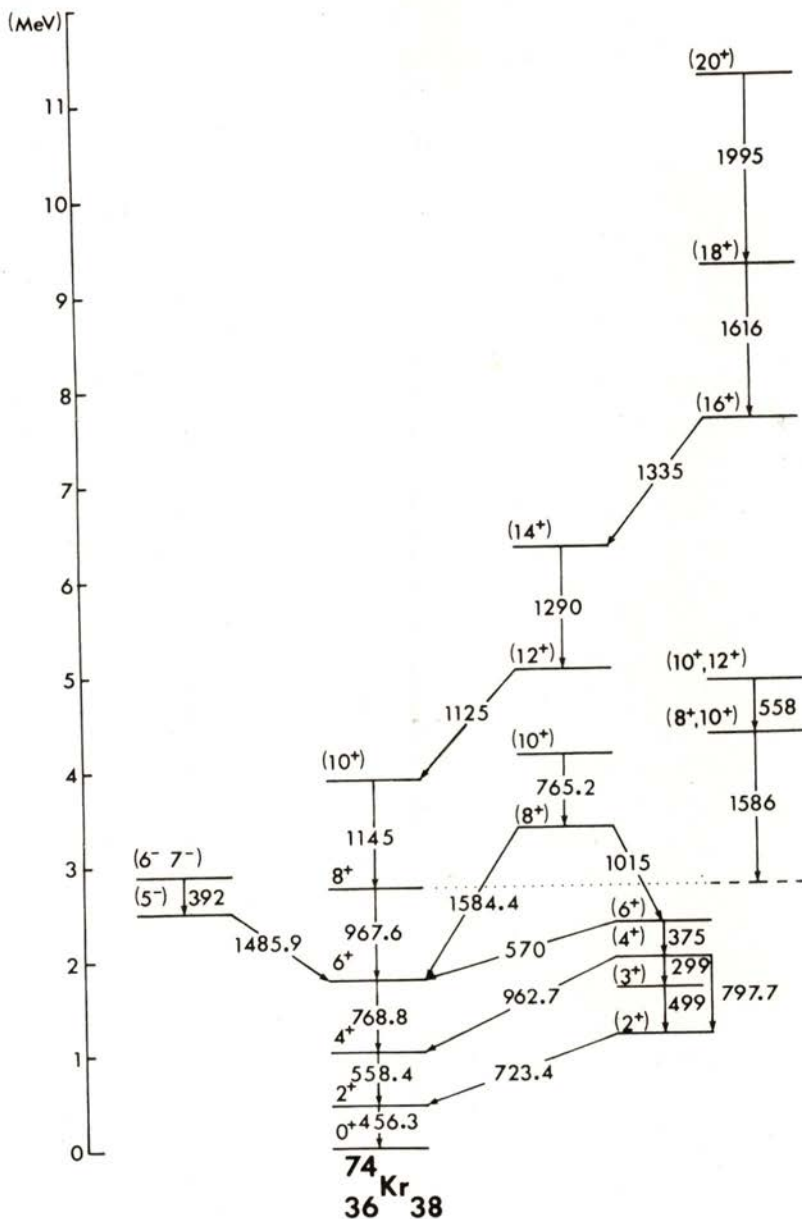
16

Portgal. Phys. — Vol. 14, fasc. 1-2, pp. 1-47, 1983

Fig. 11 — Levels in ⁷⁴Kr established from in-beam, neutron - γ coincidence studies [32, 34].

Portgal. Phys. — Vol. 14, fasc. 1-2, pp. 1-47, 1983

17

n - γ (θ) coincidence measurements with a beam energy of 66.5 MeV using a thick target and List-mode technique [32]. States up to a tentative 20^+ state were established. The multipolarities and mixing ratios of the γ - rays were deduced from an angular distribution measurement at the same energy. A γ - ray yield function and γ (θ) data and spectra obtained by gating with one and two neutron events and x^2 fitting procedure led to the spin assignments displayed in Fig. 11.

In Fig. 12 is shown a plot of the angular momentum I (ω) as a function of ω where $\hbar \omega = E_\gamma$ (($I + 1$) $\rightarrow$ ($I - 1$))/2 for our data for ^{74}Kr and other recent results for $^{76, 78}$Kr (refs. 10, 34). There are three discontinuities seen in I (ω) for ^{74}Kr. As discussed earlier, the break at 2_1^+ is interpreted as arising from an interaction of the strongly deformed 0_1^+ ground state and a low lying 0_2^+ near-spherical excited state to push down the 0_1^+ energy (and enlarge the $2_1^+ \rightarrow 0_1^+$ energy) [10]. In both ^{74}Kr and ^{78}Kr there are very similar discontinuities in I (ω) and correspondingly in $\mathcal{J}$ above 10^+. There is only a slight up bend of I in ^{76}Kr. However, in ^{80}Kr two 8^+ and 10^+ states are seen and are interpreted as the crossing of a two quasiparticle rotational aligned band with ($g_{9/2}$)^2 protons. In ^{74}Kr two 8^+ and 10^+ levels also are seen. The branching ratios and energies indicate the 8_2^+ and 10_2^+ levels form a band with the yrast 12^+ and (14^+) levels that cross the ground band above 10^+. This is in contrast to ^{80}Kr where the 8_1^+ and 10_1^+ levels are the two quasiparticle rotation aligned states. This first band to cross the ground band is interpreted as a two quasiparticle ($g_{9/2}$)^2 configuration, but it is not definite whether it is a proton or neutron configuration.

The second discontinuity of $\mathcal{J}$ occurs above 14^+ with the (16^+), (18^+), and tentative (20^+) states showing similar alignment. Their extra alignment is about the same as the extra alignment in the first band, 2-3 units. No such break in I is seen in the tentatively assigned 16^+ level in ^{78}Kr (ref. 35) which has 4 more neutrons. These data suggest a blocking effect of the extra neutrons and indicate at least two of the four quasiparticles in the highest band in ^{74}Kr are neutrons. In summary, these data provide the first evidence for a second high spin discontinuity
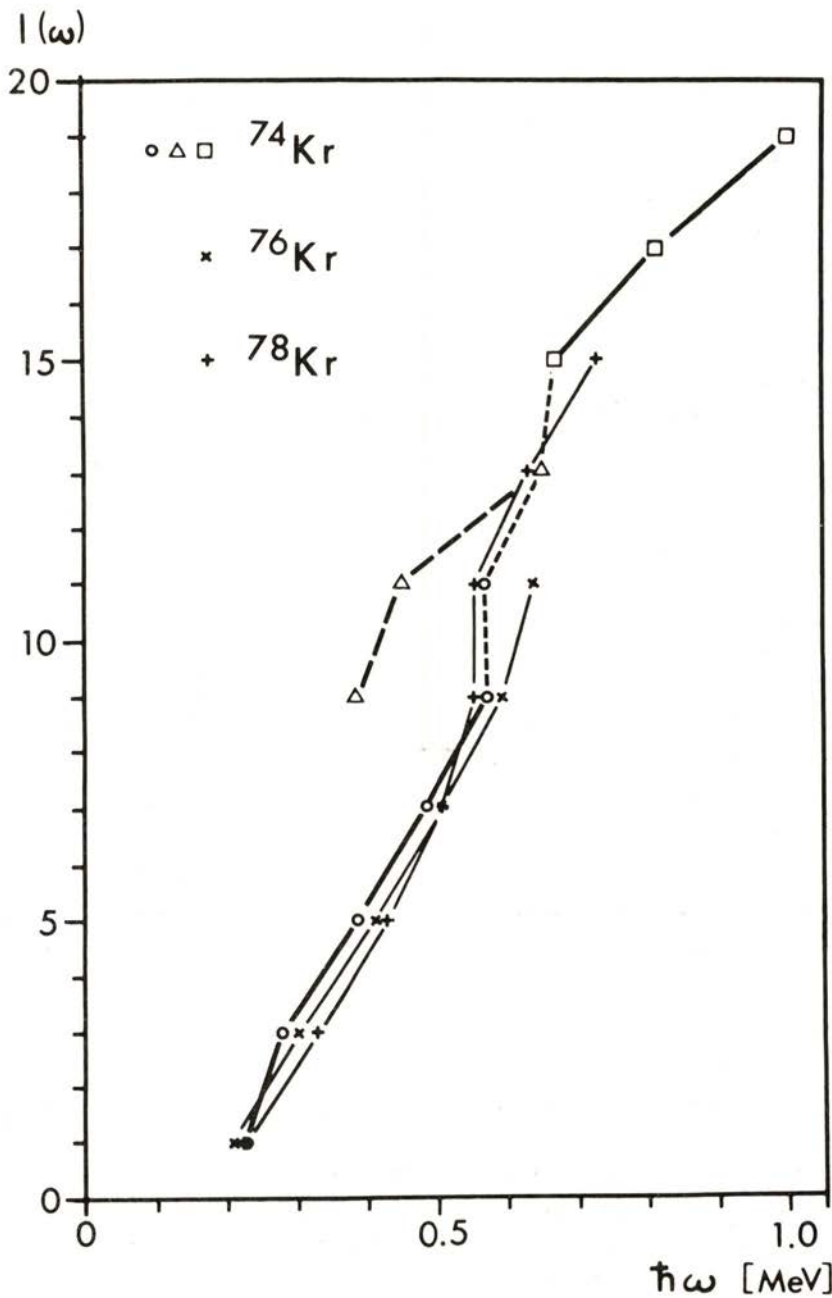
18

Fig. 12 — Plot of the angular momentum I (ω) as a function of ω (ref. 32).

in $\mathcal{J}$ in a medium-light nucleus and that collective rotations and the alignment of individual two quasiparticle configurations continue to very high energies in this region.

3.2 — *Third and Higher Discontinuities of $\mathcal{J}$ at High Spin in* ^{158}Er

The partial fusion reaction, PFR, in which a fast p, d, or t is emitted in the forward direction followed by the fusion of the remaining part of the projectile is a very promising new way to study nuclei at very high angular momentum. Yamada et al. [35, 29] have studied this reaction by bombarding $^{150,\ 154}Sm$ with 167 MeV ^{14}N from the Oak Ridge Cyclotron ORIC. The evaporation p, d, t are separated in energy from those from PFR. By gating on the fast p, d, t, the gamma ray multiplicity was measured in the ^{14}N reactions on ^{154}Sm that lead to $^{157-159}Er$. The ^{158} reaction was more than 50 % of the observed PFR and the gamma-rays from the decay of states to over 40^+ were observed in ^{158}Er.

As shown in Fig. 13, the gamma ray multiplicity is constant as a function of the spin of the yrast states to as high as statistics allow measurement, spin 26, for all three reactions p, d, t that lead to ^{158}Er. A similar multiplicity was measured for the reactions leading to $^{157,\ 159}Er$. These data indicate no side feeding below $I = 28$. The average M_γ is 31. This is the highest M_γ presently observed. The mass distribution of the residual nuclei also is appreciably more narrow than that for compound nuclear reactions. Both of these data indicate that the PF reactions in which p, d, or t are emitted are associated with a narrow, high angular momentum window [35]. The deduced average angular momentum transferred is 63 $\hbar$ which is comparable to the critical angular momentum l_{cr} predicted for the fusion of ^{13}C and ^{154}Sm.

With this high, narrow l window, the PF reaction should be a very useful tool to study nuclei at high angular momentum. Further support for this is seen in our ^{158}Er studies. In our second ^{158}Er experiment, the same PF reaction was studied with three large, well collimated NaI detectors to obtain an E_γ - E_γ correlation spectrum [29]. The E_γ - E_γ correlation method is a powerful method. To show that it is useful with NaI detectors we carried out very extensive Monte Carlo simulation calculations. These

20

Portgal. Phys. — Vol. 14, fasc. 1-2, pp. 1-47, 1983

calculations show that indeed with the order of one to five million events if the background is reasonably low, one can easily study the valley to quite high spins, of the order of 50 $\hbar$.
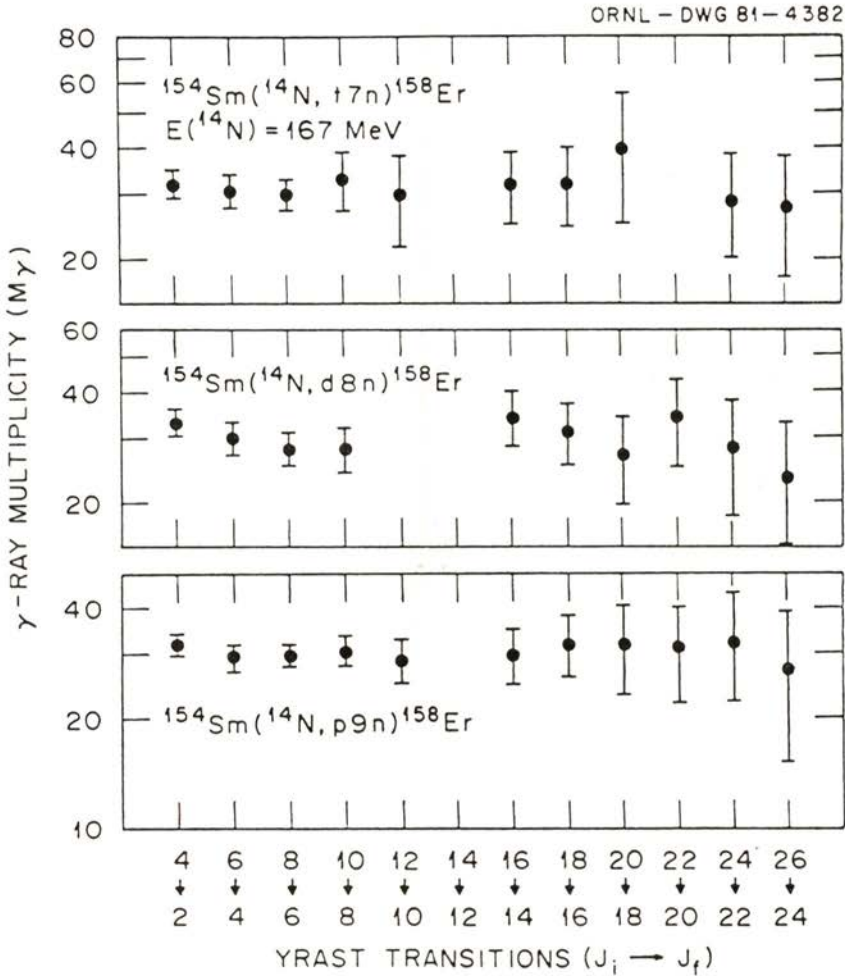

Fig 13 — Measured γ-ray multiplicities in [158]Er from PF reactions [35].

The measured and simulated spectra reproduced the known first three backbends of $\mathcal{J}$ in [158]Er very nicely. The third backbend

at 1.1 MeV was in fact observed in our data (see Fig. 14) prior to its observation from discrete gamma-ray energies [30]. These data with the Copenhagen iteration method applied to subtract
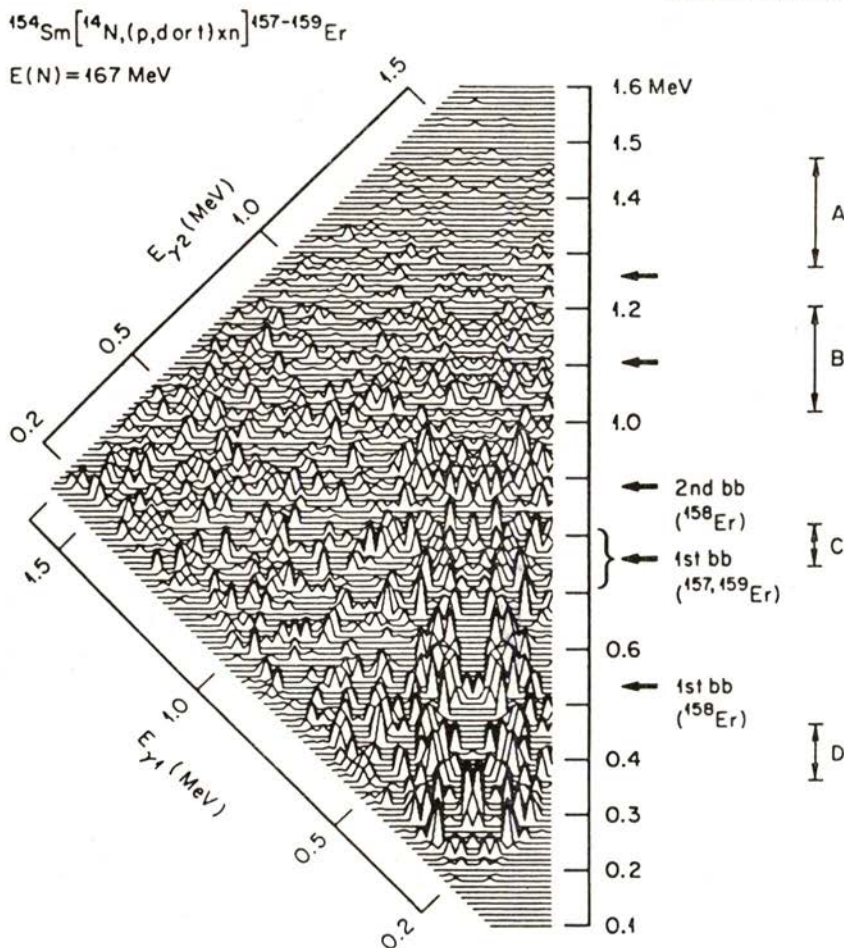

Fig. 14 — E_γ - E_γ correlations in [157-159]Er (ref. 29).

background are from five million events as compared with the 50 million required for Ge (Li) work. The difference in numbers of events required to obtain significant spectra is the essentially

22

five times higher photo peak efficiency for NaI compared to Ge (Li) detectors and the fact that the PF reactions lead to a high l-window so that many of the side feeding γ rays at lower spins are not present, e.g., the background is much reduced. Note in addition to the third backbend of $\mathcal{J}$, one sees evidence for other bridges at 1.24 and perhaps 1.46 MeV (ref. 29). These bridges are in reasonable agreement with Cranked Shell Model calculations of the next crossings produced from the alignment of the next pairs of quasiparticles [36]. The most important information from these data is the observation that the valley continues to an energy of 1.46 MeV. This valley indicates the continuation of collective excitations to this energy — the highest energy observed to date. These data support the continuation of collective motion up to a spin about $48\,\hbar$. The breakoff of the valley above 1.46 MeV can be the signal for the predicted change of phase from superfluid to normal states associated with a quenching of the pairing field [25]. This is predicted to lead to a change to an oblate shape where the angular momentum is carried by pairs of aligned particles. As discussed in more detail in another paper (Yamada and Hamilton) [29], we believe these data provide evidence for this phase change and that the change is rather sudden.

In summary, these are but two examples of nuclear research that is probing the structures of nuclei at high angular momentum. They show that indeed such studies are important from light to heavy nuclei and are providing us with fascinating new insights into how nucleons behave individually and collectively under extreme conditions of rotation.

4 — NEW CONCEPT OF THE VACUUM AND NUCLEAR MOLECULES WITH $Z = 184$

Since the days of the early Greek natural philosophers our view of the physical world has been dominated by certain paradigms, i.e. specific pictures, for selected physical entities. Such entities are space, time and matter as the basis of natural philosophy or, more specifically, of physics. Therefore, it is no surprise that our conception of the "vacuum", intimately connected with the picture of space, time and matter, ranges among the most

fundamental issues in the scientific interpretation of the world. This section draws upon earlier reviews of this field [37, 38].

The picture of the vacuum has undergone perpetual modifications during the last twenty-five centuries as the available technologies have changed; often old, abandoned ideas have been resurrected when new information became accessible. Many aspects of today's conception of the vacuum date back to the ancient Greek philosophy, but have only recently been established by modern experiments.

Over the centuries many different conceptions of the vacuum were developed by scientists, different vacua as carriers for different kinds of physical phenomena. We mention Newton's absolute space, on which the hypothesis of the vacuum as an elastic medium, the "ether", is based. It was developed in the early 19th century when the wave nature of light had been firmly established — in close analog to the theory of elasticity. In Einstein's theory of relativity and gravity the absolute space and the "ether" were abandoned and replaced by a bundle of inertial frames.

Quantum mechanics and quantum field theory, finally, laid the grounds for our present conception of the nature of the vacuum. In today's language, the vacuum consists of a polarizable gas of *virtual* particles, fluctuating randomly. It is found that, in the presence of strong external fields, the vacuum may even contain "real" particles. The paradigm of "virtual particles" not only expresses a philosophical notion, but directly implies observable effects:

1) The occurrence of spontaneous radiative emission from atoms and nuclei can be attributed to the action of the fluctuations of the virtual gas of photons.

2) The virtual particles cause effects of zero-point motion as in the Casimir effect. (Two conducting, uncharged plates attract each other in a vacuum environment with a force varying like the inverse fourth power of their separation.) Hawking's effect of pair formation by a collapsing body may also be understood as a gravitational Casimir effect.

24

Portgal. Phys. — Vol. 14, fasc. 1-2, pp. 1-47, 1983

3) The electrostatic polarizability of the virtual fluctuations can be measured in the Lamb shift and Delbrück scattering.

However, the most fascinating aspect of the vacuum of quantum field theory, which will be discussed here, is the possibility that it allows for the creation of real particles in strong, time-independent external fields. In such a case the normal vacuum state is unstable and decays into a new vacuum that contains real particles. This, in itself, is a deep philosophical insight. But it is more than an academic problem, for two reasons: first, very strong electric fields are available for laboratory experiments that are presently in progress; second it can be shown that the quantum theory of interacting fields may be constructed from the vacuum-to-vacuum amplitude W (J) of a quantized field in the presence of an arbitrary external source J. Effects that occur in strong external fields may, therefore, in some way be carried over to strongly coupled, interacting fields as they form the basis of the strong and superstrong interactions. Only recently have extensive theoretical studies in Frankfurt and independently in the Soviet Union led to new insights and full theoretical clarification of the strong field problem [39].

4.1 — *The Decay of the Vacuum*

The decay of the vacuum in strong electrostatic fields is a relative recently recognized phenomenon in quantum electrodynamics that can be studied only via low-energy heavy-ion collisions. The original motivation for developing the new concept of a charged vacuum arose in 1965-70 in connection with understanding the atomic structure of superheavy nuclei expected to be produced by the GSI-heavy ion linear accelerator.

The best starting point for discussing this concept is to consider the binding energy of atomic electrons as the charge of a heavy nucleus is increased. In view of the large mass of the heavy nucleus compared to the electron mass, the external field approximation is quite appropriate. Solving the Dirac equation in the presence of an electromagnetic field gives the well-known fine

structure formula, first derived by Sommefeld from the early theory of the atom:

$$E(nj) = m_0c^2 \left[1 + \left(\frac{Z\alpha}{n - |K| + \sqrt{K^2 - Z^2\alpha^2}} \right)^2 \right]^{1/2} \tag{1}$$

$n = 1, 2, \dots\dots\dots\dots\dots$ = principal quantum number;
$K = \pm 1, \pm 2, \dots\dots\dots$ = azimuthal quantum number;
$\alpha = e^2/c\hbar \dots\dots\dots\dots$ = fine-structure constant.

Because of the term $[K^2 - Z^2\alpha^2]^{1/2}$, equation (1) breaks down at $Z\alpha > |K|$. Thus all states with $j = 1/2$ cease to exist at $Z = 1/\alpha = 137$, as shown in Fig. 15: the corresponding wave function becomes non-normalizable at the origin; $E(1s_{1/2})$ becomes zero, i.e. the K-shell binding energy goes to $-m_0c^2$. Note from Fig. 15 that the energy levels move only very slowly away from the upper continuum as Z rises until $Z = 137$ is approached rather closely. Thus, even in the heaviest known element, the binding is only a small fraction of the rest energy.

The $Z = 137$ 'catastrophe' was well-known· but it was argued loosely that it disappears when the finite size of the nucleus is taken into account. But Greiner and his coworkers showed that the problem is not removed but merely postponed and reappears at $Z \sim 173$; the exact value of this critical Z depends on many assumptions concerning the potential in the vicinity of the nucleus, in particular the nuclear radius. One can trace any level $E(nj)$ down to a binding energy of twice the electronic rest mass if the nuclear charge is increased as a parameter. At the corresponding charge number, which we shall call Z_{cr}, the state reaches the negative-energy continuum of the Dirac equation ('Dirac sea') which, according to the hole-theory hypothesis, is totally occupied by electrons. (The hole theory of Dirac is completely equivalent in its predictions to field theory). If the strength of the external field is further increased, the bound state dives into the continuum. The overcritical state acquires a width and is spread over the continuum. Still, the electron charge distribution does remain localized.

When Z exceeds 145, $E(1s_{1/2}) < 0$, i.e. the binding energy exceeds the rest mass of the electron. Adding the electron therefore diminishes the mass of the atom. It would be energetically advantageous for an electron to be spontaneously created, thereby
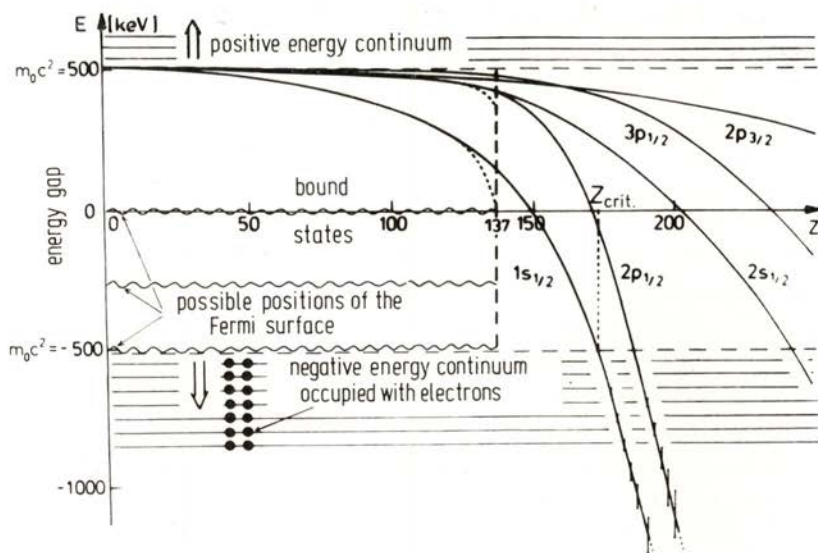
Fig. 15 — Lowest bound states of the Dirac-equation for nuclei with charge Z. While the Sommerfeld-eigenenergies (dashed lines) for $j = 1/2$ end at $Z = 137$ the solutions with extended Coulomb potential (full lines) can be traced down to the negative energy continuum which is reached at critical charge Z_{cr}. The states entering the continuum obtain a spreading width as indicated by the bars (magnified by a factor of 10). If the state was previously unoccupied two positrons will be emitted spontaneously.

reducing the total energy. This is not possible because it would violate the conservation of charge and lepton number. Similarly, when $Z > Z_{cr}$ a K-shell eletron is bound by more than twice its rest mass, so that it becomes energetically favorable to create an electron-positron pair. Now, however, the spontaneous appearance of such a pair is not forbidden by any conservation law. The electron becomes bound in the $1s_{1/2}$ orbital and the positron escapes.

We say that the overcritical vacuum state is charged. This has the following meaning. As already stated, within the hole theory, which is a lucid model for interpreting the field theoretical (quantum electrodynamical) calculations, the states of negative energy are occupied with electrons. This was postulated by Dirac to avoid the decay of electronic states with emission of an infinite amount of energy. In the undercritical situation we can define a

vacuum state $|0>$ without charges or currents by choosing the Fermi surface (up to which the levels are occupied) below the lowest bound state: we set $E_F = -m_0 c^2$. The negative-energy continuum states occupied with electrons represent the model for this vacuum; its infinite charge is renormalized to zero, and so it is a *neutral* vacuum. If now an empty atomic state dives into the negative continuum, it will be filled spontaneously with an electron from the Dirac sea with the simultaneous emission of a free positron moving to infinity. The remaining electron cloud of the supercritical atom is necessarily negatively charged. Thus, the vacuum becomes *charged*.

An atom with $Z > 173$ and an empty K-shell will spontaneously shield itself by two K-electrons and emit two positrons of rather well-defined energy. This two-electron state becomes the stable state, and it forms in a time scale of about 10^{-20} sec. If the central charge is further increased to $Z = 184$ (diving point of the $2p_{1/2}$ level), the vacuum acquires a charge of -4e. With increasing field strength, more and more electronic bound states join the negative continuum, and each time the vacuum undergoes a new phase transition and becomes successively higher charged: the vacuum sparks in overcritical fields.

Clearly, the charged vacuum is a new ground state of space and matter. The normal, undercritical, electrically neutral vacuum, is in overcritical fields no more stable: it decays spontaneously into the new stable but charged vacuum. Thus the standard definition of vacuum, "a region of space without real particles", is not true in very strong external fields. It must be replaced by the new and better definition, the "energetically deepest and stable state that a region of space can have while being penetrated by certain fields" (see Fig. 16).

4.2 — Superheavy Quasimolecules in Heavy-Ion Scattering

Inasmuch as the formation of a superheavy atom of $Z > 173$ is very unlikely, a new idea is necessary to test these predictions experimentally. That idea, based on the concept of nuclear molecules was put forward by Greiner and co-workers in 1969: a *superheavy quasimolecule* forms temporarily during the slow collision of two heavy ions.

It will be sufficient to form the quasimolecule for a very short instant of time, comparable to the time scale for atomic processes to evolve in a heavy atom, which is typically of the order 10^{-18} - 10^{-20} sec. Consider the case where a U ion is shot at
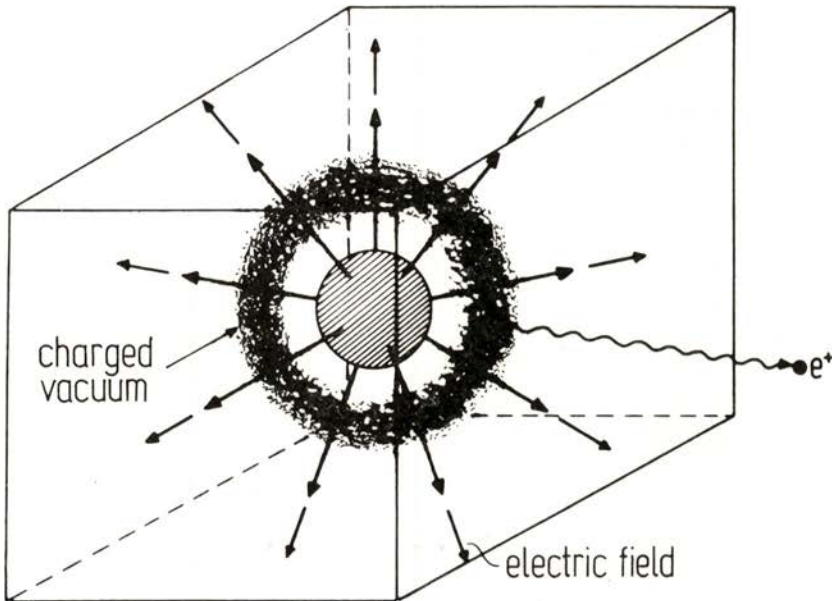

Fig. 16 — In overcritical fields space becomes charged through the emission of antiparticles. In principle the vacuum is no longer empty under these conditions. The shaded sphere in the center represents the superheavy nucleus, the source of the electric field indicated by arrows; the diffuse cloud represents the electrons of the charged vacuum. If this electron cloud is pumped away, new positrons (represented by e^+) will be emitted and the cloud will reappear. Hence under the extreme conditions of supercritical fields the vacuum is no longer empty: the vacuum is sparking.

another U ion at an energy corresponding to their Coulomb barrier and the two, moving slowly (compared to the K-shell electron velocity) on Rutherford hyperbolic trajectories, are close to each other (compared to the K-shell electron orbit radius). The two ions can be brought together as close as 20 fm for a time of $\sim 10^{-21}$ sec. Then the atomic electrons move in the combined Coulomb potential of the two nuclei, thereby experiencing a field

corresponding to their combined charge of 184 (Fig. 17). This happens because $v_{ion} \sim c/10$, $v_{el} \sim c$: the ionic velocity is much smaller than the orbital electron velocity, so that there is time for electronic molecular orbits to be established while the two ions are in the vicinity of each other.
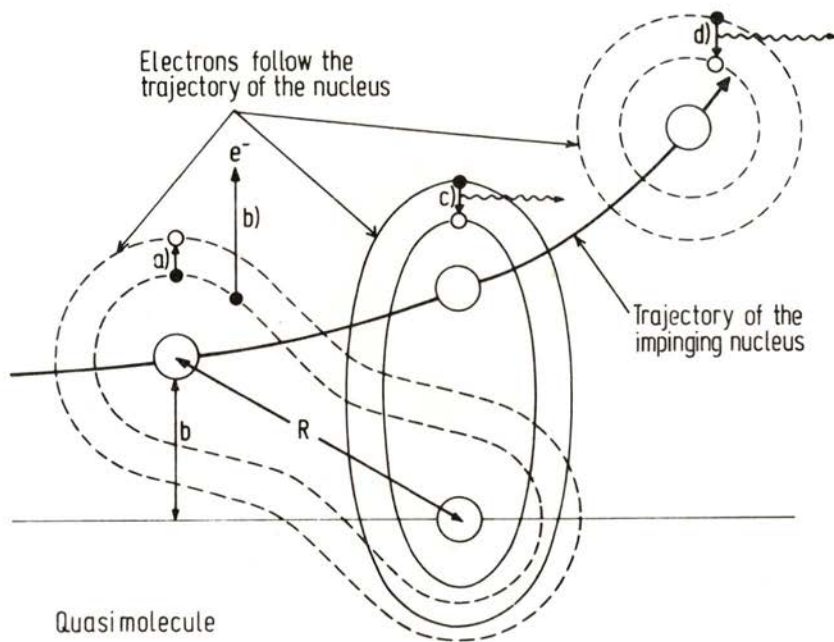

Fig. 17 — The basic concept concerning the formation of quasi molecules is shown. In the collision of two heavy ions the inner electrons orbit both nuclei together. The electron orbits follow the motion of the nuclei. Both nuclei are shown and their paths are indicated. The distance of closest approach is called the impact parameter. Processes of type a) (excitations of electrons into higher shells) and of type b) (excitations of electrons into the upper continuum) empty the K-shell. Processes c) and d) indicate the molecular and atomic X-ray transitions, respectively. The molecular X-rays are emitted from the intermediate quasi molecule, while the atomic X-rays are emitted from the rearranged atom after the collision.

The condition $v_{ion}/v_{el} \sim 1/10$ is known as adiabaticity. It will not help to make v_{ion} even smaller such that complete adiabaticity is achieved: for it is a partial breakdown of adiabaticity that

makes the inner shells of the quasimolecule ionized, i. e., empty of electrons, which, as we saw earlier, is a necessary prerequisite for the emission of positrons and the accompanying filling of the inner shell with electrons as it dives into the negative continuum.

When the two U atoms are separated by a large distance, the $Z = 184$ system is undercritical (i.e., all levels are bound by less than $2m_0 c^2$). It becomes overcritical at small R as the electrons experience the full combined charge. For the $1s_{1/2}$ level the critical separation occurs at $R_{cr} = 35$ fm. The diving is very steep as a function of R. The level energies change rapidly only in the last 150 fm of the approach to the quasimolecule. This steep diving is important for the production of K holes (see the schematic Fig. 17).

4.3 — *Dynamical Processes in Heavy-Ion Collisions*

Several dynamical processes contribute to the ionization of the inner shells and to the production of positrons in undercritical as well as overcritical systems. This is illustrated in Fig. 18 for a system that becomes overcritical at small distances. In processes *a*) and *b*) one has electron excitation and ionization. Process *c*) is the spontaneous filling of a previously produced vacancy when the level acquires a binding greater than $2m_0 c^2$ and is the decay of the vacuum described earlier. Because of the lack of full adiabaticity, energy can be drawn from the nuclear motion to lead to filling of the hole even at distances larger than R_{cr}. This effect (*d, e*) may be called an *induced transition,* and its effect on positron production is twofold: it causes a washed-out threshold for the spontaneous positron production, and it greatly enhances the production cross section. *f*) is the direct pair production process, which we now proceed to discuss in more detail.

Whereas in ordinary pair production in a Coulomb scattering process a photon is exchanged between two hadrons only once, now there are multiple interactions with the joint Coulomb field of both nuclei. Because of the very strong field, the cross section for the pair production varies as $(Z_1 + Z_2)^{19}$, which means that about 19/2 (!) photons are exchanged. This behavior illustrates the nonperturbative character of this process, which (like the induced decay mechanism) overwhelms the spontaneous positron

production process. The pair production process f) can be inter-
preted as the shake-off of the vacuum polarization (VP) cloud.

It is clear that a K hole is needed for the production of
positrons by either the spontaneous or the induced mechanisms.
Since neither the projectile nor the target atom has a K hole to
start with, it has to be produced dynamically via Coulomb excit-
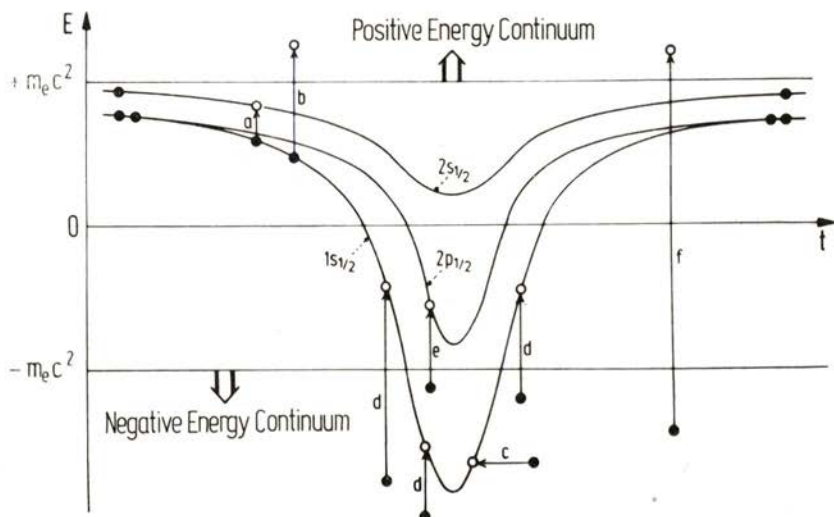ation or ionization (processes a and b of Fig. 18) in the collision

Fig. 18 — Dynamical processes connected with positron production in overcri-
tical heavy-ion collisions. The figure shows the inner electron levels in the
quasimolecule as a function of time. At the deepest point of the 1s level,
the colliding nuclei are at the distance of closest approach.

> a, b: electron excitation and ionization,
> c: spontaneous autoionization of positrons,
> d, e: induced decay of the vacuum,
> f: direct pair creation.

itself. K-hole production occurs whenever the wavefunctions
change so rapidly with R that the electrons can not adjust to the
nuclear motion (breakdown of adiabaticity) and therefore get
kicked out as δ electrons. Because of the rapid change of the
wavefunctions at the onset of diving, vacancy production in the
inner shell is concentrated at small values of R, which is advan-

tageous for the observation of induced and spontaneous positron emission.

The total K shell vacancy probability in the diving region for a U-U collision at an energy of 1600 MeV is predicted to be about 10 %, which is fully confirmed by recent experiments. [This includes both excitation and ionization, through one-step as well as multistep channels (see later)]. The other 90 % of the K electrons adjust to the nuclear motion, and hence the adiabaticity necessary for the theoretical treatment is generally valid.

The energy spectrum for positrons created in an e.g., Uranium-Uranium collision, consists of three components: the induced, the direct and the spontaneous one, which add up to a smooth spectrum. The presence of the spontaneous component leads
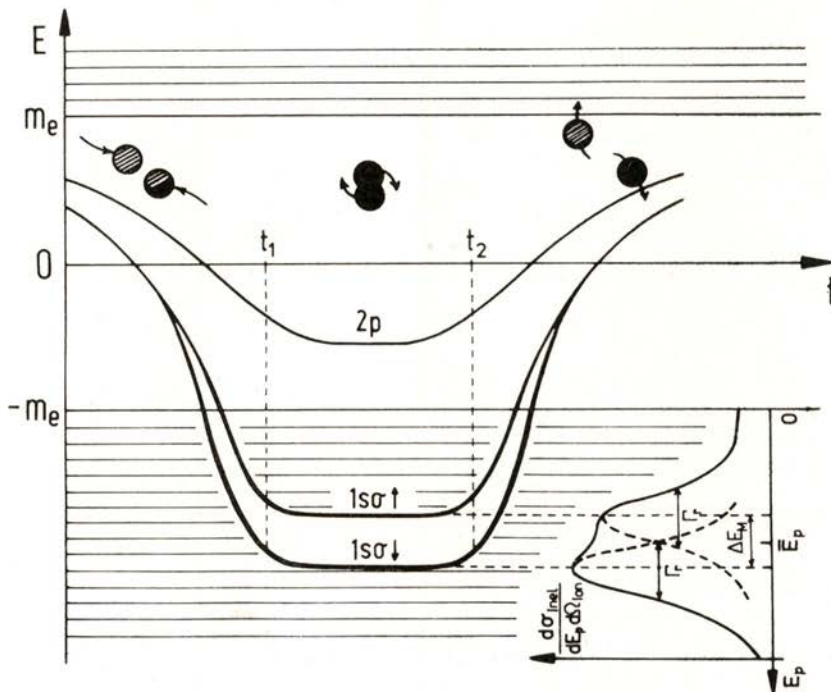
Fig. 19 — The innermost shells of the superheavy molecule (atom) as a function of time. Due to the sticking of the two nuclei, the superheavy atom lives for the time τ, thus being able to emit positrons spontaneously. There are in general two positron lines because of the Zeeman-splitting due to the strong magnetic fields from the heavy ion currents.

Portgal. Phys. — Vol. 14, fasc. 1-2, pp. 1-47, 1983

33

only to 5 - 10 % deviations for normal nuclear collisions along Rutherford trajectories. The question arises: Is there any way to get a clear qualitative signature for spontaneous positron production, as opposed to detecting it through a quantitative comparison with theory? Suppose that the two colliding ions, when they come close to each other, stick together for a certain time Δt before separating again. This will in general require the use of bombarding energies slightly above the Coulomb barrier. Then the quasimolecular levels in the overcritical region get stretched out as shown in Fig. 19 which is to be contrasted with Fig. 18. (The splitting in the energy of the $1s\sigma$ level arises from the Zeeman effect.) During the sticking, the energies of the electronic states do not change, and this has two effects: a) the emission of positrons from any given state occurs with a fixed energy; b) the induced production mechanisms do not contribute, whereas the spontaneous production (for overcritical states) continues to contribute.

The longer the sticking, the better is the static approximation. For Δt very long, one sees in the positron spectrum a very sharp line with a width corresponding to the natural lifetime of the resonant positron-emitting state (~ 3 keV for the U-U system). The observation of such a sharp line will not only indicate the spontaneous decay of the vacuum but also the formation of superheavy nuclear systems ($Z \gtrsim 180$) [40].

Naturally one is also interested in the question of what happens if the two nuclei stick, but for some yet unknown reason the $1s_{1/2}$ - level of an overcritical system does not dive, i.e., the neutral vacuum will not decay. Then an oscillatory structure as a function of the positron energy develops, which arises from the delayed interference between the incoming and the outgoing positron-creation-amplitudes along the trajectory of the colliding heavy ions. The positron spectrum will then have an oscillating structure as a function of positron energy from which the sticking time and even the structure (deformation, excited states) of the superheavy nuclear system can be deduced. In other words, we are dealing here with an *atomic clock* for short-living exotic nuclei. Because of the non-existence of a spontaneous amplitude in this case, the spontaneous positron emission line does not occur [40].

The search for spontaneous positron emission in heavy-ion collisions began in 1976 with the first acceleration of uranium

beams at Gesellschaft für Schwerionenforschung (GSI) in Darmstadt, West Germany. Experiments at this laboratory have utilized three detection systems, which have pursued complementary aspects of the problem [41-43]. We should note that in connection with these experiments it was necessary to establish that the conditions for forming quasimolecules could be met for the nuclear velocities required to achieve internuclear separations sufficiently small to produce overcritical binding. It was also critically important to demonstrate that the production probability for $1s\sigma$ vacancies was both large in magnitude and concentrated at small internuclear separations. There are several evidences for the formation of quasimolecules in heavy ion collisions such as δ electrons and molecular-orbital X rays (see review 38). Here we concentrate on the search for detection of spontaneous positron production.

One of the first experimental goals in the search for spontaneous positron emission was to determine the rate at which positrons are produced from the atomic processes relative to the rate at which they are produced from nuclear effects such as internal pair conversion of nuclear transitions. The first measurements [42] on the Pb^{208} - Pb^{208} collision system played a particularly important role in this respect and in confirming our theoretical understanding of the dynamic processes of positron production in heavy-ion collisions.

Measurements [43] on Pb-U and U-U collisions have carried these investigations into heavier systems, but under different and more complex background conditions. To investigate the consequences of this nuclear background in more detail, researchers carried out a systematic investigation of the ratio of positron intensity to γ - ray intensity over a broad range in Z. When Z_u, the combined nuclear charge $Z_1 + Z_2$, exceeds about 160, there is a spectacular increase in the total positron yield over that expected from nuclear internal pair conversion as it is extrapolated from the positron to γ-ray ratios measured for $Z_u < 160$. More precisely, for constant R_{min} and relative velocity, the production of positrons in superheavy collision systems is found to increase as $(Z_1 + Z_2)^{21}$. In this striking feature, which seems to have no other analog in nature, the theory [44] of dynamic positron creation in heavy-ion collisions again anticipated the experimental results.

The most recent experiments [45-48] have focussed on studying positron spectra and on extending the investigations to collision systems with higher total nuclear charge. With more comprehensive data, new phenomena have appeared that may be connected with the effects being sought. Of special interest are peak-like structures in the positron energy distribution. The most compelling evidence for these comes from experiments [45, 48] where coincidences between two scattered ions are used to define clearly events with two-body final states consistent with, or bordering on, elastic scattering. We illustrate these interesting results with an example.

The uranium-curium collision system, with $Z_u = 188$, has the largest combined nuclear charge investigated to date. Fig. 20 shows positron spectra from uranium-238 and curium-248 colliding at an energy close to that of the Coulomb barrier. Particularly striking in Fig. 20 is the well-defined peak centered at an energy of about 320 keV. The height of this peak above the smoother continuum is correlated with the choice of two-body final states corresponding to a selected range of scattering angles for the two heavy ions.

By comparison, if one singles out scattering angles more forward than those selected in Fig. 20 this peak is largely excluded. One finds a spectrum that mirrors the general shape of the continuum underlying the peak in Fig. 20. The continuum distributions are well represented by the spectra we expect [44] from the dynamically induced processes at the corresponding scattering angles. As we will see, it is also significant to find that the measured width of the peak in Fig. 20 is less than 100 keV. Moreover, this width is consistent with the Doppler broadening expected for a positron line spectrum emitted from a system moving with the velocity of the quasimolecular system. Therefore, the intrinsic width of the peak is surely less than 100 keV and, indeed, it could be very much smaller than this value.

Whatever the source of the peak, it is apparent that we must seek an explanation outside the scope of the theory based on Rutherford scattering alone, because this theory of dynamic positron creation does not allow for narrow peak structures in the positron spectrum. Deviations from this theory also have been demonstrated [45-47] for U-U collisions in other experiments

carried out at GSI. All experiments carried out to date indicate that there is a new source of positrons — a source that does not
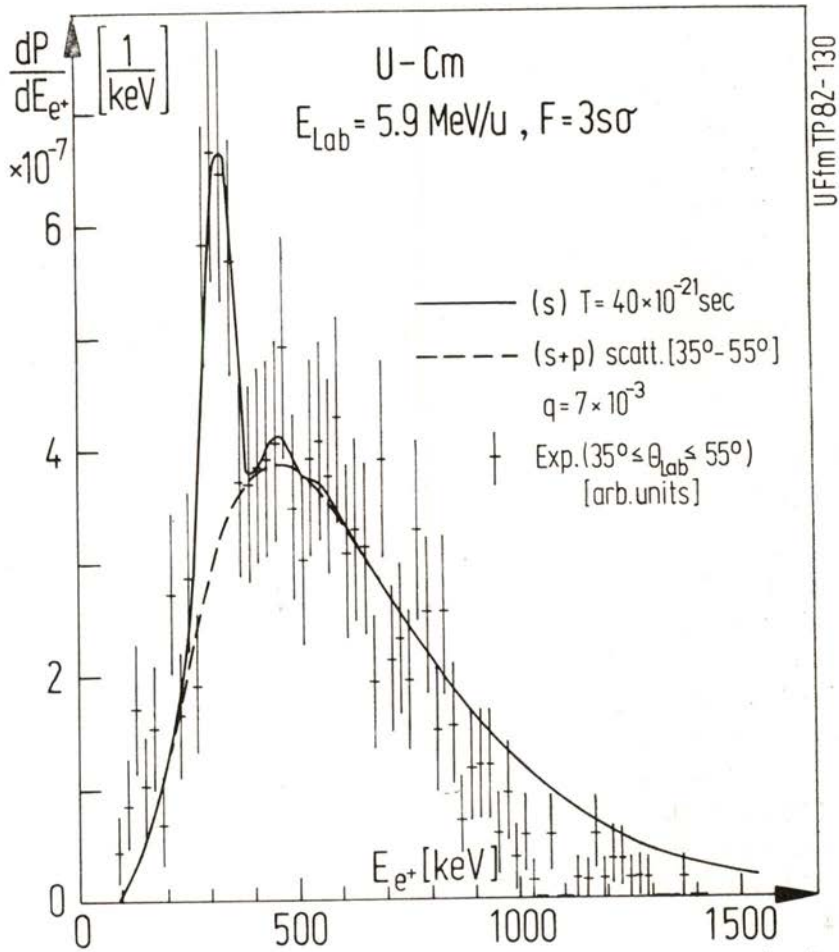

Fig. 20 — Positron spectra from 5.8 MeV/amu uranium-curium collisions. The full curve represents the theory. The line structure can only be understood, if a rather long-living (~ 10⁻¹⁹ sec) giant nucleus is formed.

originate with the known dynamic mechanisms associated in a simple way with the time-varying electric field produced in Coulomb trajectories.

It is also difficult to attribute these deviations from smooth positron spectra to pure nuclear effects. There are two prominent candidates:

— the internal pair conversion of a nuclear transition leading to a positron energy distribution that may be peaked,

— the internal pair conversion process followed by the capture of the electron into empty atomic orbits, which leads to positron line spectra.

The relatively narrow peak shapes that appear seem to preclude the former, while intensity considerations exclude the latter by orders of magnitude. But to exclude any connections with nuclear transitions, we need additional direct studies of these and other effects, and work is in progress toward this goal.

Of course, the observation of the U-Cm system's line-like positron spectrum, and the fact that it seems to appear only under particular scattering conditions, opens up to serious consideration the possibility that we may be observing the spontaneous emission of positrons. We are encouraged by the fact that this peak happens to occur at an energy consistent with a calculation [40] of the $1s\sigma$ resonance energy in the U-Cm quasiatom. Obviously, a systematic confirmation is required to follow up on these very suggestive data, but these new developments already raise the possibility of another important observation. For if the narrow positron peak does indeed represent spontaneous positron emission, the parent nuclear supercritical charge must exist for a long time compared to the collision times for scattering beneath the Coulomb barrier, as we pointed out earlier.

Therefore, Reinhardt, Müller, Müller and Greiner [40] suggested that the observation of spontaneous positron emission as a sharp line necessarily implies that, at bombarding energies close to that of the Coulomb barrier, a metastable superheavy nuclear composite system forms with a lifetime long enough to account for the relatively narrow peak. Widths of 100 keV or less correspond to lifetimes for the dinuclear system longer than about 40 times the Rutherford scattering collision time, during which the $1s\sigma$ state is overcritically bound. Indeed, without introducing a time delay it is difficult to invent any mechanism associated

with atomic positron emission that would explain the narrow peak width found in the U-Cm spectrum or the positron distribution emitted from the U-U collisions. Such a delay could be supplied by the formation of a rather cold intermediate superheavy nuclear complex as the nuclei barely touch in overcoming the Coulomb barrier.

Thus several independent measurements confront us with evidence that there are peak structures in the positron spectra of collision systems where the quasiatom can have overcritically bound electrons. We are left with the task of identifying unambiguously the sources for these structures among the possibilities we have discussed.

Of course, identifying the spontaneous emission of positrons, and thereby obtaining the first observation of the spontaneous decay of the ground state in a fundamental field theory, is the primary goal of these investigations. But it would be also interesting to find that peaks in the positron spectra reflect nothing more than the interference of induced emission amplitudes, and thus, that overcritical binding does not occur in a situation where Dirac theory predicts that it should.

We have seen that nuclear time delay such as can be produced by the formation of giant metastable nuclei, could play a central role in demonstrating the sparking of the vacuum. Conversely, from the point of view of nuclear physics, we can use the peaks in the positron spectra as an atomic clock that indicates the existence of the superheavy nuclear system and provides a measure of its lifetime and properties. These experiments portend interesting and challenging research in the months and years to come.

5 — NEW NUCLEAR APPLICATIONS IN DIAGNOSTIC MEDICINE

The applications of knowledge and techniques from nuclear physics have grown by leaps and bounds since 1950. Here we want to emphasize two new applications: positron emission tomography, PET, and nuclear magnetic resonance, NMR, that may well revolutionize the field of medical imaging or diagnostic medicine in quality of detail and, with NMR, in safety of procedures

and in our ability to view even in dynamical situations the internal parts of our bodies.

Computer Assisted Tomography, CAT, scans already have made significant advances in medical imaging. It uses X-rays, a multi-array of nuclear detectors and sophisticated computer programs to give cross-sectional views of different parts of the body.

Now, in positron emission tomography, PET, cyclotrons are being used to extend this technique in important ways. Short lived radioactive isotopes of C, N, O which emit positrons, are produced in a cyclotron. One can label a particular molecule with such an isotope so it will go to a particular area of the patient. There, when the positron is emitted, it quickly is brought to rest and when that occurs it finds an electron and they annihilate each other with all their mass emitted as two γ rays. These γ rays are emitted back to back exactly 180° with respect to each other. By detecting these γ rays in coincidence, one can tell very precisely the location of their emission. Fig. 21 shows a cross section of a brain taken with a PET system to study the visual response of the brain. When vision occurs, glucose metabolism occurs. By taking different slices through the visual cortex one can map out the performance of every part. Similar studies can be made of the functioning of other parts of brain or body. While the differences in Fig. 21 are much clearer when color is used to define different parts and different activities such as glucose metabolism, the effects can be seen in Fig. 21. The visual cortex is seen at the lowest, central part of the Figure as shown by the central arrow. On the right when no vision is occurring, no glucose metabolism is occurring. On the left, the gray center in the somewhat rectangular light area (in color the gray is red and the light area yellow) indicates glucose metabolism is taking place. From such pictures, one can see how well all parts are functioning at each level.

The development of nuclear magnetic resonance for medical imaging is the key to a major revolution in diagnostic images. The concept of using NMR techniques in tumor detection was first introduced by Ramon Damadian in 1971, when quantitative NMR parameters were measured and found to be different in solid malignant tumors than in normal tissues. A review of this field is given by Partain et al. [49] in a book on the *Physical Basis of Medical Imaging*.

40

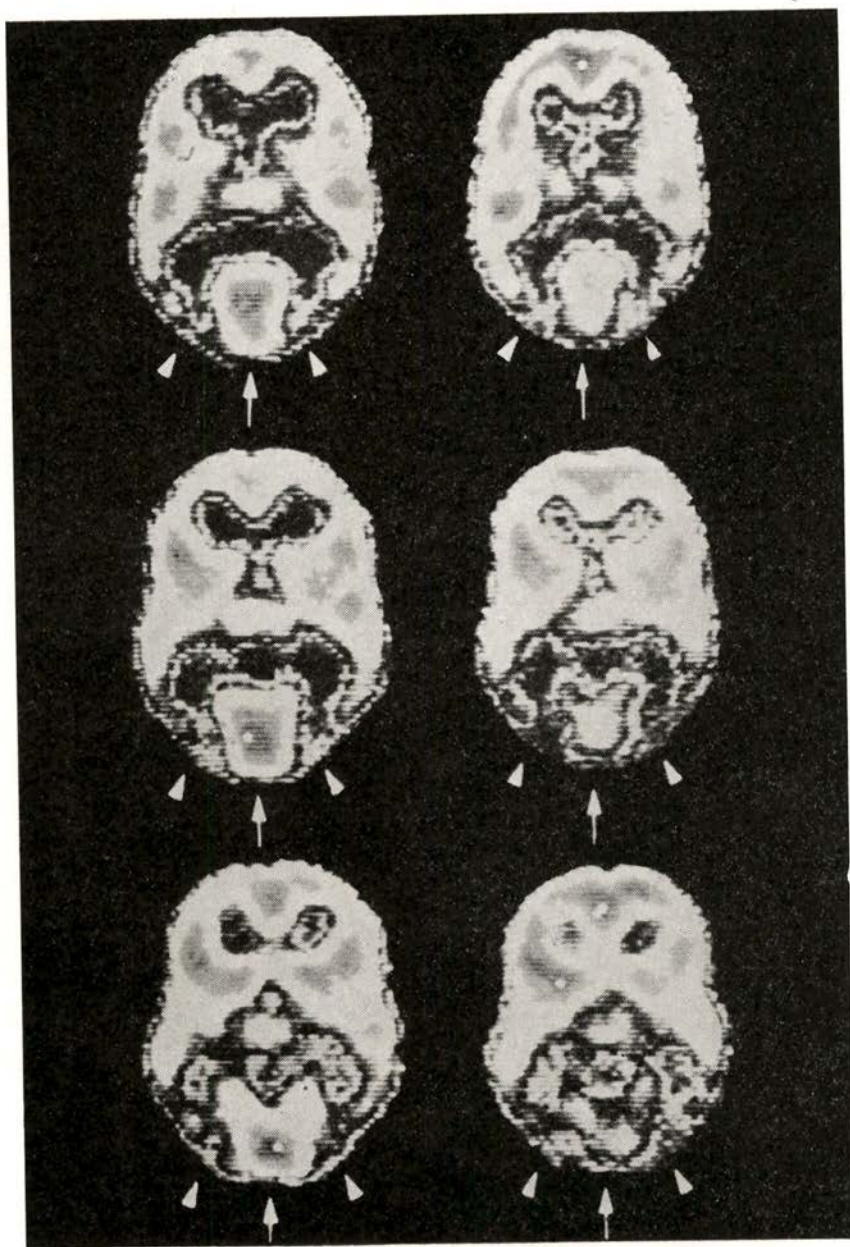*Portgal. Phys.* — Vol. 14, fasc. 1-2, pp. 1-47, 1983

Fig. 21 — Cross section of a brain taken at three different levels with PET. On the left are shown three cross sections taken while vision is occurring, and on the right when the eyes were closed.

We will not here review NMR techniques. Suffice it to show how NMR can be used with a patient (Fig. 22). In Fig. 23 is shown a view of the head of Dr. Partain from Vanderbilt taken by an
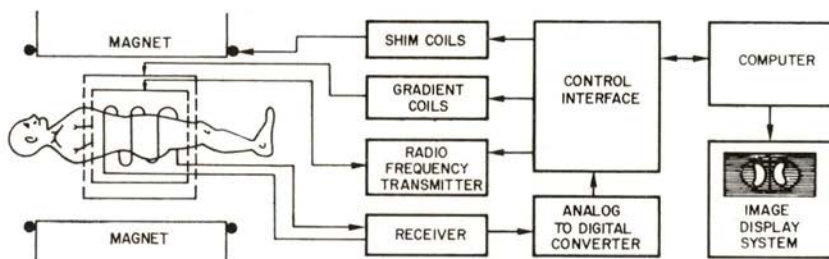

Fig. 22 — A schematic drawing of an NMR system for diagnostic imaging.

NMR system in England in early 1981. Even in this very early research-state facility, one can see details that show the exciting promise of this technique.
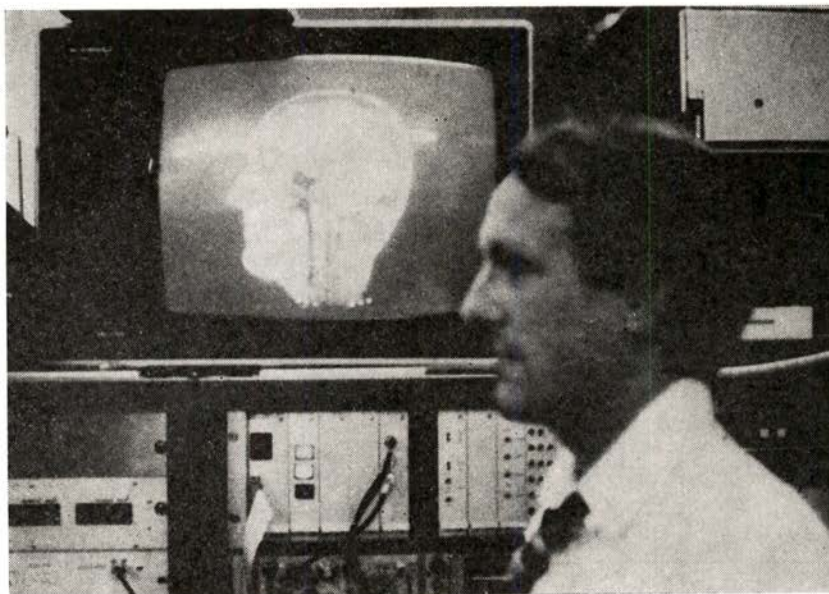
Fig. 23 — An NMR image of the head of Dr. Partain is seen on the screen. Dr. Partain is seen standing in front of the screen. The picture was taken in England.

The great interest in NMR imaging is because NMR is non-ionizing, noninvasive, without known risk, and in addition allows tomographic imaging based on the chemistry and metabolism within thin sections. That is, one does not use X- or γ-rays or radioactive materials which may have harmful side effects. Moreover, one can study dynamical effects, the actual working efficiency of an organ or component because of the dependence of NMR on the chemical state and metabolism taking place. This would include blood flow and organ motion in addition to simply identifying deseased tissue as distinguished from normal tissue. It is apparent that NMR imaging is developing into a technique of major importance in medical diagnosis and biochemical research. A tremendously bright future for NMR in medicine is seen.

REFERENCES

[1] A. BOHR and B. R. MOTTELSON, *Dan. Mat. Fys. Medd.*, **27** (1953), No. 16; *Alpha-, Beta- and Gamma-Ray Spectroscopy*, K. Siegbahn, ed., (North Holland Publ. Co., Amsterdam, 1955), p. 468.

[2] J. H. HAMILTON, A. V. RAMAYYA, E. L. BOSWORTH, W. LOURENS, J. D. COLE, B. VAN NOOIJEN, G. GARCIA-BERMUDEZ, B. MARTIN, B. N. SUBBA RAO, H. KAWAKAMI, L. L. RIEDINGER, C. R. BINGHAM, F. TURNER, E. F. ZGANJAR, E. H. SPEJEWSKI, H. K. CARTER, R. L. MLEKODAJ, W. D. SCHMIDT-OTT, K. R. BAKER, R. W. FINK, G. W. GOWDY, J. L. WOOD, A. XENOULIS, B. D. KERN, K. J. HOFSTETTER, J. L. WEIL, K. S. TOTH, M. A. IJAZ, K. S. R. SASTRY, *Phys. Rev. Letts.* **35**, 562 (1975); J. D. COLE, J. H. HAMILTON, A. V. RAMAYYA, W. G. NETTLES, H. KAWAKAMI, E. H. SPEJEWSKI, M. A. IJAZ, K. S. TOTH, R. L. ROBINSON, K. S. R. SASTRY, J. LIN, F. T. AVIGNONE, W. H. BRANTLEY, P. V. G. RAO, *ibid.*, **37**, 1185 (1976).

[3] J. H. HAMILTON, *Proc. Int. Conf. on Selected Topics in Nuclear Structure*, ed., V. G. SOLOVIEV et al. (Dubna, USSR, 1972), vol. II, p. 303; J. H. HAMILTON, *Nukleonika*, **24**, 561 (1979).

[4] J. H. HAMILTON, A. V. RAMAYYA, W. T. PINKSTON, R. M. RONNINGEN, G. GARCIA-BERMUDEZ, R. L. ROBINSON, H. J. KIM, R. O. SAYER, H. K.

CARTER, *Phys. Rev. Lett.*, **32**, 239 (1974); J. H. HAMILTON et al., *ibid.*, **36**, 340 (1976).

[5] J. H. HAMILTON, R. L. ROBINSON, and A. V. RAMAYYA, in *Nuclear Inter-actions*, B. A. ROBSON, ed. (Springer Verlag, Berlin, 1979), pp. 253-268; *Phys. Energiae Fortis et Phys. Nuclearis*, **3**, 355 (1979) (in Chinese).

[6] A. P. DE LIMA, J. H. HAMILTON, A. V. RAMAYYA, B. van NOOIJEN, R. M. RONNINGEN, H. KAWAKAMI, R. B. PIERCEY, R. L. ROBINSON, H. J. KIM, W. K. TUTTLE, L. K. PEKER, F. A. RICKEY and R. POPLI, *Phys. Letters*, **83B**, 43 (1979); *Phys. Rev.*, **C23**, 213 (1981).

[7] M. VERGNES, *Structure of Medium-Heavy Nuclei*, ed. G. S. ANAGNOSTA, *Inst. Phys. Conf. Ser.*, **49**, 25 (1980).

[8] R. LECOMTE, G. KAJRYS, S. LANDSBERGER, P. PARADIS, S. MONARO, *Phys. Rev.*, **C25**, 2812 (1982).

[9] K. KUMAR, *J. Phys. G. Nucl. Phys.*, **4**, 849 (1978).

[10] R. B. PIERCEY, J. H. HAMILTON, R. SOUNDRANAYAGAM, A. V. RAMAYYA, C. F. MAGUIRE, X.-J. SUN, Z. Z. ZHAO, R. L. ROBINSON, H. J. KIM, S. FRAUENDORF, J. DÖRING, L. FUNKE, G. WINTER, J. ROTH, L. CLEEMANN, J. EBERTH, W. NEUMANN, J. C. WELLS, J. LIN, A. C. RESTER, and H. K. CARTER, *Phys. Rev. Lett.*, **47**, 1514 (1981); R. B. PIERCEY, A. V. RAMAYYA, J. H. HAMILTON, X.-J. SUN, Z. Z. ZHAO, R. L. ROBINSON, H. J. KIM and J. C. WELLS, *Phys. Rev.*, **C25**, 1941 (1982); Z. Z. ZHAO, X.-J. SUN, R. B. PIERCEY, J. H. HAMILTON, C. F. MAGUIRE, A. V. RAMAYYA, R. L. ROBINSON, H. J. KIM, and J. C. WELLS, *Phys. Energiae Fortis et Phys. Nuclearis*, **6**, 255 (1982) (in Chinese).

[11] P. MÖLLER and J. R. NIX, *Nucl. Chemistry Symp. on Nuclei Far From Stability* (March 1982), Am. Chem. Soc. 183rd National Meeting, Abstracts Nucl. 16.

[12] M. SEIWERT, J. A. MARUHN, W. GREINER and A. V. RAMAYYA, *Int. Symp. on Dynamics of Nuclear Collective Motion*, K. OGAWA and K. TANABE, eds., published by INS, Tokyo, Japan (1982), pp. 422-430.

[13] M. BARCLAY, L. CLEEMANN, A. V. RAMAYYA, J. H. HAMILTON, J. D. COLE, A. P. DE LIMA, W. C. MA, S. C. PANCHOLI, R. SOUNDRANAYAGAM, H. YAMADA, W. ELLERBY, R. L. ROBINSON and W. MILNER, private communication (Fall 1981).

[14] M. BARCLAY et al., private communication, Vanderbilt University (Spring 1982).

[15] J. C. LISTER, B. J. VARLEY, H. G. PRICE and J. W. OLNESS, *Phys. Rev. Lett.*, **49**, 308 (1982).

[16] N. SAKAMOTO, S. MATSUKI, K. OGINO, Y. KADOTA, T. TANABE and Y. OKUMA, *Phys. Lett.*, **83B**, 39 (1979).

[17] G. WINTER, J. DÖRING, L. FUNKE, P. KEMNITZ and E. WILL, *Int. Symp. on Dynamics of Nuclear Collective Motion*, K. OGAWA and K. TANABE, eds., published by INS, Tokyo, Japan (1982), *Contributed Papers*, p. 21.

[18] R. B. PIERCEY et al., private communication, Vanderbilt University.

[19] L. FUNKE, G. WINTER, J. DÖRING, F. DUBBERS, P. KEMNITZ and E. WILL, *Future Directions in Studies of Nuclei Far From Stability*, eds. J. H. HAMILTON et al., North Holland Publ. Co. (1980), p. 231.

[20] R. E. AZUMA, G. L. BORCHERT, L. C. CARRAZ, P. G. HANSEN, B. JONSON, S. MATTSSON, O. B. NIELSEN, G. NYMAN, I. RAGNARSSON and H. L. RAVN, *Phys. Lett.*, **86B**, 5 (1979).

[21] H. WOLLNIK, F. K. WOHN, K. D. WÜNSCH and G. JUNG, *Nucl. Phys.* **A291**, 355 (1977).

[22] F. SCHUSSLER, J. A. PINKSTON, E. MONNAND, A. MOUSSA, G. JUNE, E. KOGLIN, B. PFEIFFER, R. V. F. JANSSENS and J. VAN KLINKEN, *Nucl. Phys.* **A339**, 415 (1980).

[23] J. C. HILL, K. SHIZUMA, H. LAWIN, M. SHAANAH, H. A. SELIC̆ and K. SISTEMICH, *IV Int. Conf. on Nuclei Far From Stability*, CERN 81-09 (1981), p. 443.

[24] K. SISTEMICH, W. D. LAUPPE, H. LAWIN, H. SEYFART and B. D. KERN, *Z. Physik*, **A289**, 225 (1979).

[25] A. BOHR and B. R. MOTTELSON, *Nuclear Structure*, vol. 2 (Benjamin, NY, 1975).

[26] R. S. SIMON et al., *Int. Symp. on Dynamics of Nuclear Collective Motion*, K. OGAWA and K. TANABE, eds., published by INS, Tokyo, Japan, (September 1982), p. 35; and M. JÄÄSKELÄINEN et al., *Int. Symp. on Dynamics of Nuclear Collective Motion*, K. OGAWA and K. TANABE, eds., published by INS, Tokyo, Japan (1982), p. 51.

[27] I. Y. LEE, M. M. ALEONARD, M. A. DELEPLANQUE, Y. EL-MASRI, J. O. NEWTON, R. S. SIMON, R. M. DIAMOND and F. S. STEPHENS, *Phys. Rev. Lett.*, **38**, 1454 (1977).

[28] L. L. RIEDINGER, O. ANDERSEN, S. FRAUENDORF, J. D. GARRETT, J. J. GAARDHØJE, G. B. HAGEMANN, B. HERSKIND, Y. V. MAKOVETZKY, J. C. WADDINGTON, M. GUTTORMSEN and P. O. TJØM, *Phys. Rev. Lett.*, **44**, 568 (1980).

[29] H. YAMADA et al., to be published; and H. YAMADA and J. H. HAMILTON, *Int. Symp. on Dynamics of Nuclear Collective Motion*, K. OGAWA and K. TANABE, eds., published by INS, Tokyo, Japan (1982), p. 23.

[30] J. BURGE, E. L. DINES, S. SHIH, R. M. DIAMOND, J. E. DRAPER, K. H. LINDENBENGER, C. SCHÜCK and F. S. STEPHENS, *Phys. Rev. Lett.*, **48**, 530 (1982).

[31] J. ROTH, L. CLEEMANN, J. EBERTH, T. HECK, W. NEUMANN, M. NOLTE, R. B. PIERCEY, A. V. RAMAYYA and J. H. HAMILTON, in *Proc. of. IV Int. Conf. on Nuclei Far From Stability*, CERN 81-09 (1981), p. 680.

[32] J. ROTH, L. CLEEMANN, J. EBERTH, A. V. RAMAYYA, R. B. PIERCEY, J. H. HAMILTON, to be published; and J. H. HAMILTON et al., *Proc. IV Int. Conf. on Nuclei Far From Stability*, CERN 81-09 (1981), p. 391.

[33] D. L. SASTRY, A. AHMED, A. V. RAMAYYA, R. B. PIERCEY, H. KAWAKAMI, R. SOUNDRANAYAGAM, J. H. HAMILTON, C. F. MAGUIRE, A. P. DE LIMA, S. RAMAVATARAM, R. L. ROBINSON, H. J. KIM, J. C. WELLS, *Phys. Rev.*, C23, 2086 (1981).

[34] H. P. HELLMEISTER, U. KAUP, J. KEINONEN, K. P. LIEB, R. RASCHER, R. BALLINI, J. DELAUNAY and H. DUMONT, *Phys. Lett.*, 85B, 34 (1979); *Nucl. Phys.*, A332, 241 (1979).

[35] H. YAMADA, C. F. MAGUIRE, J. H. HAMILTON, A. V. RAMAYYA, D. C. HENSLEY, M. L. HALBERT, R. L. ROBINSON, F. E. BERTRAND and R. WOODWARD, *Phys. Rev.*, C24, 2565 (1981).

[36] S. FRAUENDORF, *Phys. Scri.*, 24, 349 (1981).

[37] W. GREINER and J. H. HAMILTON, *American Scientist*, 19, 154 (1980).

[38] J. S. GREENBERG and W. GREINER, *Phys. Today*, 35 (8), 24 (1982).

[39] Review articles by: B. MÜLLER, *Ann. Rev. Nucl. Sci.*, 26, 351 (1976); J. REINHARDT, W. GREINER, *Rep. Prog. Phys.*, 40, 219 (1977); J. RAFELSKI, L. FÜLCHER, A. KLEIN, *Phys. Rep.*, 38C, 227 (1978); S. J. BRODSKY, P. J. MOHR, in *Structure and Collisions of Ions and Atoms*, I. A. SELLIN, ed., (Springer-Verlag, NY, 1978), p. 3.

[40] J. REINHARDT, U. MÜLLER, B. MÜLLER and W. GREINER, *Z. Physik*, A303, 173 (1981).

[41] See talks by P. KIENLE, H. BACKE, H. BOKEMEYER and conference summary by J. S. GREENBERG in *Proc. of NASI Conf. on the Quantum Electrodynamics of Strong Fields*, Lahnstein/Rhein, W. GREINER, ed. (Plenum, NY, 1981); J. S. GREENBERG in *Electronic and Atomic Collisions*, N. ODA, K. TAKAYANAGI, eds. (North Holland, Amsterdam, 1980), p. 351; P. KIENLE in *Atomic Physics*, vol. 7, D. KLEPPNER, F. PIPKIN, eds. (Plenum, NY, 1981), p. 1.

[42] H. BACKE, L. HANDSCHUG, F. HESSEBERGER, E. KANKELEIT, L. RICHTER, F. WEIK, R. WILLWATER, H. BOKEMEYER, P. VINCENT, Y. NAKAYAMA, J. S. GREENBERG, *Phys. Rev. Lett.*, 40, 1443 (1978).

[43] C. KOZHUHAROV, P. KIENLE, E. BEDERMANN, H. BOKEMEYER, J. S. GREENBERG, Y. NAKAYAMA, P. VINCENT, N. BACKE, L. HANDSCHUG, E. KANKELEIT, *Phys. Rev. Lett.*, 42, 376 (1979).

[44] See reviews by U. MÜLLER, J. REINHARDT, T. DE REUS, P. SCHLÜTER, G. SOFF, K. H. WIETSCHORKE, B. MÜLLER, W. GREINER in *Proc. of NASI*

Conf. on the Quantum Electrodynamics of Strong Fields. Lahnstein/Rhein, W. Greiner, ed. (Plenum, NY, 1981).

[45] H. Bokemeyer, K. Bethge, H. Folger, J. S. Greenberg, H. Grein, A. Gruppe, S. Ito, R. Schule, D. Schwalm, J. Schweppe, N. Trautmann, P. Vincent, M. Waldschmidt, in *Proc. of NASI Conf. on the Quantum Electrodynamics of Strong Fields*, Lahnstein/Rhein, W. Greiner, ed. (Plenum, NY, 1981).

[46] H. Backe, W. Bonin, E. Kankeleit, M. Krämer, R. Krieg, V. Metag, P. Senger, N. Trautmann, F. Weik, J. B. Wilhelmy, in *Proc. of NASI Conf. on the Quantum Electrodynamics of Strong Fields*, Lahnstein/Rhein, W. Greiner, ed. (Plenum, NY, 1981).

[47] P. Kienle, in *Proc. of NASI Conf. on the Quantum Electrodynamics of Strong Fields*, Lahnstein/Rhein, W. Greiner, ed. (Plenum, NY, 1981).

[48] H. Bokemeyer, K. Bethge, H. Folger, J. S. Greenberg, H. Grein, A. Gruppe, S. Ito, R. Schule, D. Schwalm, J. Schweppe, N. Trautmann, P. Vincent, M. Waldschmidt, to be published.

[49] C. L. Partain, R. R. Price, J. J. Erickson, J. A. Patton, C. M. Coulam and A. E. James, *The Physical Basis of Medical Imaging*, eds., C. M. Coulam, J. J. Erickson, F. D. Rollo and A. E. James (Appleton-Century-Crofts, NY, 1981), p. 243.

A SENSITIVE METHOD TO STUDY THE ELECTRON-PHONON RESISTIVITY IN METALS (*)

M. M. AMADO, J. B. SOUSA, M. E. BRAGA

Centro de Física da Universidade do Porto
4000 Porto, Portugal

ABSTRACT — A detailed investigation of the thermal derivative of the electrical resistivity, $d\rho/dT$, as a function of temperature (77 K $\leq$ T $\leq$ 330 K), is presented here for a series of selected high purity metals: Cu, Al, Ta, V, Pt, Nb, In, Sn and Pb. The experimental results are compared with the theoretical predictions for $d\rho/dT$ based on the Bloch-Grüneisen theory. In contrast to the case of ρ (T), considerable differences were found between theory and experiment for the case of $d\rho/dT$.

The role played by the transverse branches of the phonon spectrum is examined, and a simple model is presented leading to a better quantitative description of the results.

The anharmonicity in the vibrational lattice spectrum was found to be an important effect in the temperature range investigated for the case of the low melting point metals: In, Sn and Pb. In particular, it can explain the anomalous increase of $d\rho/dT$ at high temperatures (T $>$ θ , Debye temperature), where, according to the Bloch-Grüneisen formula, $d\rho/dT$ should become constant.

The temperature dependence of the electrical resistivity due to electron-phonon scattering has been thoroughly investigated over the years [1], the results being generally analyzed in terms of the Bloch-Grüneisen expression based on the Debye model for the phonon spectrum:

$$\rho(T) = A(T/\Theta)^5 \int_0^{\Theta/T} x^5 [(e^x - 1)(1 - e^{-x})]^{-1} \, dx \qquad (1)$$

where Θ is the Debye temperature and A is a constant which involves the coupling constant for electron-phonon scattering.

(*) Results presented at the Third General Conference of the Portuguese Physical Society (Coimbra, June 1982).

Portgal. Phys. — Vol. 14, fasc. 1-2, pp. 49-57, 1983

49

Good agreement of (1) with experiment is generally claimed, after a proper choice of Θ for each metal. This is not surprising since expression (1) gives the correct T-dependence both at high temperatures ($T \gg \Theta$; $\rho \propto T$) and low temperatures ($T \ll \Theta$; $\rho \propto T^5$) and, as an intepolation formula, works reasonably well at intermediate temperatures. The reason for the correctness of the asymptotic temperature dependence predicted by (1) lies in the fact that at $T \ll \Theta$ the relevant part of the phonon spectrum corresponds to the long wavelength phonons (which closely follow the assumed Debye model), whereas at $T \gg \Theta$ quantization effects become irrelevant and classical behaviour results ($\rho \propto T$). However, close examination of the experimental data reveals some discrepancies [1-3]: (i) The Θ-values derived from experimental fits to eq. (1) do not exactly agree with Θ-values derived from specific heat measurements; (ii) If we impose exact agreement at particular temperatures, slightly different Θ-values are required for each temperature. A better way to reveal these discrepancies is through the direct measurement of the temperature derivative $d\rho/dT$, which is a quantity far more sensitive to the peculiarities of the phonon spectrum than ρ. In fact, an important part of the resistivity change ($\Delta\rho$) produced by a small increase in the temperature (ΔT) in the vicinity of each T comes essentially from the number (and type) of extra phonons produced by the small increase of temperature. Furthermore, close agreement between experimental ρ-values and those given by (1) does not necessarily mean a good fit to the *derivative* $d\rho/dT$.

In this note we report the results of a fairly detailed investigation on the temperature dependence of the derivative $d\rho/dT$ over a wide range of temperature (80-330 K) for a series of selected high purity metals: (Cu, Al), (Ta, V, Pt, Nb) and (In, Sn, Pb). The first group was chosen to check whether agreement between experiment and theory exists in $d\rho/dT$ for these high conductivity metals. The second group (incomplete d-band transition metals) was chosen in order to investigate if $d\rho/dT$ could reveal discrepancies attributable to the more complex structure of the phonon spectra, and also to the existence of phonon-assisted interband electron transitions (between s and d-bands). The third group was chosen because the corresponding metals have fairly low melting points (156°C, 232°C, 327°C for In, Sn, and Pb, re-

spectively) and we wanted to see whether thermal expansion effects can be detected in $d\rho/dT$ measurements performed at moderate temperatures, i.e. from liquid nitrogen temperature up to room temperature.

Fig. 1 shows a plot of $(d\rho/dT)/(d\rho/dT)_\infty$ as a function of T/Θ for Cu and Al, using Θ values derived from specific heat measurements quoted in the literature. Here $(d\rho/dT)_\infty$ is the
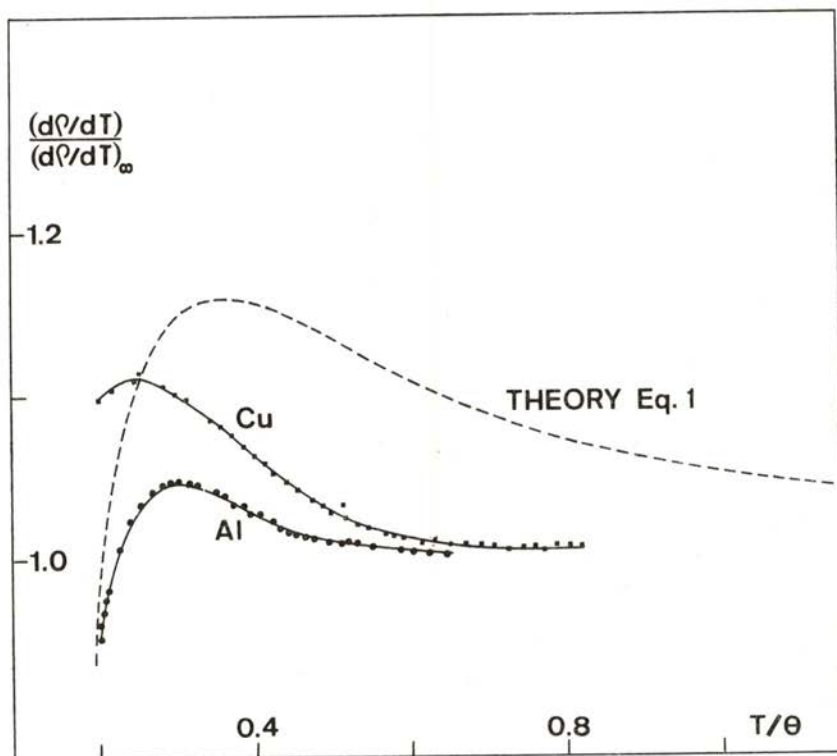

Fig. 1 — Normalised thermal derivative $(d\rho/dT)/(d\rho/dT)_\infty$ as a function of normalised temperature (T/Θ) for Cu and Al. The dashed curve represents $(d\rho/dT)/(d\rho/dT)_\infty$ obtained from differentiation of expression (1).

constant value attained by $d\rho/dT$ for T sufficiently above Θ. In the same figure we show the theoretical curve for $(d\rho/dT)/(d\rho/dT)_\infty$ obtained from differentiation of expression (1) and subsequent numerical computation.

We notice that for Cu and Al the derivative $d\rho/dT$ shows the general features predicted by the Bloch-Grüneisen expression: a sharp increase as T increases from zero, a broad maximum at $T/\Theta \simeq 0.3$, followed by a monotonic decrease towards a constant value at high temperatures.

Quantitatively, however, we observe that the normalized maxima are lower than the maximum predicted by the theory, and occur at slightly lower T/Θ values. We also notice that $d\rho/dT$ attains the high-T regime at much lower T/Θ values than predicted by the theory.

The fact that experimental and theoretical $d\rho/dT$ curves do not coincide is not surprising if we recall that the theory has some drastic oversimplifications, namely it always assumes a Debye model, taking no account of the particular phonon spectrum of each metal.

The phonon spectrum of copper, for example, exhibits two main peaks in the density of states [4], at frequencies close to $v_1 = 7 \times 10^{12}\,s^{-1}$ and around $v_2 = 3.5 \times 10^{12}\,s^{-1}$. The existence of two maxima in the density of states is essentially due to the existence of longitudinal and transverse phonons. It can be shown [1] that when the Fermi surface is spherical only longitudinal phonons are involved in the electron-phonon scattering process, but when the Fermi surface is anisotropic (as actually happens in Cu and Al) the role played by transverse phonons may become important: values of about 70 % of the total scattering processes have been quoted [1].

For Cu, a simple approach is to consider the total vibrational spectrum decomposed into three branches: one longitudinal branch with $\Theta_L = \Theta$, and two transverse branches with $\Theta_T = \Theta/2$, since $v_2 \simeq v_1/2$.

Expression (1) will take the form

$$\rho/\rho_\infty = 2.25\,\Theta\,(T/\Theta)^5\,[\,1.28\,F\,(\Theta/2\,T) + F\,(\Theta/T)\,] \qquad (2)$$

where
$$F\,(x) = \int_0^x x^5\,[\,(e^x - 1)\,(1 - e^{-x})\,]^{-1}\,dx$$

and ρ_∞ is the electrical resistivity at $T \gg \Theta$; it is assumed the same electron-phonon coupling constant for the longitudinal and transverse branches.

Fig. 2 shows the temperature derivative $d\rho/dT/(d\rho/dT)_\infty$ obtained from (2). This curve is now closer to the experimental results than the curve derived from the standard formula (1). In particular the high temperature regime ($d\rho/dT = \text{const}$) is attained faster than predicted by (1), which is in agreement with the experimental results.
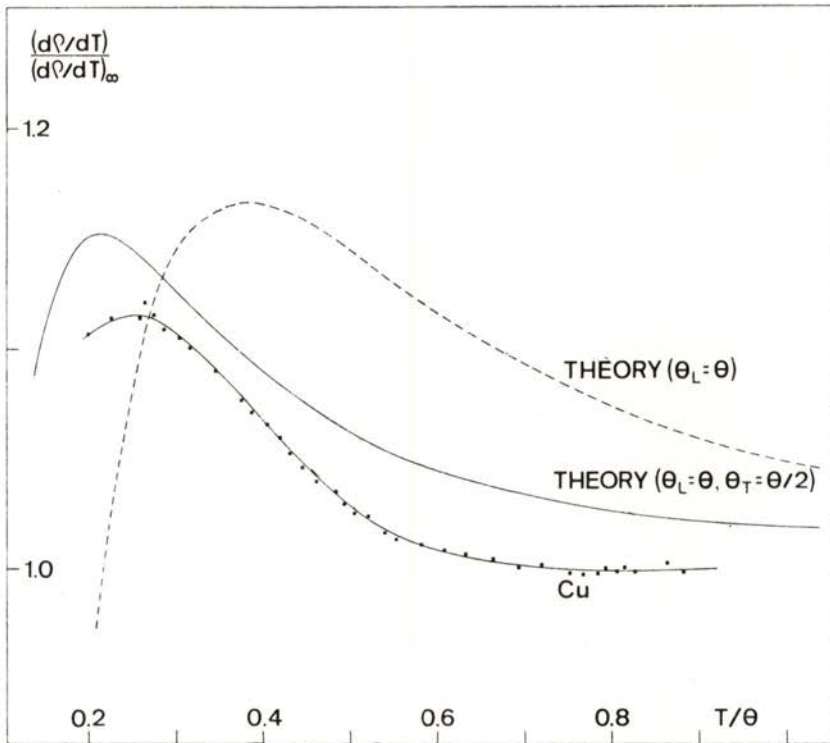

Fig. 2 — Normalised thermal derivative $(d\rho/dT)/(d\rho/dT)_\infty$ as a function of (T/θ); the dashed curve was obtained from differentiation of expression (1), while the full curve was derived from expression (2), in which two maxima in the density of states of the phonon spectrum are considered. The third curve presents the experimental results obtained for Cu.

We believe that the remaining discrepancies can be removed through a realistic consideration of the different branches of the phonon spectrum, taking also into account the probable differences in the corresponding electron-phonon coupling constants.

In the case of the transition metals (Fig. 3) we notice that with decreasing temperature $d\rho/dT$ tends to increase much faster than predicted by the Bloch-Grüneisen expression. It is not surprising that transition metals exhibit a more complex behaviour than Cu or Al, because they have an extra resistivity contribu-
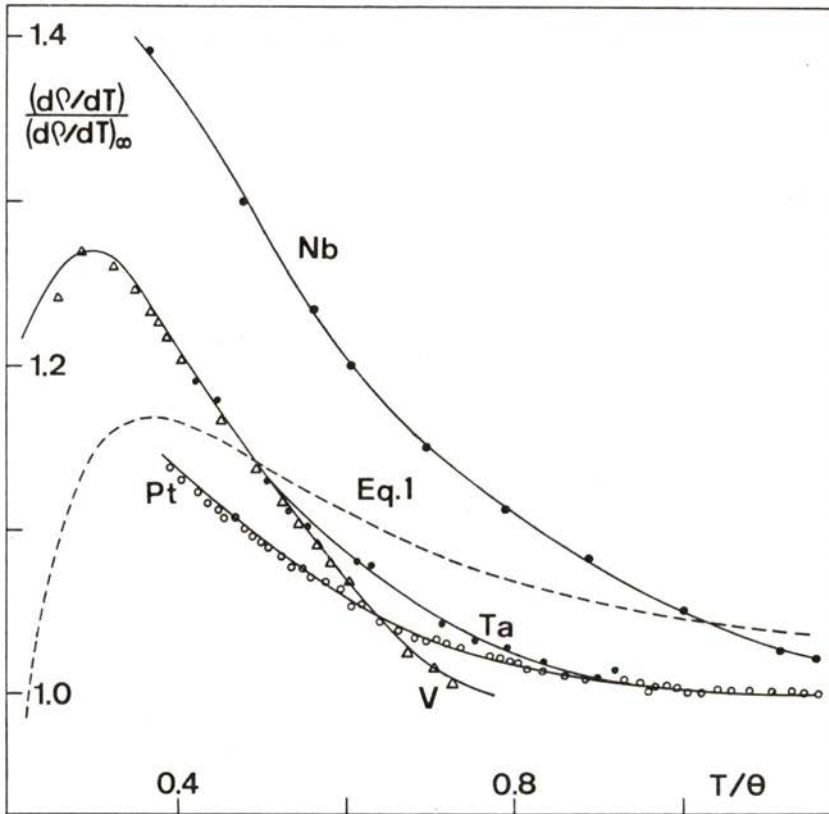
Fig. 3 — Normalised thermal derivative $(d\rho/dT)/(d\rho/dT)_\infty$ as a function of (T/Θ) for Nb, V, Ta, Pt. The dashed curve was obtained from differentiation of expression (1).

tion, due to s-d electron scattering, which greatly increases the value of ρ; it is likely that such effect also affects the values of $d\rho/dT$.

In these transition metals there is also the systematic persistence of the high temperature behaviour ($d\rho/dT = $ const)

down to temperatures considerably below the Debye temperature, as also found in Cu and Al. It is likely that such effect is also connected here with the contribution of the transverse branches of phonon spectrum to the electron scattering process.

We consider now the results of the investigation of $d\rho/dT$ in the low melting point metals In, Sn and Pb. These metals also have low Debye temperatures, $\Theta \simeq 108$ K, 199 K and 105 K, respectively. According to our previous findings, a classical regime should be expected for $T \gtrsim \Theta$, giving a $d\rho/dT$ term independent of temperature. As shown in Fig. 4, $d\rho/dT$ at T sufficiently
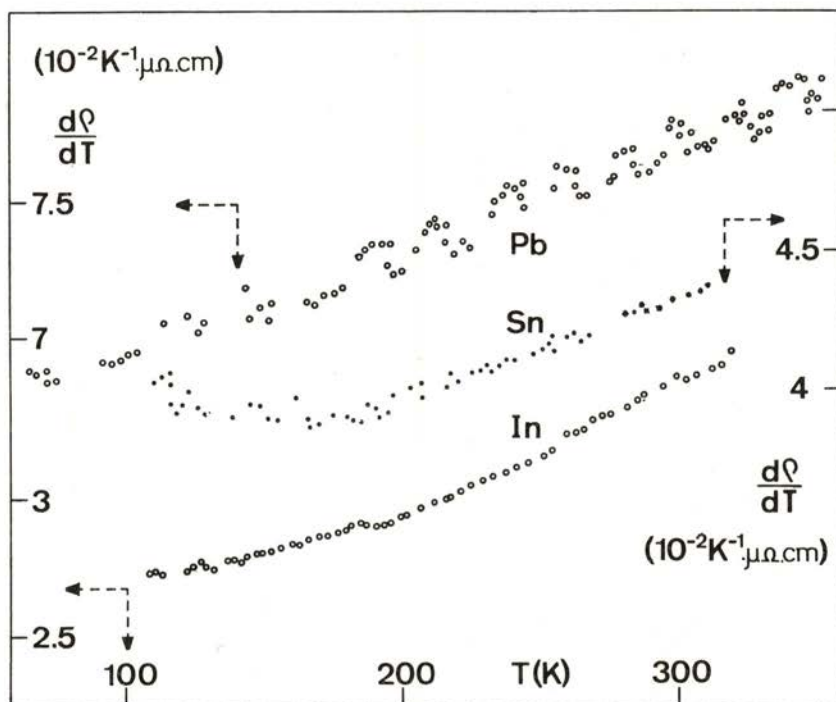
Fig. 4 — Thermal derivative, $d\rho/dT$, as a function of the temperature for the low melting point metals In, Sn and Pb.

above Θ still shows a steady *increase* with temperature in all cases. This cannot be attributed to insufficient temperature to attain the classical regime, since this regime is reached with $d\rho/dT$ *decreasing* steadily with T (see eq. 1). We believe that the

observed behaviour is at least partly due to a thermal expansion effect [1-3]. The increase of the lattice constants weakens the interatomic forces, reducing therefore the maximum vibration frequency, and thus Θ. This has a direct effect in ρ, and it can be shown [2-5] within the Debye model ($\rho/T \propto \Theta^{-2}$ at high temperatures) that the classical behaviour of ρ should have a correction:

$$\rho = A T (1 + 6 \alpha \gamma T) \tag{3}$$

where α is the linear expansion coefficient, A is a constant and γ is the Grüneisen constant, $\gamma = - d(\ln\Theta)/d(\ln V)$, V being the volume of the sample. Since $\alpha \sim 10^{-5}$ K^{-1}, the correction $6 \alpha \gamma T$ is much smaller than unity for the temperature range under investigation. We can then obtain from (3) a useful expression to analyze our $d\rho/dT$ data (using $6 \alpha \gamma T \ll 1$):

$$(1/\rho) \ d\rho/dT = (1/T) + 6 \alpha \gamma \tag{4}$$

Our experimental data agree rather well with this expression, as illustrated in Fig. 5 for Pb. From such plots we obtain:
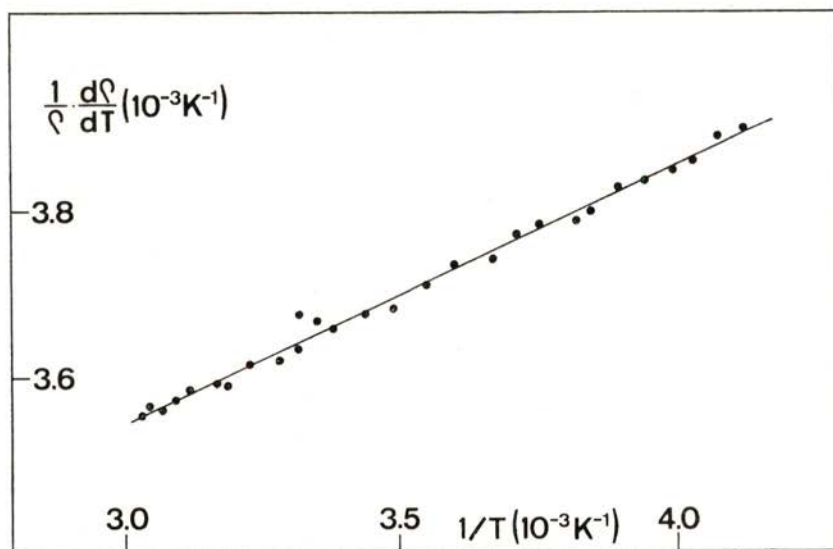
Fig. 5 — Fitting of the experimental results of Pb to expression (4).

56

Portgal. Phys. — Vol. 14, fasc. 1-2, pp. 49-57, 1983

$6\,\alpha\,\gamma = 6.7 \times 10^{-4}$ K^{-1} (In), 5.3×10^{-4} K^{-1} (Sn) and 6.8×10^{-4} K^{-1} (Pb). These figures are indeed of the right order of magnitude as expected from available α and γ-data; e.g. $6\,\alpha\,\gamma = 2.74 \times$ $\times\ 10^{-4}$ K^{-1} (Sn), 4.72×10^{-4} K^{-1} (Pb). Our results appear, however, higher than the calculated values, and so further analysis seems necessary.

REFERENCES

[1] ZIMAN, J. M., *Electrons and Phonons*, Oxf. Univ. Press (1967).

[2] MACDONALD, D., *Hand. der Physik* **14**, 137 (1956).

[3] MEADEN, G., *Electrical Resistance of Metals*, Heywood, London (1966).

[4] NICKLOW, R. M., GILAT, G., SMITH, H. S., RAUBENHEIMER, L. J. and WILKINSON, M. K., *Phys. Rev.*, **164**, 922 (1967).

[5] MOTT, N. F. and JONES, H.,*The Theory of the Properties of Metals and Alloys*, Dover Publications, Inc., New York (1958).

HALL EFFECT IN FERROMAGNETIC Tb₇₅-Gd₂₅.
ELECTRON SCATTERING AND CRITICAL BEHAVIOUR (*)

J. M. MOREIRA, J. B. SOUSA

Centro de Física da Universidade do Porto
4000 Porto, Portugal

ABSTRACT — The Hall effect resistivity (ρ_H) of a ferromagnetic alloy has been investigated in a Tb_{75}-Gd_{25} sample (hcp structure; $T_c = 244$ K), in the temperature range 77-300 K and with applied magnetic fields up to 7.96×10^5 A.m⁻¹ (10 KOe). A reversal in the sign of ρ_H has been observed at $T^* = 175$ K, suggesting the existence of competing electron scattering mechanisms. We analysed such effect in terms of the skew and side-jump contributions.

The magnitude of the Hall resistivity over the whole ferromagnetic phase investigated could be well described in terms of the Hall resistivities of pure Tb and Gd.

The high accuracy of our data enabled the observation of spin-fluctuation effects near the Curie point of Tb_{75}-Gd_{25}. In particular we obtained the quantity $d\rho_H/dT$, which exhibits the critical features associated with a second-order magnetic transition. A preliminary mean-field analysis is made in the paramagnetic phase.

1 — INTRODUCTION

The Hall resistivity $\rho_H = E_H/j$ (E_H = transverse electric field; j = longitudinal current density) results from the transverse motion of the electrons under an applied magnetic field H_a, which produces a magnetic induction **B** inside the sample. In a normal metal, the Hall resistivity is entirely due to the Lorentz force on the electrons and thus simply related to B:

$$\rho_H^o = R_o \cdot B \tag{1}$$

R_o is the so called Hall constant.

In a magnetic metal, a new contribution appears due to the finite magnetization **M** in the cooperative phase, and one then writes:

$$\rho_H = \rho_H^o + \rho_H^s = R_o . B + \mu_o . R_s . M \tag{2}$$

ρ_H^s is the "extraordinary" Hall resistivity and R_s is the extraordinary Hall constant (μ_o = vacuum magnetic permeability). Usually in heavy rare earths we have $R_s \gg R_o$ (one or two orders of magnitude). This new term is caused by the existence of several asymmetric scattering processes (α) of the electrons by the lattice spins S_i, through representative interaction Hamiltonians $H_i^{(\alpha)}$ [1, 2]. An electron with a wave vector **k** has then a different probability of being deflected to one or the other side of the plane (k, S_i).

One possible mechanism in the localized spin systems of concern here (heavy rare earths) is the spin-orbit coupling λ_1 **I** $\cdot$ S_i, where **I** is the electron orbital angular momentum and λ_1 is an interaction field [1, 2]. As shown by Kondo [1], another important asymmetric term exists, of the form λ_2 (**I** $\cdot$ S_i) (**s** $\cdot$ S_i), where **s** is the electron spin and λ_2 an appropriate interaction field. Both terms originate preferential angular deflections for the electrons ($k \to k'$), and so two distinct contributions for the Hall resistivity (skew scattering).

Besides such angular deflections, there is a purely quantum mechanical effect associated with the electron interaction (either of type λ_1 or λ_2): the corresponding wave packet effectively suffers a small transverse displacement δr with respect to its initial direction, the so called side-jump effect [3, 4]. This originates an additional contribution to the transverse current, and thus to the Hall effect.

If we calculate the Hall resistivity within the first Born approximation for the λ_1 and λ_2-skew scattering, one always finds $\rho_H = 0$. One has to go into the second Born approximation to obtain a finite contribution to the skew scattering Hall resistivity. The side jump contribution to ρ_H can be calculated by recalling that, for each collision, an electron suffers a transverse displacement $\delta r_\perp$, to which we can associate an effective transverse velocity $\delta r_\perp / \tau$, where τ is the average time between consecutive collisions.

60

Portgal. Phys. — Vol. 14, fasc. 1-2, pp. 59-70, 1983

The calculations show that [5, 6]: (i) for the λ_1-skew scattering (S. S.) and the side jump effect (S. J.) the Hall resistivity keeps the same sign over the whole cooperative phase (ii) for the λ_2-term the Hall resistivity changes sign once, as T increases from 0 up to the magnetic critical point T_c. All these contributions may be simultaneously present, and this can bring considerable difficulties to separate them out of the measured Hall resistivity. In magnetic systems like Gd, GdAl$_2$, PrAl$_2$, NdAl$_2$ [7, 8, 9] the Hall resistivity exhibits the same sign over the whole temperature range, and this indicates the predominance of the λ_1 contributions. On the other hand, in elements like Tb or Dy, the Hall resistivity changes from negative values near T_c to positive ones at lower temperatures [10, 11, 12].

In this context it is very useful to study magnetic alloys formed by elements which, when isolated, display one of these two types of behaviour. In the work reported here we study a ferromagnetic Tb$_{75}$-Gd$_{25}$ alloy, formed by Tb, which exhibits a reversal in the sign of ρ_H (when alone), with Gd, for which ρ_H exhibits an intrinsic negative sign over the whole ferromagnetic phase. Quantitatively, it is also of interest to correlate the magnitude of ρ_H in the alloy at each temperature with the corresponding values for the elements Tb or Gd.

Besides the problem of the sign and magnitude of ρ_H in the alloy, we also gave particular emphasis to the investigation of the critical behaviour of the Hall resistivity in the vicinity of the Curie point T_c. This is best achieved through the measurement of the temperature derivative $d\rho_H/dT$ in the transition region, which requires fairly high resolution in the $\rho_H(T)$ measurements. To the best of our knowledge, this brings a novel contribution to the available experimental studies on the Hall effect (see also ref. [7]).

2 — RESULTS AND DISCUSSION

High accuracy data on $\rho_H(T)$ were obtained with a lock' in technique [7], using a.c. currents of about 0.5 A through the sample, and applied magnetic fields up to 7.96×10^5 A.m^{-1} (10 KOe).

The ferromagnetic sample was a thin slab of Tb_{75}-Gd_{25} with dimensions $0.22 \times 2.65 \times 9.1$ mm³, and the measurements were performed in the temperature range 77-300 K, at several values of the applied field (H_a). This field was set perpendicular to the slab plane. Inversion of the applied field was made at each experimental point to extract the odd part of the transverse voltage, i.e. the Hall voltage.

As an illustration we show in Fig. 1 the $\rho_H(T)$ curves with $H_a = 3.88 \times 10^5$ and 7.72×10^5 A.m⁻¹. Similar measurements have been performed at $H_a = 0.80 \times 10^5$ and 1.59×10^5 A.m⁻¹.
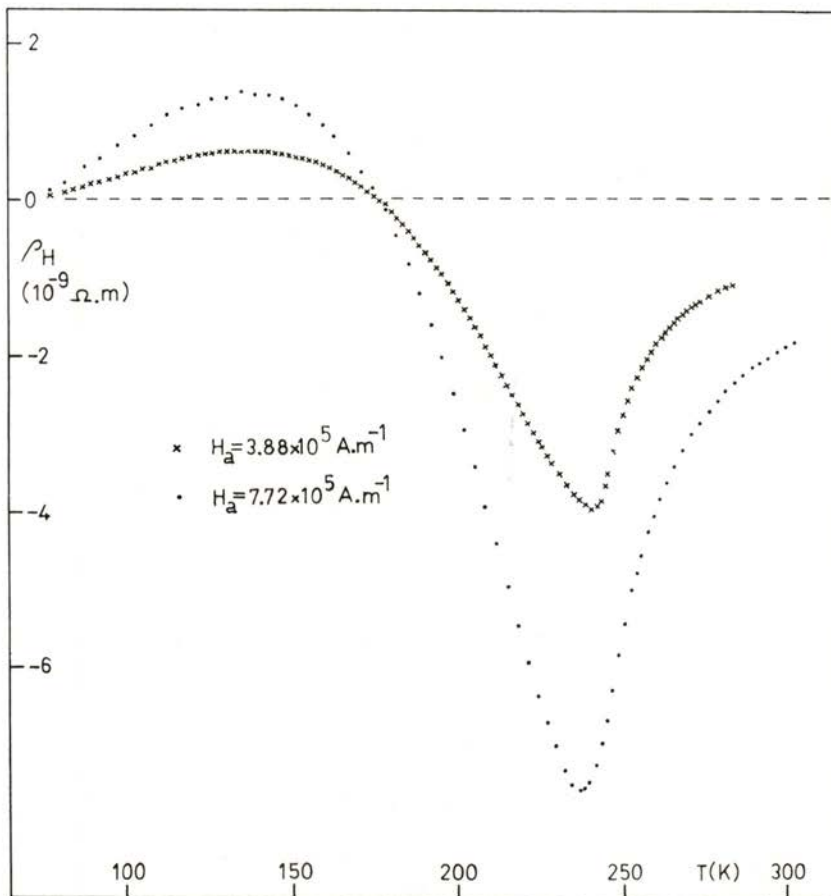
Fig. 1 — Hall resistivity of a polycrystal of Tb_{75}-Gd_{25} as a function of temperature (T) for two different values of the applied magnetic field (H_a).

The Hall resistivity vanishes and changes sign at $T^* = 175$ K, becoming positive below this temperature, with a broad maximum around 135 K. The observation that $\rho_H(T^*) = 0$, irrespective of the magnetic field, is consistent with the usual separation of the Hall resistivity as a sum of a normal (ρ_H^o) and an extraordinary contribution (ρ_H^s). In fact, under our experimental conditions, H_a is too small to produce magnetic saturation in the sample at T^* [13], and so the average magnetization is then given by [7]:

$$M = H_a/D \tag{3}$$

where D is the demagnetization factor of the sample ($D \simeq 1$ in our geometry). Then we get (from eq. 2):

$$\rho_H(T) = \mu_o[R_o(T) + R_s(T)] \cdot (H_a/D) \simeq \mu_o[R_o(T) + R_s(T)] H_a \tag{4}$$

It becomes clear that T^* is just the temperature at which the quantity inside the brackets vanishes, i.e.

$$R_s(T^*) = -R_o(T^*) \tag{5}$$

The rapid decrease of $\rho_H(T)$ in the paramagnetic phase is due to the corresponding decrease of the induced magnetization, by thermal disorder. More precisely, the induced magnetization above T_c is given by

$$M(T, H_a) = x(T)[1 + Dx(T)]^{-1} \cdot H_a \tag{6}$$

where $x(T)$ is the magnetic susceptibility in the paramagnetic phase (defined by $x = M/H_i$, where H_i is the internal magnetic field, $H_i = H_a + (1-D) \cdot M$). In this equation the denominator takes account of the effect of the demagnetizing field. Then the quantity ρ_H measured at constant H_a is approximately given by (from eq. 2):

$$\rho_H \simeq \mu_o R_o H_a + \mu_o R_s \cdot x(T)[1 + Dx(T)]^{-1} \cdot H_a \tag{7}$$

At T sufficiently above T_c, i.e. when the short range spin-spin correlations become negligible, both R_o and R_s are independent of temperature, and so the decrease of ρ_H is entirely imposed by the decrease of $x(T)$. The magnitude of ρ_H at constant T should then increase linearly with H_a, as supported by the experimental results (see Fig. 1). The same linearity is observed at sufficiently

low temperatures, when the applied field becomes insufficient to saturate the sample ($M \simeq H_a$, see eq. 3; and eq. 4 for $\rho_H \propto H_a$).

Near the Curie point, R_o, R_s and M are strongly dependent on the applied field, due to the field effect on the spin-spin correlations, and thus ρ_H ceases to be a linear function of H_a. This is clearly shown in Fig. 2, with ρ_H-data corresponding to $H_a = 0.8 \times 10^5$, 1.59×10^5 and 7.72×10^5 A.m^{-1}.
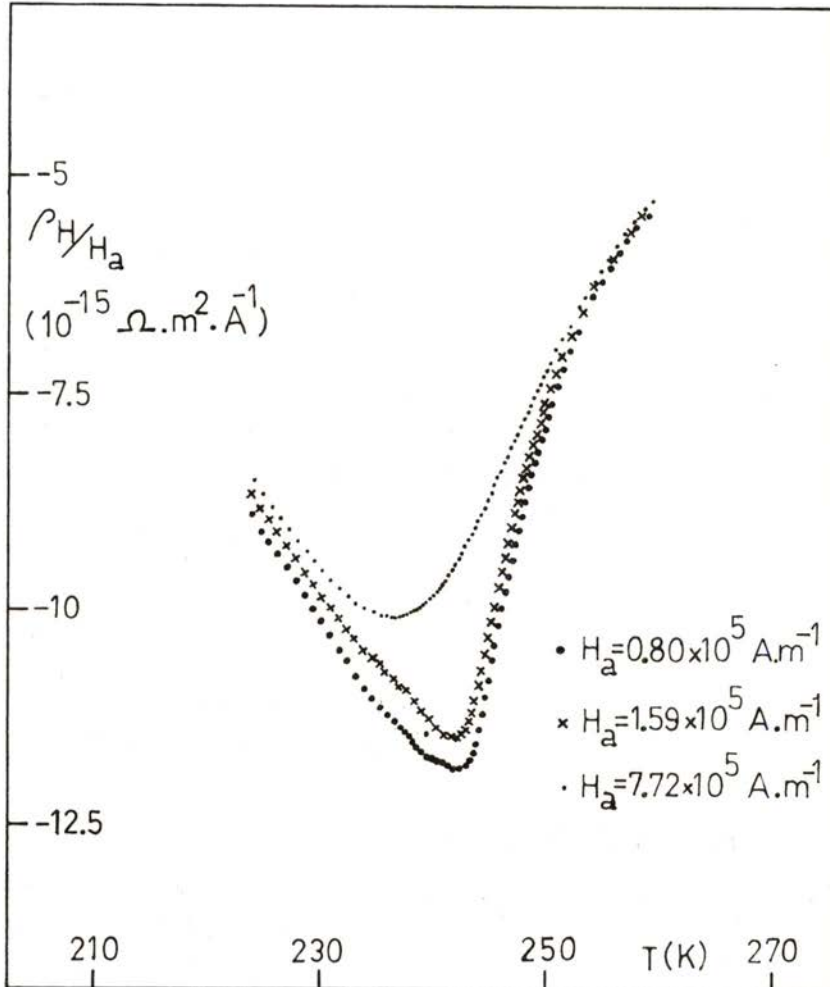
Fig. 2 — Near the Curie point the Hall resistivity ceases to be proportional to the applied magnetic field.

64

Portgal. Phys. — Vol. 14, fasc. 1-2, pp. 59-70, 1983

The general shape of $\rho_H(T)$ in polycrystalline Tb_{75}-Gd_{25} is remarkably close to the curve obtained from an interpolation of the $\rho_H(T)$ curves for polycrystalline Gd and Tb [14], weighted by the appropriate atomic percentages and with T scaled by the corresponding T_c values (Fig. 3), i.e.

$$\rho_H(T/T_c)_{alloy} = 0.75\,\rho_H(T/T_c)_{Tb} + 0.25\,\rho_H(T/T_c)_{Gd} \qquad (8)$$

One can now add some comments on the possible role of the different skew and side jump contributions. The λ_2-contributions are expected to be fairly small, since they result directly from a second order effect, i.e. from the polarization of the conduction electrons by the lattice spins. For the case of pure Gd, for which a complete separation has been achieved recently [9], the small magnitude of the λ_2-contributions has indeed been confirmed. In a first approximation we neglect these contributions in Tb_{75}-Gd_{25}. Since none of the λ_1-contributions changes sign in the ferromagnetic phase, when alone, the experimental verification of a reversal in the sign of ρ_H for Tb_{75}-Gd_{25} clearly indicates that both λ_1-contributions (skew and side jump) are important in this alloy *and* have opposite signs. A more elaborate analysis of these results is in progress, with an extension of the theory of the Hall effect to the case of magnetic alloys.

With regard to the critical behaviour, Fig. 4 displays the temperature derivative $d\rho_H/dT$ as a function of temperature, the derivative being obtained by "local" (3-point) numerical differentiation of the $\rho_H(T)$-data. For convenience the data have been normalized by a factor $\rho_H(T_c)$. The existence of "critical features" in the Hall effect is evidenced by the very sharp dip in $d\rho_H/dT$ at $T = 244.0$ K. This value is in good agreement with the Curie temperature previously obtained with Tb_{75}-Gd_{25} single crystals, using magnetization ($T_c = 245 \pm 2$ K) [13] and electrical resistivity studies ($T_c = 244.8 \pm 0.5$ K) [15]. Also, the minimum in $1/\rho_H(T_c) \cdot (d\rho_H/dT)$ at T_c gets less sharp as H_a increases, as expected from the reduction of the spin-spin fluctuations caused by the increase in H_a.

As mentioned above, the role of these fluctuations diminishes markedly as T increases in the paramagnetic phase (in heavy rare earths, they can be neglected for $\varepsilon \gtrsim 10^{-1}$, with $\varepsilon = (T-T_c)/T_c$;
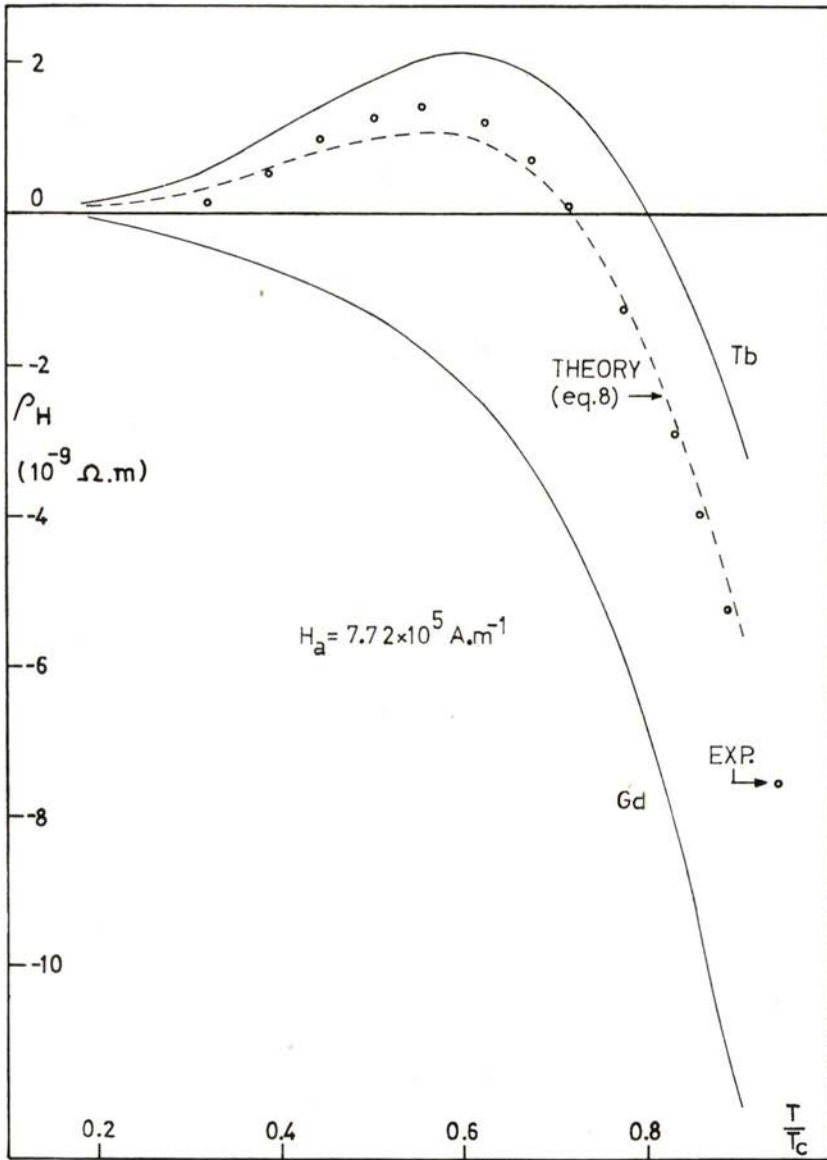
Fig. 3 — Comparison between the experimental Hall resistivity (ρ_H) of Tb_{75}-Gd_{25} and the theoretical prediction based on the Hall resistivities of polycrystalline Tb and Gd (eq. 8).
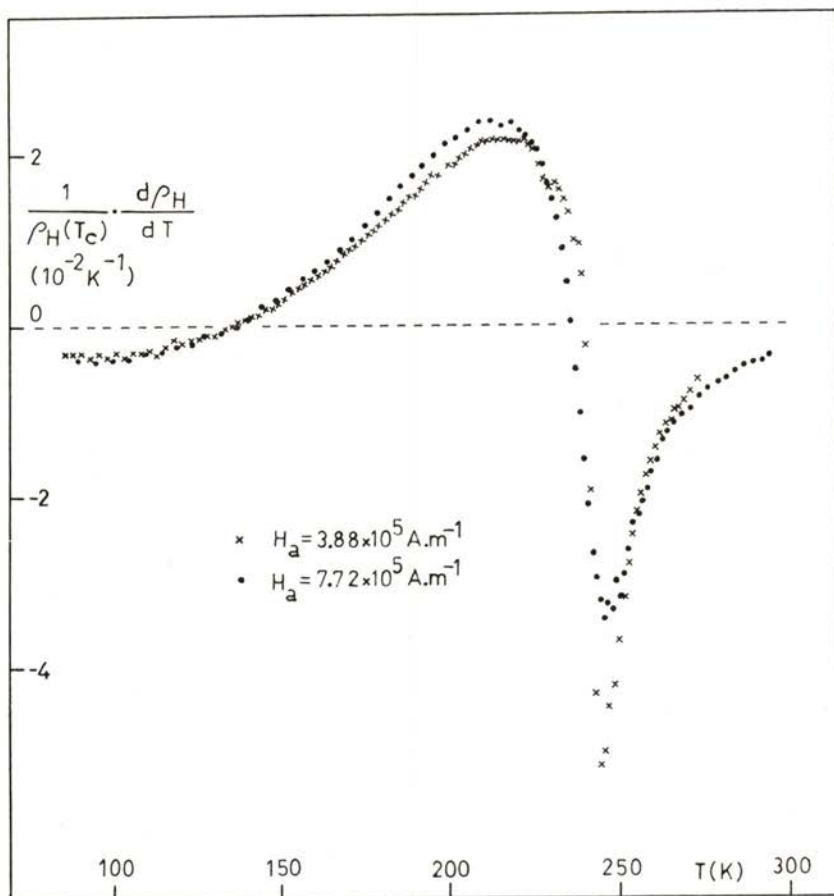
Fig. 4 — Temperature dependence of the thermal derivative, $d\rho_H/dT$, of the Hall resistivity, normalized by $\rho_H(T_c)$; $T_c = 244$ K.

see e.g. ref. [15]), and so R_o and R_s are expected to become constant. Then eq. (4) predicts

$$\rho_H \simeq R_o \, \mu_o \, H_a + R_s \, \mu_o \, x \, H_a \tag{9}$$

Assuming, for T sufficiently above T_c, that x obeys a Curie-Weiss law [13],

$$x = C / (T - T_c^*) \tag{10}$$

where T_c^* is the paramagnetic Curie-Weiss temperature and C the Curie-Weiss constant, the expression (9) takes the form:

$$\rho_H(T) = A + B/(T - T_c^*) \tag{11}$$

where A and B are constants.
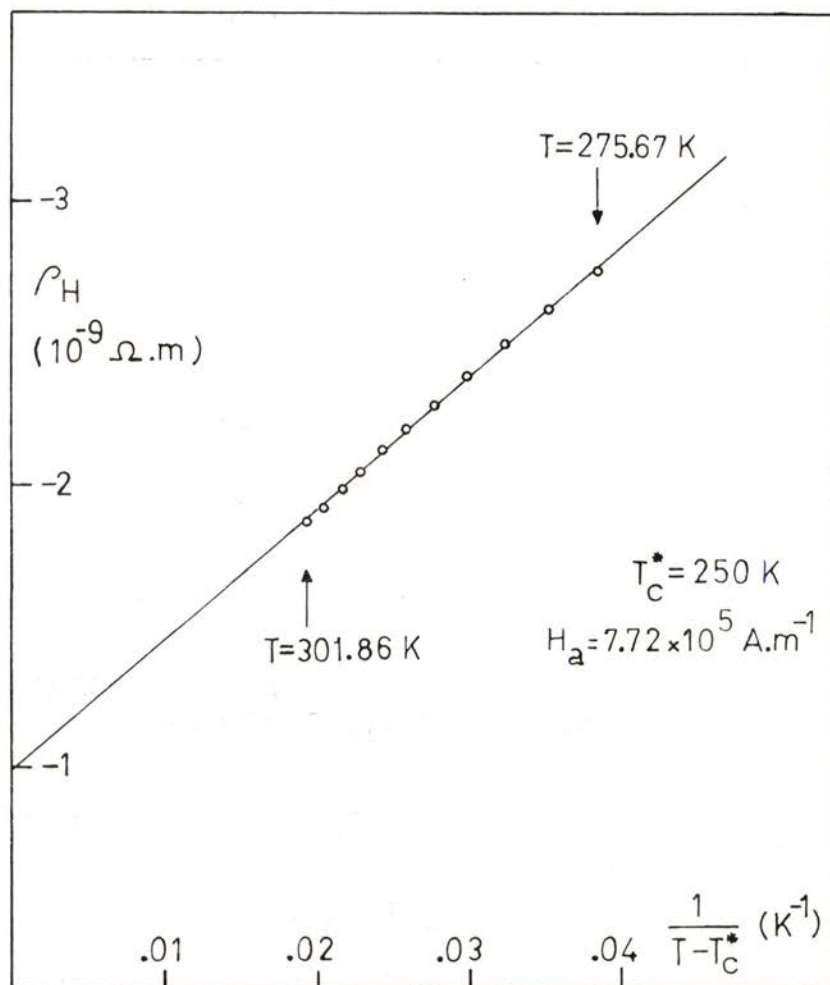
Fig. 5 — Hall resistivity of Tb_{75}-Gd_{25} versus $(T - T_c^*)^{-1}$, where T_c^* is the paramagnetic Curie temperature ($T_c^* = 250$ K); from the linear plot we obtain the constants A and B of eq. (11).

68

Portgal. Phys. — Vol. 14, fasc. 1-2, pp. 59-70, 1983

In order to check this prediction we performed a numerical analysis of our ρ_H-data above 275 K ($\varepsilon > 1.27 \times 10^{-1}$), with T$_c^*$ considered as an adjustable parameter. For a chosen T$_c^*$ value, a least squares fitting to expression (11) gave the values of A and B with the corresponding relative errors and the correlation parameter (σ), indicative of the quality of the fitting. The correlation σ was found to be maximum for T$_c^* = 250.0 \pm 0.25$ K ($\sigma = 0.9985$) and the errors in A and B were found minima at that temperature (A=(1.00±0.02).10^{-9} Ωm, B=(45.97±0.86).10^{-9} ΩmK). The good quality of the corresponding fit can be seen in Fig. 5.

Further data analysis is in progress for temperatures very close to the Curie point, in order to extract relevant information on the critical behaviour of the Hall effect. Also, the experimental investigation of the relation between the critical behaviour of $\rho_H(T)$ and that of the magnetic susceptibility $x(T)$ is being contemplated.

REFERENCES

[1] J. Kondo, *Progr. Theor. Phys.*, **27**, 772 (1962).

[2] L. L. Hirst, *Adv. in Phys.*, **27**, 231 (1978).

[3] L. Berger, *Phys. Rev.*, **B11**, 4559 (1970).

[4] P. Nozières and C. Lewiner, *J. de Phys.*, **34**, 901 (1973).

[5] B. Giovaninni, *Phys. Letters*, **36A**, 381 (1971).

[6] A. Fert, *J. de Phys. Lettres*, **35**, L-107 (1974).

[7] J. B. Sousa, J. M. Moreira, *Portgal. Phys.*, **13**, 137 (1982).

[8] M. Christen, B. Giovaninni and J. Sierro, *Phys. Rev.*, **B20**, 4624 (1979).

[9] R. Asomoza, A. Fert and R. Reich, to be published.

[10] B. Coqblin, *The Electronic Structure of Rare-Earth Metals and Alloys; the Magnetic Heavy Rare-Earths*, Academic Press, p. 611-628 (1977).

[11] J. J. Rhyne, *J. Appl. Phys.*, **40**, 1001 (1969).

[12] J. J. Rhyne, *Phys. Rev.*, **172**, 523 (1968).

[13] D. M. S. BAGGULEY, J. P. PARTINGTON, J. A. ROBERTSON and R. C. WOODS, *J. Phys. F: Metal Physics*, **10**, 967 (1980).

[14] J. J. RHYNE, J. R. CULLEN, *J. de Phys.*, **32**, C1-246 (1971).

[15] J. B. SOUSA, M. M. AMADO, M. E. BRAGA, R. P. PINTO, J. M. MOREIRA and D. HUKIN, *Communications on Physics*, **2**, 95 (1977).

Note added in proof: A recent analysis [9] has shown that the Smit asymmetric scattering mechanism (J. Smit, *Physica*, **21**, 877 (1955)) gives a fairly large contribution to ρ_H in Gd; it is likely that such mechanism may also be operative in Gd-Tb alloys.

CONTRIBUTION TO THE STUDY OF THE ELECTRON DISTRIBUTION IN VF₂ (*)

M. M. R. Costa and M. J. M. de Almeida

Centro FC1, INIC — Departamento de Física, Universidade de Coimbra
3000 Coimbra, Portugal

ABSTRACT — A contribution to the study of the electron density distribution in VF₂ is given in the present paper.

A set of observed X-ray intensities from a single crystal were placed on the same scale as corresponding values calculated for a postulated model; the scale factor was obtained from least-squares refinement of high order data $(0.6 \text{ Å}^{-1} < (\sin \theta)/\lambda < 1.1 \text{ Å}^{-1})$.

Fourier difference maps are shown for different sections through the unit cell.

1 — INTRODUCTION

The compound VF₂ has been synthesized by Stout and Boo [1]. These authors have investigated its heat capacity in the temperature range 5-300 K as well as the magnetic interactions responsible for the magnetic ordering in the compound. More recently, the crystal distortion associated with magnetic ordering has been studied by Mc-Cain et al. [2] who measured the lattice parameters of single crystals of VF₂ at different temperatures ranging from 4.2 K to 298 K.

Statistical tests on the X-ray diffraction data together with a study of the crystal structure and anisotropic thermal parameters of single crystals of VF₂ have been carried out by Almeida et al. [3].

The present study represents a further contribution leading to the determination of the electron densities in that compound in order to investigate possible asphericities in the electron distributions.

(*) Results presented at the Third General Conference of the Portuguese Physical Society (Coimbra, June 1982).

2 — DATA COLLECTION

VF_2 has a rutile type structure with space group $P4_2/mnm$ (Stout and Boo) [4].

A single crystal of VF_2 with approximate dimensions ($0.04 \times 0.05 \times 0.10$)mm³ obtained from a large specimen grown by B. J. Garrard, Clarendon Laboratory, Oxford (England) was used in the present study.

The lattice parameters have been determined as described elsewhere [3].

$$a = b = (4.803 \pm 0.005) \text{ Å} \; ; \; c = (3.235 \pm 0.005) \text{ Å}$$

Several $\omega - 2\theta$ scans were carried out to measure the integrated intensities of 1177 reflections out to $(\sin\theta)/\lambda = 1.1$ Å⁻¹ on a CAD4 four-circle diffractometer using Mo-Kα radiation and a graphite monochromator. For each hkl, between two and sixteen equivalent reflections were collected to enable a study of absorption and extinction in this crystal. The intensities of three reflections were periodically measured and used as standards against which all reflection intensities were calibrated.

3 — DATA REDUCTION

Lorentz and polarization corrections were applied to the measured integrated intensities $I_{hkl} > 3 \sigma_{hkl}$, where σ_{hkl} is the standard deviation of the intensity I_{hkl}.

An empirical absorption correction described by North et al [5] based on the method proposed by Furnas [6] was applied in an attempt to improve the agreement between equivalent reflections.

The calculated transmission factors varied between 0.946 and 0.998. For each group of equivalent reflections, thus corrected for absorption, agreement factors were calculated as:

$$R = \sum_{hkl} | F_{hkl} - F_{av} | / (\sum_{hkl} F_{hkl})$$

$$R' = \left\{ \sum_{hkl} | F_{hkl} - F_{av} |^2 / (\sum_{hkl} F_{hkl}^2) \right\}^{1/2}$$

where F_{av} represents the average of the structure amplitudes of a group of $\{hkl\}$ equivalent reflections. For most reflections the values of R and R' were of the order of 1 % and 2 % respectively; only for six reflections both R and R' varied between 2 % and 5 %.

Within each group of equivalent reflections, those for which $|F_{hkl} - F_{av}| > 3\,\sigma_{hkl}$ were rejected: the remainder were used to calculate a new value of F_{av} which was used in all subsequent calculations.

A set of structure amplitudes, F_c, were calculated on the assumption of spherical distributions of electrons around the nuclei of vanadium and fluorine atoms: the atomic scattering factors for the ionized spherical atoms were obtained from the constants a_i, b_i ($i = 1, 3$) and c listed on the International Tables for X-ray Crystallography (vol. IV); anomalous dispersion corrections for Mo - Kα radiation were included.

A least squares refinement (hereafter referred to as refinement (i)) was carried out including all 113 reflections with $0.1\ \text{Å}^{-1} < (\sin\theta)/\lambda < 1.1\ \text{Å}^{-1}$. The results obtained for the anisotropic thermal parameters and position of the fluorine atom agree with those given elsewhere [3] for this structure. They are shown in the table together with the value of the scale factor. The observed structure amplitudes multiplied by the scale factor were then plotted against the corresponding F_c. The significant deviation from the straight line of the two points representing the 110 and the 002 reflections indicated the presence of extinction affecting these intensities.

A further refinement of the above mentioned parameters based on all but these two reflections was performed, yielding refined values in good agreement with those previously obtained.

In order to bring the experimental intensities on an absolute scale, a direct measurement of the scale factor, S, would be desirable. It is reasonable to expect that this will differ significantly from the value yielded by a refinement which includes reflections with low $(\sin\theta)/\lambda$: in fact any deviation of the real electron density from the postulated spherical model is likely to modify the calculated intensities of such reflections; moreover, these low angle reflections, having usually the highest intensities, are the most significantly affected by extinction. These two effects add up to mask the "true" value of the scale factor.

However, it has been pointed out by Stevens and Coppens [7] that a refinement of positional and thermal parameters based on higher order X-ray data usually yields a scale factor in good agreement with experimental values.

On the basis of such arguments a refinement based on only 68 reflections with $0.6 \text{ Å}^{-1} < (\sin \theta)/\lambda < 1.1 \text{ Å}^{-1}$ was considered to be more correct; the results of this refinement (hereafter referred as refinement (ii)), also shown in the table, are to be compared with those obtained from the refinement of low and high order data. It may be seen that only the values of the scale factor are significantly different, as one would expect. The values of SF_0 are plotted against the corresponding F_c in Fig. 1-a, which evidences the presence of extinction.

	Refinement (i)		Refinement (ii)	
	V	F	V	F
u_{11}	0.0058 ± 0.0002	0.0116 ± 0.0009	0.0063 ± 0.0008	0.0127 ± 0.0002
u_{33}	0.0049 ± 0.0003	0.0077 ± 0.0004	0.0054 ± 0.0001	0.0085 ± 0.0003
u_{12}	-0.0002 ± 0.0003	-0.0053 ± 0.0005	-0.0002 ± 0.0001	-0.0057 ± 0.0005
x	——	0.3048 ± 0.0005	——	0.3050 ± 0.0003
S	0.150 ± 0.002		0.140 ± 0.003	
R	0.018		0.014	
R_w	0.023		0.021	
g	——		$(0.93 \pm 0.06) \times 10^{-5}$	

An attempt to correct the extinction effect was made, multipliying the calculated structure factors, F_c, by $(1 + gI_c)^{-1}$ where I_c is the calculated intensity and g an extinction parameter; the refinement of g was carried out keeping all thermal and positional parameters fixed at the values given by refinement (ii). Values of SF_0, thus corrected for extinction, are plotted in Fig. 1-b against the corresponding F_c; comparison with Fig. 1-a shows the extent to which the extinction effect has been corrected.

Fig. 1 (facing page) — (a) Plot of SF_0 against F_c, before the extinction correction. (b) Plot of SF_0 against F_c, when an extinction correction is applied to the observed structure amplitudes.

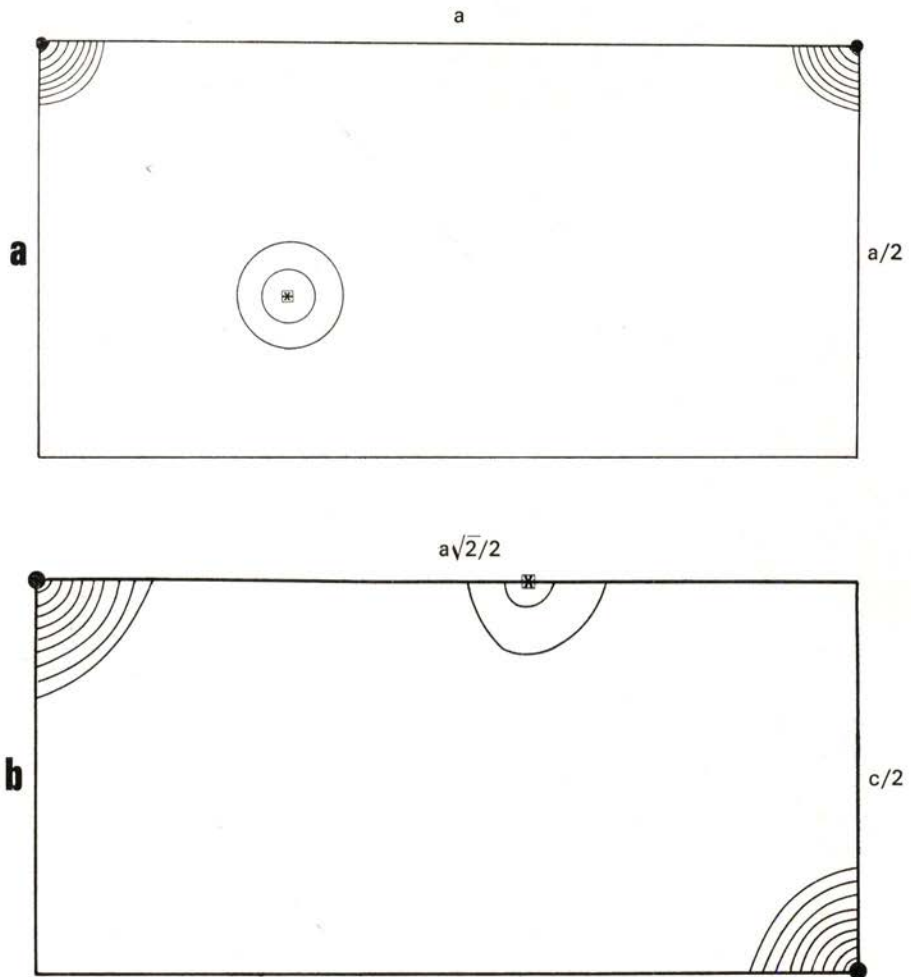74

Portgal. Phys. — Vol. 14, fasc. 1-2, pp. 71-79, 1983
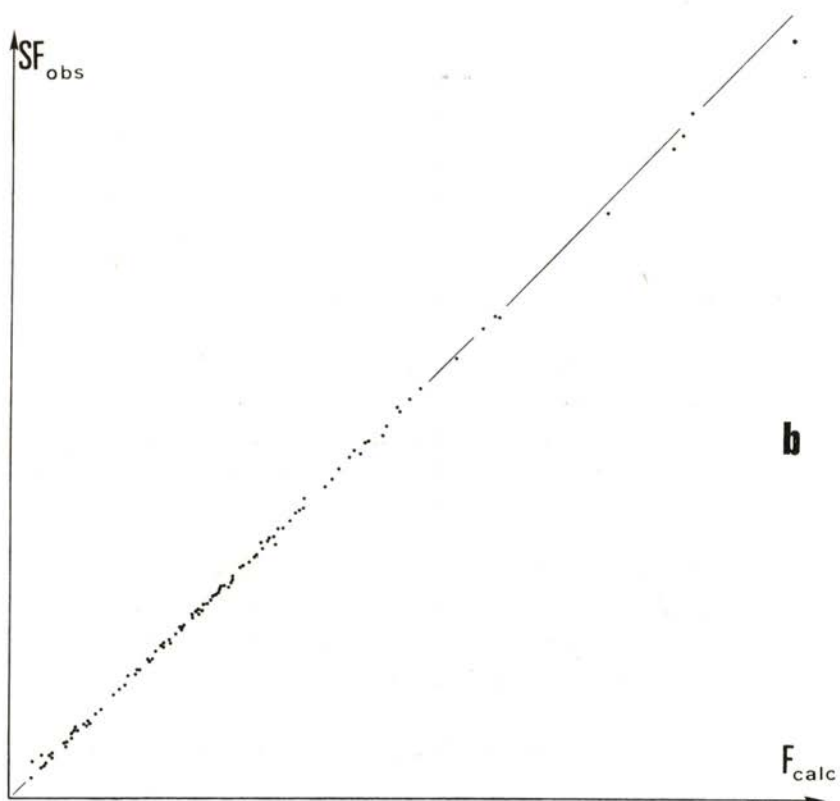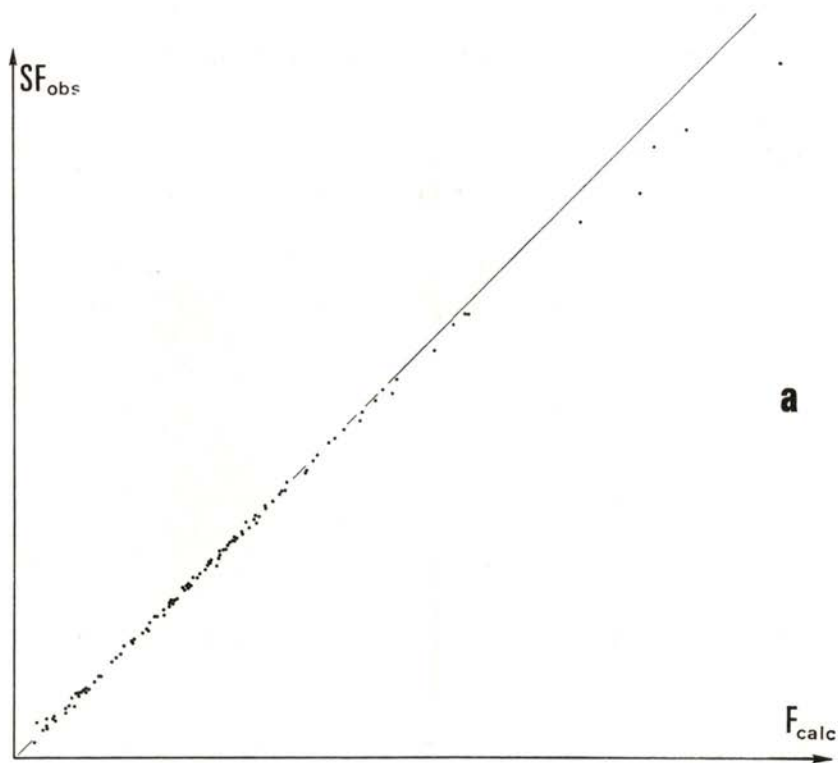
Fig. 2 — Fourier map of the observed structure amplitudes, SF$_0$.
● : position of V atoms ; □ : position of F atoms.
(a) Section [001] of the unit cell.
(b) Section [1$\bar{1}$0] of the unit cell.

Fourier analyses of the observed (scaled) structure amplitudes, SF$_0$, and of the differences (SF$_0$ - F$_c$) have been carried out. The corresponding density maps through different sections of the unit cell are shown in Figs. 2 and 3.

In all maps the curves away from the atomic positions are above the significance level. This was estimated by performing a Fourier analysis of the standard deviations of the observed data and drawing the corresponding density maps, shown in Fig. 4.
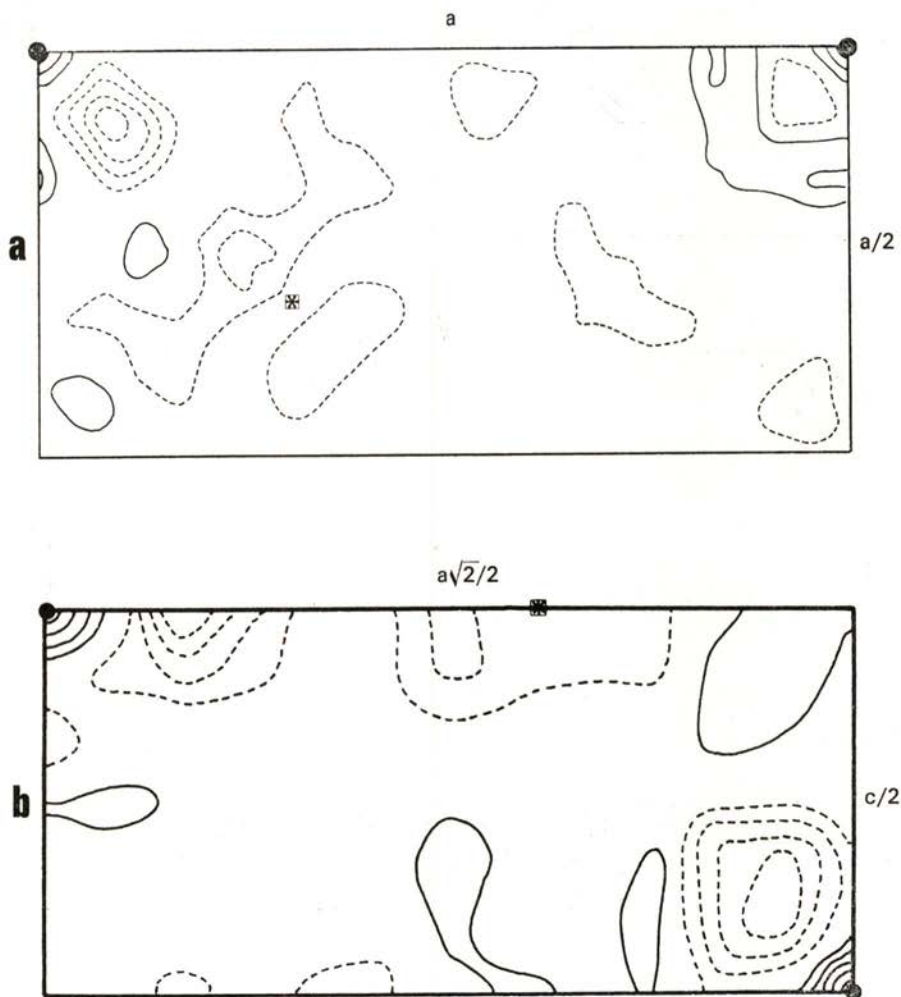
Fig. 3 — Fourier difference map, SF_o-F_c. Contours at 1/30 those of SF_o. Broken lines represent negative contours.

    (a)   Section [001] of the unit cell.
    (b)   Section [1$\bar{1}$0] of the unit cell.
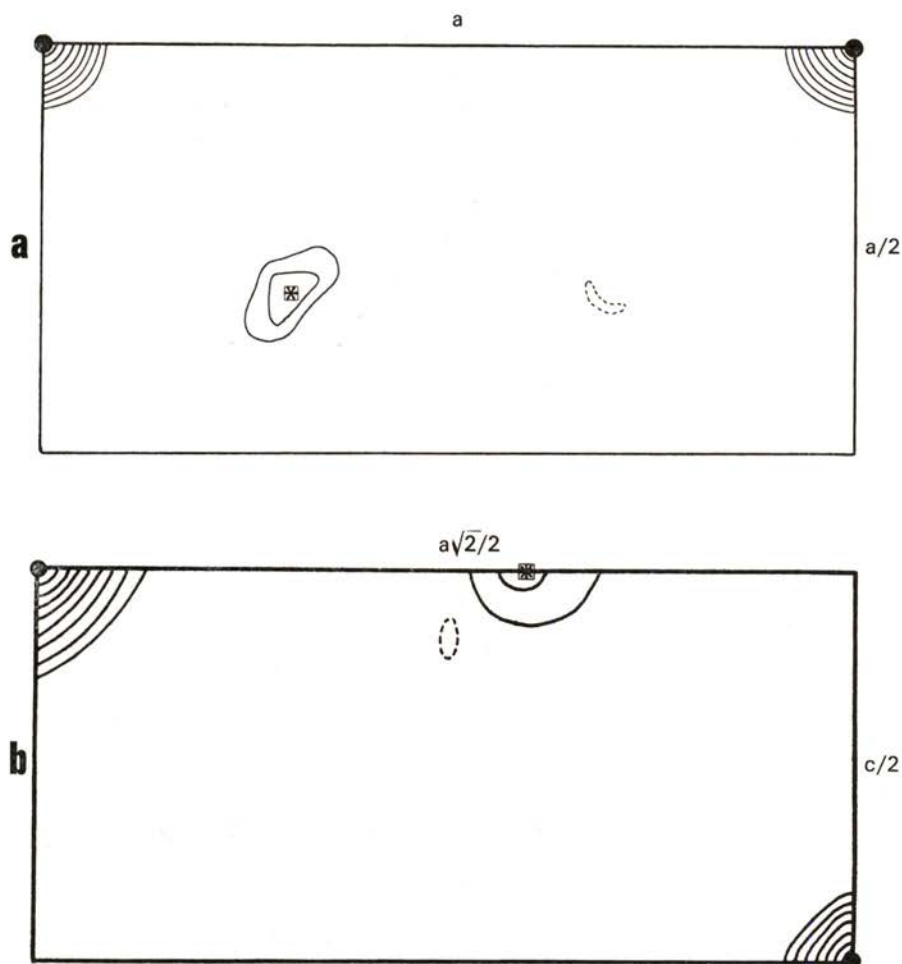
Fig. 4 — Fourier map representing the distribution of the errors in the unit cell. Contours at 1/30 those of SF_0.

    (a)   Section [001] of the unit cell.

    (b)   Section [1$\bar{1}$0] of the unit cell.

4 — DISCUSSION

A meaningful interpretation of the present results requires a direct measurement of the absolute scale, as was pointed out above; experiments leading to its determination are planned and will be carried out soon.

Comparison of Figs. 3 and 4 shows that the difference between the postulated spherical distribution of electrons in both V^{2+} and F^- ions and the real electron distribution, although rather small, is above the significance level. The possibility that the results are masked by extinction is to be taken into account, even though an extinction correction has been applied to the measured intensities. This suggests the convenience of collecting similar X-ray data from another crystal where the effect of extinction is greatly reduced; a nearly-extinction-free crystal has alread been selected and the results obtained will be compared with those of the present work.

It follows from the above arguments that definite conclusions concerning the electron density distribution in VF_2 cannot yet be drawn. However, it appears that the Fourier difference maps (Fig. 3) indicate a deficiency of electrons in the bonding directions, V - F .

REFERENCES

[1] Stout, J. W. and Boo, W. O., *J. Appl. Phys.*, **37**, 966 (1966).

[2] Mc-Cain, W. S., Albright, D. L. and Boo, W. O., *Advan. X-ray Anal.*, **14**, 433 (1971).

[3] Almeida, M. J. M., Costa, M. M. R. R. and Gonschorek, W., *Portgal. Phys.*, **13**, 101 (1982).

[4] Stout, J. W. and Boo, W. O., *J. Chem. Phys.*, **71**, 1 (1979).

[5] North, A. C. T., Phillips, D. C. and Mathews, F. S., *Acta Cryst.*, **A24**, 351 (1968).

[6] Furnas, T. C., *«Single Crystal Orienter Instruction Manual»*, Milwaukee: General Electric Company.

[7] Stevens, E. D. and Coppens, P., *Acta Cryst.*, **A31**, 612 (1975).

THE EFFECT OF STATIC ELECTRIC AND MAGNETIC FIELDS ON THE OPTOELECTRONIC PROPERTIES OF AMORPHOUS HYDROGENATED SILICON FILMS PRODUCED BY R. F. GLOW DISCHARGE (*)

R. MARTINS, A. G. DIAS and L. GUIMARÃES

Centro de Física Molecular das Universidades de Lisboa
Complexo I (I. S. T.), Av. Rovisco Pais, 1000 Lisboa, Portugal

ABSTRACT — The paper deals with the interpretation of transport properties of amorphous hydrogenated silicon films (a-Si : H) through dark conductivity and photoconductivity measurements. a-Si : H films were produced by r. f. glow discharge coupled either inductively or capacitively to a 3 % SiH_4/Ar mixture at different crossed electromagnetic static fields. The data concerned with the dark activation energy, photoactivation energy and photosensitivity, $(\sigma_{ph}/\sigma_d)_{25°C}$, of a-Si : H films can account for their optoelectronic properties, which are strongly dependent on the deposition parameters [1, 2, 3]. We also observed that crossed static electromagnetic fields applied during film formation influence hydrogen incorporation in a manner different from that proposed by Knights [4] or Fritzsche [5].

1 — INTRODUCTION

In recent years the electric and optical proprieties of a-Si : H films have received an increasing amount of attention. Work by Spear [6], Knights [7], Okamoto [8], Taniguchi [9] and Martins [1, 2], has pointed out the role played by the deposition conditions on the electric and optical properties of the films. Their results have shown that it is possible, by a correct arrangement

---

(*) Based on results presented at the Third General Conference of the Portuguese Physical Society (Coimbra, June 1982).

of the deposition parameters, to obtain a-Si : H alloys with a low density of defect gap states, high photoconductivities and well defined conduction paths. We observed that it is possible to produce a-Si : H films at high growth rates (~ 10 Å s^{-1}) [10], with good substrate adhesion and suitable optoelectronic properties. Films produced under static crossed electromagnetic fields are particularly suitable for use in photoelectric devices; their production would involve an industrial process faster and cheaper than those used for crystalline or polycrystalline materials.

2 — EXPERIMENTAL DETAILS

a-Si : H films were produced by r. f. glow discharge of a pre-mixed 3 % SiH$_4$/Ar mixture fed into a capacitively or inductively r. f. (signal) coupled deposition chamber using a gas flow rate lower than 1000 c.c. min^{-1}. The substrate temperature, reactor pressure, r. f. power and frequency of the discharge are kept constant, respectively of the order of 260°C, for inductive films (I. F.), 325°C for capacitive films (C. F.), 1 torr, 20 W and 12.9 MHz. For C. F. films, 7059 Corning Glass substrates are placed in both sides of the heated pedestal, A — C. F. and P — C. F. films [1].

Dark conductivity and photoconductivity measurements as a function of the reciprocal temperature were performed in samples provided with aluminium evaporated electrodes in a gap cell configuration. Air Mass 2 sunlight produced by a G. E. quartz-line ELH tungsten halogen lamp was used for photoconductivity measurements [1, 2].

3 — DARK CONDUCTIVITY AND PHOTOCONDUCTIVITY MEASUREMENTS

Dark conductivity (σ_d) and photoconductivity (σ_{ph}) *versus* the inverse of absolute temperature (T^{-1}) were measured in samples produced either capacitively or inductively coupled at different crossed static electromagnetic fields. In general σ_d *versus* T^{-1} plots show well defined activation energies (ε_σ) , except for a few samples produced without or at low bias. For such samples

we observed that σ_d is proportional to $T^{-1/4}$. This means that the conduction mechanism is hopping assisted. Here the indicated ε_σ value must not be regarded as an activation energy since it is correlated with the asymptote to the σ_d *versus* T^{-1} curve containing the room temperature value.

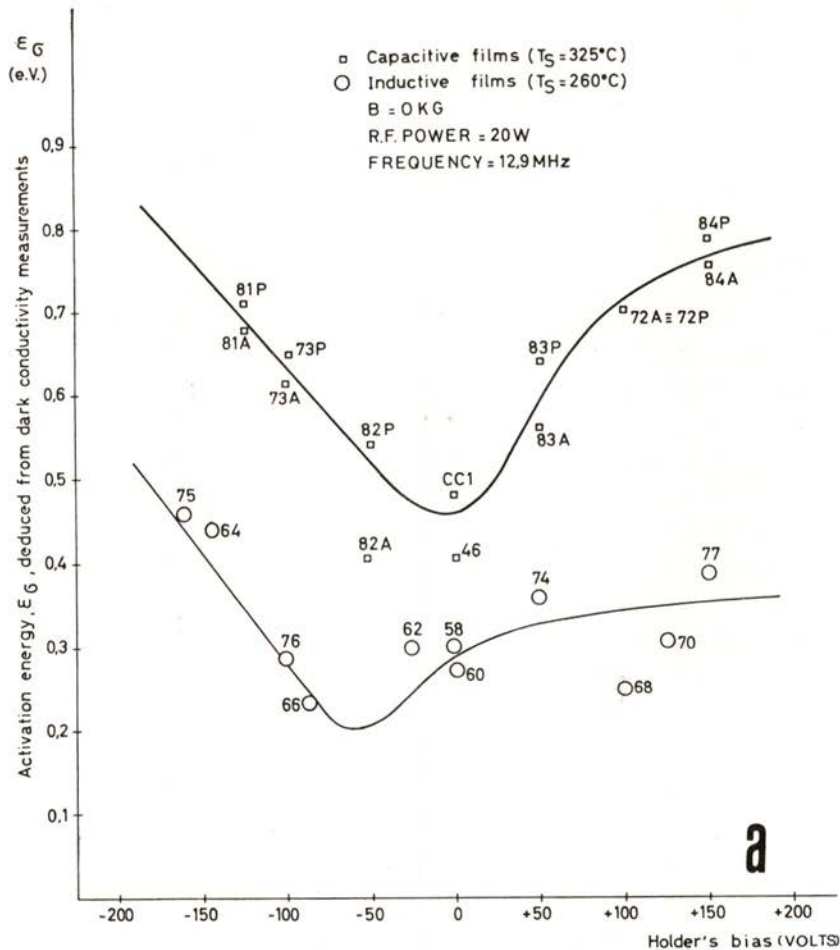Fig. 1 summarizes the ε_σ values as a function of holder's bias (V_{dc}) for C. F. and I. F. with $B = 0$ KG (Fig. 1-a) and

Fig. 1-a — Activation energy as a function of holder's bias ($B = 0$).
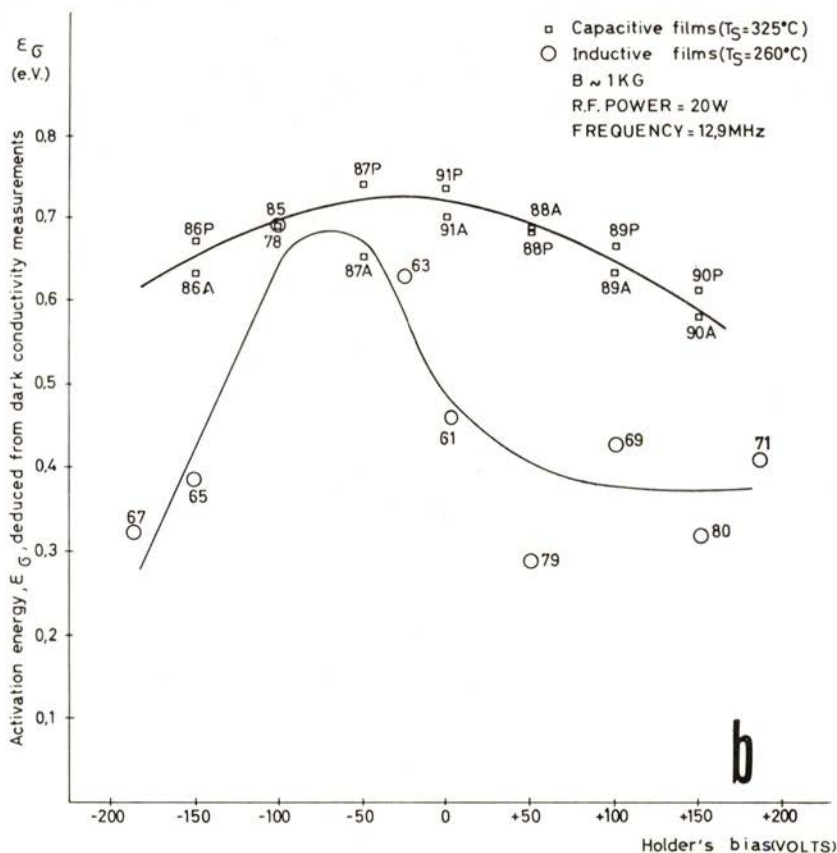
Fig. 1-b — Activation energy as a function of holder's bias (B ~ 1 KG) .

B ~ 1 KG (Fig. 1-b). The configuration of the dependence of ε_σ on V_{dc} changes completely, either for I. F. or C. F., when we apply a crossed magnetic field ~ 1 KG. This change is associated with a shift upward in ε_σ values, for I. F. and C. F., of the order of 0.25 eV, for any value of the V_{dc} signal. The maximum value of ε_σ (~ 0.73 eV) for C. F. corresponds to V_{dc} ~ 0 V. For I. F. ε_σ maximum (~ 0.7 eV) corresponds to V_{dc} ~ — 75 V. Both films were produced under the action of a static magnetic field ~ 1 KG.

Fig. 2 shows photoactivation energy values (ε_{ph}) deduced from photoconductivity measurements for I. F. and C. F. deposits
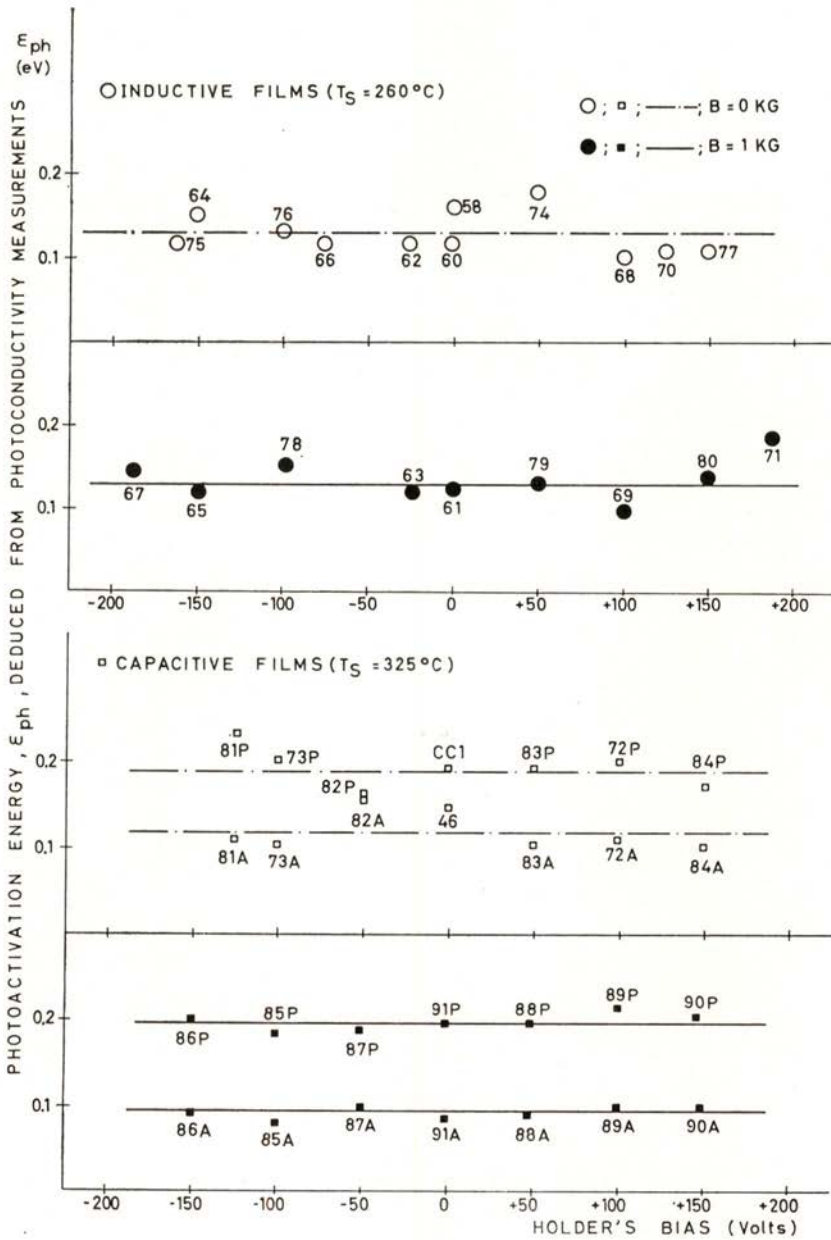
Fig. 2 — Photoactivation energy as a function of holder's bias under AM 2 excitation (75 mw cm^{-2}) .

as a function of V_{dc} with B $= 0$ KG and B of the order of 1 KG. The ε_{ph} values are of the order of 0.1 eV for I. F. deposits and respectively 0.1 eV and 0.2 eV for A — C. F. and P — C. F. deposits, independently of the applied voltage. Using a discrete model like those proposed by Rose [11] and Spear and coworkers [6] we can ascribe ε_{ph} values to transitions between localized states located near the valence and conduction band edges. Thus for I. F. and A — C. F. deposits ε_{ph} values of the order of 0.1 eV can be correlated with the existence of an activated recombination lifetime (τ_R) associated with a high density of defect-gap-states [12, 13], high concentration of charged centres located near the valence band and/or hydrogen content [7]. However when τ_R is unactivated ε_{ph} is of the order of 0.2 eV (P — C. F.), which can be associated with a low density of defect-gap-states and/or hydrogen positively charged centres.

4 — THE NORMALIZED PHOTOCONDUTIVITY AT ROOM TEMPERATURE — $\eta . \mu . \tau$ PRODUCT

Considering the importance of the normalized photoconductivity at room temperature — $(\eta . \mu . \tau)_{25°C}$, the product of the quantum efficiency, η, the drift mobility, μ and excess carrier lifetime, τ — in the characterization of photovoltaic materials, we studied its dependence on the crossed static electromagnetic fields applied during formation of the films. The quantity under consideration may be written

$$(\eta . \mu . \tau)_{25°C} = (I_{ph})_{25°C} \ L^2/(e \, f \, V)$$

where I_{ph} is the photocurrent, L the electrode spacing, e the electron charge, f the number of incident photons per unit area and second and V the applied voltage.

For I. F. deposits we observed bias dependent $(\eta \cdot \mu \cdot \tau)_{25°C}$ values reaching a maximum in the V_{dc} range $[+50, +100 \text{ V}]$ as can be observed in Fig. 3-a. For C. F. deposits the $(\eta \cdot \mu \cdot \tau)_{25°C}$ maximum value, located in the same range as observed for I. F.
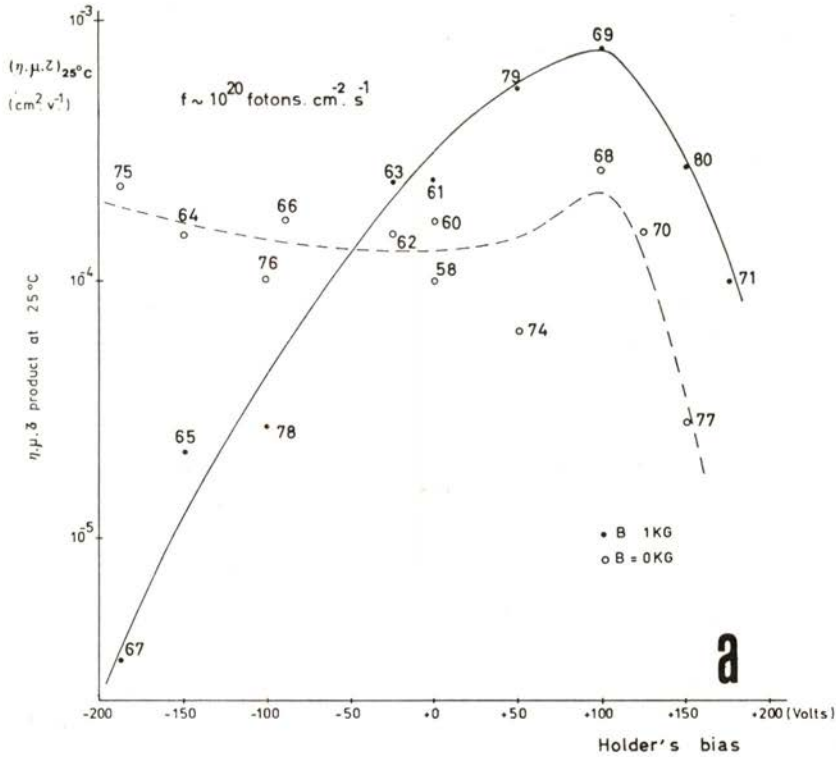

Fig. 3-a — $(\eta \cdot \mu \cdot \tau)_{25°C}$ product as a function of holder's bias for inductive films.

deposits, is shifted towards a V_{dc} range $[-30; -60 \text{ V}]$ through application of a crossed static magnetic field of the order of 1 KG during film deposition (see Fig. 3-b).
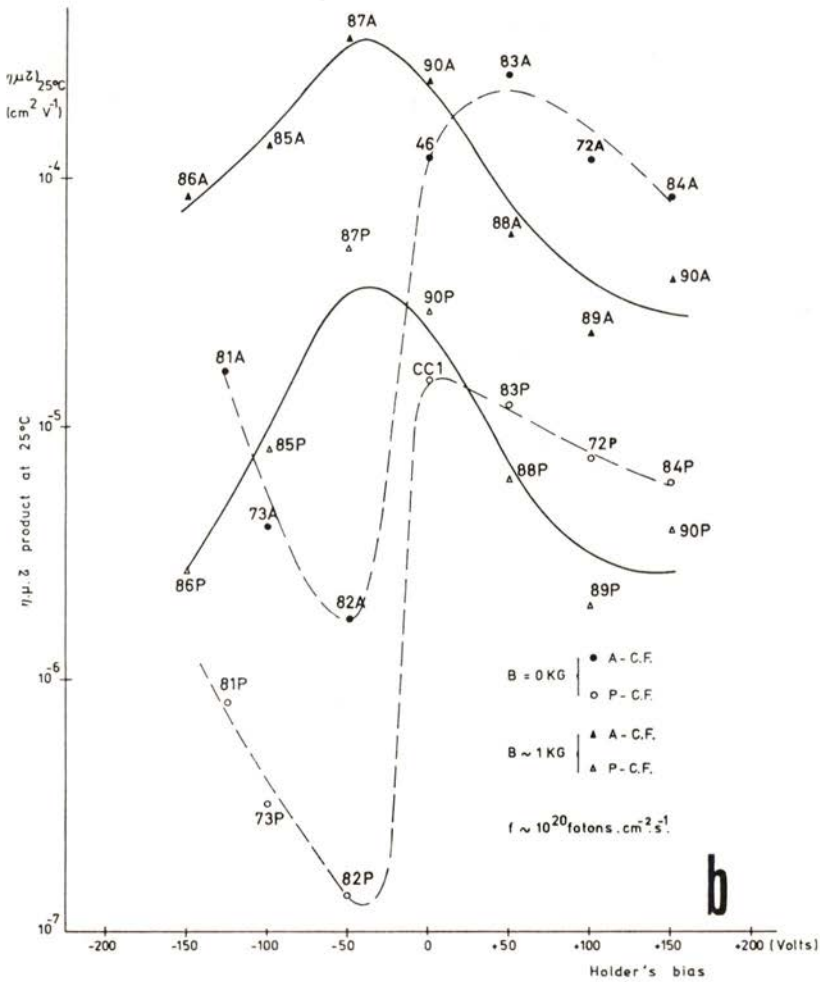
Fig. 3-b — $(\eta \cdot \mu \cdot \tau)_{25^\circ C}$ product as a function of holder's bias for capacitive films.

5 — PHOTOSENSITIVITY. PLASMA KINETICS AND SURFACE REACTIONS

We found bias dependent photosensitivity ratios $(\sigma_{ph}/\sigma_d)_{25^\circ C}$ either for C. F. or I. F. deposits produced with B = 0 KG and B of the order of 1 KG (see Fig. 4). Thus it seems important to
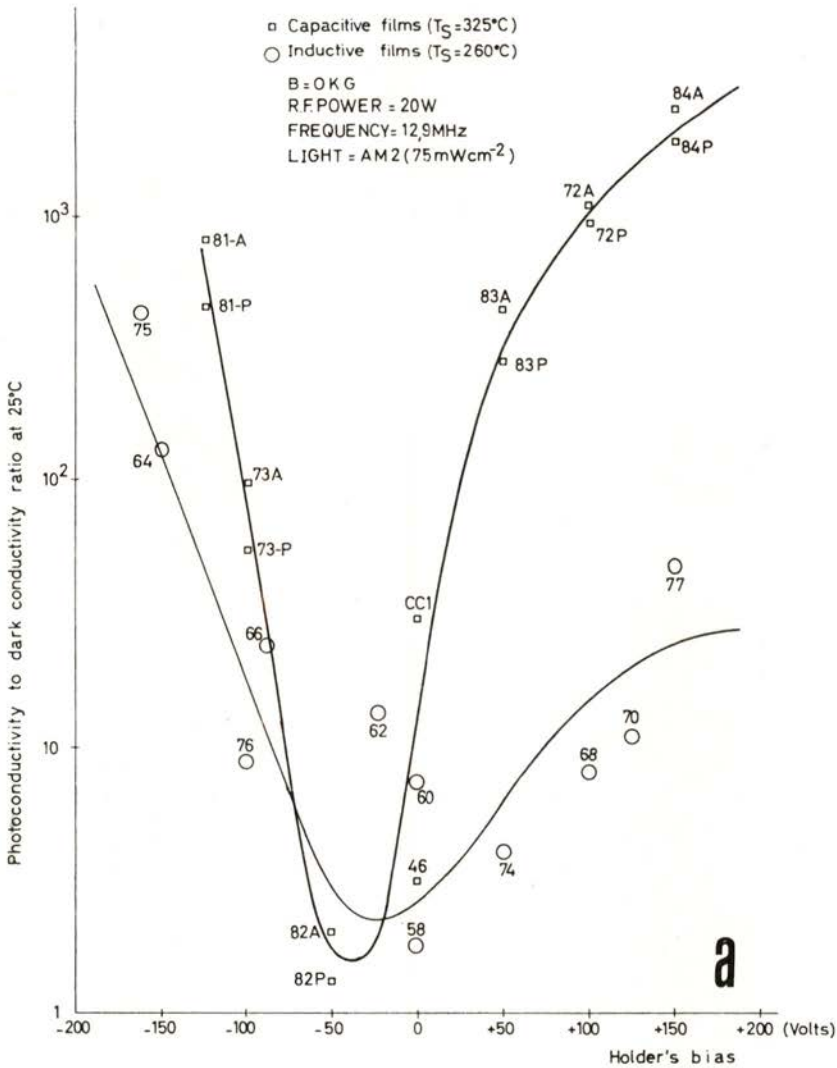
Fig. 4-a — Photosensitivity ratio (σ_{ph}/σ_d)$_{25°C}$ as a function of holder's bias (B = 0).

know the holder's potential with respect to the plasma, as well as the holder's floating potential (for the unbiased case), since both plasma kinetics and surface reactions depend on such values. In order to know the plasma potential and the holder's floating
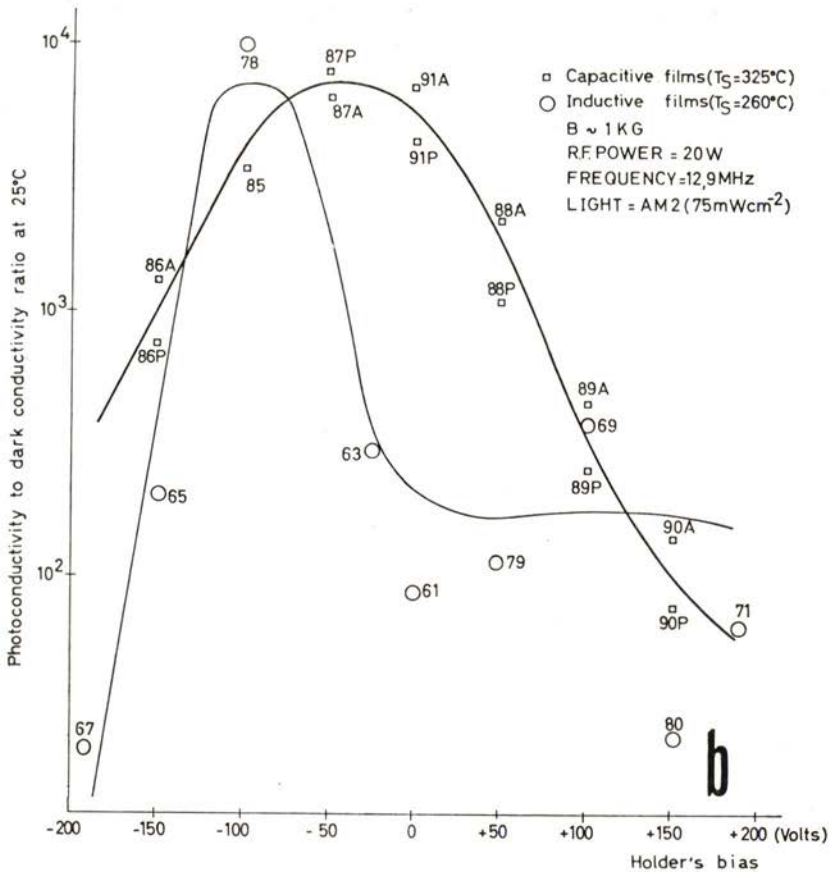
Fig. 4-b — Photosensitivity ratio $(\sigma_{ph}/\sigma_d)_{25°C}$ as a function of holder's bias (B ~ 1 KG).

potential we obtained the I(V) characteristic curves of the plasma at a fixed gas temperature (~ 280°C) and discharge pressure (~ 1.5 torr) as a function of r. f. power delivered to the discharge for B = 0 KG and B of the order of 1 KG (see Fig. 5). Such measurements have been carried out using a Langmuir plasma diagnostic probe placed near the substrate.

Our results show that when B = 0 KG the $(\sigma_{ph}/\sigma_d)_{25°C}$ ratio improves as $|V_{dc}|$ increases both for C. F. and I. F. deposits. This indicates that positive holder's bias do not enhance the amount of

hydrogen or the number of polysilicon dihydride molecules (SiH_2)$_n$ incorporated into the films, as suggested by Knights [4] and Fritzsche [5]. This result agrees with the raising photoconductivity values for such films which is indicative of a low density of
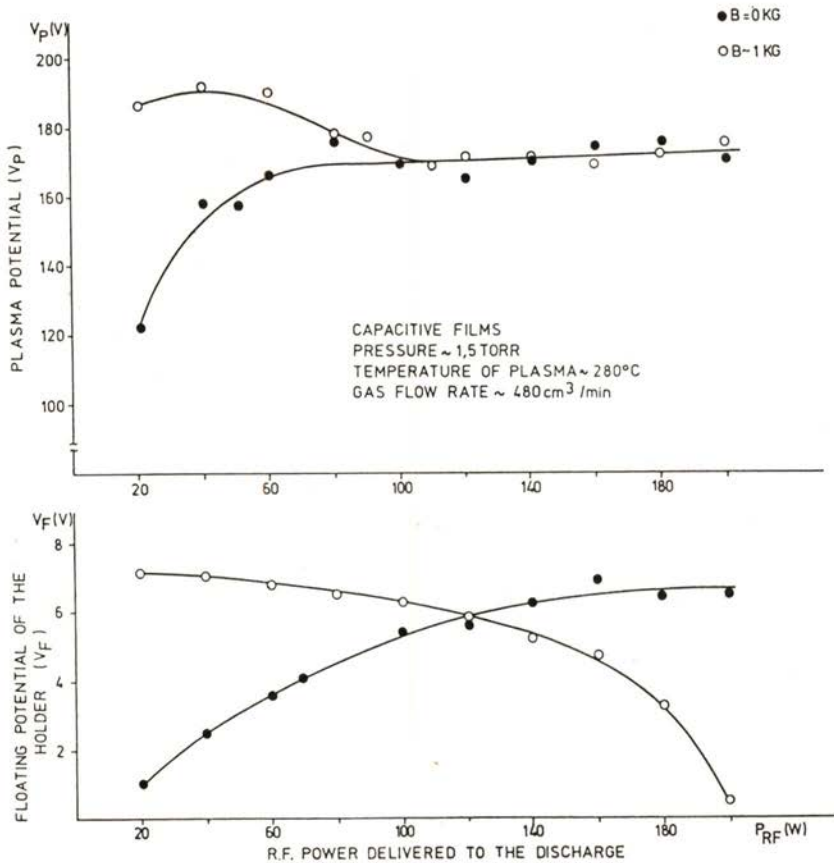

Fig. 5 — Plasma potential and floating potential as a function of R. F. power delivered to the discharge.

recombination centres related with few polymerization centres and voids [14]. Similar results have been reported by Hamakawa et al. [15] who observed a maximum in $(\sigma_{ph}/\sigma_d)_{25°C}$ ratio as a

function of V_{dc} for $B = 0$ KG at V_{dc} in the range $[0; +50$ V$]$, associated with a substrate potential of the order of -60 V with respect to the plasma. As we can see plasma kinetics and surface reactions are not ruled only by the r. f. power delivered to the discharge which in fact controls the plasma potential; the holder's bias is also important. This means that ion damage and electron bombardment, which will influence the number of incorporated defects and the local H binding, will depend on the holder's potential with respect to the plasma.

When B is of the order of 1 KG the dependence of $(\sigma_{ph}/\sigma_d)_{25°C}$ on V_{dc} is opposite to that obtained for $B = 0$ KG. This result means that, avoiding ion damage or electron bombardment of the substrate, the number of dihydride molecules (SiH_2) decreases as the number of monohydride molecules increases [5, 1].

This can be explained by the differences observed in the plasma potential values at $B = 0$ KG and $B \sim 1$ KG (Fig. 5).

6 — CONCLUSIONS

Taking into account the results concerning the dark conductivity and photoconductivity measurements we can conclude that film properties are strongly influenced by the electrode geometry (I. F. or C. F. deposits) and the kind of static electromagnetic fields used [10]. We also observe (see Fig. 3 and Fig. 4) that, for inductive or capacitive films produced under the action of negative holder's bias ($B = 0$ KG), while the $(\sigma_{ph}/\sigma_d)_{25°C}$ ratio increases (which is indicative of increasing SiH/SiH_2 ratios) the $(\eta.\mu.\tau)_{25°C}$ products decrease or remain almost constant. On the other hand, $P - C. F.$ deposits, although related with an amount of incorporated H lower than $A - C. F.$ or I. F. deposits [2] present a poor photoconductivity. Both results show that the SiH/SiH_2 ratio is not a good measure of film quality for photovoltaic application, as suggested by Knights [4] and Fritzsche [5].

As a matter of fact, our previous work [1, 2, 3] confirms that the application of static electromagnetic fields during film formation disturbs the plasma decomposition process and the surface reactions, controlling the growth rate [10] and optoelec-

tronic properties [1, 2, 16] of the films. Thus, it seems that the best films for photovoltaic purposes are the capacitive ones produced with $V_{dc} \in [\, 0 \, ; \, -50 \, V \,]$ and B of the order of 1 KG or $V_{dc} \in [\, +50 \, ; \, +100 \, V \,]$ and B = 0 KG, corresponding to holder's potentials, with respect to the plasma, of the order of $[\, -180 \, ; \, -230 \, V \,]$ and $[\, -20 \, ; \, -70 \, V \,]$, respectively (see Fig. 3, 4 and 5).

According to our results the most convenient deposition technology of amorphous silicon hydrogenated alloys for photovoltaic applications is the static electromagnetic controlled r. f. glow discharge.

REFERENCES

[1] Martins, R., Dias, A. G. and Guimarães, L., *AIP Conf. Proc.*, **73** (1981), 36.

[2] Dias, A. G., Guimarães, L. and Martins, R., *Thin Solid Films*, **89** (1982), 307.

[3] Guimarães, L., Martins, R. and Dias, A. G., *Journal de Physique*, Colloque, **C4**, Supplément au n.° 10, Tome **42** (1981), C4-609.

[4] Knights, J. C., *Appl. Phys. Lett.*, **35** (1979), 244.

[5] Fritzsche, H., Tsai, C. C. and Pearsons, P., *Solid State Tech.*, **21** (1978), 55.

[6] Madan, A., Le Comber, P. G. and Spear, W. E., *J. of Non-Cryst. Sol.*, **20** (1976), 239; Anderson, D. A. and Spear, W. E., *Phil Mag.*, **36** (1977), 695; Loveland, R. J., Spear, W. E. and Al-Sharbaty, A., *J. of Non-Cryst. Sol.*, **13** (1973/74), 55.

[7] Knights, J. C., *J. of Non-Cryst. Sol.*, **35-36** (1980), 159.

[8] Okamoto, H., Yamaguchi, T., Nitta, Y. and Hamakawa, Y., *Proc. of 8th Int. Conf. on Am. and Liq. Semic.* (Boston 1979), 201.

[9]   TANIGUCHI, M., HIROSE, M. and OSAKA, Y., *Proc. of 8th Int. Conf. on Am. and Liq. Semic.* (Boston 1979), 189.

[10] MARTINS, R., *Thin Solid Films,* **90** (1982), 307.

[11] ROSE, A., *Concepts in Photoconductivity and Allied Problems,* Interscience, (New York 1970).

[12] FUHS, W., MILLEVILLE, M. and STUKE, J., *Phys. Status Solidi,* **B89** (1978), 495.

[13] WRONSKY, C. R. and CARLSON, D. E., *Proc. 7th Int. Conf. on Am. and Liq. Semic.* (Edinburgh 1977), 452.

[14] HOHEISEL, B., FISCHER, R. and STUKE, J., *Journal de Physique,* Colloque, **C4**, *Supplément* au n.° 10, Tome 42 (1981), C4-819.

[15] HOTTA, S., TAWADA, Y., OKAMOTO, H. and HAMAKAWA, Y., *Journal de Physique, Colloque,* **C4**, Supplément au n.° 10, Tome 42 (1981), C4-631.

[16] GUIMARÃES, L., MARTINS, R., DIAS, A. G. and BARRADAS, F., in «A model for analysis of optical measurements carried on a-Si : H films for photovoltaic applications», *4th European Photovoltaic Solar Energy Conference,* Italy 1982.

ON THE QUEST OF NEW CERAMICS FOR VARISTORS (*)

C. S. Furtado

Centro de Física da Radiação e dos Materias (INIC), Universidade,
3000 Coimbra, Portugal

ABSTRACT — The varistor effect is described in the Bi doped ZnO and the theory which attributes this effect to a space-charge layer between semiconducting grains is briefly related. The structure of a single-contact varistor is presented. The ideas underlying a quest for new ceramics, which might show the varistor effect, are expressed. The results obtained with sandwich-type structures, either Li doped Ni O or Ti doped Fe_2O_3, having intermediate foils of Bi, Sb, Cr, Mn and Co oxides are presented.

1 — INTRODUCTION

The varistor effect in bismuth-doped zinc oxide.

In some polycrystalline ceramics, such as silicon carbide and zinc oxide with small additions of certain oxides [1, 2, 3], one observes the so-called varistor effect, characterized by a rectifier, bidirectional effect through several orders of magnitude of the current intensity, as illustrated in Fig. 1. At low voltage, the material shows great ohmic resistance; at a somewhat higher voltage nonlinearity sets in, a breakdown occurs and the current intensity increases very steeply with the voltage, according to a relation usually described by a power law, $I = k V^\alpha$; for still higher voltages, we come to the up-turn region and the resistance takes again ohmic character.

(*) Results presented at the Third General Conference of the Portuguese Physical Society (Coimbra, June 1982).

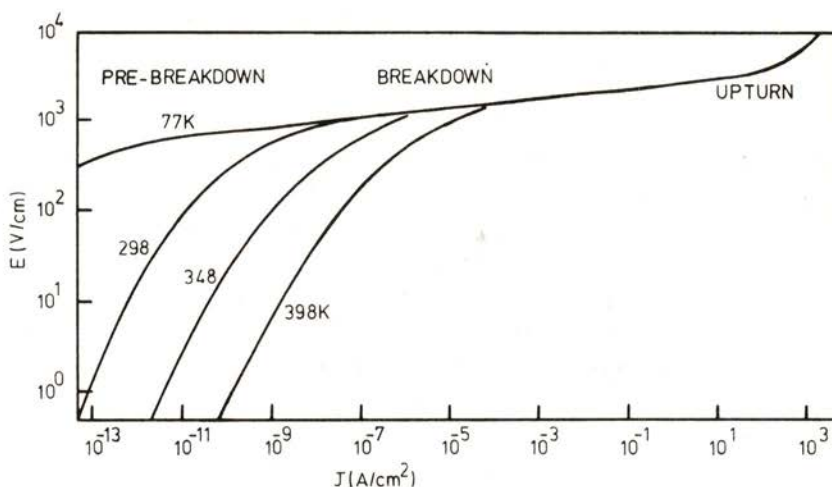*Portgal. Phys.* — Vol. 14, fasc. 1-2, pp. 95-103, 1983

95

Fig. 1 — Current voltage characteristic of a bismuth doped zinc oxide varistor.

The varistor effect is generally attributed to a boundary effect at the interface of the grains [2]. The microstructure of a zinc oxide varistor, which gives support to this interpretation, is shown in Fig. 2 [4]. It can be seen that between the semiconducting
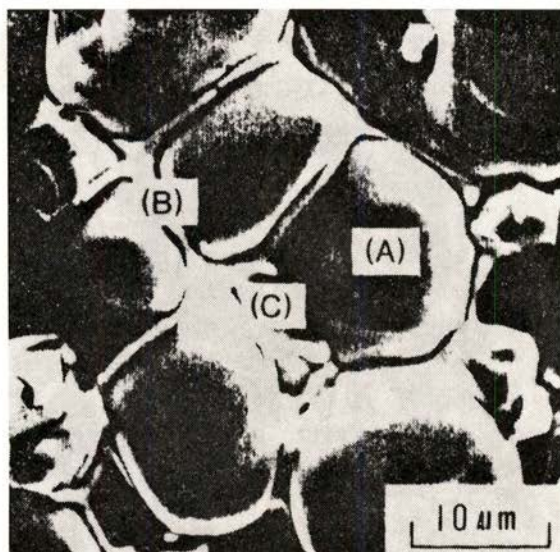

Fig. 2 — Microstructure of zinc oxide doped with bismuth [4].

grains of zinc oxide with dimensions of order 10 μm (A), there is a layer rich in bismuth (B), and regions with spinel (C). The existence of bismuth is generally considered fundamental in order to allow, during the sinterization, that the grains have their surfaces wetted, thus promoting their oxidation and, consequently, the intergranular fixation, as oxides, of other elements which are added in green ($Bi_2 O_3$, $Co_3 O_4$, $Mn O$, $Cr_2 O_3$, ...). The substitution of a divalent zinc ion for a trivalent ion gives rise to an extra positive charge, 50 Angstroms wide, internally adjacent to the grain surface, which implies the formation of a negative charge in the intergranular region. This corresponds to back-to-back Schottky diodes, consisting of a charged interface in association with a space-charge layer, which has both ionic and electronic parts.

A metal-oxide varistor is very often described by the simple equivalent circuit shown in Fig. 3. A pure capacitance, C_p, in parallel with a voltage dependent resistance, R_p, represents the intergranular layers, while r_g is the resistance of the semiconducting grains. For low applied voltages, R_p exhibits an Ohmic behaviour.
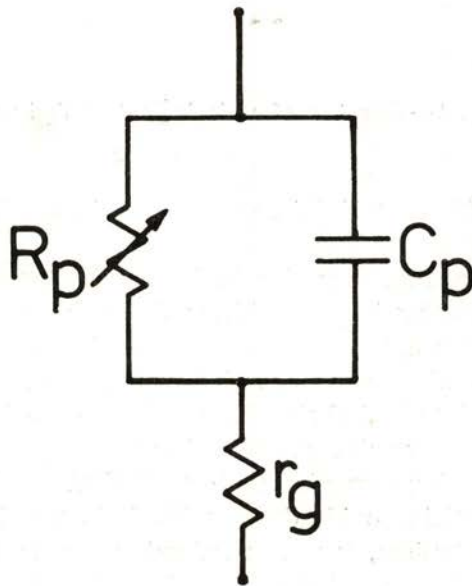

Fig. 3 — Simple equivalent circuit representing a metal-oxide varistor.

Single-Contact Varistor.

In order to reproduce the structure "grain-intergranular region-grain", it was thought to make a single-contact varistor. This consists (see Fig. 4) of a structure of two slices of zinc oxide doped with other oxides in very small percentages [5], or of zinc oxide single-crystals [6], between which a foil with a thickness of the order of 100 μm is placed. This assembly is sintered under pressure, leading, in a controlled way, to a single contact of sequence zinc oxide grain (semiconductor) — potential barrier — zinc oxide grain (semiconductor).
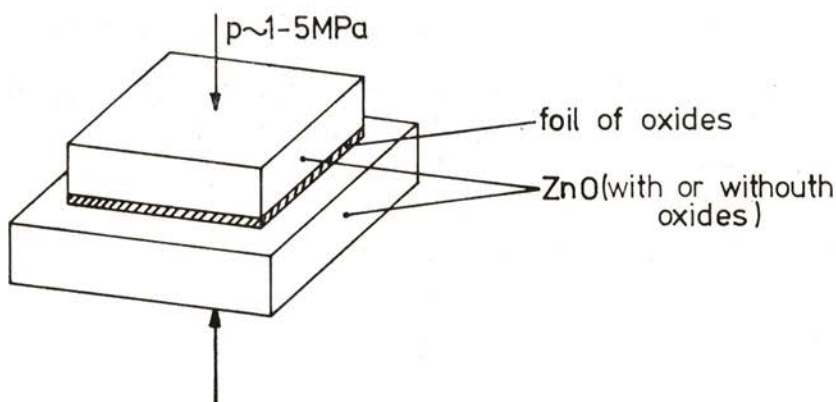

Fig. 4 — Structure of a Single-Contact Varistor.

2 — LOOKING FOR NEW SUBSTANCES FOR VARISTORS

The quest of new ceramics, which exhibit the varistor effect, was mainly influenced by two ideas: 1) to find an oxide, simple or adequately doped, which manifests a semiconducting behaviour and has a convenient charge carrier concentration, and 2) to discover the additives and their adequate concentrations which can originate an intergranular potential barrier.

Semiconducting ceramics with controlled carrier concentration, based on nickel oxide doped with lithium and ferrous oxide doped with titanium, were obtained after suitable thermal treatments. In the formation of the foil, to be placed between the semiconducting oxide slices, oxides were used which have a metal

with a) valence different from that of the metal in the oxide of the grains (Ni or Fe) and b) a greater atomic diameter. It is supposed that, for reasons of minimum of free energy, the impurities will segregate predominantly at the grain interface [7] originating, in that way, a space charge layer, already referred to in Section 1.

3 — EXPERIMENTAL

The approximate dimensions of the slices of semiconductor ceramics, with polished or unpolished faces, were $1.5 \times 1.5 \times 1.0$ mm³. To prepare the foils, a mixture of 2 grams of the chosen oxides, dispersed in 2 grams of deionized water, was ground, and 3 grams of an organic binder (Poliviol at 20 %) were added. The resulting emulsion was afterwards conveniently stirred. A paste was spread on a smooth sheet of glass (or plastic) with a brass roller whose surface was completely full of grooves. The depth of these grooves is the same as that of the required foil. We have used foils 250 μm thick. A sandwich was formed by inserting this thin foil between a pair of the Zn O plates.

This assembly was sintered either in a horizontal or a vertical oven. In the horizontal oven, the pressure was obtained through a spring, while, in the vertical one, this was achieved by means of weights. Temperatures, durations of sintering, as well as the used pressure, are reported in Table I.

To get the characteristics $I = I(V)$, good ohmic contacts with the ceramics were needed, for which we have applied the indium-gallium alloy at the eutectic point. The current intensity was measured with an electrometer (Model 610, of Keithley Instruments). For current intensities above $10^{-8} - 10^{-7}$ Ampères the measurements were made using pulses to avoid self-heating which causes thermal instability (thermal run-away).

4 — RESULTS

We have tried to make varistors by using ceramics of nickel oxide doped with lithium and of ferrous oxide doped with titanium. The foils we employed were of: oxides of Bi and Ba in the proportion of Bi : Ba = 2 : 1; and oxides of Sb, Bi, Cr, Mn and Co in the proportion of Sb : Bi : Cr : Mn : Co = 4 : 2 : 2 : 1 : 1 .

TABLE I

Attempt Nr.	Slices	State of the faces	Foil	Thermal Treatment	Results
1	NiO, 4 % Li	As cut	Bi:Ba = 2:1	$T = 1000°C$, $p = 1.3$ MPa, $t = 1$ hr	Unsuccessful
2	NiO, 4 % Li	Idem	Idem	$(T = 1000°C$, $p = 2.6$ MPa, $t = 1$ hr 30 mn$)$ $+ (T = 1100°C$, $p = 2.6$ MPa, $t = 1$ hr$)$	Idem
3	NiO, 4 % Li	Idem	Idem	$(T = 1120°C$, $p = 1.0$ MPa, $t = 1$ hr$)$ $+ (T = 1200°C$, $p = 0$ Pa, $t = 1$ hr$)$	Mechanically stable
4	Fe_2O_3, 1.5 % Ti	Polished	Sb:Bi:Cr:Mn:Co = 4:2:2:1:1	$T = 960°C$, $p = 1.6$ MPa, $t = 1$ hr	Unsuccessful
5	Fe_2O_3, 1.5 % Ti	Idem	Idem	$T = 1030°C$, $p = 1.6$ MPa, $t = 1$ hr	Weak cohesion
6	Fe_2O_3, 1.5 % Ti	Idem	Idem	$T = 1050°C$, $p = 3.0$ MPa, $t = 1$ hr 40 mn	Mechanically stable
7	Fe_2O_3, 1.5 % Ti	Idem	Idem	As the last attempt $+ (T = 1150°C$, $p = 0$ Pa, $t = 1$ hr 40 mn$)$	Idem
8	Fe_2O_3, 1.5 % Ti	Idem	Idem	As the last attempt $+ (T = 1150°C$, $p = 3.0$ Pa, $t = 45$ mn$)$	Idem
9	Fe_2O_3, 0.5 % Ti	As cut	Idem	$T = 950°C$, $p = 5.0$ MPa, $t = 1$ hr	Unsuccessful
10	Fe_2O_3, 0.5 % Ti	Idem	Idem	$T = 1050°C$, $p = 5.0$ MPa, $t = 1$ hr	Idem
11	Fe_2O_3, 0.5 % Ti	Idem	Idem	$T = 1200°C$, $p = 0.2$ MPa, $t = 18$ hr	Mechanically stable
12	Fe_2O_3, 0.2 % Ti	Idem	Idem	$T = 1200°C$, $p = 0.2$ MPa, $t = 16$ hr	Idem
13	Fe_2O_3, 0.5 % Ti	Polished	Idem	$T = 1050°C$, $p = 5.0$ MPa, $t = 1$ hr	Unsuccessful
14	Fe_2O_3, 0.5 % Ti	Idem	Idem	$T = 1100°C$, $p = 5.0$ MPa, $t = 1$ hr	Idem
15	Fe_2O_3, 0.5 % Ti	Idem	Idem	$T = 1050°C$, $p = 1.7$ MPa, $t = 1$ hr	Mechanically rather stable

100

Portgal. Phys. — Vol. 14, fasc. 1-2, pp. 95-103, 1983

A preliminary objective, of obvious and fundamental importance, is concerned with the mechanical stability of the structure. The attempts which were made and their results are concisely shown in Table I. We can conclude, although cautiously waiting further trials, that the duration of the treatment and the smoothness of the faces will favour mechanical stability. As to the influence of the pressure it seems there exists a recommended range of values.

On the mechanically stable structures, measurements were made which led to the establishment of the $I = I(V)$ characteristics. In Fig. 5 it is shown the characteristic of the structure
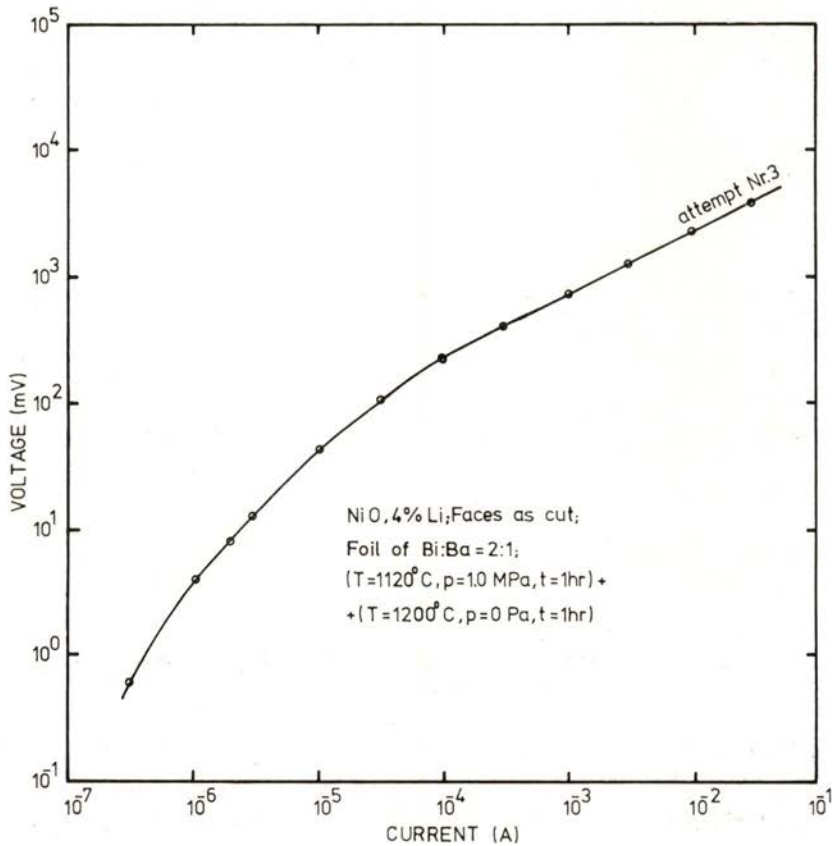

Fig. 5 — Characteristic $I = I(V)$ of the structure of Attempt Nr. 3.

corresponding to attempt Nr. 3 (Ni O, 4 % Li; foil Bi : Ba = 2 : 1) .
In Fig. 6, can be seen the characteristics of structures where the
slices were made of $Fe_2 O_3$, with 1.5 % (Attempt Nr. 6), 0.5 %
(attempts Nrs. 11 and 15) or 0.2 % (Attempt Nr. 12) Ti, the foil
being, in all cases, formed with oxides of elements in the pro-
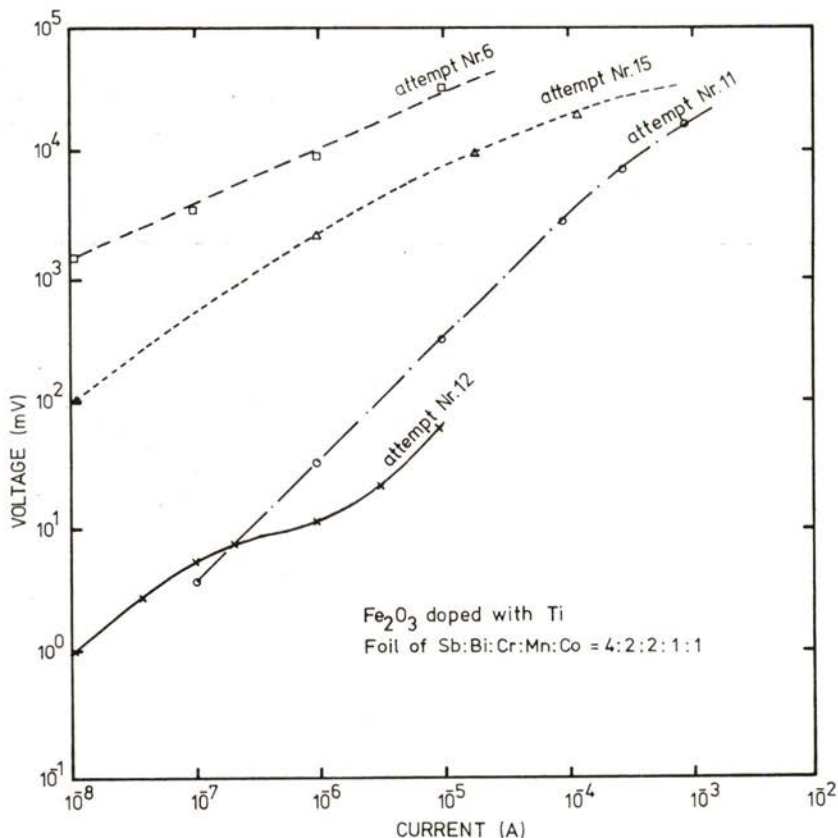portions Sb : Bi : Cr : Mn : Co = 4 : 2 : 2 : 1 : 1 .

Fig. 6 — Characteristics I = I (V) of the structures of Attempts
Nrs. 6, 11, 12 and 15.

Taking as a measure of the nonlinearity the value of the
exponent α (in the relation $I = k V^\alpha$) we have, for each of the
characteristics, the following maximum values: $\alpha_m = 2$ (Attempt
Nr. 3); $\alpha_m = 2.2$ (Attempt Nr. 6); $\alpha_m = 1.4$ (Attempt Nr. 11);
$\alpha_m = 4$ (Attempt Nr. 12) and $\alpha_m = 2.5$ (Attempt Nr. 15).

We consider our results rather promising, intending therefore to go on looking for new ceramics which exhibit the varistor effect.

REFERENCES

[1] KH. S. VALEV, *Sov. Phys. Tech. Phys.*, **2**, 1533 (1957).

[2] M. MATSUOKA, *Jpn. J. Appl. Phys.*, **10**, 736 (1971).

[3] W. G. MORRIS, *J. Am. Ceram. Soc.*, **56**, 360 (1973).

[4] M. MATSUOKA, *Advances in Ceramics*, vol. 1, Grain Boundary Phenomena in Electronic Ceramics, Ed. Lionel M. Levinson, p. 290, American Ceramic Society (1981).

[5] B. HOFFMANN and U. SCHWING, ibid., p. 343.

[6] U. SCHWING and B. HOFFMANN, *ibid.*, p. 386.

[7] W. D. KINGERY, *J. Amer. Ceram. Soc.*, **57**, 74 (1974).

MULTICHANNEL ANALYSER TO MICRO-COMPUTER SOFTWARE INTERFACE FOR ON-LINE DATA ANALYSIS (*)

A. M. GONÇALVES, M. H. GONÇALVES

Departamento de Física, Faculdade de Ciências, 1294 LISBOA Codex

P. BARAHONA (¹)

Departamento de Informática, Universidade Nova de Lisboa,
2825 MONTE DA CAPARICA

ABSTRACT — A general purpose Multichannel Analyser (MCA) to a micro-computer (μC) software interface has been developed. The system is based on a small low cost 8-bits μC running under the CP/M disk operating system, and it allows bidirectional data transfer betwenn a MCA and a μC, the storage of the acquired data on the MCA into a disk file, the decoding and condensing of the data, and it enables the user to perform an immediate data analysis. The concept of the design is user independent and it can be configured at any given time by a simple modification of some data files. Specially suited for an easy implementation on common situations in physics laboratories, the system developed offers (in many respects) the same facilities as those available in data acquisition systems based on PDP mini-computers, for a fraction of the cost.

1 — INTRODUCTION

The application of computing power in the physics laboratory is an expanding field, specially after microprocessors became generally available in the last few years. These applications

---

(¹) Present Address: Departamento de Estatística, Invest. Operac. e Computação, Faculdade de Ciências, 1294 LISBOA CODEX.

concern different requests in laboratory measurement work, which we may classify in the following groups: i) control; ii) data logging; iii) data analysis.

It is possible or even, in some cases, essential for laboratory on-line computing to support an integrated philosophy comprising the above functions. However it is more efficient when approaching a given problem to start by the identification of its specific and less complex aspects.

In many cases, the standard general purpose instrumentation could be the best answer for one or more of those requests. This is the case of the Multichannel Analysers (MCAs), used in many experimental devices as a sophisticated data logger. The use of a MCA in a laboratory strongly suggests, as first priority, the use of computational means for the handling of the acquired data. The use of paper punched tape to carry out the data to a computer is still used in several physics laboratories, but it is increasingly being considered as a slow and less convenient method. The industrial standard answer is the application of sophisticated and expensive systems based on PDP 11 minicomputers to perform data analysis, as they provide on-line fast and easy data transfer with MCAs.

Our aim is to develop for the same task a low cost system taking advantage of the existing industrial standard instrumentation, without using any special bus. We can find a support for our point of view in a recent review article by Brignell and Young [1].

The low price of up-to-date 8-bits μCs, together with a flexible software with increasing capabilities, provides an attractive and efficient alternative to produce in the laboratory an immediate data analysis even with a large amount of numerical treatment. Apparently the main problem which arises is how to transfer the data from the MCA to the μC without any expensive and specific interface. This problem is easy to solve as many modern MCAs have standard interfaces (e.g. RS 232 or 20 mA current loop) for data transmission to peripheral devices such as a teletype. These interfaces also provide the way to connect directly the MCA to a μC equiped with a similar interface. This restricts the problem to writing the appropriate software. The easy solution is to write programs for a given experimental situation based on

a particular personal μC hardware configuration running under a resident BASIC interpreter. However, the most attractive and efficient way is to design a general purpose system, configurable to different users and experimental requirements, being hardware independent, and allowing typical procedures in data manipulation and analysis.

In this work, we report on a system program, written in a modular way, easy to fit to different experimental requirements. The system allows the data transfer from a MCA to a μC (and vice-versa), the storage of the data into a disk file, the decoding of the data, and enables the user to perform an immediate data analysis. The program runs under the CP/M disk operating system [2] which is the most frequently used in 8-bits machines based on 8080-like μPs. Consequently, this software offers great portability, and is hardware independent for systems under CP/M.

In the following sections, we describe briefly the system hardware and software. In section 3 we give particular emphasis to the description of modifications that may be required to fit different hardware configuration and users' needs. In section 4 we present an example of the system implementation.

2 — SYSTEM DESIGN

2.1 — *Hardware*

There are several microcomputers running under CP/M on the market that answer the necessary requirements. The selection of the microcomputer, based on budgetary limitations, made it attractive to choose a Zenith Z 89 [3]. This system has been equiped with a 48 k memory (8 bit word), one mini floppy disk drive (allowing a mass storage area for programs and data of 90 k), and two serial interfaces RS 232C. Unfortunately the video terminal is not equiped with vector graphic capabilities allowing only alpha numeric display. It should be stressed that this is the minimum possible configuration for any CP/M based system.

In the main tests we have used the low cost MCA Inotech 5200 [4] provided with a 20 mA current loop interface without

hand shaking. This interface is designed for data output in ASCII characters on a teletype, with a data transfer rate of 110 baud. This MCA has 1024 channels, with a maximum storage capacity of 10^6-1 counts per channel. In Fig. 1, we show an overview of the system.
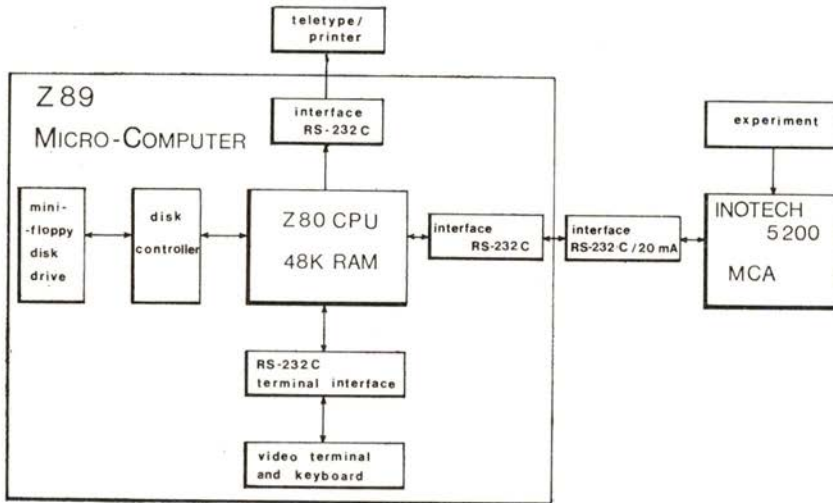

Fig. 1 — The system overview, showing the micro-computer configuration and peripherals used.

The communication between the MCA and the μC is performed through a laboratory made interface, which transforms the 20 mA current loops' signals into RS 232 C standard signals and vice-versa. To increase the transfer rate, the MCA I/O baud rate was changed from 110 baud to 1200 baud. This means that a whole spectrum of 1024 channels is transferred in less than one minute.

2.2 — *Software*

Our approach to software has been to write the program in extended BASIC (from Microsoft) [5]. Although this language does not assist a modular program structure (as it does not allow

for local scope of the variables and to pass on parameters to the subroutines) this is not a major problem when the programs are not too long. On the other hand the interactive nature of the BASIC interpreter, with text editing facilities, and run time error messages, significantly reduces the effort required for program development.

The BASIC also allows to read and write external devices and to examine and alter memory locations. This facilities have been extensively used by many groups when "personal" micro-computers with a resident BASIC interpreter are applied as data-acquisition systems [6-10]. However due to the slow speed of the interpreter, we prefer to write assembly code routines (easily called from a BASIC program) to communicate with the MCA and to create a file using directly the system calls of the CP/M Operating System [2].

Using the BASIC interpreter, we need a system with almost 64 k bytes of main memory to run the whole program. In this program version, the machine code routines must be loaded into memory, before the BASIC interpreter and the BASIC source program itself. To overcome this evident drawback, the BASIC program has been compiled and linked with the relocatable modules produced by the Macro Assembler M80 [11] from our Assembly routines. In this way, we get an absolute code, transparent to the user, running significantly faster under the CP/M operating system, and demanding only a 48 k system.

3 — DESCRIPTION OF THE PROGRAMS

In Fig. 2 we show the block diagram of the whole program. In the first module, MAIN-INIT, the μC performs a dialogue with the user, and initiates the experience variables. In the module TRANSFER the data is transferred from the MCA to the μC accordingly with the variable "I". The module DECODE generates a direct access file with the number of counts of each channel, in a binary form, for future treatment. The module OPTIONS allows for the implementation of user defined data processing programs, for the immediate data analysis, using a
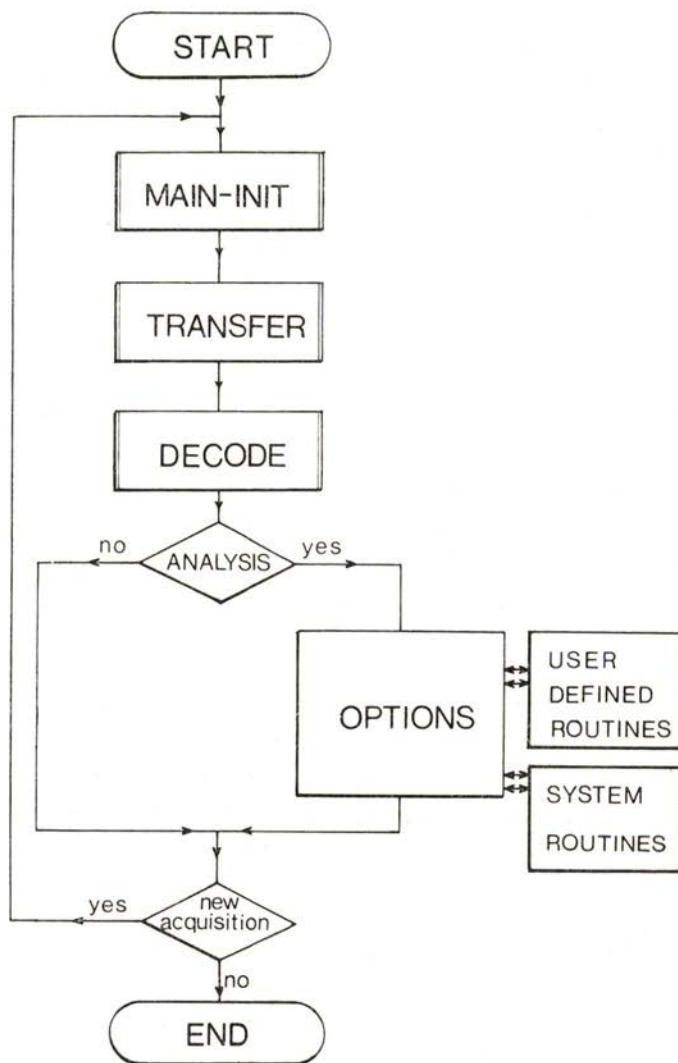
Fig. 2 — Flowchart of the acquire program. At least two parameters are generated in the MAIN-INIT module: the «filename» for the present run (FN, a string of 8 alphanumeric characters) and the number of channels to be transferred (NC). These parameters are passed through the entire program.

chaining structure. After the treatment, and since with our µC we can not view the spectrum in the video terminal, the module ENCODE generates a file in the MCA format from a direct access file of the above type. The module TRANSFER allows this data to be transferred from the µC to the MCA according with the variable "O".

In the next sections we give a detailed description of each module.

3.1 — Main-Init

The dialogue with the user is performed following the data read from the file PROTOCOL.DAT. This file must be defined by the user according with his own experience and can be changed at any time, to answer new requests. The file is organised in order to give the number of questions and for each of them the text defining the parameter to be inputed (e.g. material to be analized, temperature, pressure, radiation wave length etc.), the type of entry (integer, real or string) and the data variation limits for data entry validation. For integers we assume that they are the lower and the higher limits and the step eventually given as a power of 2 or 10. For reals we assume that they are the radix, and for the mantissa and the exponent the same as for integers. For strings the number of character or a special format — as DD-MMM-YY for date.

The PROTOCOL. DAT file must contain the key definition of the file name for the present run.

After the data entry, MAIN-INIT allows the optional data printing in the hard-copy device and creates a sequential file with the same data. This file has the name defined for the present run with the extention DAT.

The entry and validation process uses extensively the video attributes and cursor addressing in a user oriented mode. As other video terminals may answer differently from the H 19 we use, the video attributes and cursor addressing are defined in the file VIDEO. DAT. In Fig. 3 we show a block diagram of the whole module.
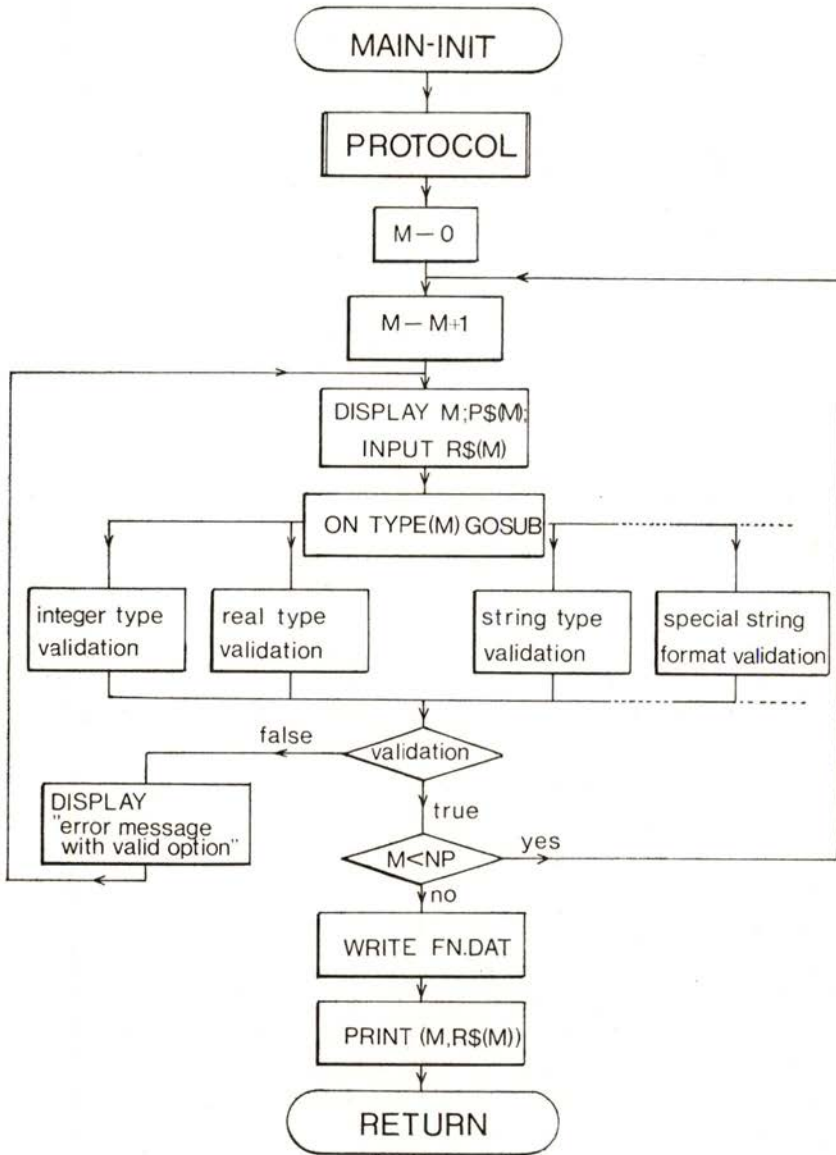
Fig. 3 — Flowchart of the MAIN-INIT module. In this module data are inputed and validated accordingly with data definitions made in the PROTOCOL.DAT file. NP is the number of parameters to be inputed, P$ represents the corresponding prompt, and R$ is the operator answer. The file FN.DAT is generated.

3.2 — *Transfer*

The data transfer from the MCA to a diskette file or from a diskette file to the MCA is handled by the TRANSFER module. Then, the entry parameters to this module are the name of the file, the number of channels to be transferred, and the direction of the transfer.

The MCA we use has no protocol to suspend the transmission of the data. To guarantee the data transfer in real time with this kind of serial interface the module TRANSFER calls two subroutines in sequence:

i) IODATA, that supervises the data transfer between the multichannel and the memory, using the "punch" and "reader" CP/M standard logical devices;

ii) RWFILE, that supervises the data transfer between the memory and the diskette.

These subroutines have been written in Assembly because with a BASIC interpreter we were not able to transfer the data, in real time, from the multichannel at high baud rates, and with Microsoft BASIC it is not possible to access the registers of the CPU (8080-like). This last facility is essential to call the CP/M system functions.

IODATA handles the data transfer, character by character, from the reader device to a buffer in the memory or from this buffer to the punch device. At the same time, the characters are echoed to the console. This routine uses the CP/M functions READER INPUT, PUNCH OUTPUT and CONSOLE OUTPUT.

RWFILE opens or creates a file with the name received by the calling module. Afterwards the number of 128 bytes sectors, which is determined by the number of channels to transfer, is loaded from the file (opened) to the memory or is stored from the memory to the file (created). Finally the file is closed. The CP/M functions called by this subroutine are: OPEN FILE or MAKE FILE, CLOSE FILE, SET DMA, READ SEQUENTIAL or WRITE SEQUENTIAL. In Fig. 4 we show a block diagram of the whole module.
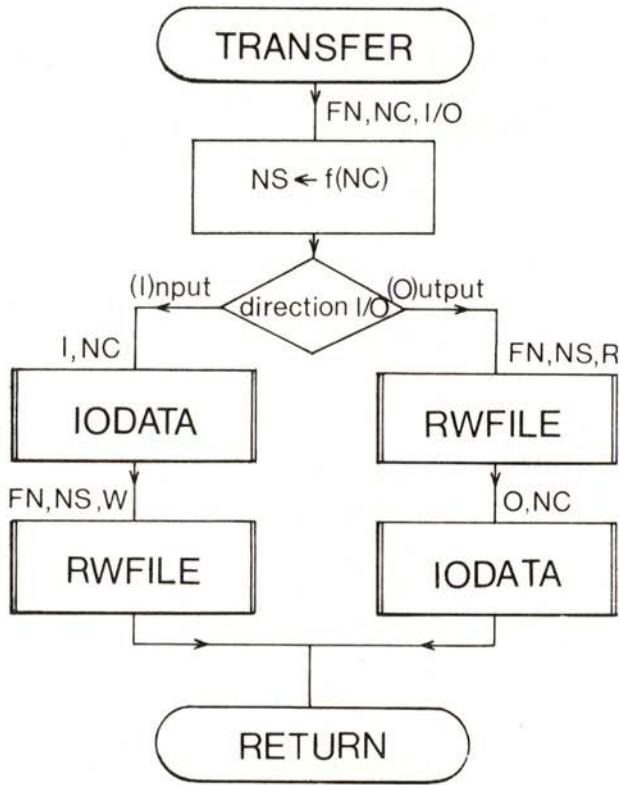
Fig. 4 — Block diagram of the TRANSFER module. FN is the «filename», NC the number of channels to be transferred, NS the number of sectors on the file FN.RDM as generated (or read) by the RWFILE subroutine, and I/O a variable which defines the direction of the transfer.

3.3 — Decode-encode

Since the MCA output/input presents a particular format in ASCII characters, e.g.

```
, 0000   000006   000011   000009   000014   000019
, 0005   000012   000016   000023   000020   000036
, 0010   000027   000038   000047   000031   000048
, 0015   000059   000051   000048   000061   000068
, 0020   000060   000064   000067   000079   000081
, 0025   000064   000101   000069   000084   000092
```

....

the module DECODE generates a direct access file with the extension RDM with the counts of each channel in binary format.

For pratical uses, we assume that the maximum value of each channel does not exceed 2^{15}. The maximum value allowed by the MCA is 10^6-$1 < 2^{20}$. If an "overflow" condition arises, a warning message is edited, and only the remaining value is stored. This procedure is practical in our case, as we do not expect such high counting rates, and so we could store a whole spectrum in only 2 kbytes. If necessary, a simple modification of the file specification can be done allowing greater values. Alternatively, a spline interpolation method could restore the original spectrum before treatment.

The module ENCODE performs the inverse procedure. These modules are designed to deal with the common MCA output format, described before. For different MCA's I/O formats one could implement equivalent modules, without significant effort.

3.4 — Options

In the module OPTIONS, user defined data processing programs can be specified allowing for immediate data analysis, using a chainning structure. Essentially, this module is a menu driven routine, and it uses the file MENU. DAT specified by the user, containing the filenames of his own data analysis programs.

After the treatment, and since with our microcomputer we can not view the spectrum on the video terminal, the ENCODE-TRANSFER modules — system routine VIEW — allow the transfer of the spectrum for display in the MCA.

4 — AN IMPLEMENTATION EXAMPLE

This system was implemented and field proven in the environment of a photoelectron spectrometer. For each run, some relevant parameters are stored, following the procedure described

in section 3.1. In Fig. 5 we show the corresponding hard-copy form. The file name for this run, as determined by the key specification, was AR314118. This name is used through all the system programs for the present run, allowing the identification of all data files produced during the data manipulation process.

```
PHOTOELECTRON SPECTRUM                              Pag 1



RUN AR314118                                      11-AUG-81
==============


        UV source : selected power    :    1
                    He pressure        :    1E-1 torr
                    temperature        :    38 'C
        Sample    : gas               :    ARGON
                    inicial pressure  :    1E-5 torr
                    final pressure    :    8E-5 torr
        Sweep control : scale         :    3
                    off-set           :    14
                    time/channel      :    2 s
                    number of sweeps: 1
                    inicial channel   :    400

   Number of channels to be transferred :    150
```

Fig. 5 — Relevant parameters recorded during a photoelectron spectrometer run, which are saved in the file AR314118.DAT. The «filename» FN for this run includes abridged information about the sample (the first two letters), the scale and the off-set of the sweep control (3 and 14), and the date (11th August) [14].

As specified (see fig. 5) only the first 150 channels have been transferred and stored in the file AR314118.MCA. This file, in ASCII characters, is an image of the MCA output, according to the format presented in 3.3, and could be transferred to the MCA at any given time through the system routine VIEW.

Once the transfer is finished, the DECODE module produced a new file, AR314118.RDM, in binary format. The original file could now be deleted, if storage space in the diskette is not enough, as the module ENCODE could reconstruct the original file from this binary file. In fact, for a 1024 channel spectrum, the original file occupies 9k bytes. In the condensed binary format, the same spectrum requires only 2k bytes of storage space.

The channel contents could be printed, optionally, in the form presented in Fig. 6.

PHOTOELECTRON SPECTRUM   Pag 2

RUN AR314118   11-AUG-81
============

```
            CHANNEL = N*10+D

+-----+------+------+------+------+------+------+------+------+------+------+
: \   :      :      :      :      :      :      :      :      :      :      :
: \   :      :      :      :      :      :      :      :      :      :      :
: \D  :  0   :  1   :  2   :  3   :  4   :  5   :  6   :  7   :  8   :  9   :
: N \ :      :      :      :      :      :      :      :      :      :      :
:   \ :      :      :      :      :      :      :      :      :      :      :
+-----+------+------+------+------+------+------+------+------+------+------+
:     :      :      :      :      :      :      :      :      :      :      :
: 40  :   6  :  11  :   9  :  14  :  19  :  12  :  16  :  23  :  20  :  36  :
: 41  :  27  :  38  :  47  :  31  :  48  :  59  :  51  :  48  :  61  :  68  :
: 42  :  60  :  64  :  67  :  79  :  81  :  64  : 101  :  69  :  84  :  92  :
: 43  :  97  :  91  : 109  : 101  :  93  : 105  :  89  : 124  : 115  : 101  :
: 44  : 122  : 138  : 128  : 150  : 151  : 182  : 159  : 216  : 227  : 220  :
: 45  : 262  : 295  : 316  : 420  : 469  : 525  : 752  :1164  :1949  :2895  :
: 46  :3982  :3900  :2667  :1400  : 788  : 508  : 316  : 284  : 190  : 176  :
: 47  : 154  : 121  : 129  : 102  :  95  : 103  :  79  :  82  :  78  :  80  :
: 48  :  76  :  83  :  78  :  72  :  84  :  77  :  92  :  84  :  85  : 119  :
: 49  :  99  : 115  :  99  : 112  : 114  : 122  : 146  : 149  : 160  : 196  :
: 50  : 224  : 284  : 320  : 393  : 604  : 906  :1326  :2005  :2063  :1625  :
: 51  : 950  : 482  : 316  : 208  : 176  : 127  : 107  :  79  :  92  :  77  :
: 52  :  46  :  56  :  42  :  50  :  45  :  43  :  37  :  45  :  38  :  24  :
: 53  :  32  :  35  :  27  :  22  :  35  :  32  :  33  :  23  :  28  :  27  :
: 54  :  33  :  34  :  24  :  30  :  42  :  29  :  30  :  30  :  29  :  24  :
+-----+------+------+------+------+------+------+------+------+------+------+
```

Fig. 6 — Decoded spectrum contents as they have been saved in the random access file AR314118.RDM .

In the present example, the user has implemented some routines for data analysis [12]. These programs use the files AR314118.DAT (containing the experimental parameters) and AR314118.RDM (containing the spectrum). The result of the

analysis performed is shown in Fig. 7, the processing time being less than 2 minutes. This on-line analysis presents evident advantages over any other performed on a later stage of the

PHOTOELECTRON SPECTRUM   Pag 3

RUN AR314118   .11-AUG-81
============

Resonance Line : He I (21.2175 eV)

Working temperature 311 'K

Peak	Position (channel number)	Ioniz. Potential (eV)	Kinetic Energy (eV)	f.h.w. (meV)	Intensity	Assimetry (%)
2P 3/2	461.311	15.759	5.459	17.87	13826.8	+10.34
2P 1/2	508.711	15.937	5.281	17.41	7060.2	+2.84

Peak	f.h.w. (meV)	Natural Width (meV)	Act.Inst. Width (meV)	Teor.Inst Width (meV)	Other Widths (meV)
2P 3/2	17.87	4.72	17.23	16.15	6.01
2P 1/2	17.41	4.64	16.79	15.63	6.13

Fig. 7 — Condensed output produced by an immediate data analysis program [12], for which files presented in formated «hard-copy» form (Figs. 6 and 7) have been used.

experimental procedure. For example, any drift in the applied voltage changing the calibration condition of the spectrometer is immediately detected after spectrum recording. This allows the immediate correction of the anomaly. The same would happen with the mechanical adjustment of the slits, which produces

sharp differences in the achieved instrumental resolution. These facilities have reduced drastically the time consumed in the "mise au point" of the spectrometer and in spectra analysis.

5 — CONCLUSIONS

Based on a small 8-bits microcomputer running under the disk operating system CP/M, we have developed a general purpose system allowing data transfer between a MCA and a μC. The system gives the necessary facilities for an immediate data analysis.

In spite of the small dimensions of the peripheral memory used in the tests, the system offers possibilities comparable to those available on systems based on PDP 11 mini-computers [13] for a fraction of the price and with simplified installation procedures. Without any sofware modification, the performance of the system could be increased by an order of magnitude using a more sophisticated hardware, with greater mass memory, DMA controller and arithmetic processor, once it is CP/M compatible. Vector graphics capabilities on video-terminal are also desirable for a convenient spectrum display.

Higher baud rates than used are provided by the μC serial interfaces — till 9600 baud — and supported by the TRANSFER module. The use of those transfer rates is only restricted by the MCA interface. The use of 64 k bytes of main memory will allow the manipulation of a larger spectrum of 8192 channels.

As a final remark we shall refer that this system is suited to small budgets. It offers the means to provide computer power in the laboratory through a low cost μC. If more powerfull computing power is required, the same μC operating as a virtual terminal can be connected to a main-frame system, allowing data submission for (later on) complex data analysis. In this sense, the μC acts as an "intelligent interface" between a MCA and a main-frame in a dial-up type "on-line" connection, allowing for the decision to transfer only valuable experimental data and relevant parameters.

REFERENCES

[1] J. E. Brignell and R. Young, *J. Phys. E: Sci. Instrum.*, **12** (1979), 455.

[2] CP/M Operating System ver 2. 1979 (Digital Research, POB 579 Pacific Grove, CA 93950, USA).

[3] Z89 Operation and Hardware Manual, 1979 (Zenith Data Systems-Heath Company, Benton Harbour, MI 49022, USA).

[4] IT 5200 Instruction Manual (INO-TECH Inc., Nordland Drive, Fort Atkinson, WI 53538, USA).

[5] BASIC-80 Reference Manual, 1979 (Microsoft, 10800 N. E. Eighth, Suite 819, Bellevue, WA 96004, USA).

[6] J. M. Jedju, *Rev. Sci. Instrum.*, **50** (1979), 1077.

[7] A. R. D. Rodrigues and D. P. Siddons, *J. Phys. E: Sci. Instrum.*, **12** (1979), 403.

[8] J. W. Farley, A. H. Johnson and W. H. Wing, *J. Phys. E: Sci. Instrum.*, **13** (1980), 84.

[9] Ron C. Estler, *Rev. Sci. Instrum.*, **51** (1980), 1428.

[10] R. Shaw, J. A. Hardcastle, A. R. B. Juson and M. J. Bongkik, *J. Phys. E: Sci. Instrum.*, **14** (1981), 301.

[11] Microsoft Utility Software Manual, 1979 (Microsoft, ibid).

[12] M. H. Gonçalves and A. M. Gonçalves, to be published.

[13] N. Nuding, G. Will and E. Hinze, *Nucl. Instr. and Meth.*, **173** (1980), 329.

[14] M. H. Gonçalves, *Internal Report*, Centro de Física Molecular, 1982.

PORTUGALIAE PHYSICA publishes articles or research notes with original results in theoretical, experimental or applied physics; invited review articles may also be included.

Manuscripts, with an abstract, may be written in English or French; they should be typewritten with two spaces and in duplicate. Fi ures or photographs must be presented in separate sheets and be suitable fo. reproduction with eventual reduction in size; captions should make the figures intelligible without reference to the text. Authors are requested to comply with the accepted codes concerning references.

There is no page charge. Author(s) will get 50 free reprints (without covers); these are to be shared among all the authors of the article. Authors interested in more reprints should say so when sending their manuscripts; quotations shall be sent with the proofs.

Subscription rates for volume 14:

PORTUGALIAE PHYSICA may also be sent on an exchange basis; we wellcome all suggestions to such effect.

PORTUGALIAE PHYSICA

VOL. 14 · NUMB 1/2 · 1983

CONTENTS

PORTUGALIAE PHYSICA

PORTUGALIAE PHYSICA

MODERN TRENDS IN RESEARCH ON WAVES IN FLUIDS, PART I: GENERATION AND SCATTERING BY TURBULENT AND INHOMOGENEOUS FLOWS

L. M. B. C. Campos ([1])

Instituto Superior Técnico, 1096 Lisboa, Portugal

ABSTRACT — We consider the effects of turbulence and inhomogeneities upon waves in fluids (§1), both on extensive scales and as localized phenomena: on an extensive scale, in connection with the spectral and directional broadening of sound by turbulent and irregular shear layers separating a jet from a medium at rest (§ 2); as localized phenomena, producing forces and stresses, of hydrodynamic and electromagnetic origin, which are responsible for the generation of waves in fluids occuring in nature (§ 3). These problems are relevant in a variety of situations (Figures 1 to 4) of physical and engineering interest.

1 — INTRODUCTION

In the first part of this essay on some of the current trends in research on waves in fluids, we consider the effects of non-uniform and unsteady flow, leaving for the second part the consideration of external force fields. Most fluids commonly occurring in nature (Lamb 1879, Prandtl & Tietjens 1934, Landau & Lifshitz 1953, Batchelor 1967) give rise to flows containing inhomogeneities and turbulence (Batchelor 1953, Townsend 1956) in a variety of scales, and these disturbances affect the properties of waves (Rayleigh 1877, Brekhovskikh 1960, Morse & Ingard 1968, Whitham 1974, Levine 1978, Lighthill 1978), both as regards

---

([1]) On leave at *D.A.M.T.P., Cambridge University, Silver Street, Cambridge CB3 9EW, U.K.*

Portgal. Phys. — Vol. 14, fasc. 3-4, pp. 121-143, 1983

121

generation by localized phenomena and propagation in extensive regions.

Extensive inhomogeneous regions occur as interfaces, generally irregular, separating two media, solid or fluid, at rest or in relative motion; in the case of jets, the convection of the interface with the atmosphere at rest, may produce shear stresses, and thus entrain a layer of turbulence. The sound from sources in the interior of the jet is scattered by the interface, and diffracted by the turbulence, changing its directivity and spectrum. The combination of attenuation and interference effects leads to a directional and spectral broadening of an initially monochromatic beam; thus the reception of waves from a certain direction at a given frequency gives no assurance that there is a source of that frequency or radiating in that direction, unless the effects of scattering and diffraction on the spectrum and directivity have been taken into account.

Localized inhomogeneities and strong turbulence are associated with force and stress concentrations in a flow. The vector character of forces, and tensor character of stresses, suggests that they act respectively as dipole and quadrupole sources of the waves which are often observed in the fluids occuring in nature. Monopole radiation is also possible, in two-phase flow, e.g., a liquid with bubbles, as consequence of the variations in volume of one of the phases. The wave fields radiated by these mono-, di- and quadrupoles may be modified by boundaries constraining the flow or reflecting bodies deflecting the stream. In all cases, the estimation of the energy in the radiation field gives a measure of the effectiveness and importance of the wave generation mechanism in question.

2 — SPECTRAL AND DIRECTIONAL BROADENING BY SHEAR LAYERS

The classical wave equation, satisfied by the velocity perturbation $\mathbf{v}$ of an adiabatic acoustic wave in a medium at rest is (D'Alembert 1747, Rayleigh 1877):

$$\{ \partial^2/\partial t^2 - c^2 \nabla^2 \} \quad \mathbf{v} (\mathbf{x}, t) = 0, \tag{1}$$

where c is the adiabatic sound speed, which is constant for a perfect gas in a mean state of isothermal equilibrium. For a medium moving with a constant velocity $\mathbf{U}$, equation (1) is only valid in a frame $\mathbf{y}$ moving with the fluid; and returning to coordinates at rest, $\mathbf{x} = \mathbf{y} - \mathbf{U}\,t$, the Laplacian is unchanged, $\partial^2/\partial y_i^2 = \partial^2/\partial x_i^2$, but the local time derivative $\partial/\partial t$ is replaced by the material derivative, $d/dt = \partial/\partial t + U_i\,\partial/\partial x_i$, including the effect of the fluid motion $U_i\,\partial/\partial x_i = \mathbf{U} \cdot \nabla$. We obtain the convected wave equation (Morse & Ingard 1968, Lighthill 1978)

$$\{ (\partial/\partial t + \mathbf{U} \cdot \nabla)^2 - c^2 \nabla^2 \}\ \mathbf{v}\,(\mathbf{x}, t) = 0, \qquad (2)$$

describing the propagation of sound in an uniform flow of arbitrary velocity (subsonic, sonic or supersonic), and leading by the usual spectral methods, to Doppler (1893) effect, of changing the frequency ω to $\omega/(1 - M \cos \Theta)$, where $M \equiv U/c$ is the Mach number of the flow and Θ the angle of the flow velocity with the direction of propagation.

In order to derive the wave equation in a non-uniform and/or unsteady flow, for which the mean velocity depends on space and/or time $\mathbf{U}\,(\mathbf{x}, t)$, a different method is required, using as variable (Howe 1975, Campos 1978a) the stagnation enthalpy Q, defined by:

$$dQ = d\,(\rho V^2/2) + \mathbf{E} \cdot d\mathbf{D} + \mathbf{B} \cdot d\mathbf{H} + \nu\,dN + (1/\rho)\,dp + T\,dS, \qquad (3)$$

as the sum of the kinetic, electric, magnetic and chemical energies (per unit volume) with the Legendre transform $(1/\rho)\,dp$ of the mechanical work $-pd\,(1/\rho)$ and heat $T\,dS$; ρ denotes the mass density, $\mathbf{V} = \mathbf{U} + \mathbf{v}$ the total velocity of flow plus wave, $\mathbf{E}, \mathbf{D}$ the electric field and displacement, $\mathbf{B}, \mathbf{H}$ the magnetic induction and field, ν the chemical potential and N the mole number (for each chemical species), p the pressure and $1/\rho$ the specific volume, T the temperature and S the entropy.

In an homogeneous fluid of density ρ_0, not subject to external force fields, and in uniform motion at Mach number M, the stagnation enthalpy $Q \sim \{ (1 + M \cos \Theta)/\rho \}\,P$ scales on the acoustic pressure P, and thus is an acoustic variable. The exact wave equation statisfied by the stagnation enthalpy Q, in the

absence of sources (which will be considered in § 3), in a variable flow of velocity **V** and pressure p, is:

$$\{ c^2 \, d/dt \; c^{-2} \, d/dt - \rho^{-1} \nabla p \cdot \nabla - c^2 \, \nabla^2 \} \; Q(\mathbf{x}, t) = 0, \qquad (4)$$

where $d/dt \equiv \partial/\partial t + \mathbf{V} \cdot \nabla$ is the material derivative, and the sound speed c generally depends on position for a high-speed (or compressible) mean flow.

Considering a non-uniform but low Mach number $M^2 \ll 1$ (or incompressible) mean flow, so that the only compression of the medium is the acoustic wave, equation (4) is simplified since: (i) the sound speed $c = c_0 \{ 1 - (\gamma - 1) \, M^2/2 \}$, where γ is the ratio of specific heats (Landau & Lifshitz 1953), becomes constant and equal to the value in a medium at rest $c \sim c_0$; (ii) the pressure is approximated by the dynamic pressure $p \sim \rho V^2/2$, so that the second term of (4) is negligible compared with the third since $(\nabla p \cdot \nabla)/(\rho \, c^2 \, \nabla^2) \sim p/\rho \, c^2 \sim V^2/c^2 = M^2 \ll 1$. Neglecting the second term of (4), and setting c constant, it reduces to the convected wave equation, which thus also applies to non-uniform, low Mach number flows. In conclusion, the convected wave equation (2) describes the propagation of sound in: (i) an uniform flow of arbitrary velocity, including Mach number $M \sim 1$, in which case the mean flow, and not only the wave perturbation, is compressible; (ii) a non-uniform mean flow of low Mach number $M^2 \ll 1$, which is incompressible, leaving as sole compression the wave perturbation.

Thus the convected wave equation is adequate to describe the propagation, diffraction and scattering of sound in quite complex situations, e.g., the irregular and turbulent shear layer which separates a jet from a medium at rest, which can be modelled (Barratt, Davies & Fisher 1963) as: (i) an irregular interface moving at a fraction $\alpha \sim 0.6$ of the jet velocity **V**, across which the density and sound speed change, and which scatters an incident wave into a reflected and transmitted wave, with reflection and transmission coefficients calculated from the continuity of pressure and displacement across the interface; (ii) the interface usually entrains turbulence, whose velocity consists of a constant global convection α**V**, and a local unsteady, non-uniform perturbation **u**(**x**, t), whose r.m.s. value is typically a fraction $\beta \sim 0.15$ of the jet velocity, so that even

for a bi-sonic jet $M \sim 2$, the turbulence is locally incompressible, $(\beta \ V/c)^2 \sim \beta^2 \ M^2 \sim (0.3)^2 \ll 1$, and (2) can be used to study the refraction of waves by the flow of velocity $\mathbf{U}(\mathbf{x}, t) = \alpha \mathbf{V} + \mathbf{u}(\mathbf{x}, t)$. The scattering of sound (or other waves) by irregular interfaces (Born & Wolf 1959, Sholnik 1962, Beckman & Spizzichino 1963, Berry 1973, Clarke 1973, Howe 1976, Campos 1978b) and the refraction in turbulence and other random media (Lighthill 1953, Philips 1960, Chernov 1967, Tatarski 1967, Howe 1973, Uscinski 1977, Ishimaru 1978, Campos 1978c), is relevant to the transmission of sound from the interior of jets (Mani 1976a, b, Balsa 1976, Jones 1977, Munt 1977, Howe & Ffowcs-Williams 1978, Campos 1984c), and thus to the problem of aircraft noise (Lighthill 1961, Nayfeh, Kaiser & Telionis 1975, Doak 1976, Crighton 1981, Campos 1984b) which is central to aerodynamic acoustics.

When sound is scattered by an irregular interface the phase of the reflected and transmitted wave depends on height of the scattering element, so that identical wave components scattered by different elements have different phases, i.e., a coherent incident beam is reflected and transmitted as an incoherent bundle. Random phase changes also occur when sound is refracted by turbulence, e.g., the aleatory magnitude and direction of the turbulent velocity causes random Doppler shifts of frequency, and an initially monaural beam (of a single frequency) is broadened into a widening spectrum. This phenomenon of spectral broadening of sound pulses propagating across turbulence and interfaces has been observed in air and water (Schmidt & Tillman 1970, Ho & Kovaznay 1967a, b, Beyer & Korman 1980, Juvé & Blanc-Benon 1981, 1982), and corresponds to the broadening of atomic emission lines (Rayleigh 1873, 1889, 1915) of the Bunsen burner, and can be modelled (Campos 1978b, c) by: (i) determining the acoustic pressure field emitted by a source in a jet and transmitted across the turbulent and irregular shear layer to the outside; (ii) calculating the energy radiated at each frequency and each direction, from the correlations of the acoustic pressure, which in turn depend on the statistical properties (Lindeberg 1922, Khinchin 1948, von Mises 1960) of the shear layer.

Fig. 1 shows the good agreement of the spectra calculated theoretically (Campos 1978b, c; Campos 1984c) using a computer program in Cambridge's IBM 370 and 8031 (large plot), with the
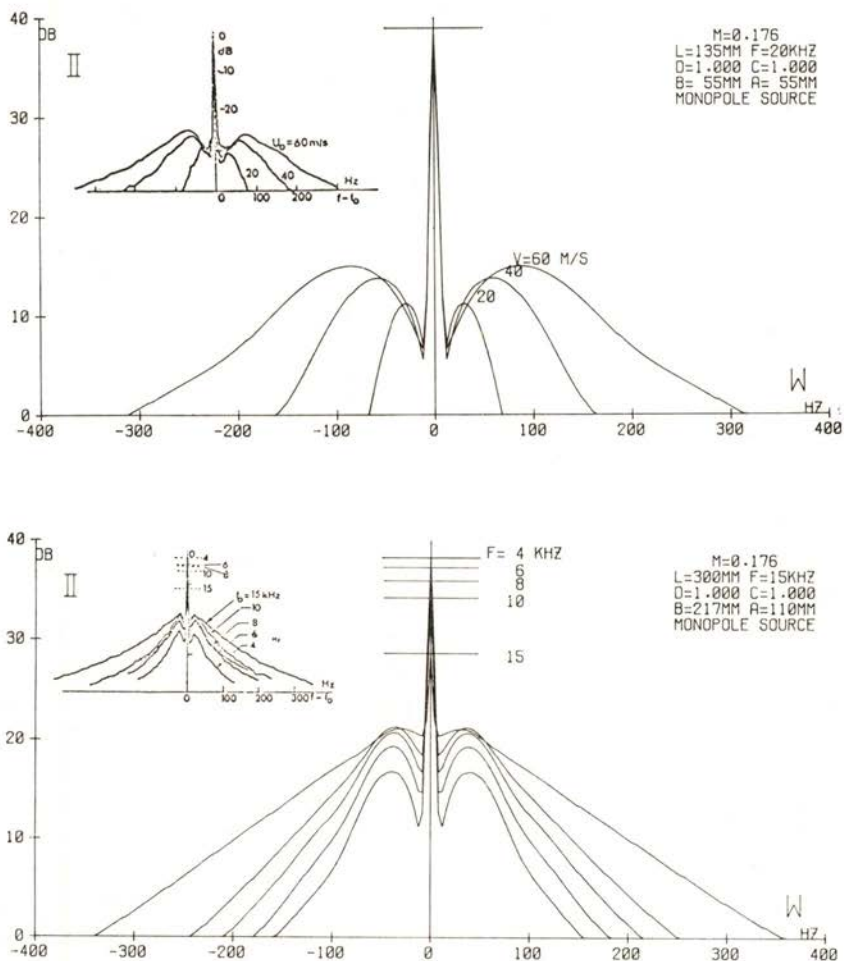
Fig. 1 — Spectra from a monochromatic point source in a cold, low-spped air jet, received outside, after transmission across the irregular and turbulent shear layer separating the jet from the ambient medium at rest. The experimental spectra (inset) were measured by Candel, Guédel & Julienne (1975) in an anechoic chamber at the von Karman Institute; the theoretical spectra (plot) were computed in the IBM 370-8031 in Cambridge University, using the theory of Campos (1978a, b; 1984c). The spectra show the effects of increasing the jet velocity (top) in broadening the spectra, and of increasing the source frequency (bottom) in attenuating the spike and reinforcing the broadband.

measurements (Candel, Julienne & Julliand 1975, Candel, Guédel & Julienne 1976) of sound sources in jets (smaller inset graph). Although the sources are monochromatic, with a frequency corresponding to that of the 'spike', the spectrum received after transmission across the turbulent and irregular shear layer shows the effects of spectral broadening in the appearance of prominent side bands, in a frequency range absent from the source. The effect of increasing the jet velocity, for the same source, is seen (top) in more intense and separated sidebands and a spectrum wider overall; if the frequency of the source is increased, for the same jet velocity, then (bottom) the spike is attenuated, and part of the energy transfered to the sidebands, that become wider and higher. The theory can be used to calculate the spectra received outside the jet in any direction, for a source with arbitrary spectrum, spatial distribution and multipolar character, within cold or hot jets, for various scales of turbulence and irregularity in the shear layer.

Having validated the theory by comparison with measurements on cold, low-speed air jets in anechoic chambers, we proceed to the prediction of the noise spectra of hot, high-speed jet exhausts, taking as an example Concorde in the take-off configuration. The cases of (i) a vertical dipole source representing sound emission by patches of unburned gas in the exhaust (Howe 1975, Campos 1978a), and (ii) a shear quadrupole modelling noise generation by turbulence in a jet (Lighthill 1952, 1954; Campos 1977), have been illustrated elsewhere (Campos 1978c, 1984c). Here we consider another turbulent source of sound, namely, a compressive quadrupole, of frequency 8 kHz corresponding to the turbine tone of the Olympus 593D turbojet of Concorde, and the corresponding "spectra and directivity data sheet" is given in Fig. 2. The spectra II are given in nine directions spaced 15° between 30° and 150°, for a shear layer (a) whose statistical properties roughly correspond to those of Concorde's exhaust, and for (b) a shear layer twice as irregular and thick: (i) the effects of spectral broadening are considerable, since the sound from the monochromatic source of frequency 8 kHz is received over the spectral band 3-16 kHz; (ii) for the single irregular and turbulent shear layer, there is a prominent 'spike' at source's frequency in the directions 105-120°, just *before* the aircraft flies by, this discrete tone being attenuated into the band

128

Portgal. Phys. — Vol. 14, fasc. 3-4, pp. 121-143, 1983

in other directions; (iii) if the shear layer is made twice as irregular, and the region of entrained turbulence becomes twice as thick, then the acoustic energy in the spike is scattered into the bands in all directions, and the source's tone is just barely visible at 105°, where before it was most prominent.

The directivity III, or total energy received at all frequencies is plotted (Fig. 2, bottom) as a function of direction in three cases: (solid line) a plane vortex sheet between the same jet and environment, which radiates only a 'spike' at source's frequency (no broadband), and has a downstream 'zone of silence' $\theta < 74°$; (asterisks) the irregular and turbulent shear layer radiates a band into what would be the 'zone of silence' of the plane vortex sheet, and in all other directions radiates a band and 'spike', with the latter showing the importance of attenuation by the irregularities of the interface and the layer of entrained turbulence; (stars) the shear layer twice as thick and irregular gives slightly lower noise levels (~ 3 dB) in all directions except the range 105-120°, where the absorption of the formerly prominent spike into the band yields a significant attenuation ~ 10-12 dB. We conclude that: (i) the model of the plane vortex sheet between the jet and a medium at rest is at fault, since it cannot predict spectral broadening or radiation into the 'zone of silence', and overestimates peak noise levels by up to 20 dB as a consequence of neglecting attenuation mechanisms: (ii) the irregular and turbulent shear layer can reduce the audible noise disturbance, by distributing the acoustic energy over a wider range of directions, including the 'zone of silence', and scattering 'spikes' into spectral broadbands.

Fig. 2 — Simulation of the transmission of sound from a compressive quadrupole source, at the frequency 8 kHz of the turbine tone of the Olympus 593D turbojet, modelling turbulence in the jet exhaust of Concorde in the take-off configuration. The spectra II received outside are given in nine directions, for a single turbulent and irregular shear layer, and for a shear layer of double thickness which provides increased attenuation of spikes. The directivity III, or spectrum integrated over all frequencies, is plotted (at the bottom) as function of direction, for the single (asterisks) and double (stars) irregular and turbulent shear layers, in comparison with an idealized plane vortex sheet (solid line) between the same media.

These methods of attenuation of jet noise have been used in successive generations of transport aircraft: (I) the first jet airliners used multi-lobe nozzles, which produce an irregular shear layer, and entrain a layer of turbulence, to scatter and diffract sound; (II) the current wide-body airliners use high by-pass ratio turbofans, with the hot, high-speed core jet exhaust surrounded by a cold, low-speed by-pass flow, that acts as a double shear layer, providing greater sound attenuation; (III) in future jet-powered aircraft, the methods of noise reduction based on scattering by irregular interfaces and diffraction by turbulent layers have to be harmonized with reduced fuel consumption and increased propulsion efficiency.

3 — EMISSION BY HYDRODYNAMIC AND ELECTROMAGNETIC FORCES AND STRESSES

The classical theories of generation of acoustic waves by mass or momentum sources, e.g., sirens, pipes, membranes, or of emission of electromagnetic waves by electric charges and currents, assume that the sources of waves are physically separate from the medium of propagation, and they appear as an inhomogeneous, forcing term in the wave equation. The modern theories of wave generation in natural (atmosphere, ocean) or engineering (jets, exhausts) fluids, have to contend with a situation where the sources cannot be identified or isolated 'a priori', since they lie in the medium of propagation. In order to identify the physical processes whereby waves are generated, it is necessary to start from the general equations of fluid motion under force and stress fields, consider the flow as the superposition of a mean state and a wave perturbation, say, represented by the velocity $v_i(x, t)$, and: (i) separate the linear terms, and eliminate between them for the velocity, thus obtaining an expression $\square_{ij} v_j = 0$, which could describe propagation in the absence of sources or damping, and thus allow us to identify the wave operator as $\square_{ij}$; (ii) retain all the non-linear and dissipative terms, and group them as forcing the wave equation, viz.:

$$\{ \square_{ij} (\partial/\partial t, \partial/\partial x_i) \} \, v_j (x, t)$$

$$= -\rho^{-1} (\partial/\partial t) \{ \partial Q/\partial x_i + P_i + \partial R_{ij}/\partial x_j \},$$

(5)

where the terms on the right-hand-side can be interpreted as sources, respectively of monopole Q , dipole P_i and quadrupole R_{ij} character.

Considering waves under the combined influences of compressibility, magnetism and gravity, we have (Yu 1965, McLellan & Winterberg 1968, Bel & Mein 1971, Stein & Leibacher 1974, Campos 1977, 1983b, 1984a), the magneto-acoustic-gravity wave operator:

$$\Box_{ij} = \delta_{ij} \, \partial^2/\partial t^2 - c^2 \, \partial^2/\partial x_i \, \partial x_j - g_j \, \partial/\partial x_i - (\gamma - 1) \, g_i \, \partial/\partial x_j$$

$$- a^2 \, (\delta_{ij}\partial^2/\partial m^2 - m_j\partial^2/\partial m \, \partial x_i) + a^2 \, (m_i\partial^2/\partial m \, \partial x_j - \partial^2/\partial x_i \, \partial x_j),$$

$$\tag{6}$$

where c , a denote respectively the sound and Alfvèn speeds:

$$c^2 = \gamma \, RT , \qquad a^2 = \mu \, H^2/4 \, \pi \, \rho , \tag{7a, b}$$

where γ is the ratio of specific heats, R the gas constant, T the temperature, μ the magnetic permeability, ρ the density, **g** the acceleration of gravity, and **H** the constant external magnetic field of direction $\mathbf{m} \equiv \mathbf{H}/H$, so that the derivative along magnetic field lines is $\partial/\partial m = m_i\partial/\partial x_i = \mathbf{m} \cdot \nabla$. The terms in (6) may be interpreted as follows, from left to right (Bray & Loughhead 1974, Athay 1976, Campos 1983a, b): (i) second order time dependence allowing wave propagation in opposite directions and their superposition into standing modes; (ii) acoustic propagation, involving the sound speed c and fluid dilatation $\partial v_j/\partial_j = \nabla \cdot \mathbf{v}$ (iii) internal wave propagation, involving the acceleration of gravity g_j , (iv) acoustic-gravity coupling, through the gravity g_j and dilatation; (v-vi) magnetic wave propagation along magnetic field lines $\partial/\partial m$ at Alfvèn speed a ; (vii-viii) magneto-acoustic coupling through the Alfvèn speed a and dilatation $\partial v_j/\partial x_j$, the former involving gravity effects through the density ρ stratification.

The theories of aerodynamic generation of sound (Lighthill 1952, 1954; Curle 1955; Powell 1968; Ffowcs-Williams & Hawkins 1968; Crighton & Ffowcs-Williams 1969; Howe 1975; Dowling, Ffowcs-Williams & Goldstein 1978; Campos 1978a), have been extended to stratified (Parker 1964, Stein 1967, 1981) and to ionized

(Kulsrud 1955, Lighthill 1967, Campos 1977) fluids, in connection with acoustic-gravity and magneto-acoustic waves. Considering the generation of the latter we have the following dynamic and magnetic quadrupole sources: (i) the anisotropic Reynolds and Maxwell stresses minus the isotropic dynamic and magnetic pressures:

$$R_{ij}^{(1)} = \rho\, v_i\, v_j - \rho\, v^2/2\; \delta_{ij}, \tag{8a}$$

$$S_{ij}^{(1)} = -(\mu/4\pi)\; h_i\, h_j + (\mu h^2/8\pi)\; \delta_{ij}, \tag{8b}$$

which scale quadratically on the velocity **v** and magnetic field **h** perturbations, and model the generation of waves by hydro-magnetic turbulence; (ii) the inhomogeneous terms in the equation of state and Alfvèn equation:

$$R_{ij}^{(2)} = \{\, p - (\partial p/\partial \rho)_s\, \rho - (\partial p/\partial s)_\rho\, s\,\}\, \delta_{ij}, \tag{9a}$$

$$\partial S_{ij}^{(2)}/\partial t = -(\mu/4\pi)\, \{\, H_j\, \nabla \wedge (\mathbf{v} \wedge \mathbf{h})_i + H_i\, \nabla \wedge (\mathbf{v} \wedge \mathbf{h})_j$$
$$- \mathbf{H} \cdot \nabla \wedge (\mathbf{v} \wedge \mathbf{h})\; \delta_{ij}\,\}, \tag{9b}$$

which would vanish (9a) for homogeneous, isentropic acoustics since then there is a single equation of state $p(\rho, s)$, and (9b) for Alfvèn waves in a perfectly conducting medium since then $\mathbf{v} \wedge \mathbf{h} = 0$, so that these terms represent the emission of waves by ionized inhomogeneities.

The dissipation tensor has terms corresponding to the viscous stresses τ_{ij}, thermal conductivity κ and electrical resistivity $1/\sigma$ (where σ is the Ohmic conductivity):

$$\partial D_{ij}/\partial t = \{\, \partial \tau_{ij}/\partial t - \tau_{kl}\, (\partial v_k/\partial x_l)\; \beta\; \delta_{ij}\,\} - \kappa\; \nabla^2 T\; \beta\; \delta_{ij}$$
$$+ (c_*^2/16\,\pi^2\,\sigma)\, \{\, H_i\; \nabla^2 h_j + H_j\; \nabla^2 h_i - (\nabla \wedge \mathbf{h})^2\; \beta\; \delta_{ij}\,\}; \tag{10}$$

where c_* is the speed of light in vacuo and β is the thermodynamic parameter $\beta \equiv (\rho T)^{-1}\, (\partial p/\partial s)_{\rho^2}$, which is a constant $\beta = 2/N$ for a perfect gas whose molecules have N degrees of freedom, i.e. $\beta = (2/3, 2/5, 1/3)$ for mono-, di- and polyatomic gases. The dissipation tensor (10) causes damping of the waves in the propagation region, and diffuses the sources in the generation region.

The hydrodynamic (8a, 9a) and magnetic (8b, 9b) sources scale respectively on the dynamic $R \sim \rho\,v^2/2$ and magnetic $S \sim \mu h^2/8\pi$ pressures, and comparing with the viscous D_v, thermal D_K and resistive D_σ terms in the dissipation tensor (10), we obtain:

$$\frac{D_v/R}{1-\beta} \sim \frac{\nu}{\rho\,U\,L} \equiv \frac{1}{Re} \,,\; \frac{D_K/R}{-\beta} \sim \frac{\kappa/C_p}{\rho\,U\,L} \equiv \frac{1}{Pe} \,,\; \frac{D_\sigma/s}{1-\beta} \sim \frac{c_*^2/4\pi\mu}{\sigma\,U\,L} \equiv \frac{1}{Me} \,,$$

$$(11a, b, c)$$

where Re, Pe, Me define respectively the Reynolds, Péclet and magnetic Reynolds numbers. If Re, Pe, Me < 1 the dissipation predominates over the generation of waves, otherwise it diffuses some of the energy flux of the sources. The momentum equation $\partial R_{ij}/\partial_j$ shows that if the forces P_i integrated over the wave generation region do not vanish, the source is equivalent to a dipole P_i; an energy source Q would correspond to a monopole, and all three appear in the forcing term of the complete wave equation (5).

Provided that we consider linear waves in an homogeneous medium, even if the modes are anisotropic, dispersive or dissipative, and the source is any combination of multipoles, equation (5) can be solved by Fourier analysis and the asymptotic solution found explicitly using the method of stationary phase (Lighthill 1960, 1964, 1978; Ffowcs-Williams & Hawkins 1968; Adam 1982; Campos 1977, 1983d). The solution distinguishes non-dissipative waves, and cases where the wavenumber surface $k_1(k_2, k_3, \omega)$ is flat, has a single or a double curvature, i.e., is plane, cylindrical or spheroidal, the appearance of inflexion edges or caustics being also amenable to the method. We give the example of a three-dimensional, non-dissipative wave due to a quadrupole source, for which the asymptotic velocity perturbation is given by:

$$v_i(\mathbf{x}, t) \sim \Sigma\,(4\,\pi^2\,i/r)\,|g|^{-1/2}\left\{\omega\,k_j\,\hat{T}_{jk}\,\Lambda_{ki}/\,|\partial\Lambda/\partial k|\right\}$$
$$\exp\left\{i(\mathbf{k}\cdot\mathbf{x} + \Phi)\right\},\qquad (12)$$

where: (i) the summation extends to all wavemodes and to all points on the wavenumber surface where the group velocity $\partial\omega/\partial\mathbf{k}$ points to the observer; (ii) ω, $\mathbf{k}$ are the frequency and

wavevector, $\hat{T}_{ij}$ is the spectrum of the source quadrupole, Λ_{jk} the inverse of the dispersion matrix, and $\partial\Lambda/\partial\mathbf{k}$ the derivative of its determinant in wavenormal direction; (iii) the asymptotic field decays with distance r like r^{-1}, and radiation occurs over a fraction of the solid angle 4π determined by the inverse square root of the Gaussian curvature g ; (iv) the emission phase $\mathbf{k}.\mathbf{x}$ is unchanged by the focal phase $\Phi = o$ for anticlastic beams whose principal curvatures are of opposite signs $g = g_1\,g_2 < o$, but for synclastic beams $g > o$ the focal phase is $\Phi = \pi/2$ in the divergent g_1, $g_2 > o$ and $\Phi = -\pi/2$ in the convergent g_1, $g_2 < o$ case, so that passage through a focus causes a phase jump $\Delta\Phi = \pi$.

In the case of dipolar sources, the stress quadrupoles (8, 9a, b), can be replaced by forces: the electromagnetic dipole is the Laplace-Lorentz force $\mathbf{F}$, whereas the hydrodynamic dipole is the hydrodynamic force $\mathbf{G}$:

$$\mathbf{F} = q\,\mathbf{E} + (1/c_*)\;\mathbf{J}\wedge\mathbf{B}\;,\;\mathbf{G} = [\,(\rho/\rho_0)-1\,]\,\nabla p + (\nabla\wedge\mathbf{v})\wedge\rho\mathbf{v}\,,$$

$$(13a, b)$$

and considering an ionized inhomogeneity there is an analogy between: (I) the inhomogeneous force equal to the dimensionless $\delta \equiv \rho/\rho_0 - 1$ density difference between fluid ρ and blob ρ_0 times the pressure gradient ∇p, and the electric force on a charge q due to the electric field $\mathbf{E}$; note that in the electrostatic case the electric field $\mathbf{E} = \nabla\Phi$ is the gradient of a potential Φ, and takes the role of the pressure gradient ∇p, and a positive $q > 0$ / negative $q < 0$ charge corresponds $\delta > / < 0$ to a blob respectively lighter $\rho_0 < \rho$ / denser $\rho_0 > \rho$ than the fluid, which is compressed by/expands against the flow; (II) the Lamb's force on vorticity $\mathbf{w} = \nabla\wedge\mathbf{v}$ crossing streamlines $\mathbf{w}\wedge\mathbf{v}$, and the magnetic force on currents $\mathbf{J}$ transverse to the induction field lines $\mathbf{B}$; in the magnetostatic case the electric current is related to the curl of the magnetic induction $(1/c_*)\;\mathbf{J} = (\mu/4\pi)\,\nabla\wedge\mathbf{B}$, much as the vorticity to the velocity $\mathbf{w} = \nabla\wedge\mathbf{v}$, and the mass density ρ is replaced by $\mu/4\pi$, where μ is the magnetic permeability, which plays the role of a 'magnetic mass'. This can be seen by noting that if the mass density ρ is replaced by the magnetic permeability $\mu/4\pi$, and the velocity $\mathbf{V}$ by the magnetic field $\mathbf{H}$, the dynamic pressure $p_v = \rho V^2/2$ corresponds to the magnetic pressure

$p_h = (\mu/8\pi)$ H² and the Reynolds stresses (8a) correspond to (8b), the Maxwell stresses. Thus we have extended the classical analogy between electro- and magnetostatic fields (Jeans 1908, Stratton 1944, Jones 1964) and potential flow (Lamb 1879, Landau & Lifshitz 1953, Milne-Thomson 1958) from the field variables and sources to the hydrodynamic and electromagnetic forces (13a, b) and stresses (8a, b).

As the ionized inhomogeneity is convected by the flow past the external fields, it describes a trajectory **y** (τ) with velocity **U**, and is acted upon by hydrodynamic (13b) and electromagnetic (13a) forces, that perform an activity (work per unit time) given by (**G**/ρ + **F**/ρ_0) . **w**, where **w** is the group velocity. If the activity is conserved along the trajectory, there is no net exchange of energy between the blob and the surrounding fluid, no sound is emitted, and the blob is convected silently. Conversely, if the activity varies along the blob's trajectory, then the excess or default of energy, in the absence of dissipation, is transferred to the surrounding fluid by expansion or contraction, i.e., the blob emits a sound pulse whose acoustic pressure is given asymptotically, for an observer in the far field, by:

$$P(\mathbf{x}, t) \sim \{ 4\pi c^2 \, |\mathbf{x}| \, (1 + M \cos\Theta) \}^{-1}$$
$$\{ \partial/\partial\tau + \mathbf{U} \cdot \partial/\partial\mathbf{y} \} \{ (\mathbf{F}/\rho_0 + \mathbf{G}/\rho) \cdot \mathbf{w} \}, \tag{14}$$

where (**y**, τ) are the position and time of emission, and (**x**, t) those of reception. In order to determine the shape of the sound pulse it is necessary to calculate in detail the sound field (14), for example, for an ionized inhomogeneity (blob) which is: (i) convected along the streamlines of a flow, e.g., potential, past an electrified body, say, a sphere with surface electric currents; (ii) the presence of the body deforms the incident flow, and creates a pressure gradient, which exerts on the blob (13b) a displacement force ($\rho/\rho_0 - 1$) ∇p, which acts as an hydrodynamic dipole source; (iii) the electric currents on the body create an external magnetic field, which exerts (13a) a Lorentz force ($1/c_*$) **J** $\wedge$ **B** on the blob, and acts as an electromagnetic dipole source; (iv) the total, hydrodynamic plus electromagnetic, dipole source radiates directly to the observer in the far-field, and is modified by the wave reflected from the body, which is also dipolar, and hence of comparable magnitude.

In Fig. 3 are illustrated the hydrodynamic sound pulses emitted by the blob streaming past the neutral sphere, received at two positions in the far-field: (left) for an observer midstream (at $\Theta = 90°$, above the sphere), the pulse is symmetrical, since both the direct and reflected wave are; (right) for an observer downstream (at $\Theta = 180°$) the pulse has lost its symmetry as a consequence of the asymmetry of the reflected wave. In Fig. 4 we show the electromagnetic sound pulses received, in the far-field in the midstream ($\Theta = 90°$) direction, due to electric currents on the sphere, whose axis is either alligned with (left) or perpen-
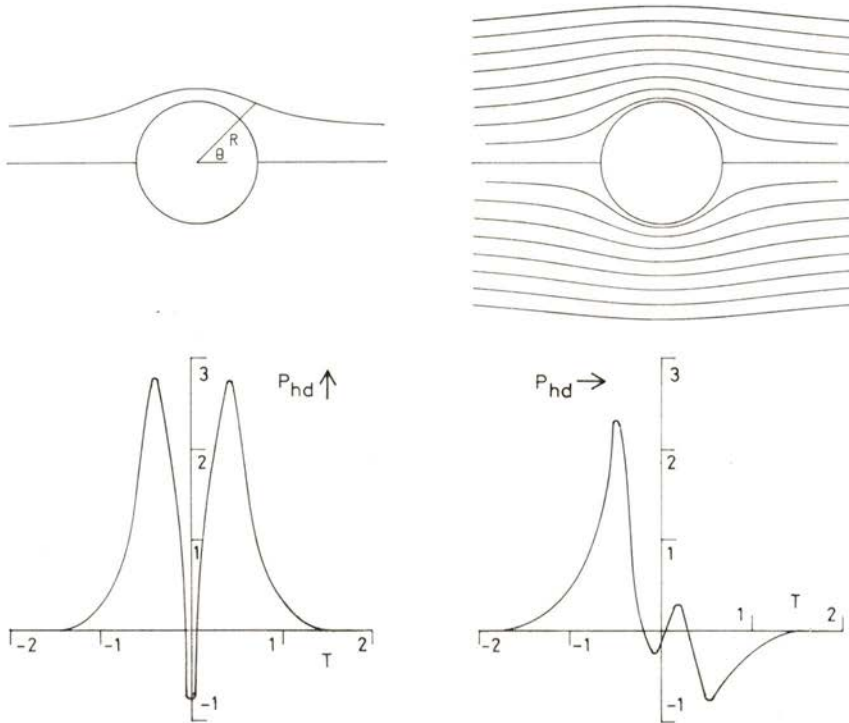
Fig. 3 — Emission of hydrodynamic sound by an inhomogeneity (blob) convected by a potential flow past a sphere, along the streamline of aiming distance half the sphere's radius. The sound pulse is plotted as received by an observer in the far-field in two directions: (left) midstream ($\Theta = 90°$), i.e., along the perpendicular to the incident flow direction, passing through the centre of the sphere; (right) downstream ($\Theta = 180°$), i.e., along the axis of the flow.
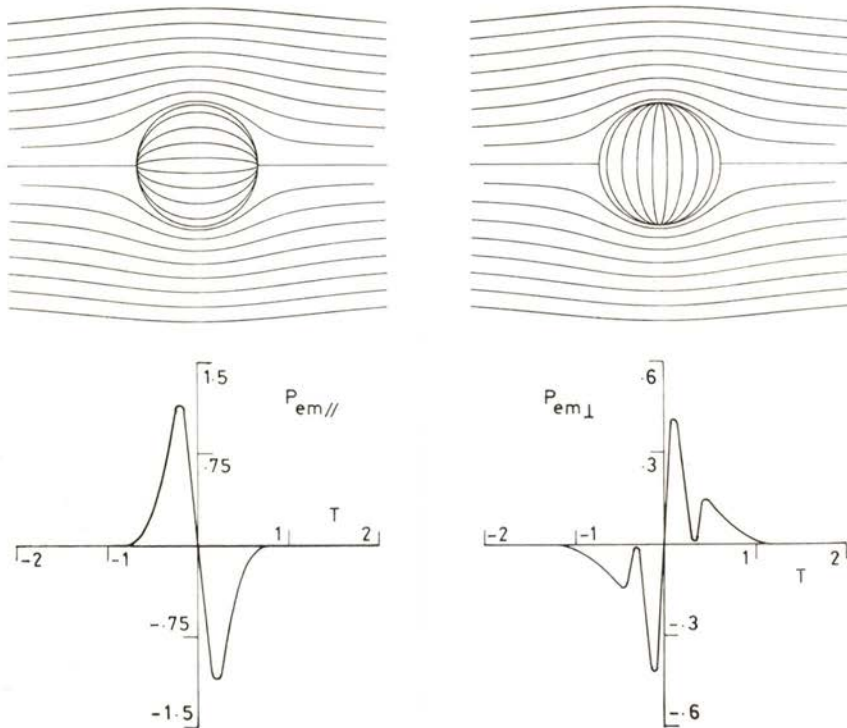
Fig. 4 — Emission of electromagnetic sound by an ionized blob as it is convected by the flow through a non-uniform magnetic field created by electric currents on the sphere. The sound pulse is plotted as received by an observer in the far-field in the midstream direction, for the cases in which the axis of the electric currents is parallel (left) and perpendicular (right) to the direction of the incident flow.

dicular to (right) the flow; the sound pulses are anti-symmetrical, due to the skew-symmetry of the magnetic field and force. As an example of interpretation of a pulse, we consider the hydrodynamic sound received midstream (fig. 3, left): (i) as the blob approaches the sphere it encounters first a region of diverging streamlines, hence reducing velocity and increasing pressure, so that the positive pressure gradient causes the emission of a compression pulse; (ii) as the blob is convected nearer to the sphere the streamlines converge, the velocity increases and the pressure reduces, and the reversal of the pressure gradient is signalled by emitting a rarefaction pulse; (iii) as the blob goes past the point of closest

approach to the sphere the process is reversed both as concerns the direct and reflected wave, and a pulse symmetric overall results.

From the wave fields (12) or (14) the total intensity of radiation can be calculated, and in the general case when the gas $\rho U^2/2$ and magnetic $\mu H^2/8\pi$ pressures are comparable, it scales as:

$$I \sim (L^2/\rho\bar{c}) \ (M^0 , M^2 , M^4) \ (\rho U^2 + \mu H^2/4\pi)^2 , \qquad (15)$$

respectively for mono-, di- and quadrupole sources, where L is the linear size of the source region, $\bar{c}$ the phase speed and $M \equiv U/\bar{c}$ the Mach number measuring the relative amplitude of the wave. If the magnetic field is absent or the magnetic pressure negligible we obtain the acoustic intensity I_v scaling on the fourth power of velocity (16a), whereas if the magnetic pressure predominates (e.g., in a rarefied ionized fluid under strong magnetic fields), we obtain the hydromagnetic intensity I_h, which scales on the fourth power of the magnetic field:

$$I_v \sim (\rho L^2/\bar{c}) \ U^4 \ (M^0 , M^2 , M^4), \qquad (16a)$$

$$I_h \sim (\mu^2 L^2/\rho\bar{c}) \ H^4 \ (M^0 , M^2 , M^4) , \qquad (16b)$$

with factors $1 , M^2 , M^4$ respectively for mono-, di- and quadrupoles. The scaling of the noise of turbulent jets of low Mach number $M^2 \ll 1$ on the eighth power of the velocity (16a) $M^4 U^4 \sim U^8$ has been demonstrated experimentally (Lighthill 1954), confirming the predicted low efficiency (Lighthill 1952) of the quadrupole generation mechanism. Thus sound emission is dominated by the more efficient $\sim M^2$ dipole process $\sim M^2 U^4 \sim U^6$, in the presence of inhomogeneities convected by the mean flow (Howe 1975, Campos 1978a); even if the latter are absent, the presence of solid boundaries acting as dipolar reflectors can enhance the far-field of quadrupole turbulence sources (Curle 1955), e.g., a loose panel in an aerodynamic tunnel can be noisier than the flow itself. The greatest efficiency $\sim M^0$, and higher intensity $\sim U^4$, corresponds to monopole emission in two-phase flow (Crighton & Ffowcs-Williams 1969), of which cavitation noise is an example. Thus the dipolar effect of boundaries confining the flow and

reflecting the sound is negligible for monopole sources, dominant for quadrupole sources, and of comparable magnitude to direct emission for the dipole source case.

The scaling laws for the intensity of radiation discussed above have an extensive field of application: (16a) applies to the aerodynamic acoustics of jets, and has been used in connection with the estimation of sound radiation by turbulence and inhomogeneities in free and confined flows; (16b) is of analogous form replacing the gas by the magnetic pressure, and applies to hydromagnetic waves in ionized fluids under dominant magnetic fields, e.g., to magnetohydrodynamic energy generators and thermonuclear fusion devices, where the plasma is confined by strong magnetic fields; (15) includes the case of comparable kinetic and magnetic pressures, and the transitions to dominance by one or the other, and applies in a variety of situations, from the molten interior mantle to the ionized upper layers of the atmosphere of the earth, and to phenomena in the sun and other stars, clusters, galaxies and matter scattered through the vast expanses of the universe.

REFERENCES

ADAM, J. A. 1982 Asymptotic solutions and spectral theory of linear wave equations. *Phys. Rep.* **86**, 217-316.

D'ALEMBERT, J. R. 1747 Recherches sur les vibrations des cordes. *Oposc. Math.* **1**, 1-73.

ATHAY, R. G. 1976 *The solar chromosphere and corona.* D. Reidel, Dordrecht.

BALSA, T. F. 1976 The far-field of high-frequency convected singularities in sheared flows, with application to jet noise prediction. *J. Fluid Mech.* **74**, 193-208.

BARRAT, M. J., DAVIES, P. O. A. L. & FISHER, M. J. 1963 The characteristics of turbulence in the mixing region of a round jet. *J. Fluid Mech.* **16**, 337-367.

BATCHELOR, G. K. 1953 *The theory of homogeneous turbulence.* Cambridge U. P.

BATCHELOR, G. K. 1967 *Introduction to fluid mechanics.* Cambridge U. P.

BECKMANN, P. & SPIZZICHINO, A. 1963 *The scattering of electromagnetic waves from rough surfaces.* McGraw-Hill.

BEL, N. & MEIN, P.   1971   Propagation of magneto-acoustic waves along the gravitational field in an isothermal atmosphere. *Astron. Astrop.* **11**, 234-250.

BERRY, M. V.   1973   The statistical properties of echoes diffracted from rough surfaces. *Phil. Trans. Roy. Soc. Lond.* **A273**, 611-654.

BEYER, R. T. & KORMAN, M. S.   1980   The scattering of sound by turbulence in water *J. Acoust. Soc. Am.* **67**, 1980-1987.

BORN, M. & WOLF, E.   1959   *Principles of Optics.* Pergamon, 5th ed. 1975.

BRAY, R. J. & LOUGHHEAD, R. E.   1974   *The solar chromosphere.* Chapman & Hall.

BREKHOVSKIKH, L. M.   1960   *Waves in layered media.* Academic P., 2nd ed. 1980.

CAMPOS, L. M. B. C.   1977   On the generation and radiation of magneto-acoustic waves. *J. Fluid Mech.* **81**, 529-549.

CAMPOS, L. M. B. C.   1978a   The emission of sound by an ionized inhomogeneity. *Proc. Roy. Soc. Lond.* **A359**, 65-91.

CAMPOS, L. M. B. C.   1978b   The spectral broadening of sound by turbulent shear layers. Part I: The transmission of sound through turbulent shear layers *J. Fluid Mech.* **89**, 723-749.

CAMPOS, L. M. B. C.   1978c   The spectral broadening of sound by turbulent shear layers. Part II: The spectral broadening of sound and aircraft noise. *J. Fluid Mech.* **89**, 751-783.

CAMPOS, L. M. B. C.   1983a   On three-dimensional acoustic-gravity waves in model non-isothermal atmospheres. *Wave Motion,* **5**, 1-14.

CAMPOS, L. M. B. C.   1983b   On magneto-acoustic-gravity waves propagating or standing vertically in an atmosphere. *J. Phys.* **A16**, 417-437.

CAMPOS, L. M. B. C.   1983c   On waves in non-isothermal, compressible, ionized and viscous atmospheres. *Solar Phys.* **82**, 355-368.

CAMPOS, L. M. B. C.   1984a   On anisotropic, dispersive and dissipative wave equations. *Port. Math.* (to appear).

CAMPOS, L. M. B. C.   1984b   On the propagation of sound in nozzles of varying cross-section containing a low Mach number flow. *Zeits. Flugwiss. Weltraumf.* (to appear).

CAMPOS, L. M. B. C.   1984c   Sur la propagation du son dans les écoulements non-uniformes et non-stationaires. *Revue d'Acoust* (to appear).

CANDEL, S. M., GUÉDEL, A. & JULIENNE, A.   1976   Refraction and scattering of sound in an open wind tunnel flow. *Proc. 6th Int. Cong. Instr. Aerosp. Simul. Facil.* Ottawa, 288-296.

CANDEL, S. M., JULIENNE, A. & JULLIAND, M.   1975   Étude de l'effet de masque produit par un écran fluide. *Dep. Aerod. Acoust.-Dir. Tech.,* SNECMA, Villaroche (Paris), Fiche Tech. YKA-869.

CHERNOV, L. A.   1967   *Wave propagation in a random medium.* Dover.

CLARKE, R. H.   1973   Theory of acoustic propagation in a variable ocean. *NATO Saclant ASW Res. Cent.,* La Spezia (Italy), Memo SM-28.

CRIGHTON, D. G.   1981   Acoustics as a branch of fluid mechanics. *J. Fluid Mech.* **106**, 261-298.

CRIGHTON, D. G. & FFOWCS-WILLIAMS, J. E.   1969   Sound generation by turbulent two-phase flow. *J. Fluid Mech.* **36**, 585-603.

CURLE, N.   1955   The influence of solid boundaries upon aerodynamic sound. *Proc. Roy. Soc. Lond.* **A231**, 505-513.

DOAK, P. E. (ed.)   1976   *Special course on acoustic propagation.* AGARD Rep. 686.

DOPPLER, C.   1893   Ueber das Farbige Licht der Doppelsterne und Einiger Anderer Gestirne des Himmels, *Abh. Bohm. Ges. Wiss.* **2**, 467-498 *(Ostw. Klass. Ex. Wiss.* **161**, 3-34).

DOWLING, A., FFOWCS-WILLIAMS, J. E. & GOLDSTEIN, M. E.   1978   Sound production in a moving stream. *Phil. Trans. Roy. Soc. Lond.* **A286**, 321-349.

FFOWCS-WILLIAMS, J. E. & HAWKINS, D. L.   1968   Sound generation by turbulence and surfaces in arbitrary motion. *Phil. Trans. Roy. Soc. Lond.* **A264**, 321-383.

HO, C. M. & KOVASZNAY, L. S. G.   1976a   Propagation of a coherent acoustic wave through a turbulent shear flow. *J. Acoust. Soc. Am.* **60**, 40-45.

HO, C. M. & KOVASZNAY, L. S. G.   1976b   Acoustical shadowgraph. *Phys. Fluids* **19**, 1118-1123.

HOWE, M. S.   1973   Mutiple scattering of sound by turbulence and other inhomogeneities, *J. Sound. Vib.* **27**, 455-476.

HOWE, M. S.   1975   Contribution to the theory of aerodynamic sound with application to excess jet noise and the theory of the flute. *J. Fluid Mech.* **72**, 625-673.

HOWE, M. S.   1976   The attenuation of sound by a randomly irregular impedance layer. *Proc. Roy. Soc. Lond.* **A347**, 513-535.

HOWE, M. S. & FFOWCS-WILLIAMS, J. E.   1978   On noise generated by an imperfectly expanded supersonic jet. *Phil. Trans. Roy. Soc. Lond.* **A289**, 271-314.

ISHIMARU, I.   1977   *Wave propagation and scattering in random media.* Academic. P.

JEANS, J.   1908   *The theory of electricity and magnetism.* Cambridge U. P., 5th ed. 1932.

JONES, D. S.   1964   *Electromagnetic theory.* Pergamon.

JONES, D. S.   1977   The scattering of sound by a simple layer. *Phil. Trans. Roy. Soc. Lond.* **A284**, 287-328.

JUVÉ, D. & BLANC-BENON, P.   1981   Effet d'un jet turbulent sur le niveau d'onde cohérente et sur l'intensité du faisceau acoustique. *Comp. Rend. Acad. Sci. Paris* **393**, 493-496.

JUVÉ, D. & BLANC-BENON, P.   1982   Corrélations spatio-temporelles d'un faisceau ultrasonore après traversée d'une turbulence cinématique. *Comp. Rend. Acad. Sci. Paris* **294**, 1255-1258.

KHINCHIN, S. I.   1948   *Mathematical foundations of statistical mechanics.* Dover.

KULSRUD, R. M.   1955   The effect of magnetic fields on the generation of noise by isotropic turbulence. *Astrop. J.* **121**, 461-480.

LAMB, H.   1879   *Hydrodynamics.* Cambridge U. P., 6th ed. 1932.

LANDAU, L. D. & LIFSHITZ, E. F.   1953   *Fluid Mechanics.* Pergamon.

LEVINE, H.   1978   *Unidirectional wave motion.* North-Holland.

LIGHTHILL, M. J.   1952   On sound generated aerodynamically: I. General theory. *Proc. Roy. Soc. Lond.* **A211**, 564-587.

LIGHTHILL, M. J.   1953   On the energy scattered from the interaction of turbulence with sound and shock waves. *Proc. Camb. Phil. Soc.* **44**, 531-551.

LIGHTHILL, M. J.   1954   On sound generated aerodynamically: II. turbulence as source of sound. *Proc. Roy Soc. Lond.* **A222**, 1-32.

LIGHTHILL, M. J.   1960   Studies in magnetohydrodynamic waves and other anisotropic wave motions. *Phil. Trans. Roy. Soc. Lond.* **A252**, 397-430.

LIGHTHILL, M. J.   1961   On sound generated aerodynamically. Bakerian Lecture. *Proc. Roy. Soc. Lond.* **A267**, 147-182.

LIGHTHILL, M. J.   1964   Group velocity. *J. Inst. Math Appl.* **1**, 1-28.

LIGHTHILL, M. J.   1967   Predictions on the velocity field coming from acoustic noise and a generalized turbulence in a layer overlaying a convectively unstable atmospheric region. *Aerodynamic Phenomena in Stellar Atmospheres.* 429-453, Academic P.

LIGHTHILL, M. J.   1978   *Waves in fluids.* Cambridge U. P.

LINDEBERG, J. W.   1922   Eine neue Erleitung der Exponential Gezetses in der Wahrscheinlichtkeitsrechnung *Math. Zeits.* **15**, 211-225.

MANI, R.   1976a   The influence of jet flow on jet noise. Part I. The noise of unheated jets. *J. Fluid Mech.* **73**, 753-778.

MANI, R.   1976b   The influence of jet flow on jet noise. Part II. The noise of heated jets. *J. Fluid Mech.* **73**, 779-793.

MCLELLAN, A. & WINTERBERG, F.   1968   Magneto-gravity waves and the heating of the solar corona. *Solar Phys.* **4**, 401-408.

MILNE-THOMSON, L. M.   1958   *Theoretical aerodynamics.* MacMillan, Dover 1966.

MISES R. V. von   1964   *Mathematical theory of probability and statistics.* Academic P.

MORSE, P. M. & INGARD, K.   1968   *Theoretical acoustics.* McGraw-Hill.

MUNT, R. M.   1977   The interaction of sound with a subsonic jet issuing from a semi-infinite cylindrical pipe. *J. Fluid Mech.* **83**, 609-640.

NAYFEH, A. H., KAISER, J. E. & TELIONIS, D. P.   1975   Acoustics of aircraft engine-duct systems. *A.I.A.A. Journ.* **13**, 650-704.

PARKER, E. N.   1964   A mechanism for the enhancement of sound wave generation and the dynamical origin of spicules. *Astrop. J.* **140**, 1170--1175.

PHILIPS, O. M.   1960   On the generation of sound by supersonic turbulent shear layers. *J. Fluid Mech.* **9**, 1-28.

POWELL, A.   1968   Vortex Sound. *J. Acoust. Soc. Am.* **36**, 117-185.

PRANDTL, L. & TIETJENS, O. J.   1934   *Fundamentals of hydro-and aeromechanics.* Dover.

RAYLEIGH, J. W. S.   1873   Note on a natural limit to the sharpness of spectral lines. *Nature* 8, 474-475 (*Papers* 1, 83-84).

RAYLEIGH, J. W. S.   1877   *Theory of sound.* MacMillan, Dover 1945.

Rayleigh, J. W. S.   1889   On the limit to interference when light is emitted from moving molecules. *Phil. Mag.* **27**, 298-304 (*Papers* **3**, 258-263).

Rayleigh, J. W. S.   1915   On the widening of spectrum lines. *Phil. Mag.* **29**, 274-284 (*Papers* **6**, 291-299).

Schmidt, D. W. & Tilmann, P. M.   1970   Experimental study of sound phase fluctuations caused by turbulent wakes. *J. Acoust. Soc. Am.* **47**, 1310-1324.

Sholnik, M. I.   1962   *Introduction to radar systems.* McGraw-Hill.

Stein, R. F.   1967   Generation of acoustic and acoustic-gravity waves by turbulence in an isothermal stratified atmosphere. *Solar Phys.* **2**, 385--432.

Stein, R. F.   1981   Stellar chromospheric and coronal heating by magnetohydrodynamic waves. *Astrop. J.* **246**, 966-971.

Stein, R. F. & Leibacher, J.   1974   Waves in the solar atmosphere. *Ann. Rev. Astron. Astrop.* **12**, 407-435.

Stratton, J. A.   1944   *Electromagnetic theory.* McGraw-Hill.

Tatarski, V. I.   1967   *Wave propagation in a turbulent medium.* Dover.

Townsend, A. A.   1956   *Structure of turbulent shear flow.* Cambridge U. P.

Uscinski, B. J.   1977   *Elements of wave propagation in random media,* McGraw-Hill.

Yu, C. P.   1965   Magneto-atmospheric waves in an horizontally stratified conducting medium. *Phys. Fluids* **8**, 650-656.

Whitham, G. B.   1974   *Linear and non-linear waves.* Interscience.

MODERN TRENDS IN RESEARCH ON WAVES IN FLUIDS, PART II: PROPAGATION AND DISSIPATION IN COMPRESSIBLE AND IONIZED ATMOSPHERES

L. M. B. C. Campos [1]

Instituto Superior Técnico, 1096 Lisboa, Portugal

ABSTRACT — We consider the propagation and dissipation of waves in fluids, in the presence of external force fields (§ 1), namely the magnetic and gravity fields: the former in connection with Alfvèn-gravity waves (§ 2) in an ionized atmosphere, including the damping by Ohmic electric resistance; the latter in connection with acoustic waves of large amplitude (§ 3), which tend to shock formation, delayed by diffusive processes such as viscosity. The propagation and dissipation of waves in atmospheres is an effective physical process of transfering mass, momentum and energy; analogous problems of engineering interest occur in the propagation of sound in ducts of varying cross-section, such as the horns of loudspeakers and the nozzles of jet engines.

1 — INTRODUCTION

Two of the main trends in current research on waves in fluids are the study of the effects of internal inhomogeneities and turbulence, which were discussed in the first part of the present essay, and the consequences of external applied force fields, which we consider in the present, concluding part. Gravity, being intrinsically associated with the existence of matter, is an ever present force field, which causes fluids to become stratified, and affects considerably waves in the oceans (Stoker 1953, Eckart

---

[1] On leave at D.A.M.T.P., Cambridge University, Silver Street, Cambridge CB3 9EW, U.K.

1960, Philips 1960, Kraus 1977) and atmosphere (Yih 1965, Beer 1974, Hines 1974, Gossard & Hooke 1975, Pedlosky 1979) of the earth. More than a few miles away from the earth's surface magnetic fields are important, both in the mantle and ionosphere, and ionized matter is predominant in most regions of the universe (Chapman & Cowling 1949, Spitzer 1952, Akasofu & Chapman 1972, Parker 1979), the basic properties of waves in these conditions being a standard topic in magnetohydrodynamics (Alfvèn 1948, Landau & Lifshitz 1956, Cowling 1957, Ferraro & Plumpton 1961, Alfvèn & Falthammar 1962, Cabannes 1970, Priest 1982).

The Alfvèn speed, which characterizes the propagation of transverse (and hence incompressible) hydromagnetic waves, scales on the inverse square root of the mass density, and thus increases rapidly with altitude in an atmosphere. The acceleration of the Alfvèn-gravity waves with altitude implies that the wave forms are *not* sinusoidal, neither for standing nor for propagating modes; also, the phase of propagating waves, instead of increasing linearly with altitude, has an increasing *slope*, and tends to a finite asymptotic value. The effects of dissipation, say, by electrical resistance, on the Alfvèn-gravity wave, are significant at low altitude, where it propagates slowly, and become less important at higher altitudes, as the wave speed increases, and there is less time to dissipate its energy; thus there is a transition layer between the low-altitude, diffusion regime and the high-altitude, propagation regime.

Acoustic-gravity waves have rather different properties, since the sound speed is determined by temperature alone, and thus varies slowly. As the atmospheric density decays with altitude, the amplitude of the acoustic-gravity wave increases, until non-linear effects become important and shocks may form. The steepening of the wave front that leads to shock formation is opposed and delayed by dissipation effects, such as viscosity. Even if the static viscosity is small, the kinematic viscosity, which varies inversely with the mass density, may be significant at high-altitude, and thus be a moderately effective dissipation mechanism. Thus acoustic-gravity waves can cause significant compression and mass transport in an atmosphere, together with moderate heating; the Alfvèn-gravity waves, which can be dissipated by electrical resistance, are a more effective mechanism of energy transport and heating, but carry no net mass flux since

they are transversal. Another contrast is that the combination of compressibility and gravity can cause the appearance of cut-off frequencies for acoustic waves, whereas Alfvèn waves are not affected by filtering effects.

2 — DAMPING OF HYDROMAGNETIC WAVES WITH VARIABLE SPEED

Waves of small amplitude in homogeneous media are described by linear partial differential equations with constant coefficients, e.g., for magnetic (Alfvèn 1942, Lehnert 1952, Lighthill 1960) and magneto-acoustic (Herlofson 1950, Jones 1964, Campos 1977) waves, and spectral methods can be used in space and time (Lighthill 1978, Adam 1982, Campos 1984a). In the case of stratified media, e.g., atmospheres, the equations describing small amplitude waves are linear with variable coefficients, and exact solutions can be found usually in terms of special functions, e.g., for Alfvèn-gravity (Ferraro 1955, Hide 1956, Ferraro & Plumpton 1958, Zhugzhda 1971, Hollweg 1972, Leroy 1982, Campos 1983b, d) and magnetosonic-gravity (Nye & Thomas 1976, Adam 1977, Campos 1983b, c) waves. We choose among these, as an example, Alfvèn waves propagating in an ionized atmosphere under a vertical external magnetic field B, in the presence of electrical resistance $1/\sigma \neq \infty$ where $\sigma \neq 0$ is the Ohmic conductivity. The only propagating components of the velocity $\mathbf{v}$ and magnetic field $\mathbf{h}$ perturbations are horizontal and parallel $\mathbf{v} = v\,\mathbf{e}_x$, $\mathbf{h} = h\,\mathbf{e}_x$, they depend on altitude z and time t, and satisfy the equation of momentum and induction, viz.:

$$\partial v/\partial t - B^{-1}\left\{A(z)\right\}^2 \partial h/\partial z = 0, \tag{1a}$$

$$\partial h/\partial t - B\ \partial v/\partial z = \zeta(z)\ \partial^2 h/\partial z^2, \tag{1b}$$

where the Alfvèn speed $A(z)$ and magnetic diffusivity $\zeta(z)$ generally depend on altitude:

$$\left\{A(z)\right\}^2 = \mu B^2/4\pi\rho(z), \quad \zeta(z) = c_*^2/4\pi\mu\sigma(z), \tag{2a, b}$$

through the density stratification $\rho(z)$ and Ohmic conductivity $\sigma(z)$; we have denoted by μ the magnetic permeability and by c_* the speed of light.

Eliminating between (1a, b) respectively for the velocity v and magnetic field h perturbations, we obtain the wave equations:

$$\{ \partial^2/\partial t^2 - \partial/\partial z \, (A(z))^2 \, \partial/\partial z - \zeta(z) \, \partial^3/\partial t \partial z^2 \} \, h(z,t) = 0 ,$$
(3a)

$$\{ \partial^2/\partial t^2 - (A(z))^2 \, \partial^2/\partial z^2 - (A(z))^2 \, \partial/\partial z \, \zeta(z)$$

$$\partial/\partial z \, (A(z))^{-2} \, \partial/\partial t \} \, v(z,t) = 0 ;$$
(3b)

it is clear that: (i) in an homogeneous medium, for which (2a, b) are constants, the two wave variables satisfy the same equation:

$$\{ \partial^2/\partial t^2 - A^2 \, \partial^2/\partial z^2 - \zeta \, \partial^3/\partial t \partial z^2 \} \, v, h(z,t) = 0 ,$$
(4)

and have the same altitude dependence; (ii) in a stratified medium the magnetic field (3a) and velocity (3b) satisfy different equations, as suggested by (1a), and their waveforms are generally different. Resistive Alfvèn-gravity waves are characterized by four parameters, namely the frequency ω which is conserved if the atmosphere is at rest, the scale height $L(z) \equiv \{ d(\log \rho)/dz \}^{-1}$ specifying the density stratification $\rho(z)$, the Alfvèn speed $A(z)$ and the magnetic diffusivity $\zeta(z)$, with which we can form two dimensionless parameters:

$$\alpha(z) \equiv \omega L(z)/A(z), \qquad \beta(z) \equiv \omega \zeta(z)/\{ A(z) \}^2 ,$$
(5a, b)

which may be interpreted as follows: (i) $\alpha \sim 2\pi \lambda/L$ is the compactness since it compares the wavelength λ to the atmospheric scale height L, and describes non-dissipative waves; (ii) in the presence of electrical resistance an additional dissipation parameter $\beta \sim 2\pi \chi/L$ appears, comparing the damping scale $\chi \equiv \zeta/A$ to the scale height.

The Ohmic electrical conductivity σ, and hence the magnetic diffusivity ζ (2b) are independent of density and are functions of temperature, so that they are bounded in a non-isothermal atmosphere (provided the temperature be finite); the mass density, on the other hand, tends to zero $\rho \to o$ as altitude tends to infinity $z \to \infty$, and thus the Alfvèn speed (2a) diverges asymptotically $A \to \infty$. From the second terms of (3a, b), since $A^2 \, \partial^2 v/\partial z^2$, $A^2 \, \partial h/\partial z$ must remain finite as $z \to \infty$ and $A(z) \to \infty$, and we

have $\partial^2 v/\partial z^2$, $\partial h/\partial z \to o$, i.e.: (i) Alfvèn-gravity waves, with electrical resistance or not, propagating in a non-isothermal atmosphere (of bounded temperature), have a velocity perturbation which grows linearly and a magnetic field perturbation which tends to a constant in the asymptotic regime as $z \to \infty$:

$$v (z ; \omega) \sim f_1 (\omega) \, z + f_2 (\omega) \, , \qquad (6a)$$

$$h (z ; \omega) \sim i (B/\omega) \, f_1 (\omega) \, , \qquad (6b)$$

where f_1 , f_2 depend on frequency ω ; (ii) in the case of a standing mode perfectly reflected from infinity the velocity perturbation is bounded and thus the magnetic field perturbation decays to zero:

$$v (z ; \omega) \sim f_2 (\omega) \, , \quad h (z ; \omega) \sim 0 \, . \qquad (7a, b)$$

Thus, although initially the velocity and magnetic field perturbations are proportional $v/A \sim h/B$, in agreement (1a) with equipartition of kinetic and magnetic energy $\rho v^2/2 \sim \rho \, (A^2/B^2)$ $h^2/2 \sim \mu h^2/8\pi$, asymptoticaly: (i) for standing modes (7a, b) both the kinetic $E_v = \rho v^2/2 \sim o$ and magnetic $E_h = \mu h^2/8\pi \sim o$ energies (per unit volume) tend to zero; (ii) for propagating waves (6a, b) only the kinetic energy $E_v = \rho v^2/2 \sim O (z^2 \, e^{-z/L}) \to o$ since the density decays exponentially on altitude $\rho \sim O (e^{-z/L})$, but the magnetic energy $E_h = \mu h^2/8\pi \sim \mu B^2 f_1^2/8\pi\omega^2$ tends to a constant, so that asymptoticaly all energy is magnetic, i.e., the opposite of equipartition.

The preceding results can be checked in the case of an isothermal atmosphere, for which the wave fields can be calculated exactly at all altitudes and frequencies. In an isothermal atmosphere the density decays exponentially $\rho (z) = \rho (o) \, e^{-z/L}$ on the scale height $L \equiv RT/g$, and the Alfvèn speed (2a) and compactness (5a) are given by:

$$A (z) = \{ \mu/4\pi \rho (o) \}^{1/2} \, B \, e^{z/2L} \equiv a \, e^{z/2L} \, , \qquad (8a)$$

$$\alpha (z) = (\omega L/a) \, e^{-z/2L} \qquad (8b)$$

Considering non-dissipative Alfvèn-gravity waves ($\zeta = o$ in 2b), and using as variable the compactness (2α given by 8b) instead of altitude z , the velocity perturbation spectrum $V (z ; \omega)$ at

altitude z for a wave of frequency ω is shown to satisfy a Bessel equation of order zero. The solution is a linear combination of Hankel functions $H_0^{(1)}(2\alpha)$, $H_0^{(2)}(2\alpha)$ but if we want to select a wave propagating upward, i.e., in the direction of increasing z and decreasing α (8b), we must select $H_0^{(2)}$. The constant of integration is determined from the initial velocity spectrum $V(0;\omega)$ at altitude $z = 0$, and we have:

$$V(z;\omega) = V(o;\omega)\ \{H_0^{(2)}((2\omega L/a)\ e^{-z/2L})/H_0^{(2)}\ (2\omega L/a)\}; \quad (9)$$

for the exact wave field at all altitudes. The solution (9) specifies the transition between the initial and asymptotic regimes, respectively of exponential and linear growth:

$$V(z;\omega) = V(o;\omega)\ e^{z/4L}\ e^{i\,(\omega/a)\,z}\ \{1 + O\ (\omega z^2/2\,a\,L)\}, \quad (10a)$$

$$V(z;\omega) = \{V(o;\omega)/H_0^{(2)}\ (2\omega L/a)\}\ \{1 + \psi - i\,2\,z/\pi\,L\} \atop \{1 + O((\omega^2 L^2/a^2)\ e^{-z/L})\}, \quad (10b)$$

where $\psi \equiv (2/\pi)\ \log\ (\omega L/a) + \phi$, and ϕ is Euler's constant.

In the case of Alfvèn-gravity waves perfectly reflected from infinity, the velocity perturbation spectrum $V(z;\omega)$ must be bounded as $z \to \infty$, and the solution is given by (9) with the Hankel functions of second kind $H_0^{(2)}$ replaced by Bessel functions of first kind J_0. The vanishing of the denominator $J_0(2\omega L/a) = o$ corresponds to resonance, so that the roots p_n of the Bessel function $J_0(p_n) = o$ specify through $p_n = 2\omega L/a = 4\pi L/\lambda$ the frequencies ω_n and wavelengths λ_n of the standing modes:

$$\omega_n = a\,p_n/2\,L, \quad \lambda_n = 4\,\pi\,L/p_n, \quad (11a, b)$$

$$\omega_n/\omega_1 = \lambda_1/\lambda_n = p_1/p_n; \quad (11c)$$

it will be noted that the frequencies of the eigenmodes depend on the Alfvèn speed and scale height (11a), the wavelengths depend only on the scale height (11b), and their ratios are absolute non-integral numbers (11c) independent of wave or atmospheric

properties. The velocity perturbation is the superposition of all standing modes with non-vanishing initial spectrum $V(0; \omega_n)$:

$$v(z, t) = (\pi a / 2L) \sum_{n=1}^{\infty} \text{Im} \{ V(0; \omega_n) \exp(-i\omega_n t) \}$$

$$q_n^{-1} J_0(p_n e^{-z/2L}), \tag{12}$$

where $q_n \equiv J_0'(p_n) = -J_1(p_n)$ is the slope of the Bessel function J_0 at its zero p_n. The exact solution (12) is valid at all altitudes, and shows the transition between the initial and asymptotic regimes:

$$v(z, t) = (a/L)(\pi/2)^{1/2} e^{z/4L} \sum_{n=1}^{\infty} \text{Im} \{ V(0; \omega_n) e^{-i\omega_n t} \}$$

$$q_n^{-1} p_n^{-1/2} \sin \{ (\omega/a)(z - 2L) \} \{ 1 + O(\omega z^2 / 2 a L) \}, \tag{13a}$$

$$v(z, t) = (\pi a / 2L) \sum_{n=1}^{\infty} \text{Im} \{ V(0; \omega_n) e^{-i\omega_n t} \} q_n^{-1}$$

$$\{ 1 + O((p_n^2 / 4) e^{-z/L}) \}, \tag{13b}$$

respectively of exponential growth and finite amplitude.

In the presence of resistive dissipation, bearing in mind that the magnetic diffusivity is bounded (2b) and the Alfvèn speed unbouded as $z \to \infty$ (2a), the dissipative wave equations (3a, b) have at most three regular singularities: (i) the singularity at $z = 0$ specifies the initial wave field; (ii) the singularity at $z = \infty$ specifies the asymptotic radiation field; (iii) an intermediate singularity at $z = z_*$ specifies a transition layer where the effects of propagation and diffusion balance:

$$\omega \zeta(z_*) = \{ A(z_*) \}^2; \quad z_* = L \log(\omega \zeta / a^2), \tag{14a, b}$$

specifies the altitude of the transition layer for an isothermal atmosphere, where the magnetic diffusivity ζ is constant and the Alfvèn-speed $A(z)$ increases exponentially with altitude according to (8a) from the initial value $a \equiv A(0)$. The transition layer separates the atmosphere in two regions: (i) in the low-altitude

region $z < z_*$ the magnetic diffusivity predominates, the wave equations resemble the Schrodinger's type, and we have mainly resistive dissipation modified by propagation; (ii) in the high--altitude region $z > z_*$ the Alfvèn speed predominates, the wave equations resemble the hyperbolic type, so that we have propagation with damping which decays with altitude, and preserves the form of the asymptotic laws (6, 7a, b). The situation is similar to the plane, isentropic, compressible flow, for which the transition is specified by local Mach number unity $M = 1$, separating subsonic flow for which the hodograph equations are elliptic from supersonic flow for which they are hyperbolic (Molenbroek 1890, Chaplygin 1904, Lighthill 1947, von Mises 1960); another case is wave absorption at critical levels (Bretherton 1966, Booker & Bretherton 1967, McKenzie 1973, Eltayeb 1977, Ahmed & Eltayeb 1978, Rudraiah & Venkatachalappa 1979).

The dissipation parameter β (5b) is unity at the transition layer (14a), and if we chose it as independent variable instead of altitude, the singularities are located at $\beta = 0, 1, \infty$. The simplest special function with three regular singularities is the hypergeometric, and indeed the fields of resistive Alfvèn-gravity waves propagating in an isothermal atmosphere can be expressed exactly in terms of hypergeometric functions of parameters $c = 1$ and:

$$a = 1 + (1-i) \, K \, L \equiv \upsilon, \quad b = 1 - (1-i) \, K \, L \equiv 2 - \upsilon,$$

$$K \equiv \sqrt{\omega/2\zeta}, \qquad \qquad (15a, b, c)$$

where the frequency ω is related quadratically to the effective wavenumber K through (twice) the magnetic diffusivity, $\omega = 2\zeta K^2$. The velocity perturbation spectrum is given by:

$$V(z;\omega) = V(0;\omega) \, (ia^2/\omega\zeta + e^{-z/L})^{-\upsilon}$$

$$\{ F(\upsilon, \upsilon-1; 2\upsilon-1; (1 - i(\omega\zeta/a^2) \, e^{-z/L})^{-1}) \} \qquad (16)$$

$$\{ F(\upsilon, \upsilon; 2\upsilon-1; i \, a^2/\omega\zeta) \}^{-1}$$

which applies at all altitudes $0 \leq z \leq \infty$, including the transition layer.

Considering standing modes, the spectrum is discrete, and the eigenvalues for the complex frequency ω_n are given by the roots of:

$$0 = F(\upsilon, 2-\upsilon; 1; i\omega\zeta/a^2)$$

$$= 1 + \sum_{p=1}^{\infty} (i\omega\zeta/a^2)^p (p!)^{-2} \prod_{q=0}^{p-1} (q^2 + 2q + 1 + i\omega\zeta/a^2);$$

(17)

the roots $\omega_n = f_n - i\, d_n$ specify, through their real part, the frequency $f_n = \mathrm{Re}(\omega_n)$, and through minus the imaginary part, the damping rate $d_n = \mathrm{Im}(-\omega_n)$, since $\exp(-i\omega_n t) = \exp(-if_n t)$ $\exp(-d_n t)$. The wave field is the superposition of all standing modes with non-vanishing initial spectrum $V(0; \omega_n)$:

$$v(z, t) = \sum_{f_n, d_n > 0} \mathrm{Im}\{V(0; \omega_n)\, e^{-if_n t}\}\, e^{-d_n t}$$

(18)

$$\{\partial F(\upsilon, 2-\upsilon; 1; i\omega\zeta/a^2)/\partial\omega_n\}^{-1} F(\upsilon, 2-\upsilon; 1; i(\omega\zeta/a^2)\, e^{-z/L}),$$

in the case of perfect reflection above the transition layer.

We choose for illustration the case of non-dissipative Alfvèn--gravity waves perfectly reflected from infinity in an isothermal atmosphere, and plot in Fig. 1 the waveforms of the first three standing modes, using an altitude z made dimensionless by dividing by the scale height L. The waveforms are shown for the velocity (top) and magnetic field (bottom) perturbations, made dimensionless by dividing by initial reference values, respectively $V_n, H_n = \{e^{-i\omega_n t}/\omega_n\, V(0; \omega_n)\}\{v_n(z, t), (a/B)\, h_n(z, t)\}$ From the waveforms for the first (left), second (centre) and third (right) standing modes it follows that: (i) the velocity perturbation vanishes at the node $z = 0$, whereas the node at infinity (where the density is zero) corresponds to a constant asymptotic amplitude, decreasing in value (when divided by ω_n) and alternating in sign with the order of the mode; (ii) the magnetic field perturbation starts out-of-phase with a non-zero value at $z = 0$, and decays exponentially to zero in the asymptotic regime, which is attained at higher altitude for higher order modes; (iii) as typical of Sturm-Liouville problems, the velocity and magnetic field perturbations of the n-th mode have $(n-1)$ nodes at intermediate altitudes, with interlacing between the nodes of velocity
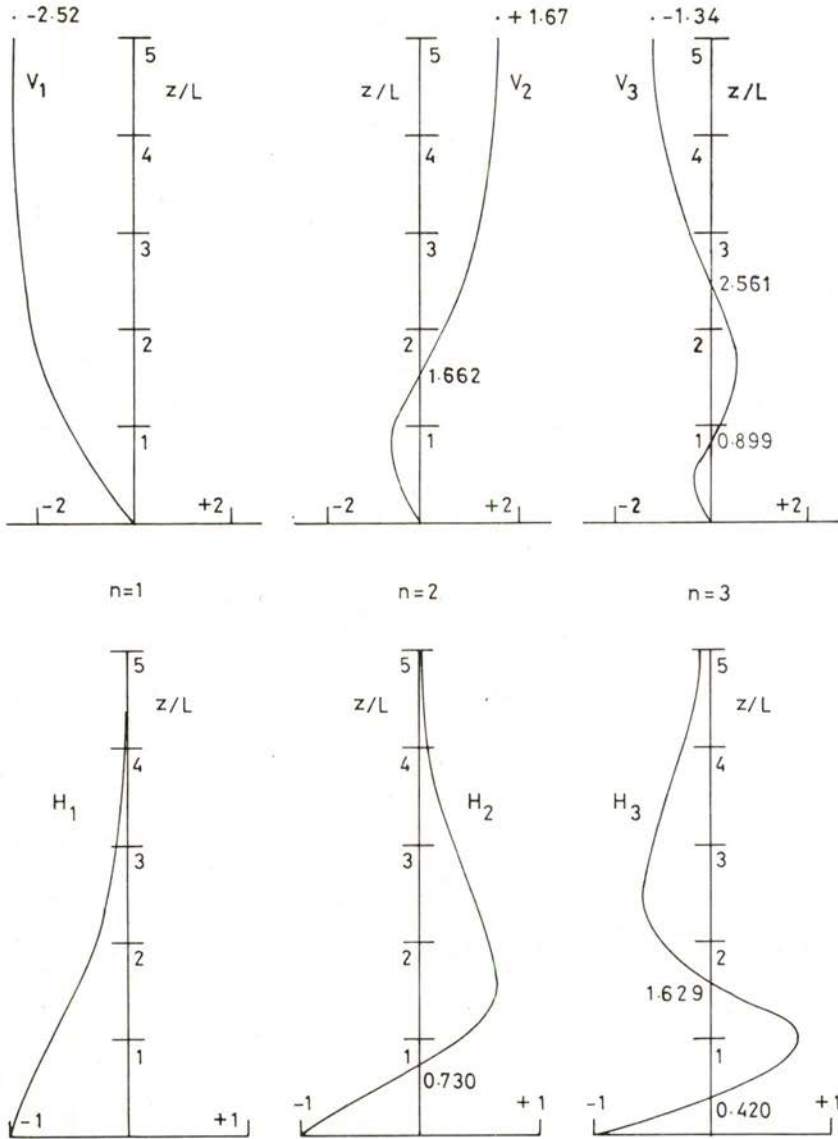
Fig. 1 — Alfvén-gravity modes standing vertically in an isothermal atmosphere, with perfect reflection between altitude zero and infinity. The first three normal modes n = 1, 2, 3 are illustrated by plotting the waveforms for the dimensionless velocity (top) and magnetic field (bottom) perturbations as function of altitude z divided by the scale height L. Note that the magnetic field perturbation starts out-of-phase to the velocity, and decays to zero asymptotically as the velocity tends to a constant value.

154

Portgal. Phys. — Vol. 14, fasc. 3-4, pp. 145-173, 1983

and magnetic field of the same mode n, and between sucessive modes $n, n + 1$. The compactness (5a, 11a) $\alpha_n = \omega_n L/a = p_n/2 = 1.202, 2.760, 4.327$ respectively for the modes of orders $n = 1, 2, 3$, specifies the local wavelength measured on the scale height $\lambda_n/L = 2\pi/\alpha_n = 5.225, 2.276, 1.452$, and shows that the atmospheric density change over a wavelength $\Delta \equiv \rho(0)/\rho(\lambda_n) = \exp(\lambda_n/L) = 185.95, 9.74, 4.27$, is substantial, and thus the effects of atmospheric stratification could not have been neglected or treated approximately by procedures like the W. K. B. J. method.

In Fig. 2 is illustrated the case of non-dissipative Alfvèn--gravity waves propagating vertically, for a compactness (5a) $\alpha = 1$, corresponding to a local wavelength equal to 2π times the scale height $\lambda = 2\pi L$, and an atmospheric density change $\alpha = e^{2\pi} = 535$ in a wavelength. The altitude z is divided by the scale height, and the velocity and magnetic field perturbation spectra for a wave of frequency ω at altitude z are rendered dimensionless by dividing by initial values $V \equiv V(z;\omega)/V(0;\omega)$ and $H \equiv (a/B) H(z;\omega)/V(0;\omega)$. The amplitude of the velocity perturbation (bottom left) initially grows exponentially on four times the scale height $\sim e^{z/4L}$ (10a), and asymptoticaly grows linearly (6a, 10b); the amplitude of the magnetic field perturbation (bottom centre) evolves differently, since it decays initially on four times the scale height $\sim e^{-z/4L}$, and tends asymptoticaly to a constant value (6b). Since the magnetic field perturbation is horizontal, and hence transverse to the direction of propagation, there is an associated electric current, according to Maxwell's law:

$$\nabla \wedge H = (4\pi/c) J; \quad j(z,t) = (c/4\pi) \partial h(z,t)/\partial z, \qquad (19a, b)$$

specifies the electric current propagated with the wave, which for a frequency component ω at altitude z is rendered dimensionless by dividing by initial values $J \equiv 4\pi a^2 J(z;\omega)/c_* B_0 V(0;\omega)$; the magnitude of the electric current (bottom right) decays exponentially with height, initially on four-thirds the scale height $\sim e^{-3z/4L}$, and asymptoticaly on the scale height $\sim e^{-z/L}$, thus tending to zero. The phases (top) of the velocity perturbation (left), magnetic field (centre) and electric current (right), initially vary linearly with altitude, and, as a consequence of the increase of propagation speed with height, the slope increases, so that asymptoticaly the value is finite in all cases.
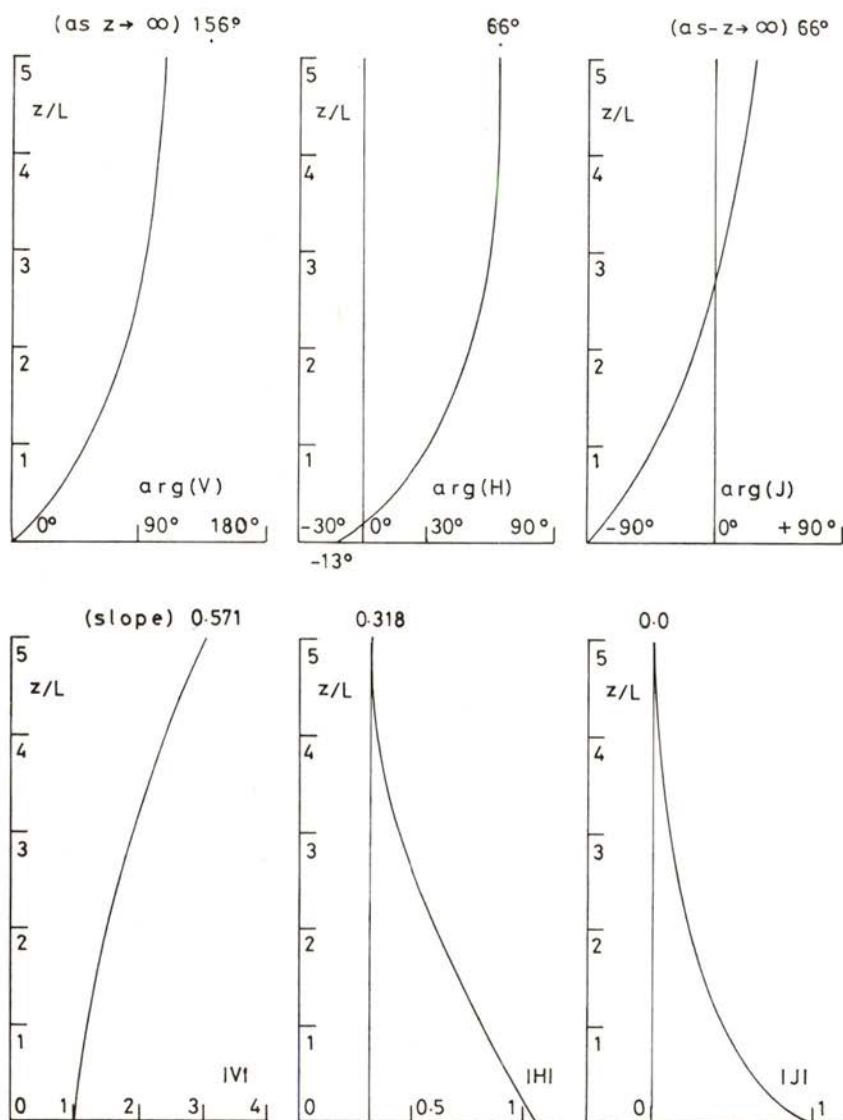
Fig. 2 — Alfvèn-gravity waves propagating vertically in an isothermal atmosphere, for a compacteness parameter unity, corresponding to a change in atmospheric density by a factor of $e^{2\pi} = 535$ over a local wavelength. The wave fields are illustrated by the phases (top) and amplitudes (bottom) of the velocity (left), magnetic field (centre) and electric current (right) propagated with the wave, plotted against dimensionless altitude as in Fig. 1. Note the different initial and asymptotic amplitude laws for each wave variable, and the finite asymptotic phase in all cases.

Since the Alfvèn-gravity waves propagate an electric current j, they supply heat to the atmosphere by Joule effect at the rate $W = (1/\sigma) j^2$, and thus are an effective energy transfer mechanism for atmospheric heating (Osterbrock 1961, Uchida & Kaburaki 1975, Ionson 1982, Campos 1984b). On the other hand, being transversal and incompressible, the Alfvèn modes carry no mass flux. The transfer of mass is more appropriate to the acoustic modes, in particular non-linear or of finite amplitude, which can cause a strong compression of the medium. Acoustic modes can be dissipated by viscosity, which is generally much less effective than electric resistance in transfering energy to the medium. Thus the different modes of magneto-acoustic-gravity waves provide effective mechanisms of transfer of mass, energy and momentum, by propagating from one atmospheric region to another, and then depositing their flux. Having considered Alfvèn-gravity waves, for which the variation of propagation speed with altitude is important (8a), but non linear effects are not, since the Alfvèn number $N \equiv v/A(z) \sim z \, e^{-z/2L}$ decreases with height, we consider next acoustic modes, which will be shown to have contrasting properties.

3 — FILTERING OF HYDRODYNAMIC WAVES AND NON-LINEAR COMPRESSION

Returning to small amplitude magneto-acoustic-gravity waves (eq. (6) of Part I), in an homogeneous medium, the velocity perturbation may be represented by a Fourier decomposition in space and time:

$$v_j(\mathbf{x}; t) = \int_{-\infty}^{+\infty} a_j(\mathbf{k}, \omega) \exp\{i(\mathbf{k} \cdot \mathbf{x} - \omega t)\} \, d^3k \, d\omega; \qquad (20)$$

since application of $(\partial/\partial t, \partial/\partial x_i, \partial/\partial m)$ to v_j is equivalent to multipying a_j by $(-i\omega, i k_i, i(\mathbf{k} \cdot \mathbf{m}))$, where ω denotes the frequency and k_i the wave vector, the homogeneous wave equation $\square_{ij}\{v_j\} = 0$ leads to the algebraic condition $\Pi_{ij} a_j = 0$, where the dispersion matrix is given by:

$$\Pi_{ij} = -\omega^2 \, \delta_{ij} + (c^2 + a^2) \, k_i k_j - i(k_i g_j - k_j g_i) - i \gamma g_i k_j$$
$$+ a^2 (\mathbf{k} \cdot \mathbf{m}) \{(\mathbf{k} \cdot \mathbf{m}) \delta_{ij} - k_i m_j - k_j m_i\}, \qquad (21)$$

where c, a are respectively the sound and Alfvèn speeds, and $m \equiv B/B$ the unit vector in the direction of the external magnetic field B, assumed constant. In order for waves to exist the amplitude cannot vanish, and the roots of the equation $|\Pi_{ij}| = 0$ specify the dispersion relations $\omega(k)$ for each mode. We can consider three cases: (i) for pure acoustic waves $m_i = 0 = g_i$, the first two terms of (21) show that the dispersion matrix is quadratic in ω, k, so that the frequency is a linear function of wavenumber, and acoustic waves are isotropic, and non-dispersive, i.e., propagate at the same speed (of sound c) in all directions and for all frequencies; (ii) in the presence of magnetic field $m_i \neq 0 = g_i$, the dispersion matrix is quadratic on frequency ω and wavevector k_i so that the frequency is linear in the wavenumber k but depends on the wavenormal $n_i = k_i/k$, and magneto-acoustic waves are non-dispersive and anisotropic, i.e., the speed of propagation depends on direction, and the wavefronts are not spherical (they are plane for the Alfvèn mode and curved for the slow and fast modes); (iii) in the presence of gravity $g_i \neq 0$, with or without compressibility and/or magnetic field, the dispersion matrix involves terms of the first and second degree, so that the frequency depends non-linearly on the wave vector, and gravity, acoustic-gravity, magneto-gravity, and magneto-acoustic-gravity modes are all anisotropic and dispersive, since the wave speed depends both on direction and frequency.

Similar methods apply to the wave equations in homogeneous elastic solids, either isotropic or crystals (Love 1927, Cady 1946, Schouten 1953, Achenbach 1973, Hudson 1980); surface waves in fluids and solids can also be isotropic or anisotropic, dispersive or non-dispersive, their dispersion relation being determined from the boundary conditions applying at the interface along which propagation occurs. As an example of the derivation of dispersion relations, we consider the determinant of the dispersion matrix (21), in the case of vertical propagation, when the wavevector $k \equiv (0, 0, k)$ is anti-parallel to gravity $g \equiv (0, 0, -g)$, taken in the x_3-direction, and the plane (x_1, x_3) can be chosen to contain the direction of the external magnetic field $m \equiv (m_1, 0, m_3)$:

$$0 = (\omega^2 - a^2 k^2 m_3^2) \begin{vmatrix} \omega^2 - a^2 k^2 m_3^2 & a^2 k^2 m_1 m_3 \\ a^2 k^2 m_1 m_3 & \omega^2 - c^2 k^2 - a^2 k^2 m_1^2 - i\gamma gk \end{vmatrix} \quad (22)$$

Since (22) is a cubic in ω^2 there are three wave modes, of which one is uncoupled from the other two, as shown by the factor in curved brackets, which corresponds to the dispersion relation $\omega(k)$, phase speed u and group velocity w:

$$\omega = \pm akm_3 = \pm a(k \cdot m), \quad u \equiv \omega/k = \pm a(n \cdot m),$$

$$w \equiv \partial\omega/\partial k = \pm a\,m; \tag{23a, b, c}$$

thus the uncoupled mode is an Alfvèn wave (23a), since it propagates energy at the group velocity (23c), which coincides with the Alfvèn speed a along magnetic field lines m, and the wave crests move at the phase speed $u = w \cdot n$, which corresponds to the group velocity w projected on the wavenormal direction $n \equiv k/k$.

The other two modes, described by the determinant of (22):

$$\omega^4 - \{(a^2 + c^2)\,k^2 + i\gamma gk\}\,\omega^2 + a^2\,(k \cdot m)^2\,(c^2k^2 + i\gamma gk) = 0, \tag{24}$$

are generally coupled, and are distinguished by their speeds as slow and fast. The slow and fast modes decouple when the sound and Alfvèn speeds are of very different orders of magnitude, i.e., one of the gas or magnetic pressures dominates the other. In hydrodynamics, the magnetic pressure is small compared with the gas pressure $a^2 \ll c^2$, and the equation (24) decouples in two factors:

$$\{\omega^2 - a^2\,(k \cdot m)^2\}\,\{\omega^2 - c^2k^2 - i\gamma gk\} = 0; \tag{25a}$$

the first factor specifies again the Alfvèn wave (23a, b, c) propagating along magnetic field lines m at a small speed a, and is the slow mode, and the second factor specifies an acoustic-gravity wave, which corresponds to the fast mode. In the converse case, of dominant magnetic field $a^2 \gg c^2$, $\gamma g/k$, in the vertical direction $m_1 = 0$, $m_3 = 1$, equation (24) factors:

$$\{\omega^2 - a^2k^2\}\,\{\omega^2 - c^2k^2 - i\gamma gk\} = 0, \tag{25b}$$

into an acoustic-gravity wave (second factor) as in (25a), but now corresponding to the slow mode, whereas the first factor specifies the fast mode:

$$\omega = \pm \, a \, k, \quad u \equiv \omega/k = \pm \, a, \quad w \equiv \partial \omega/\partial k = \pm \, a \, n, \quad (26a, b, c)$$

which is a wave propagating isotropically in all directions n at Alfvèn speed a.

Thus we find that the vertical acoustic-gravity wave, of dispersion relation $\omega^2 - c^2 k^2 - i\gamma g k = 0$ exists, uncoupled from magnetic modes, in two opposite circunstances: (a) in the case of a magnetic field so weak (25a) that it cannot affect the acoustic-gravity wave; (b) in the case of a magnetic field so strong (25b) that the gas cannot cross magnetic field lines, and the acoustic-gravity wave is forced to propagate along the magnetic flux tube. In the absence of gravity $g = 0$, the dispersion relation reduces to $\omega^2 - c^2 k^2 = 0$, implying (26a, b, c) with c replacing a, i.e., isotropic propagation at the sound speed $c^2 = \gamma RT$, where γ is the ratio of specific heats, R the gas constant and T the temperature. The presence of gravity affects acoustic waves by introducing anisotropy, dispersion and filtering, as can be seen from the dispersion relation (second factor in 25a, b) written for the vertical wavenumber k:

$$k^2 + (i/L) \; k - \omega^2/c^2 = 0, \quad L \equiv c^2/\gamma g = RT/g, \quad (27a, b)$$

which involves the atmospheric density scale height given by (27b). Solving (27a) for the vertical wavenumber:

$$k = - (i/2L) \; \{ 1 \pm \sqrt{1 - \omega^2/\omega_*^2} \}, \quad (28a)$$

$$\omega_* \equiv c/2L = (g/2) \sqrt{\gamma/RT}, \quad (28b)$$

we conclude that it is pure imaginary $k = - i\delta/2L$, and the wave field non-oscillating $\exp(ikz) = \exp(\delta z/2L)$, for frequencies below (28b) $\omega < \omega_*$, which is designated cut-off frequency, since below it propagating waves cannot exist. Above the cut-off frequency $\omega > \omega_*$, the wavenumber k (28a) has a real part:

$$k = - i/2L \pm K, \quad K \equiv (\omega/c) \sqrt{1 - \omega_*^2/\omega^2}, \quad (29a, b)$$

and propagation is possible, so that the cut-off frequency ω_* (28b) separates the standing ($\omega < \omega_*$) and propagating ($\omega > \omega_*$) parts of the spectrum, and specifies the properties of the atmosphere as a filter of acoustic waves.

The quantity K defined by (29b) plays the role of an effective wavenumber, since by (29a):

$$\exp i\,(\,kz - \omega t\,) = \exp\,(\,z/2L\,)\cdot\exp i\,(\,Kz - \omega t\,) \qquad (30)$$

it determines the phase $Kz - \omega t$ of a propagating wave $\omega > \omega_*$. The effective wavenumber K (29b) simplifies to the acoustic form $K \sim \omega/c$ for frequencies much higher than the cut-off $\omega^2 >> \omega_*^2$, is smaller than the acoustic value $K < \omega/c$ for intermediate frequencies $\omega > \omega_*$, and vanishes $K = 0$ at the cut-off $\omega = \omega_*$ when propagation becomes impossible. The phase speed u and group velocity w corresponding to the effective wavenumber K (29b):

$$u \equiv \omega/K = c\,\{\,1 - \omega_*^2/\omega^2\,\}^{-1/2}, \qquad (31a)$$

$$w \equiv \partial\omega/\partial K = c\,\{\,1 - \omega_*^2/\omega^2\,\}^{1/2}; \qquad (31b)$$

coincide with the sound speed $u \sim c \sim w$ only at high-frequencies $\omega^2 >> \omega_*^2$; at intermediate frequencies $\omega > \omega_*$ the phase speed is higher than the sound speed and the group velocity lower $u > c > w$. At the cut-off $\omega = \omega_*$ the phase speed diverges $u \to \infty$ since the wave ceases to oscillate and wavecrests disappear, and the group velocity vanishes $w \to 0$ since the energy flux vanishes for standing modes. The factor $\exp\,(\,z/2L\,)$ shows that the amplitude of acoustic waves grows exponentially on twice the density scale height in an isothermal atmosphere, and thus, even if the initial amplitude is small, after propagating a few scale heights the waves grow to finite amplitude, so that non-linear effects become important and shock formation may occur. This law of amplitude growth can also be obtained from energy conservation, bearing in mind that the sound speed is constant in an isothermal atmosphere: (i) the equipartition of kinetic and compression energies at all altitudes implies that the total energy $E = \rho v^2$ is twice the kinetic part, and the energy flux is $F = Ec = \rho v^2 c$; (ii) since the energy flux must be conserved for a non-dissipative

wave $v \sim \rho^{-1/2}$, and as the mass density decays exponentially on the scale height $\rho \sim \exp(-z/L)$ the wave velocity perturbation grows exponentially on twice that scale $v \sim \exp(z/2L)$.

There is a considerable contrast between the properties of Alfvèn-gravity (§2) and acoustic-gravity (§3) waves, say, in an isothermal atmosphere: (i) the latter have a constant propagation speed, namely the sound speed c, whereas the former are accelerated with height at an exponentially increasing Alfvèn speed A (8a); (ii) the velocity perturbation increases linearly with altitude $v \sim z$ in the former (6a) and exponentially $v \sim e^{z/2L}$ in the latter (30) cases; (iii) for the former, the Alfvèn number $N \equiv v/A \sim z\, e^{-z/2L}$ reduces with altitude, whereas for the latter the Mach number $M \equiv v/c \sim e^{z/2L}$ increases with height; (iv) for the former a linear, non-homogeneous theory is appropriate, whereas for the latter a non-linear, homogeneous approach may be needed; (v) the latter satisfy equipartition of (kinetic and compression) energies at all altitudes, and the former violates the initial equipartition of (kinetic and magnetic) energies as it propagates upward. These contrasts for non-dissipative waves (Campos 1983a, b) extend to the dissipative modes (Campos 1983c, d), since: (vi) among the main dissipation mechanisms, viscous damping is effective on hydrodynamic and resistive damping on hydromagnetic waves; (vii) the electrical resistance depends mainly on temperature and is approximately constant in an isothermal atmosphere, whereas the kinematic viscosity, defined as the ratio of the static viscosity to the mass density increases with height as the atmosphere becomes more rarefied; (viii) resistive dissipation is important at low altitudes for Alfvèn waves, when their propagation speed is small, and becomes negligible at high-altitudes, whereas for acoustic modes viscous damping increases in importance as the kinematic viscosity grows with height, and is most significant at high altitudes.

The simple preceding example of the high-pass filtering of vertical acoustic-gravity waves in a magnetic field tube illustrates three general properties: (a) the filtering of waves in stratified media, e.g., three-dimensional acoustic-gravity waves have *two* cut-off frequencies (one vanishes in the case of vertical propagation outlined before), in atmospheres either nearly isothermal (Lamb 1879, Moore & Spiegel 1964, Yih 1965, Yeh & Liu 1974, Campos 1984a) or with strong temperature gradients (Lamb 1910, Groen

1948, Thorpe 1968, Lindzen 1970, Campos 1983a); (b) the propagation along tubes is also relevant in the acoustics of ducts of variable cross-section, either without a mean flow, such as the horns of loudspeakers and musical instruments (Webster 1919, Ballantine 1927, McLachlan 1934, Jordan 1963, Olson 1972, Zamorski & Myrzykowski 1981, Kergomard 1982, Bostrom 1983, Campos 1984c), or with a mean flow, such as the nozzles of jet engines (Powell 1959, Eisenberg & Kao 1969, Morfey 1971, Nayfeh, Kaiser & Telionis 1975, Nayfeh, Shaker & Kaiser 1980, Campos 1978, 1984d); (c) the growth in wave amplitude with altitude leads to non-linear waves and shock formation (Riemann 1860, Raiser & Zeldovitch 1966, Wentzel & Solinger 1967, Chiu 1971, Whitham 1974, Roberts & Rae 1982, Campos 1984e), which is oppposed and delayed by dissipative effects (Lighthill 1951, 1978; Yanowitch 1967a, b, 1969; Lyons & Yanowitch 1974; Campos 1983c, d). In these as in all other types of waves, it is possible to consider three types of propagation and dissipation theories: (I) for waves of small amplitude in media for which the propagation speed and damping rates are uniform, the wave equations are linear with constant coefficients, and can be solved by Fourier analysis, leading to the use of dispersion relations, as in the preceding example (§3) of acoustic-gravity waves in an isothermal atmosphere; (II) for waves of small amplitude in an inhomogeneous or strongly stratified medium, for which the speed of propagation and dissipation parameters are non-uniform, the wave equations are linear with variable coefficients, dispersion techniques are inadequate, and exact solutions must be obtained, often in terms of special functions, as illustrated in the case of resistive Alfvèn-gravity waves (§2); (III) for waves of large amplitude, which cause a disturbance in the medium of propagation comparable with the mean state, the wave equations are non-linear and the methods of superposition generally do not apply, and apart from cases of short wavelength where non-linear ray theory may be used, the derivation of exact solutions may depend on finding a special transformation into a known equation, as in the example which follows in the remaining part of the present section.

We consider as example a one-dimensional acoustic wave of finite amplitude, with dissipation by the kinematic viscosity η ,

for which the velocity v and density ρ are functions only of position z and time t , and satisfy the exact, non-linear equations of continuity and momentum:

$$\partial \rho / \partial t + v \, \partial \rho / \partial z + \rho \partial v / \partial z = o \qquad (32a)$$

$$\partial v / \partial t + v \, \partial v / \partial z + (c^2 / \rho) \, \partial \rho / \partial z = \eta \, \partial^2 v / \partial z^2 ; \qquad (32b)$$

in the latter we have substituted the pressure gradient $(\partial p / \partial z) = c^2 \, (\partial \rho / \partial z)$, where $c^2 = (\partial p / \partial \rho)_s$ is the adiabatic sound speed. Multiplying (32a) by $\pm c / \rho$ and adding to (32b), we obtain:

$$\{ \partial / \partial t + (v \pm c) \, \partial / \partial z \} \, J_+ = \eta \, \partial^2 v / \partial z^2 , \qquad (33a)$$

$$J_\pm \equiv v \pm \int (c / \rho) \, d \rho , \qquad (33b)$$

which can be interpreted as follows: (i) in the absence of viscosity $\eta = o$ and for linear waves $v \ll c$, from $J_+ \sim 2v$ and $\partial v / \partial t + c \, \partial v / \partial z = o$, it follows that the velocity perturbation $v (z , t) = f (z - ct)$ propagates at sound speed without deformation; (ii) in the non-linear case the Riemann invariants $J_\pm$ are conserved along the characteristics $\Gamma_\pm$, which are the 'trajectories' of the wave travelling at a speed $(dx / dt)_\pm = v \pm c$ equal to the superposition of the velocity v and sound speed $\pm c$, in the same or opposite direction; (iii) in the presence of viscosity $\eta \neq o$ the Riemann invariants $J_\pm$ (33b) decay along the characteristics $\Gamma_\pm$ since (33a) may be viewed as non-linear diffusion equations, and the wave profile is deformed by two opposing effects: steepening by non-linear convection and decay by viscous dissipation.

Considering a simple wave, for which the invariant J_- is zero, the invariant J_+ can be expressed in terms of the propagation speed $u \equiv v + c$, so that we obtain Burger's equation:

$$\partial u / \partial t + u \, \partial u / \partial z = (\eta / 2) \, \partial^2 u / \partial z^2 ; \qquad (34)$$

the latter balances the linear local and non-linear convective acceleration against dissipation by the kinematic viscosity halved, and apart from the factor 1/2 coincides with the one-dimensional form of Navier-Stokes equation. The equation (34) can be trans-

formed, by means of the change of variable (Burgers 1948, Cole 1951, Hopf 1951):

$$\Phi(z,t) = \exp\left\{-\eta^{-1} \int_{-\infty}^{z} u(y,t)\,dy\right\},\qquad (35a)$$

$$u(z,t) = -\eta\,\partial(\log\Phi)/\partial z,\qquad (35b)$$

into the linear heat equation:

$$\partial \Phi/\partial t = (\eta/2)\,\partial^2\Phi/\partial z^2,\qquad (35c)$$

of which many solutions are known (Fourier 1876, Carslaw & Jaeger 1946).

As an example of the use of the transformation (35a), we consider a velocity pulse of magnitude U emitted at altitude $z = 0$:

$$u(z,o) = U\delta(z),\ \Phi(z,o) = H(-z) + e^{-U/\eta}\,H(z),\quad (36a,b)$$

using the properties of Dirac's delta δ and Heaviside's unit H functions (Schwartz 1949, Lighthill 1958); the solution of the classical (Fourier 1876, Carlslaw & Jaeger 1946) heat problem (35c, 36b) specifies $\Phi(z,t)$ from which we may calculate $u(z,t)$ using (35b), viz.:

$$u(z,t) = (2\eta/\pi t)^{1/2}\left\{\exp(-z^2/2\eta t)/\mathrm{erfc}\ (z/\sqrt{(2\eta t)})\right\};\qquad (37a)$$

the pulse thus broadens with time to a scale $\chi \sim \sqrt{(2\eta t)}$, and asymptoticaly $z \to \infty$ as the error function erfc $\to 1$, it takes a pure Gaussian shape:

$$u \sim (2\eta/\pi t)^{1/2} \exp(-z^2/2\eta t) \sim (2\eta U/\pi z)^{1/2} \exp(-Uz/2\eta),\ (37b)$$

where in the second expression we have used $z/t \sim U$.

The dissipation by viscosity acts as a heat source (per unit volume):

$$Q(z) = \rho\eta(\partial v/\partial z)^2 = \left\{2\rho\eta/(\gamma+1)^2\right\}(\partial u/\partial z)^2$$
$$\sim \left\{\rho U^3/\pi(\gamma+1)^2 z\right\}\exp(-Uz/\eta),\qquad (38a)$$

Portgal. Phys. — Vol. 14, fasc. 3-4, pp. 145-173, 1983

165
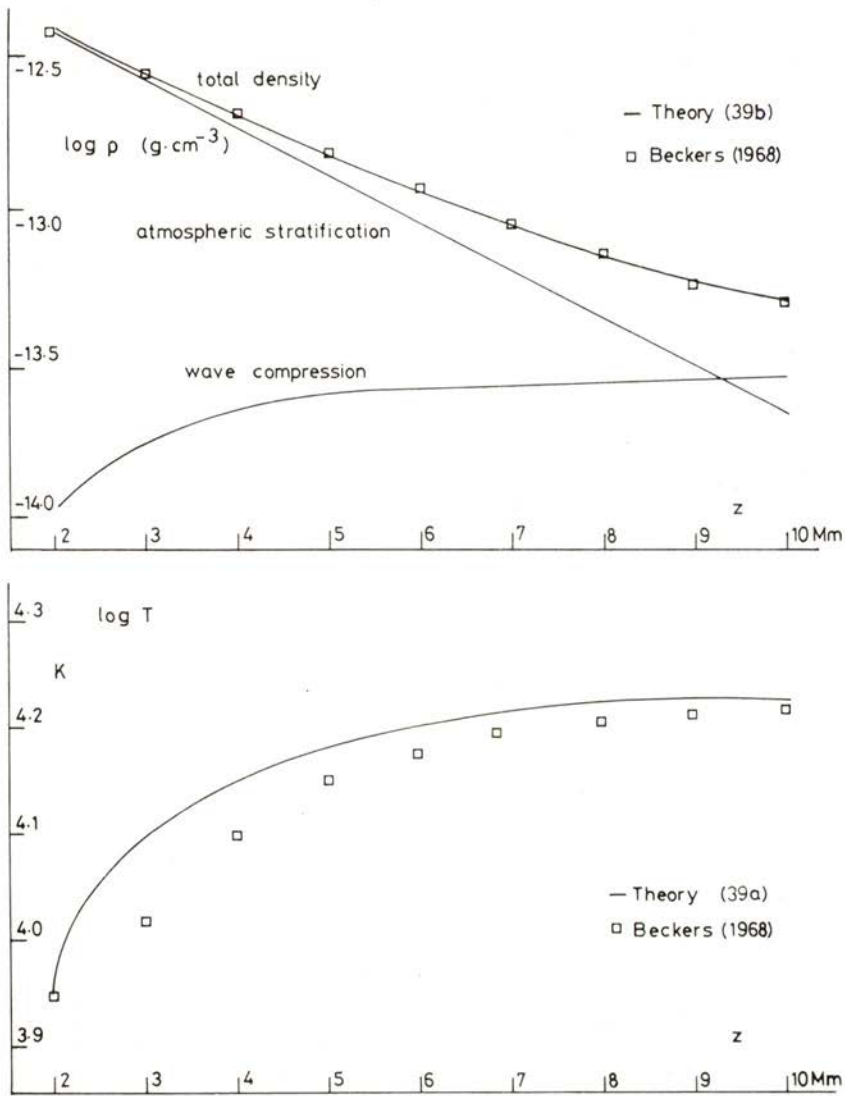
Fig. 3 — The theory of compression and heating of an atmosphere by acoustic waves of finite amplitude with viscous damping (solid line) is compared with observations (squares) in solar spicules. The temperature profile (bottom) shows an initial rise when the heating function (fig. 4, top) is larger, and levels--off as the latter decays with altitude. The total density profile (top) demonstrates the increasing contribution of the wave compression relative to the atmospheric stratification, showing that the presence of waves is essential to explain the observed total density.

which in a rarefied medium is balanced by the thermal radiation flux:

$$Q = dS/dz, \quad S = (16 \, \nu/3 \, \varepsilon) \ T^3 \ dT/dz, \qquad \text{(38b, c)}$$

which is proportional to the cube of temperature and temperature gradient through a factor involving Stefan-Boltzmann constant ν and the opacity ε. Integrating (38b) with (38a, c) we obtain the temperature profile of a medium in radiative equilibrium, heated by viscous dissipation of acoustic waves of finite amplitude:

$$\{T(z)\}^4 = \{T(z_0)\}^4 + (B/A) \ \{E_2(Az_0) - E_2(Az)\}, \qquad \text{(39a)}$$

where E_2 is the exponential integral of order 2 and $A \equiv U/\eta$, $B \equiv 3\rho U^3 \varepsilon/4\nu\pi(\gamma+1)^2$. The medium may be an atmosphere, provided that the stratification be gradual on the scale of the wave, and in this case the total mass density consists of: (i) the atmospheric stratification which decays exponentially on a scale D from its initial value ρ_1 at altitude z_0 ; (ii) a wave compression which increases from the initial value ρ_2 at altitude z_0 according to an adiabatic relation with temperature:

$$\rho(z) = \rho_1 \exp\{-(z-z_0)/D\} + \rho_2 \{T(z)/T(z_0)\}^{\gamma/(\gamma-1)}.$$

$$\text{(39b)}$$

The temperature and density profiles (39a, b) are plotted versus altitude in Fig. 3, showing satisfactory agreement with the observations (Beckers 1968, 1972) in spicules, which are regions of the sun (Bray & Loughhead 1974, Athay 1976) where matter moves upward towards the corona, compensating for the mass loss due to the solar wind. It can be seen that: (bottom) the temperature gradient reduces with altitude as viscous dissipation becomes weaker and thermal radiation more effective; (top) the wave compression gives an increasing contribution to the total density compared with the atmospheric stratification. The presence of the compression front due to the acoustic-gravity wave is thus essential to the adequate modelling of the density profile. The mass and energy transfer to the atmosphere can be related to the
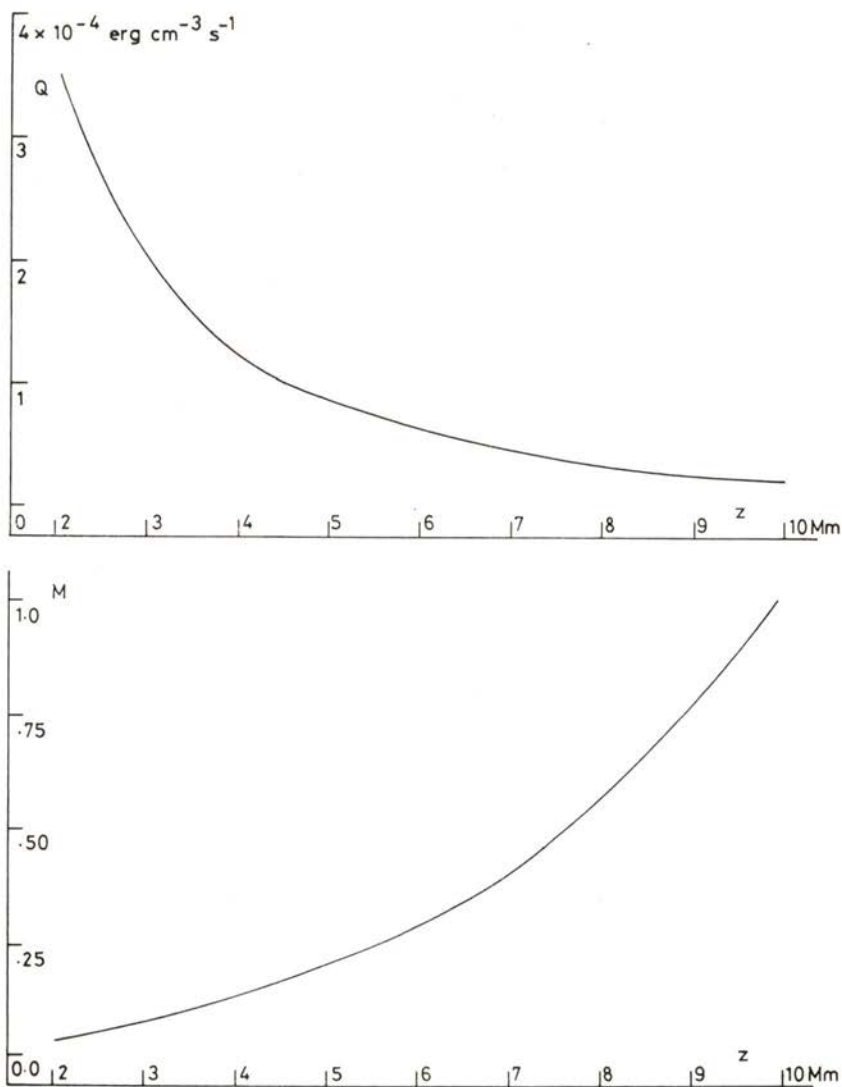
Fig. 4 — An acoustic wave tends to steepen its wavefront and form a shock due to non-linear effects, and this tendency is opposed by viscous dissipation, which extracts energy from the wave and transfers it to the medium in the form of heat. The heating function (top) specifying the rate of transfer of energy from the acoustic waves to the solar atmosphere decays with altitude, as there is less energy per unit volume left in the wave; in spite of this energy loss, the decaying atmospheric density implies that the wave compression becomes gradually more significant in relative terms, and the Mach number (bottom) increases steadily up to shock strength.

properties of the wave, shown in Fig. 4: (top) the heating function due to viscous dissipation decays with altitude, as the temperature levels-off (Fig. 3, bottom); (bottom) the Mach number $M \simeq v/c$ increases rapidly with altitude, as the wave compression becomes more significant compared with the atmospheric density (figure 3, top), showing the growth of the wave from small amplitude $M^2 \ll 1$ at low altitude to shock strength $M \sim 1$ at the top.

REFERENCES

ACHENBACH, J. D.   1973   *Elastic waves in solids.* North-Holland.

ADAM, J. A.   1977   On the occurrence of critical levels in solar magnetohydrodynamics. *Solar Phys.* **52**, 293-307.

ADAM, J. A.   1982   Asymptotic solutions and spectral theory of linear wave equations. *Phys. Rep.* **86**, 217-316.

AHMED, B. M. & ELTAYEB, I. A.   1978   On the propagation, reflexion, transmission and stability of atmospheric Rossby-gravity waves on the beta-plane in the presence of latitudinally sheared zonal flows. *Phil. Trans. Roy. Soc. Lond.* **A298**, 45-95.

AKASOFU, S. I. & CHAPMAN, S.   1972   *Solar-terrestrial physics.* Clarendon.

ALFVÈN, H.   1942   The existence of electromagnetic-hydrodynamic waves, *Ark. Mat. Astr. Fys.* **B29**, 1-7.

ALFVÈN, H.   1948   *Cosmical electrodynamics.* Oxford U. P.

ALFVÈN, H. & FALTHAMMAR, C. G.   1962   *Cosmical electrodynamics.* Oxford.

ATHAY, R. G.   1976   *The quiet sun.* D. Reidel, Dordrecht.

BALLANTINE, S.   1927   On the propagation of sound in the general Bessel horn of infinite length. *J. Franklin Inst.* **203**, 85-101.

BECKERS, J. M.   1968   Solar spicules. *Solar Phys.* **2**, 367-433.

BECKERS, J. M.   1972   Solar spicules. *Ann. Rev. Astron. Astrop.* **10**, 73-100.

BEER, T.   1974   *Atmospheric waves.* J. Wiley.

BOSTROM, A.   1983   Acoustic waves in a cylindrical duct with periodically varying cross-section. *Wave Motion* **5**, 59-67.

BOOKER, J. R. & BRETHERTON, F. P.   1967   The critical layer for internal waves in a shear flow. *J. Fluid Mech.* **27**, 513-539.

BRAY, R. J. & LOUGHHEAD, R. E.   1974   *The solar chromosphere.* Chapman & Hall.

BRETHERTON, F. P.   1966   Propagation of groups of internal waves in a shear flow. *Quart. J. Roy. Met. Soc.* **92**, 466-482.

BURGERS, J. M.   1948   A mathematical model illustrating the theory of turbulence. *Adv. Appl. Math.* **10**, 171-179.

CABANNES, H.   1970   *Theoretical magnetofluiddynamics.* Academic P.

CADY, W. G.   1946   *Piezo-electricity.* McGraw-Hill.

CAMPOS, L. M. B. C.   1977   On the generation and radiation of magneto-
-acoustic waves. *J. Fluid Mech.* **81**, 529-549.

CAMPOS, L. M. B. C.   1978   The spectral broadening of sound by turbulent
shear layers. Part 1: The transmission through turbulent shear layers.
J. Fluid Mech. **89**, 723-749.

CAMPOS, L. M. B. C.   1983a   On three-dimensional acoustic-gravity waves in
model non-isothermal atmospheres. *Wave Motion* **5**, 1-14.

CAMPOS, L. M. B. C.   1983b   On magnetoacoustic-gravity waves propaga-
ting or standing vertically in an atmosphere. *J. Phys.* **A16**, 417-437.

CAMPOS, L. M. B. C.   1983c   On waves in non-isothermal, compressible,
ionized and viscous atmospheres. *Solar Phys.* **82**, 355-368.

CAMPOS, L. M. B. C.   1983d   On viscous and resistive dissipation of hydro-
dynamic and hydromagnetic waves in atmospheres. *J. Méc. Theor Appl.*
(to appear in vol. **2**, n.º 6).

CAMPOS, L. M. B. C.   1984a   On anisotropic, dispersive and dissipative
wave equations. *Port. Math.* (to appear).

CAMPOS, L. M. B. C.   1984b   On the heating of the solar chromosphere
by hydromagnetic waves with a five-minute period. *Mem. Soc. Astron.
Ital.* (to appear).

CAMPOS, L. M. B. C.   1984c   Some general properties of the exact acoustic
fields in horns and baffles. *J. Sound Vibr.* (to appear in vol. **95**, n.º 2).

CAMPOS, L. M. B. C.   1984d   On the propagation of sound in nozzles of
variable cross-section containing low Mach number mean flows. *Zeits.
Flugwis. Weltraumf.* (to appear).

CAMPOS, L. M. B. C.   1984e   A new theory of solar spicules and the atmo-
spheric mass balance. *Month. Not. Roy. Astron. Soc.* (to appear in
vol. **206**, n.º 1).

CARSLAW, H. S. & JAEGER, J. C.   1946   *Conduction of heat in solids.* Oxford.
U. P., 2nd ed. 1959.

CHAPLYGIN, S. A.   1904   On gas jets. *Ann. Sci. Mosc. Imp. Univ. Math.
Phys. Sect.* **21**, 1-119 (*Werke* **3**, 18-137).

CHAPMAN, S. & COWLING, T. G.   1949   *Non-Uniform Gases* Cambridge U. P.,
3rd ed. 1970.

CHIU, Y. T.   1971   Arbitrary amplitude magneto-acoustic waves under
gravity: an exact solution. *Phys. Fluids* **14**, 1717-1724.

COLE, J. D.   1951   On quasi-linear parabolic equation ocurring in aerody-
namics. *Quart. Appl. Math.* **9**, 225-236.

COWLING, T. G.   1957   *Magnetohydrodynamics.* Interscience, 2nd ed. 1980.

ECKART, C.   1960   *Hydrodynamics of oceans and atmospheres.* Pergamon.

EISENBERG, N. A. & KAO, T. V.   1969   Propagation of sound through a
variable area duct with a steady, compressible mean flow. *J. Acoust.
Soc. Am.* **32**, 1640-1646.

ELTAYEB, I. A.   1977   Linear wave motions in magnetic-velocity shears.
Phil. Trans. Roy. Soc. Lond. **A285**, 607-630.

FERRARO, V. C. A.   1955   On the reflection and refraction of Alfvèn waves.
Astrop. J. **119**, 393-402.

FERRARO, V. C. A. & PLUMPTON, C.   1958   Hydromagnetic waves in an horizontally stratified atmosphere. *Astrop. J.* **129**, 459-476.

FERRARO, V. C. A. & PLUMPTON, C.   1961   *An introduction to magneto--fluid dynamics.* Oxford U. P., 2nd ed. 1966.

FOURIER, J. B.   1876   *Théorie analytique de la chaleur.* Dover 1950.

GOSSARD, E. & HOOKE, W.   1975   *Waves in the atmosphere.* Elsevier.

GROEN, P.   1948   Contribution to the theory of internal waves. *Kon. Ned. Met. Inst.* **B11**, 11-40.

HERLOFSON, N.   1950   Waves in a compressible fluid conductor. *Nature* **165**, 1020-1021.

HIDE, R.   1956   Waves in a heavy, viscous, incompressible, electrically conducting fluid of variable density, in the presence of a magnetic field. *Proc. Roy. Soc. Lond.* **A223**, 376-395.

HINES, C. O.   1974   *The upper atmosphere in motion.* Am. Geophys. Un., Washington.

HOLLWEG, J. V.   1972   Supergranulation-driven Alfvèn waves in the solar chromosphere and related phenomena. *Cosmic Electr.* **2**, 423-444.

HOPF, E.   1951   The partial differential equation $u_t + uu_x = u_{xx}$. *Comm. Pure Appl. Math.* **3**, 201-230.

HUDSON, J. A.   1980   *Excitation and propagation of elastic waves.* Cambridge U. P.

IONSON, J. A.   1982   Resonant electrodynamic heating of stellar coronal loops: an LRC circuit analog. *Astrophys. J.* **254**, 318-334.

JONES, D. S.   1964   *Electromagnetic theory.* Oxford U. P.

JORDAN, E. J.   1963   *Loudspeakers.* Focal Press, London.

KERGOMARD, J.   1982   Propagation des ondes dans les lignes finites: discussion des notions d'onde évanescente et de fréquence de coupure. *Rev. Phys. Appl.* **17**, 307-327.

KRAUS, E. B.   1977   *The upper layers of the ocean.* Oxford U. P.

LAMB, H.   1879   *Hydrodynamics.* Cambridge U. P., 6th ed. 1932.

LAMB, H.   1910   On the theory of waves propagated vertically in the atmosphere. *Proc. Lond. Math. Soc.* **7**, 122-141.

LANDAU, L. D. & LIFSHITZ, E. F.   1956   *Electrodynamics of continuous media.* Pergamon.

LEHNERT, B.   1952   On the behaviour of an electrically conducting liquid in a magnetic field. *Ark Fys.* **5**, 69-74.

LEROY, B.   1982   Propagation of waves in an atmosphere in the presence of a magnetic field: Alfvèn waves in the solar atmosphere. *Astron. Astrop.* **97**, 245-250.

LIGHTHILL, M. J.   1947   The hodograph transformation in transsonic flow: I. Symmetrical channels. *Proc. Roy. Soc. London.* **A190**, 323-344.

LIGHTHILL, M. J.   1951   Viscosity effects on sound waves of finite amplitude. *Surveys in Mechanics* 250-351, Cambridge U. P.

LIGHTHILL, M. J.   1958   *Fourier Analysis and generalized functions.* Cambridge U. P.

LIGHTHILL, M. J.   1960   Studies in magnetohydrodynamic waves and other anisotropic wave motions. *Phil. Trans. Roy. Soc. Lond* **A252**, 397-430.

LIGHTHILL, M. J.   1978   *Waves in fluids.* Cambridge U. P.

LINDZEN, R.   1970   Internal gravity waves in atmospheres with realistic dissipation and temperature. Part I: Mathematical development and propagation of waves into the thermosphere. *Geop. Astrop. Fluid Dyn.* **1**, 303-355.

LOVE, A. E. H.   1927   *Mathematical theory of elasticity.* Cambridge U. P.

LYONS, P. & YANOWITCH, M.   1974   Vertical oscillations in a viscous and thermally conducting atmosphere. *J. Fluid Mech.* **66**, 273-288.

MCKENZIE, J. F.   1973   On the existence of critical levels, with application to hydromagnetic waves. *J. Fluid Mech.* **58**, 709-726.

MCLACHLAN, N. W.   1934   *Loudspeakers.* Oxford U. P.

MISES, R. v.   1960   *Mathematical theory of compressible fluid flow.* McGraw-Hill.

MOLENBROEK, P.   1890   Ueber einige Bewegungen eines Gases bei Annahme einer Geschwindigkeitspotentials. *Grunert's Arch. Math. Phys.* **9**, 157--195.

MOORE, D. W. & SPIEGEL, E. A.   1964   The generation and propagation of waves in a compressible atmosphere. *Astrop. J.* **139**, 48-64.

MORFEY, C. L.   1971   Sound transmission and generation in ducts with flow. *J. Sound Vib.* **14**, 37-55.

NAYFEH, A. H., KAISER, J. E. & TELIONIS, D. P.   1975   Acoustics of aircraft engine-duct systems. *A.I.A.A. Journ.* **13**, 130-153.

NAYFEH, A. H., SHAKER, B. E. & KAYSER, J. E.   1980   Transmission of sound through non-uniform circular ducts with compressible mean flows. *A.I.A.A. Journ.* **18**, 515-525.

NYE, A. H. & THOMAS, J. H.   1976   Solar magneto-atmospheric waves. I. Exact solution for a horizontal magnetic field. *Astrop. J.* **204**, 573-581.

OLSON, H. F.   1972   *Modern sound reproduction.* Van Nostrand.

OSTERBROCK, D. E.   1961   The heating of the solar chromosphere, plages and corona by magnetohydrodynamic waves. *Astrop. J.* **140**, 347-388.

PARKER, E. N.   1979   *Cosmical magnetic fields.* Oxford U. P.

PEDLOSKY, J.   1979   *Geophysical fluid dynamics.* Springer-Verlag.

PHILIPS, O. M.   1960   *The dynamics of the upper ocean.* Cambridge U. P., 2nd ed. 1979.

POWELL, A.   1959   Propagation of a pressure pulse in a compressible flow. *J. Acoust. Soc. Am.* **31**, 1527-1535.

PRIEST, E. R.   1982   *Solar magnetohydrodynamics.* D. Reidel, Dordrecht.

RAISER, Y. P. & ZELDOVICH, Y. B.   1966   *Physics of shock waves and high--temperature hydrodynamic phenomena.* Academic P.

RIEMANN, B.   1860   Ueber die Fortpflanzung Ebener Luftwellen von Endlicher Schwingungsweite. *Ges. Werke* 156-175.

ROBERTS, B. & RAE, I. C.   1982   Pulse propagation in a magnetic flux tube. *Astrop. J.* **256**, 761-767.

RUDRAIAH, N. & VENKATACHALAPPA, M.   1979   Propagation of hydromagnetic waves in a perfectly conducting non-isothermal atmosphere in the presence of rotation and a variable magnetic field. *J. Fluid Mech.* **89**, 785-792

SCHOUTEN, J. A.   1953   *Tensor analysis for physicists.* Cambridge U. P.

SCHWARTZ, L.   1949   *Théorie des distributions.* Hermann, 2ème ed. 1973.

Spitzer, L.   1952   *Physics of fully ionized gases.* Interscience.

Stoker, J. J.   1953   *Water waves.* Interscience.

Thorpe, S. A.   1968   On the shape of progressive internal waves. *Phil. Trans. Roy. Soc. Lond.* **A263**, 563-614.

Uchida, Y. & Kaburaki, O.   1975   Excess heating of the corona and chromosphere above magnetic regions by non-linear Alfvèn waves. *Solar Phys.* **35**, 451-465.

Yanowitch, M.   1967a   Effect of viscosity on gravity waves and the upper boundary condition. *J. Fluid Mech.* **29**, 209-231.

Yanowitch, M.   1967b   Effect of viscosity on vertical oscillations of an isothermal atmosphere. *Can. J. Phys.* **45**, 2003-2008.

Yanowitch, M.   1969   A numerical study of vertically propagating waves in a viscous isothermal atmosphere. *J. Comp. Phys.* **4**, 531-542.

Yeh, K. C. & Liu, C. H.   1974   Acoustic-gravity waves in the upper atmosphere. *Rev. Geop. Space Phys.* **12**, 193-216.

Yih, C. S.   1965   *Dynamics of non-homogeneous fluids.* Mac-Millan.

Webster, A. G.   1919   Acoustical impedance and the theory of horns and of the phonograph. *Proc. Nat. Acad. Sci.* **5**, 275-282.

Wentzel, D. G. & Solinger, A. B.   1967   On the motion of shocks through the solar chromosphere. *Astrop. J.* **148**, 914-925.

Whitham, G. B.   1974   *Linear and non-linear waves.* Interscience.

Zamorski, T. & Wyrzykowski, R.   1981   Approximate methods for the solution of the equation of acoustic wave propagation in horns. *Arch. Acoust.* **6**, 237-255.

Zhugzhda, Y. D.   1971   Low frequency oscillatory convection in the strong magnetic field. *Cosmical Electr.* **2**, 267-279.
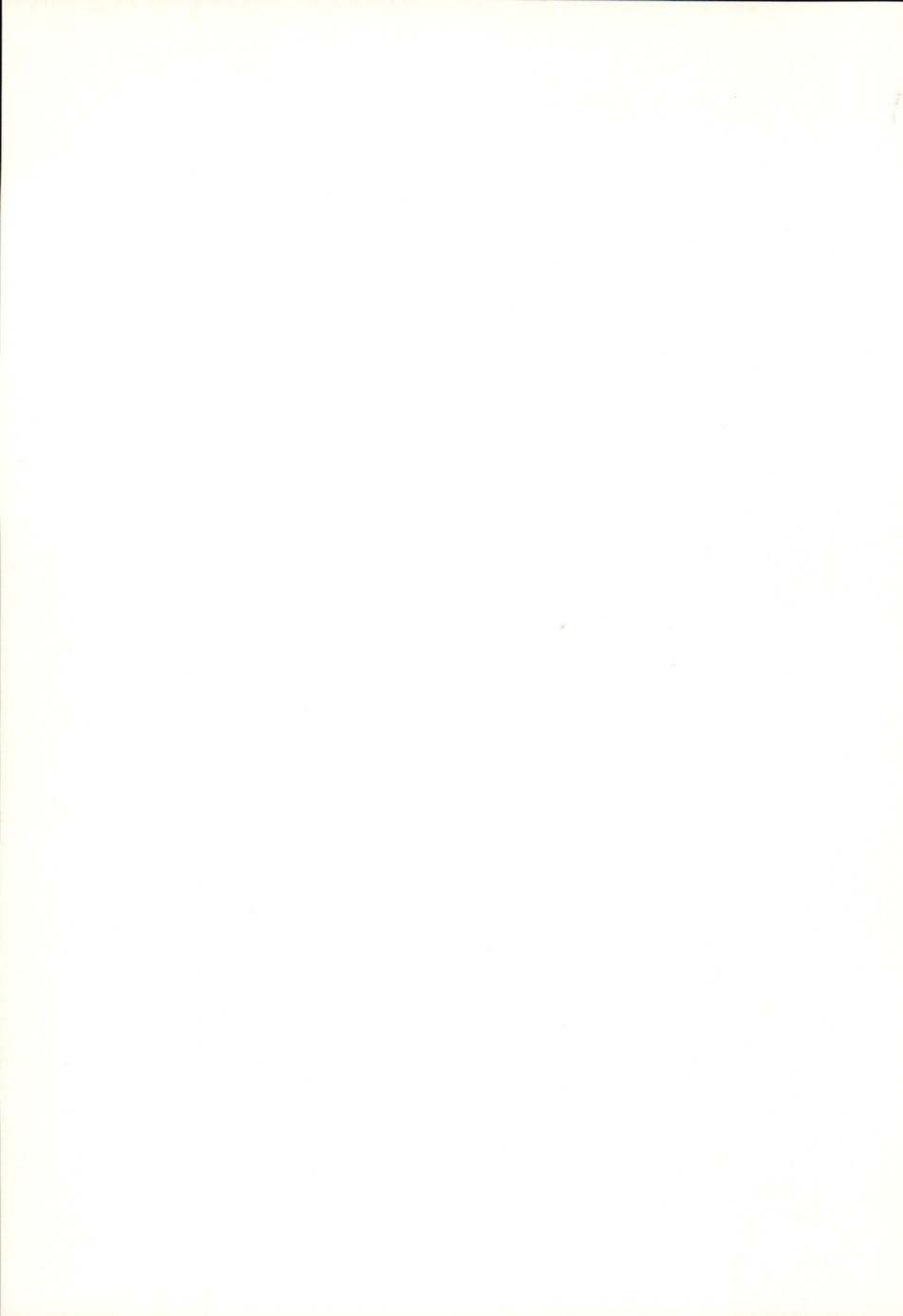
LATTICE LOCATION STUDIES OF HEAVY IONS IMPLANTED IN MAGNESIUM

M. R. DA SILVA, A. MELO and J. C. SOARES

Centro de Física Nuclear da Universidade de Lisboa, Portugal

E. ALVES and M. F. DA SILVA

Departamento de Física, LNETI, Sacavém, Portugal

P. M. J. WINAND and R. VIANDEN

Institut für Strahlen und Kernphysik, University of Bonn, FRG

ABSTRACT — The Rutherford backscattering channeling technique has been used to study the quality of magnesium single crystals for lattice location measurements. First results using Hf, Au, Tl and Pb atoms implanted in magnesium are presented and discussed. Particular relevance is given to the experimental set-up.

1 — INTRODUCTION

It is well known that defects such as vacancies or interstitials might modify many properties of materials. In most of the cases, however, it is not possible to predict the result of the creation of defects or their behaviour under various parameters like the temperature.

Defects might be introduced in materials using classical methods. Ion implantation, however, increasingly used in recent years, has become a more powerful and versatile alternative. In particular, it allows the simulation of production of unwanted effects present in research and power reactors and in the walls of plasma containers used in the development of fusion reactors.

In the present work the first results of a systematic investigation of defects in magnesium are presented. The defects are

introduced by implanting heavy ions in magnesium single crystals, and the Rutherford backscattering-channeling technique is used for the analysis.

Special relevance is given in this work to the experimental apparatus and analysing technique, including the preparation of samples, the orientation of the single crystals and the location of the implanted impurities.

Preliminary results obtained with the Hf, Au, Tl, and Pb impurities implanted in magnesium are presented and discussed.

2 — MEASUREMENT TECHNIQUE AND EXPERIMENTAL PROCEDURE

2.1 — *The Rutherford-Backscattering (RBS) / Channeling Technique*

If a beam of positive ions with energy E_0 impinges on the surface of a solid, Rutherford scattering occurs and the energy
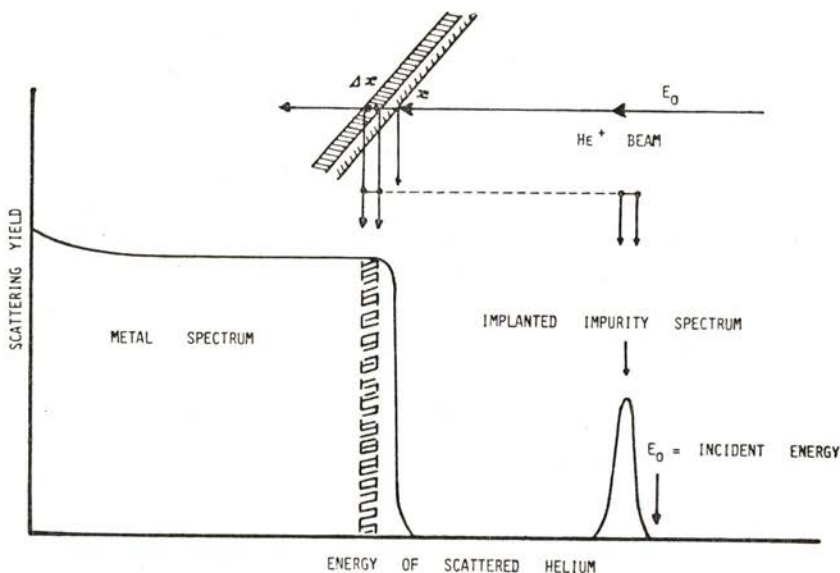
Fig. 1 — Schematic diagram of the He+ backscattered from a light metal implanted with a heavy impurity.

of the particles scattered at an angle relative to the beam direction is given by $E = k^2 E_0$. The kinematic factor, k, depends on the scattering angle and on the masses of the incident beam and target atoms.

Fig. 1 shows, schematically, the energy spectrum of He^+ ions scattered from the surface of a metal implanted with a heavy impurity.

The strong dependence of E on the mass of the scattering nucleus makes the RBS technique very useful to distinguish different elements in the near surface region of the solids. Further, the continuous energy loss of the in and outgoing ions, mainly due to the interaction with the electrons of the solid, allows the conversion of the energy scale to a depth scale. Thus, depth profiles of impurities in solids can easily be obtained.

If in the magnesium crystal heavy impurities like Hf, Au, Pb or Tl are dissolved, the ions scattered from these impurities have higher energies than those scattered from the Mg atoms making this method very sensitive for the qualitative and quantitative analysis of these impurities. For impurities concentrated in a layer near the surface, this technique gives with accuracy the thickness of the layer and the depth at which the layer is located [1].

Atoms lighter than magnesium, like oxygen and carbon, can also be detected with this technique. However, the sensitivity is poorer due to the lower Rutherford yield and to the fact that these impurities appear as peaks superimposed on a continuous magnesium RBS spectrum.

Fig. 2 shows RBS spectra of a magnesium single crystal with implanted lead. Apart from impurities like Si, P and Ca, it can be seen that at the surface of the magnesium two thin layers of oxygen and carbon are present and their thicknesses are calculated to be less than 100 Å.

When a sufficiently collimated ion beam is directed along a major symmetry direction of a single crystal, like the $< 11\bar{2}0 >$ axis of the Mg crystal shown in Fig. 2, a strong reduction of the Rutherford backscattering yield is observed. This is due to a reduced collision probability of the ions with the target nuclei. The repulsive potential of the lattice atoms steers the ions which

have a very low transverse momentum away from the rows or planes of the crystal atoms. This phenomenon is called the «Channeling effect» [2].
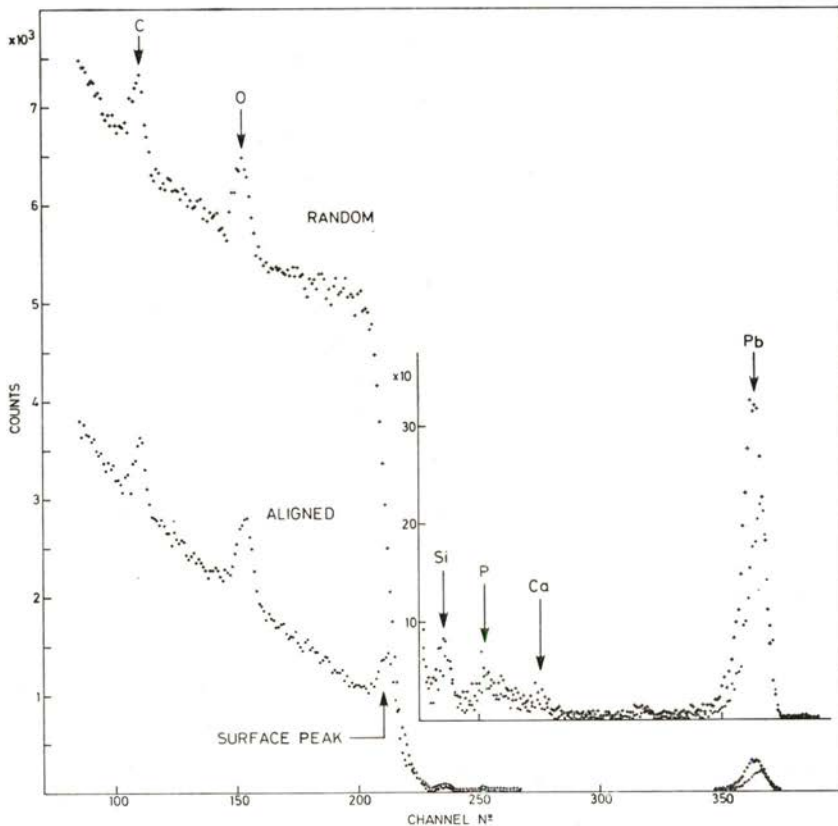
Fig. 2 — RBS spectra of a magnesium single crystal under ramdom and aligned orientation with respect to the beam axis.

2.2 — *Sample preparation*

The magnesium samples used in this work were 12 mm diameter by 2 mm thick disks, spark cut approximately normal to the axis $< 10\bar{1}0 >$ of a magnesium single crystal. They were cleaned by chemical etching in HNO_3 (65 %, P. A.), rinsed with water and dried.

The quality of the crystals was studied with the RBS channeling technique. From typical spectra as shown in Fig. 2, the concentration of the impurities remaining in the sample after cleaning can be obtained. Most of these residual impurities do not interfere with the heavy implanted impurities we intend to study in this work.

The implantation of the single crystals was performed using the electromagnetic mass separator of the Institut für Strahlen-und Kernphysik der Universität Bonn. The magnesium crystal was mounted on a support isolated from the implanting chamber evacuated to a pressure better than 5×10^{-6} mbar. During the implantation, the ion beam current was controlled and kept as low as possible to reduce heating effects on the crystals. The standard implantation energy used in this work was 80 keV for single charged ions. The implanted doses were in the range of 1 to 5×10^{14} atom/cm². Some samples implanted with the highest dose showed some darkening at the surface after implantation.

2.3 — *Experimental set-up*

The measurements were performed at the 2 MeV Van de Graaff accelerator of the LNETI, Sacavém. The 1.2 MeV He⁺ beam is collimated by two circular tantalum diaphragms (1 mm diameter) at a distance of 230 cm. The maximum beam divergence is 0.045° and the beam spot size at the target about 1 mm². The beam current is kept at a value of the order of 4×10^{-9} A to avoid radiation damage of the crystal during the measurements.

The samples are mounted in a two axis goniometer described below, located inside the scattering chamber (Fig. 3). This chamber is evacuated by means of a turbo-molecular pump to a pressure better than 10^{-6} mbar. The sample holder is surrounded by a copper shield cooled to liquid nitrogen temperature to reduce surface contamination during the experiment. A secondary electron suppression shield around the sample allows an accurate charge measurement by integration of the beam current on the sample.

The backscattered particles are counted with two silicon surface barrier detectors: a 100 mm² annular detector placed at 180° with an energy resolution of about 25 keV, and a 50 mm²

detector positioned at a scattering angle of 140° and with a resolution of 15 keV. The signals of both detectors are analysed and stored in a multichannel analyser with pile up rejection facilities.
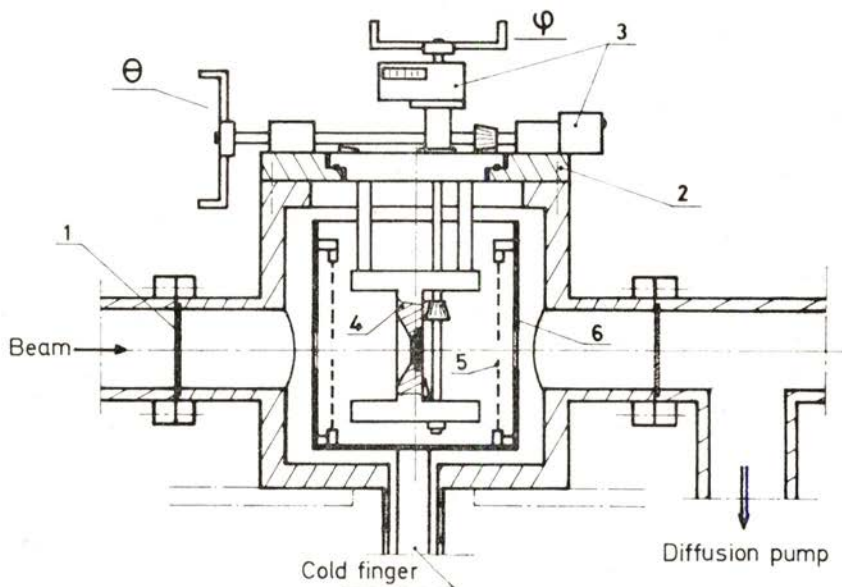
Fig. 3 — Scattering chamber: 1. diaphragm; 2. chamber lid with the goniometer; 3. θ and φ counters; 4. sample holder; 5. electrostatic shield; 6. thermal shield.

The two axis goniometer built at the ISKP-Bonn University allows the orientation of the single crystals with respect to the beam direction with a positional accuracy of 0.01° around the vertical axis and 0.02° around the horizontal axis. This goniometer, shown in Fig. 4, allows tilt motions of 360° around the two axes. The settings are read in two mechanical counters. The linearity of the counters and the accuracy to reproduce a setting better than 0.01° was tested using a laser beam reflected in a mirror mounted in the position of the sample. With this goniometer the crystal can be set in different orientations relative to the direction of the incident collimated beam. When rotating the crystal around the vertical axis the only restriction is the shadow of the crystal support on the particle detectors. A rotation of 180° around the vertical axis is particularly useful for investigations using not too

thick crystals. After this rotation the backside of the crystal can be studied and the accuracy of the goniometer can be tested.

The zero of the goniometer, $\theta = 0$, is defined as the angle in which both the direction of the beam and the rotation axis are coincident. This zero has been determined by two different methods: a) using a front silvered mirror mounted in the sample
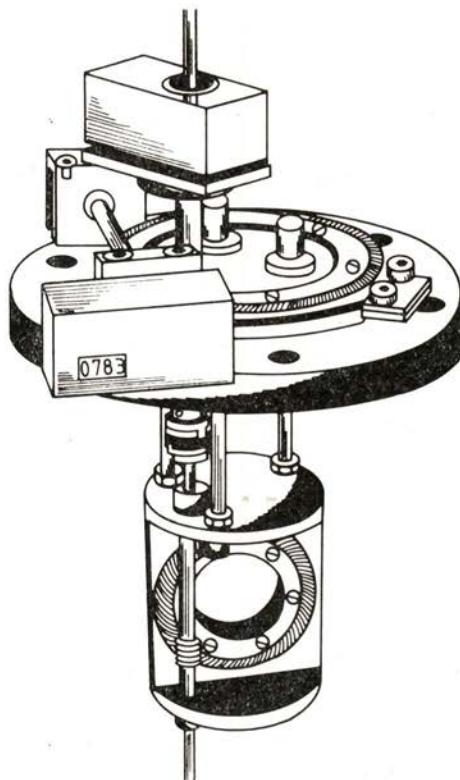
Fig. 4 — Goniometer built at the ISKP — Bonn University with drawings from M. A. Augustiniak (Bell Lab.) adapted by W. Schaub (ISKP).

holder and with the aid of a theodolit, a "pin point" was aligned with the beam. The $\theta = 0$ position was the one when both the "pin point" and its image were coincident in the theodolit axis; b) the other method was based on the fact that the same channeling direction is found when the crystal orientation is changed from (θ, φ) to $(-\theta, \varphi + 180°)$. Fig. 5 shows the

results of these measurements for the (0001) symmetry plane of a magnesium crystal.

With both methods the same zero value was found with an accuracy of 0.02°.
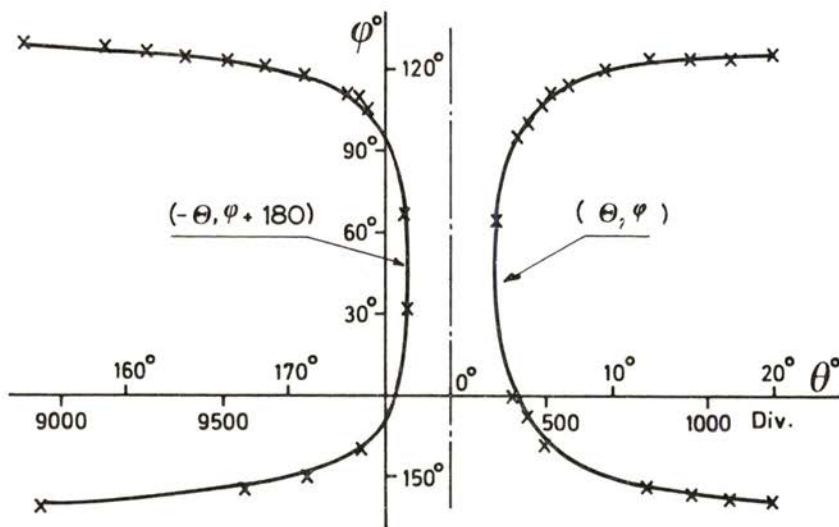
Fig. 5 — Coordinates of the (0001) plane near normal incidence for $+ \theta$ and $- \theta$.

2.4 — *Experimental Procedure*

Typical energy spectra of He$^+$ ions backscattered from a Mg single crystal are shown in Fig. 2, for a random and for a major symmetry direction. The aligned spectrum shows clearly the so called "surface peak" due to the first atomic layers of the crystal.

In channeling measurements windows are set in the RBS spectra to select particles scattered from the implanted impurity and from the magnesium host at the depth of the implanted layer.

The RBS yield of the Mg host, inside the window, as a function of the angle between a crystalographic direction and the beam direction shows a dip with a minimum in the channeling direction (Fig. 6). The yield at this minimum relative to a random yield is the χ_{min}. The critical angle, $\psi_{1/2}$, is determined from the
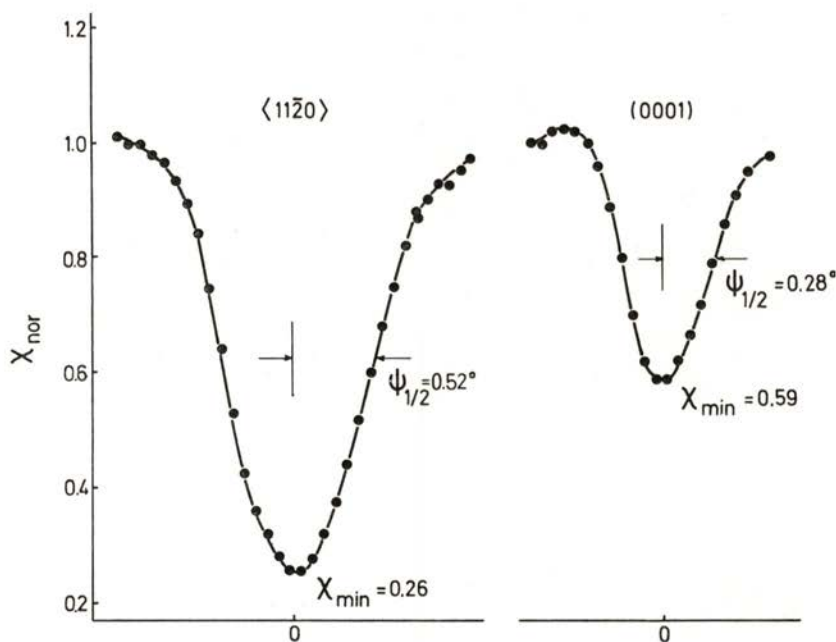
Fig. 6 — Axial and planar angular scans for the not implanted magnesium single crystal.

channeling angular scan by the half width at a level halfway between the minimum yield and the random level. These parameters, χ_{min} and $\psi_{1/2}$, are two characteristic quantities for channeling. They give information on the quality of the crystal and on the lattice location of impurities. The smaller χ_{min} is, the more perfect is the crystal. Any perturbation of the lattice will increase χ_{min}. The angle $\psi_{1/2}$ characterizes the "openness" of the channel.

To control possible effects of radiation damage and surface contamination of the crystal during the measurement sequence, the scans are normally done in two halves comparing the minimum yield obtained at the beginning with that at the end of the scan. Corrections are made, when necessary, for the shift in the energy, due to the accumulation of a carbon layer at the surface, during the experiment.

The comparison of the measured dips with the theoretical predictions [3] gives information on the crystal lattice perfection
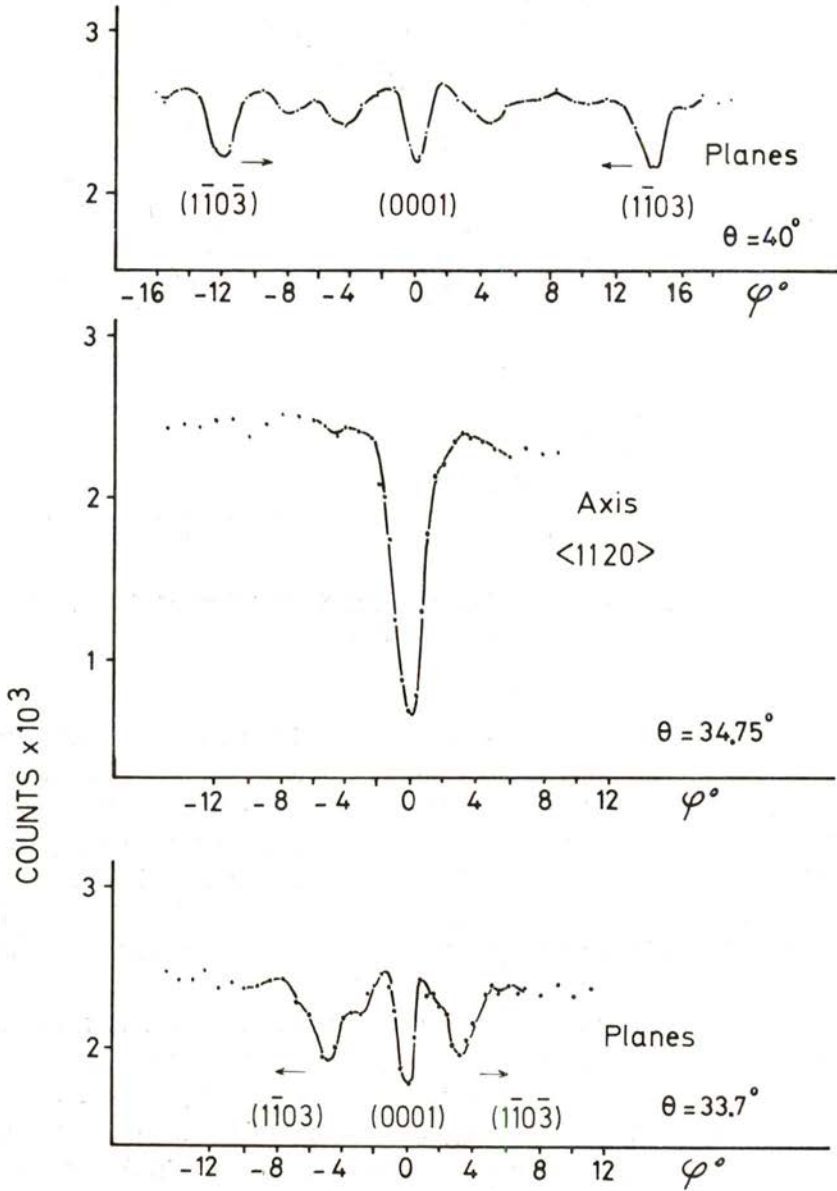
Fig. 7 a) — Scan for three different values of θ; yields not normalized.

184

Portgal. Phys. — Vol. 14, fasc. 3-4, pp. 175-193, 1983

and on the experimental set-up misalignment. The comparison of the dips corresponding to the single crystal with those of the implanted impurities gives information about the impurity location in the crystal matrix.

In a lattice location measurement the first step is to orientate the single crystal with respect to the beam direction. Though not essential, it is useful to know the approximate orientation of a major axis prior to the alignment of the crystal. This information can be obtained from X-ray diffraction measurements. In this circumstance the procedure to find one axial direction (in this case the $<11\bar{2}0>$ axis of the Mg crystal) is schematically represented in Fig. 7a. For two positions of constant θ ($\theta_1 = 40°$, $\theta_2 = 33.7°$) a scan is done by varying φ. Several planar dips are seen corresponding to the ($1\bar{1}0\bar{3}$), (0001) and ($1\bar{1}03$) planes. The intersection of these planes on a stereographic projection determines the location of the $<11\bar{2}0>$ axis which is confirmed by the axial angular scan as represented in Fig. 7b.
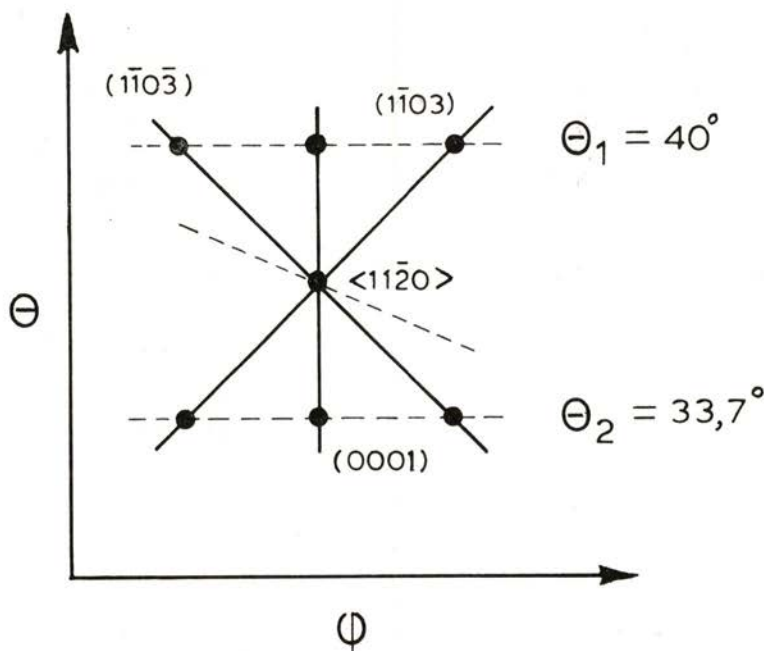
Fig. 7 *b*) — Stereographic projection to find the $<11\bar{2}0>$ coordinates.

The correct identification of other axes is confirmed by the agreement of the calculated values with the experimental ones for the angles between the axes. The stereographic projection of the main directions found for the magnesium crystal, which belongs to the hexagonal closed packed (hcp) configuration, is shown in Fig. 8.
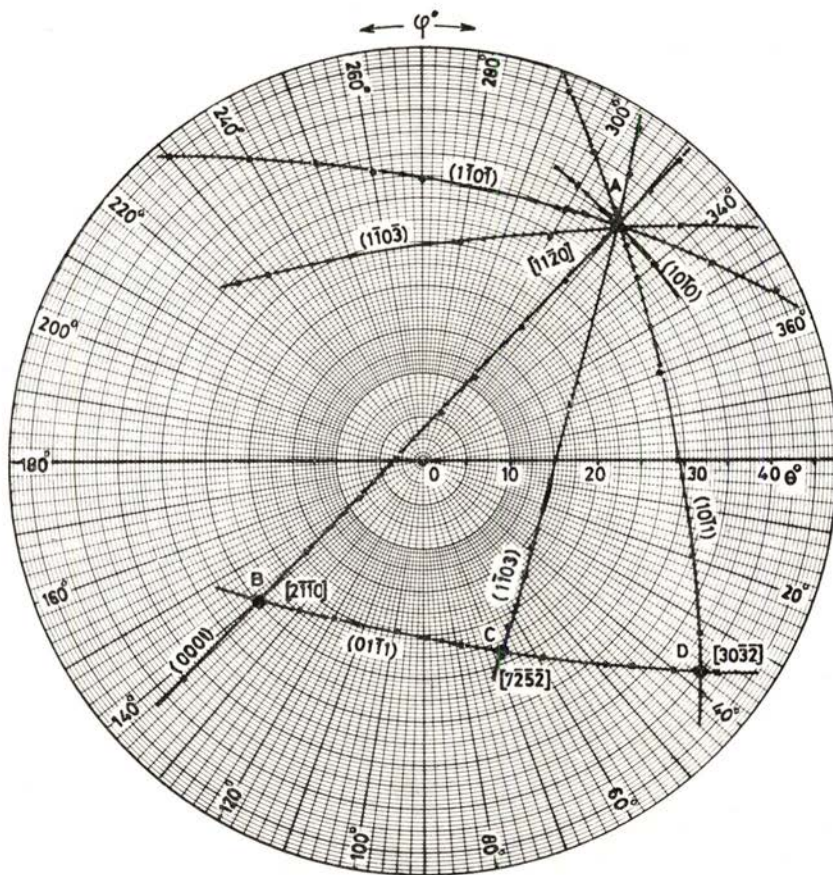
Fig. 8 — Stereographic projection of the main directions for the magnesium crystal.

3 — RESULTS AND DISCUSSION

Table 1 shows the channeling parameters obtained for several crystalographic directions of the magnesium single crystal. The theoretical predictions are also included for comparison. There is a fair agreement for the $\psi_{1/2}$ parameter. The high values obtained for χ_{min} means the existence of some disorder at the magnesium surface. In particular, the observed layers of carbon and oxygen can explain this fact. However, the magnesium crystal shows enough quality for studies of defects using ion implanted heavy impurities.

Experimental and theoretical values of channeling parameters for the magnesium single crystal

	$\psi_{1/2}$		χ_{min}	
	Exp.	Theor.	Exp.	Theor.
$<11\bar{2}0>$	0.52 ± 0.05	0.59	0.26 ± 0.05	0.05
$<10\bar{1}0>$	0.48 ± 0.05	0.45	0.35 ± 0.06	0.08
(0001)	0.28 ± 0.03	0.28	0.59 ± 0.10	0.26

The measured axial and planar angular scans for Hf and Pb are shown in Fig. 9, 10 and 11. The data are normalized such that the average value of the scattered yield off the channeling direction is unity.

The good coincidence between the Hf and the Mg scans for the major directions (Fig. 9) indicate total occupancy of substitutional sites by the Hf atoms in the host lattice.

This does not occur with the lead impurity (Fig. 10). Similar scans along the $<10\bar{1}0>$ axial direction and the $(10\bar{1}0)$ plane shown in Fig. 11 were also measured. These results indicate that only a fraction of about 50 % of lead impurity is substitutional in magnesium. The remaining fraction is probably randomly located in the oxide layer at the magnesium surface.
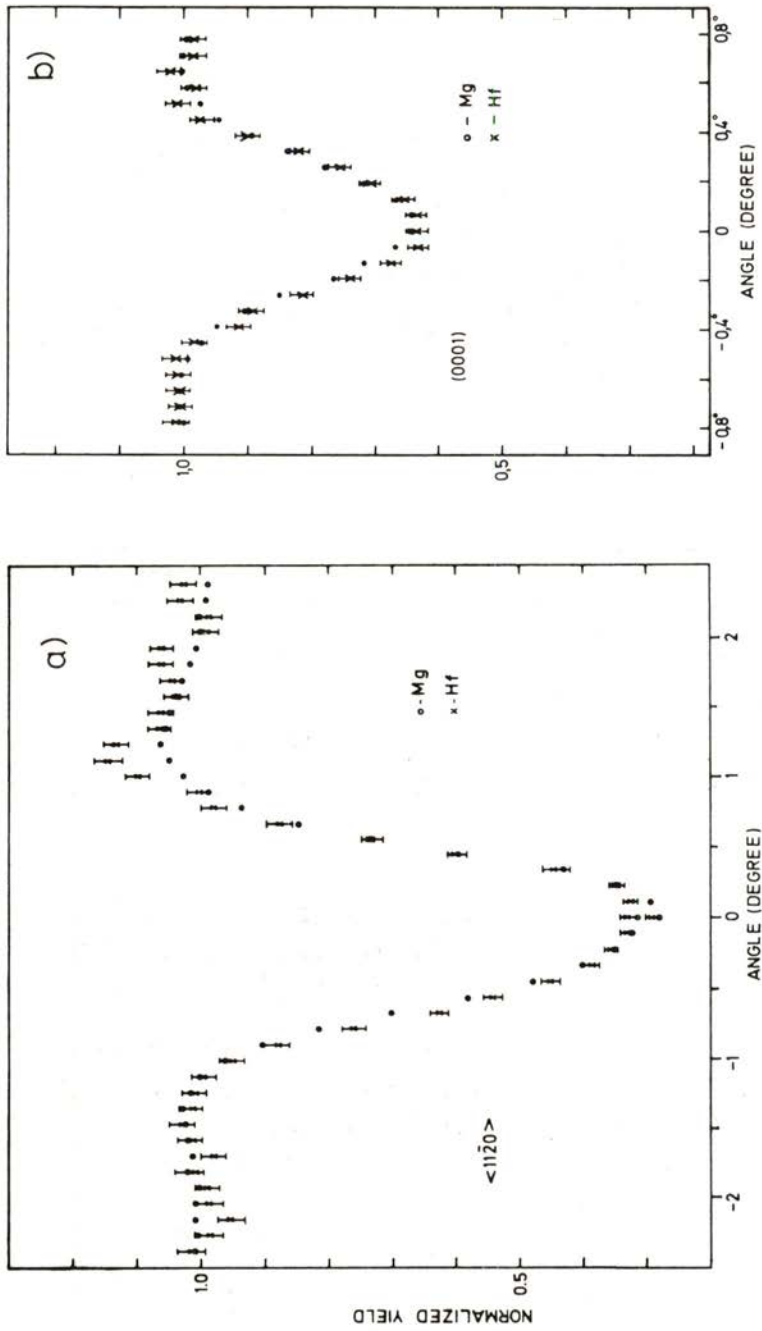
Fig. 9 — *a*) Angular scan curves along the <1120> axial direction for Hf in Mg. *b*) idem for the (0001) plane

188

Portgal. Phys. — Vol. 14, fasc. 3-4, pp. 175-193, 1983
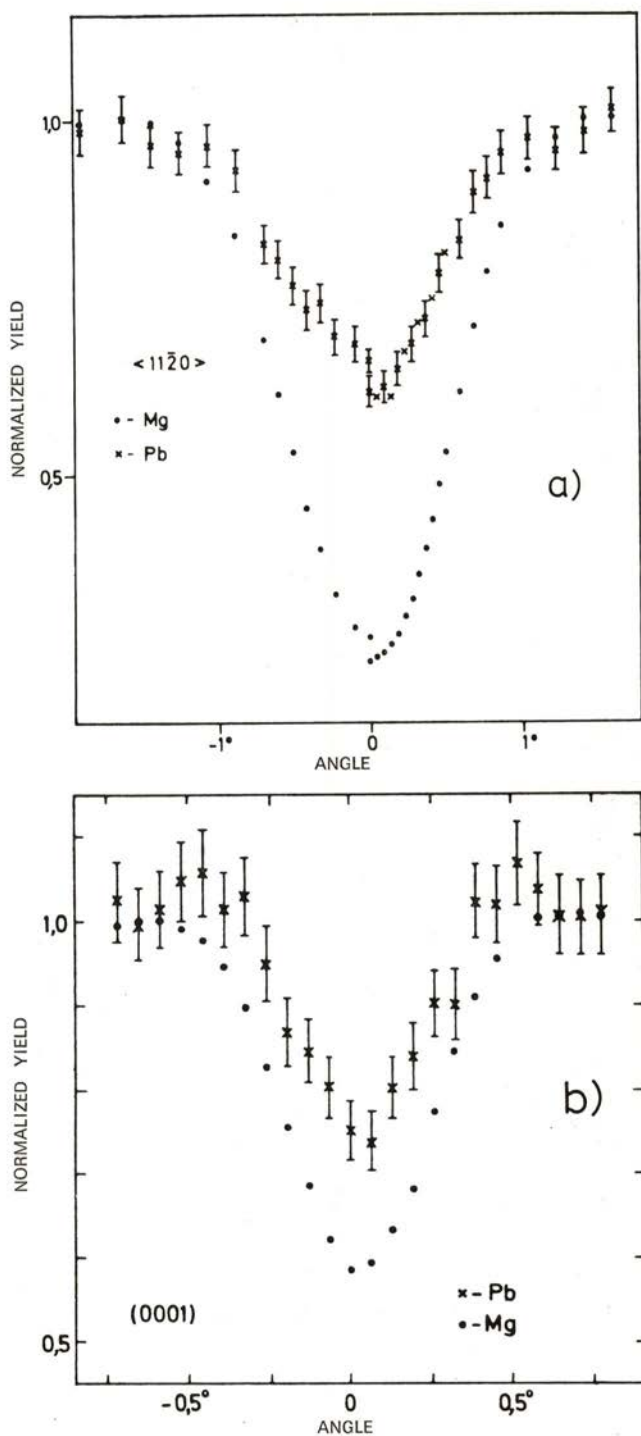
Fig. 10 — a) Angular scan curves along the <11$\bar{2}$0> axial direction for Pb in Mg. b) idem for the (0001) plane.
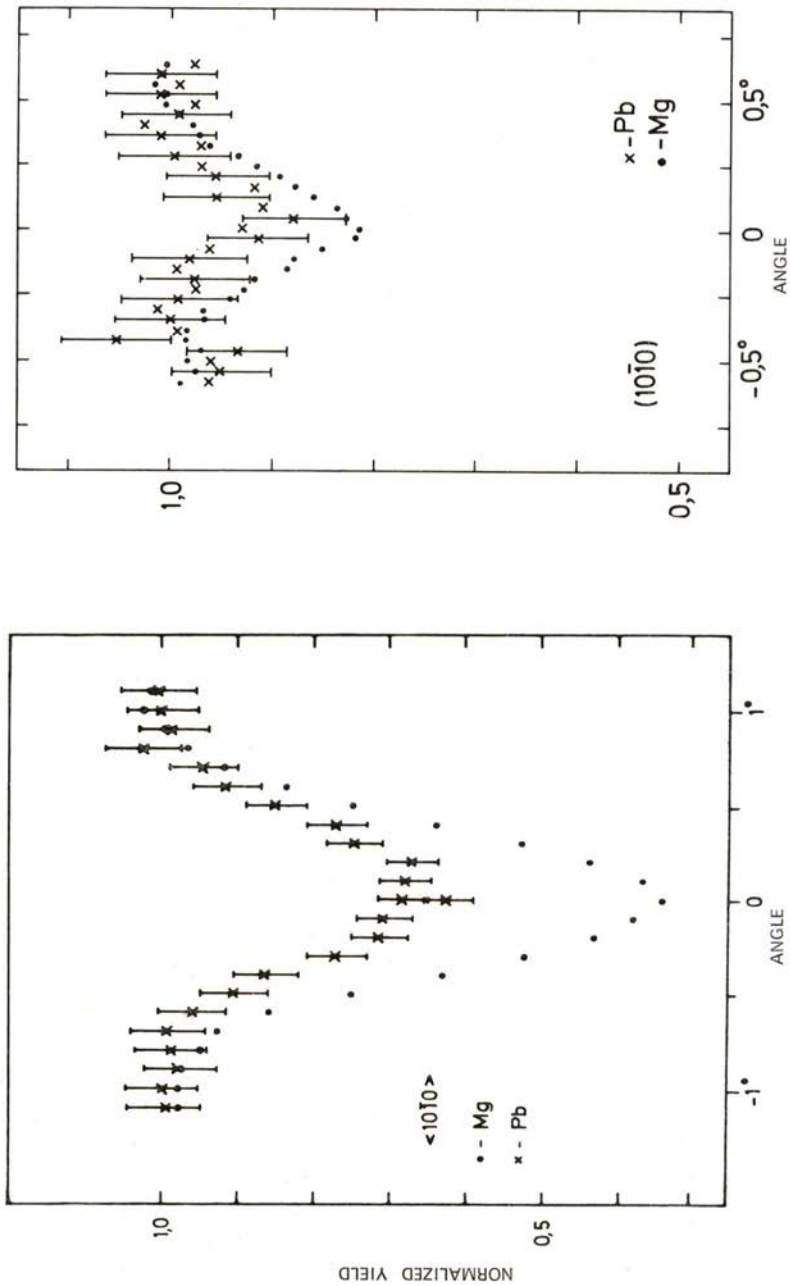
Fig. 11 — *a*) Angular scan curves along the <10$\bar{1}$0> axial direction for Pb in Mg. *b*) i̇c̈em for the (10$\bar{1}$0) plane.

190

Portgal. Phys. — Vol. 14, fasc. 3-4, pp. 175-193, 1983

Completely different results were obtained for Au in Mg (Fig. 12). Small substitutionality was observed in the $< 11\bar{2}0 >$ axial direction while almost complete substitutionality was observed along the (0001) plane. These results may indicate that gold is interstitially located in the magnesium lattice.
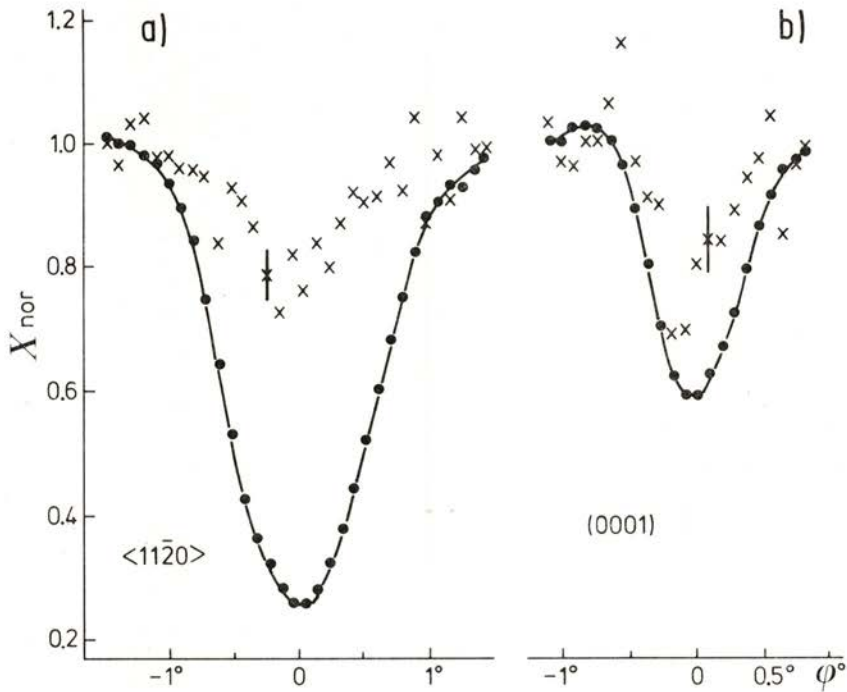
Fig. 12 — *a*) Angular scan curves along the <1120> axial direction for Au in Mg. *b*) idem for the (0001) plane (• Mg; × Au).

Fig. 13 shows preliminary results for the Tl impurity. The small substitutionality observed in the $< 11\bar{2}0 >$ direction might indicate either that Tl is interstitially located in Mg or that during the implantation it segregates to the surface.

Further measurements, will be done with better statistics and in other directions to improve the quality of these results.

In order to test theoretical predictions [4, 5, 6] this work will be pursued using other impurities implated in Mg. Similar

measurements are also planned using higher implantation energies before and after annealing treatment of the samples.
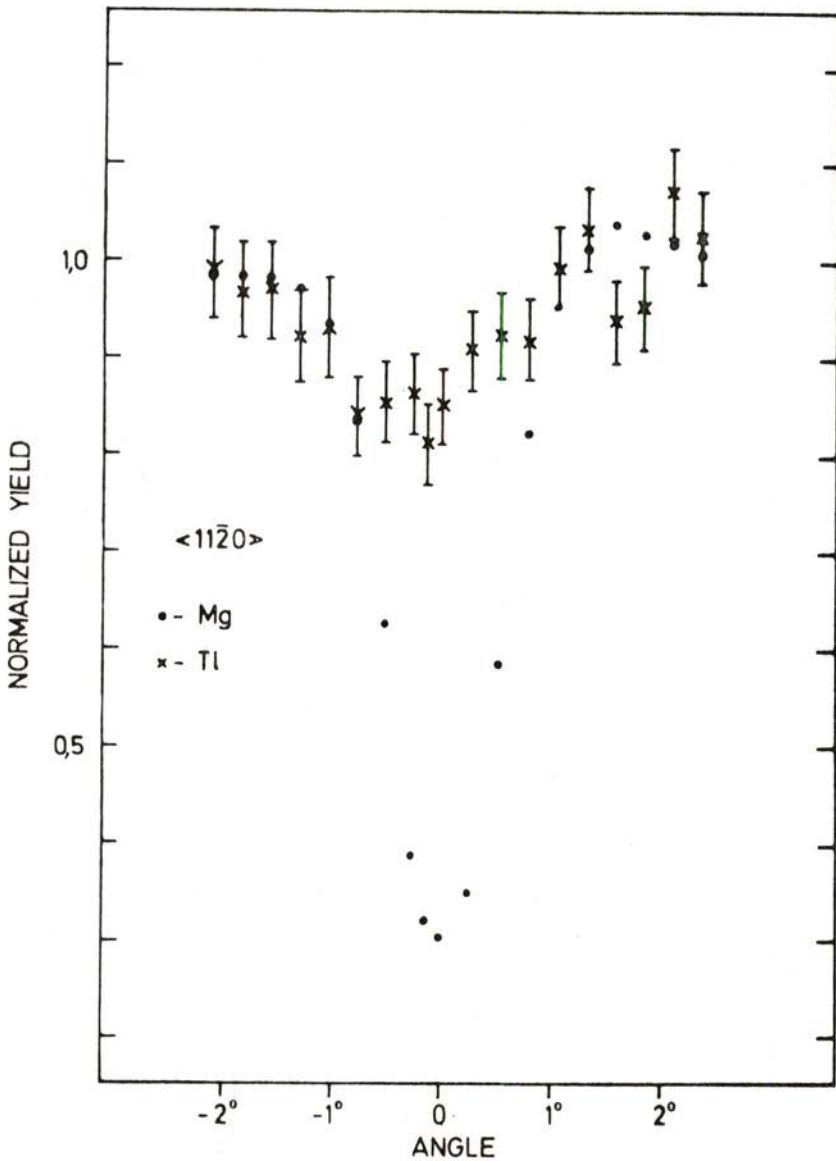
Fig. 13 — Angular scan curve along <11$\bar{2}$0> axial direction for Tl in Mg.

REFERENCES

[1] W. K. CHU in «*Uses of Low Energy Accelerators*», pag. 135 ed. by James F. Ziegler — Plenum Press — New York and London, 1975.

[2] A. P. PATHAK, *Rad. Eff.* **61** (1982) 1 and references therein.

[3] D. S. GEMMEL, *Rev. of Mod. Phys.* **46** (1979), 129.

[4] J. R. CHELIKOWSKY, *Phys. Rev.* **B19** (1979), 686.

[5] D. K. SOOD, *Phys. Lett.* **A68** (1978), 469.

[6] V. A. SINGH, A. ZUNGER, *Phys. Rev.* **B25** (1982), 907.

DECAY TIMES OF LUMINESCENCE FROM BROWN DIAMONDS

Maria Isabel B. Jorge, Maria Estela Pereira, M. F. Thomaz

Departamento e Centro de Física (INIC)
Universidade de Aveiro, 3800 Aveiro, Portugal

Gordon Davies, Alan T. Collins

Wheatstone Physics Laboratory
King's College, Strand, London WC2R 2LS, U. K.

ABSTRACT — Brown diamonds form an appreciable fraction of all natural diamonds. This paper reports the first measurements of the decay times of luminescence from these diamonds. The red luminescence excited by visible light (~ 500 nm wavelength) has a decay time of 6 ns, almost independent of temperature over the range $80 < T < 600$ K. Yellow luminescence (caused by an emission band centred on 540 nm) has a decay time of 6 ns at low temperature, decreasing with increasing temperature as expected for a centre with a thermally activated nonradiative decay. Decay times are also reported for four zero-phonon lines observed in cathodoluminescence. The lines, at 515.8, 500.2, 395.5 and 491 nm have decay times at 80 K of 32.5, 40, 45 and 70 ns respectively.

We also show that the red photoluminescence band may consist, depending on the wavelength of the exciting light, of a series of overlapping vibronic bands which are very similar to each other. This implies the existence of a 'family' of closely related optical centres in these diamonds.

1 — INTRODUCTION

About 2 to 5 % of all gem-quality natural diamonds are brown in colour. Of these 1 to 50 % (depending on the geological source of the sample) emit yellow luminescence when excited by 365 nm Hg radiation (Collins and Mohammed 1982). Despite their common occurrence and the ease with which they may be selected,

it is only recently that this class of diamonds has been subjected to spectroscopic studies (Collins and Mohammed 1982, Mohammed et al. 1982). It has been shown that the yellow luminescence arises partly from a vibronic band with its zero-phonon line at 455.5 nm (2.721 eV), and partly from a featureless underlying background (Collins and Mohammed 1982). The absorption spectra of these diamonds apparently always contain a broad absorption band peaking near 480 nm (2.6 eV). Absorption of light in this band produces luminescence in the red part of the spectrum.

The cathodoluminescence spectra of these diamonds are typically as shown in Fig. 1. The cathodoluminescence spectrum consists of a red band (very similar to the red photoluminescence band); luminescence in the yellow region (which is partly made up of the 455.5 nm (2.721 eV) band seen in photoluminescence, but with a strong underlying component); and luminescence peaking in the blue part of the spectrum near 430 nm (2.9 eV). Superimposed on this luminescence are many sharp zero-phonon lines, some of which are labelled A to J in figure 1. This complicated picture has been simplified slightly by recent studies of the effect of uniaxial stresses on the zero-phonon lines. It has been shown that the optical centres producing lines C, D and E at 467.9, 459.2 and 451.1 nm (2.649, 2.699 and 2.748 eV) respectively have rhombic I symmetry, and the centre producing the 2.721 eV line has monoclinic I symmetry; however, these four optical centres are only slightly modified versions of each other (Mohammed et al. 1982). Thus these four optical centres form a "family" of almost identical crystal defects. Similarly line H (386.9 nm, 3.204 eV) which occurs at a trigonal centre, line J (384.5 nm, 3.224 eV) which occurs at a monoclinic I centre, and line F (393.5 nm, 3.150 eV), which occurs at a centre with unknown symmetry, are all produced by a second "family" of very similar optical centres (Mohammed et al. 1982).

To date, luminescence decay times have not been reported for any of the optical transitions listed above. By luminescence decay time we mean the time taken for the luminescence to decay to 1/e of its original value, when the excitation source is switched off. The luminescence decay time is an extremely useful parameter, giving microscopic information about the optical transition. For

example, it is directly related to the matrix elements of the luminescence transition when there are no competing de-excitation mechanisms. Non-radiative de-excitation within the optical centre by internal conversion may sometimes be detected from the
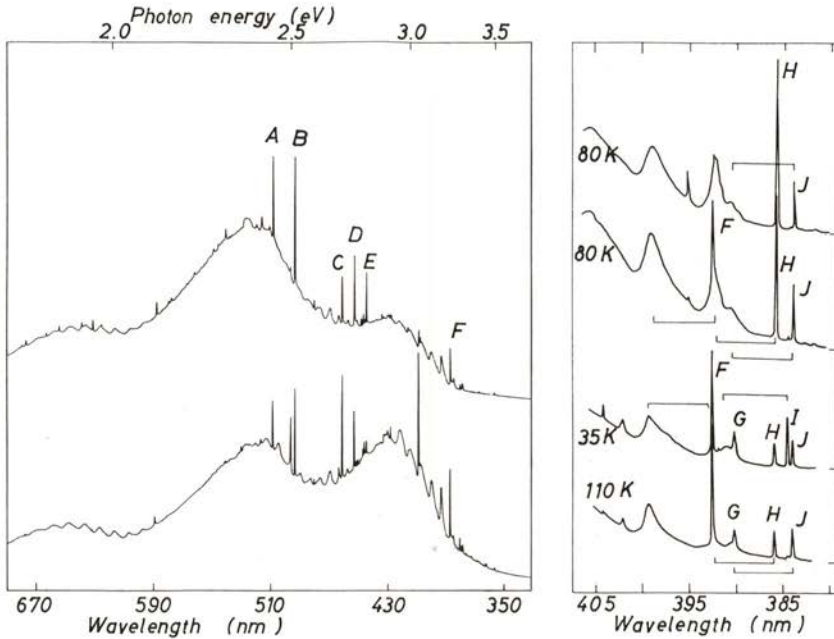
Fig. 1 — At left: Cathodoluminescence spectra of two yellow-photoluminescent brown diamonds, recorded at 77 K using an extended-red-response (RCA 31034A) photomultiplier. The spectra have not been corrected for the wavelength-dependent response of the photomultiplier and spectrometer.
At right: Detailed spectra of the I, J, H, F, G lines in two specimens at 80 K and in the same specimen at 35 K and 110 K. The braces link zero-phonon lines and assigned one-phonon sidebands with quanta of 54 meV.

temperature dependence of the decay time, as at the " N3 " centre in diamond (Thomaz and Davies 1978), while non-radiative de-excitation involving energy transfer from the optical centre to another crystal defect may be identified by the specimen dependence of the decay time, as at the " H3 " centre in diamond (Crossfield et al. 1974).

The purpose of this paper is to report the luminescence decay times of some of the transitions observed in the yellow-luminescing brown diamonds. We will also show that the red luminescence can be composed of one band or several overlapping bands, depending on the energy of the exciting radiation. This occurs in a way consistent with there being another "family" of very similar optical centres in these brown diamonds. The experimental data are listed in §3, and briefly discussed in §4. We begin by describing the experimental techniques.

2 — EXPERIMENTAL DETAILS

Photoluminescence was excited by a high pressure xenon arc filtered by a Bausch and Lomb high intensity grating monochromator. Photoluminescence decay time measurements were made using the single photon statistical technique (see, for example, Birch and Imhof 1977). The flashlamp source was a free-running discharge in air at normal pressure or in nitrogen at 2 atmospheres (Thomaz and Barreto 1971), operating at 7 kV at a frequency of ~ 10 kHz. The band of excitation wavelengths was selected using a filter or the Bausch and Lomb monochromator and focussed on to the diamond. The luminescence was collected from the diamond and focussed through a filter on to the photocathode of the photomultiplier. An electrical signal derived from the spark, and the output from the photomultiplier, were connected respectively to the start and stop inputs of a time-to-amplitude converter, the output of which was fed to a multichannel analyser (Fig. 2). Provided that the count rate from the photomultiplier was kept below 100 s^{-1} the data accumulated on the multichannel analyser correctly represented the build-up and decay of the luminescence from sample (Birch and Imhof 1977).

Three different sample mounting arrangements enabled the decay time to be measured with the sample at ~ 77 K, at a range of temperatures between 90 and 300 K, or at a range of temperatures between 300 and 700 K.

The cathodoluminescence equipment operated at 45 kV with beam currents of typically ~ 10 μA. The electron beam was

focussed to a spot about 350 μm in diameter on to the diamond mounted at the end of a liquid nitrogen cold-finger. By applying pulses to parallel plates in the electron flight tube the beam could be deflected on or off the sample in about 1 ns.
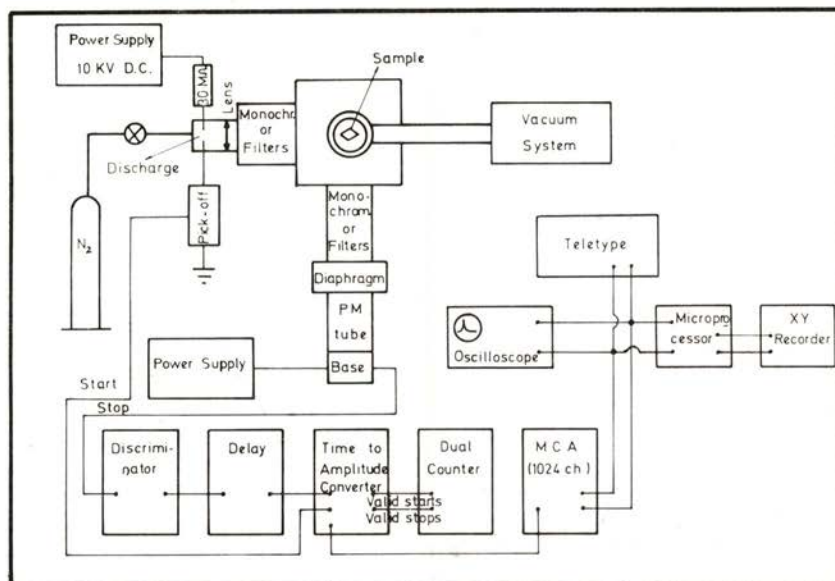
Fig. 2 — Single-photon system block diagram.

The luminescence from the sample was collected by a spherical mirror and focussed on to the entrance slit of a Spex 1500 mono-chromator. The photomultiplier used (I. T. T. type 4027) differed from a conventional tube in having a fine mesh grid structure immediately behind the photocathode. By applying a small bias potential to the so-called "gate" the photomultiplier could be turned on or off, depending on the polarity of the bias. For time resolved spectroscopy the photomultiplier was pulsed on for a short time by a Tektronix type 111 pulse generator which was triggered by the pulse generator deflecting the electron beam (Fig. 3). The time interval between the excitation of the sample and switching on the photomultiplier could be varied, enabling spectra to be recorded at different delays. The normal practice

was to excite the sample for a period somewhat longer than the decay time of the luminescence system being measured, and to gate the photomultiplier on for a time period about half that of the decay time. Thus, for example, for a decay time of 20 ns the
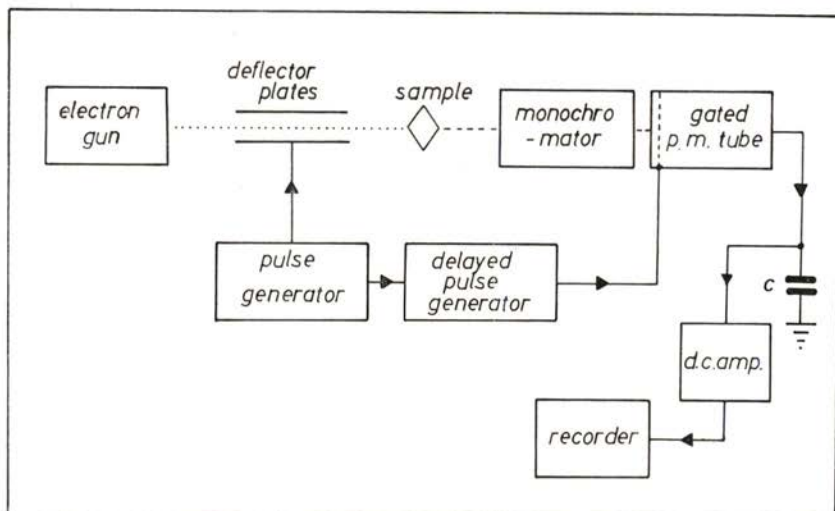
Fig. 3 — Time resolved spectroscopy system diagram.

sample would be excited for 50 ns at a repetition rate of 30 kHz and the photomultiplier would be gated on for 10 ns. In such a case the delay between excitation and gating the photomultiplier on would be varied in the range 0 to 100 ns. Pulse lengths and delays were all determined by standard lengths of coaxial cable.

3 — EXPERIMENTAL DATA

3.1 — Red luminescence band

Exciting the diamonds with light of 460 nm (2.69 eV) produces luminescence as shown in Fig. 4a. This spectrum is similar to the

Fig. 4 — (facing page) — Photoluminescence spectra (uncorrected) of a brown diamond at 77 K using excitation light of: a) 460 nm; b) 500 nm; c) 525 nm
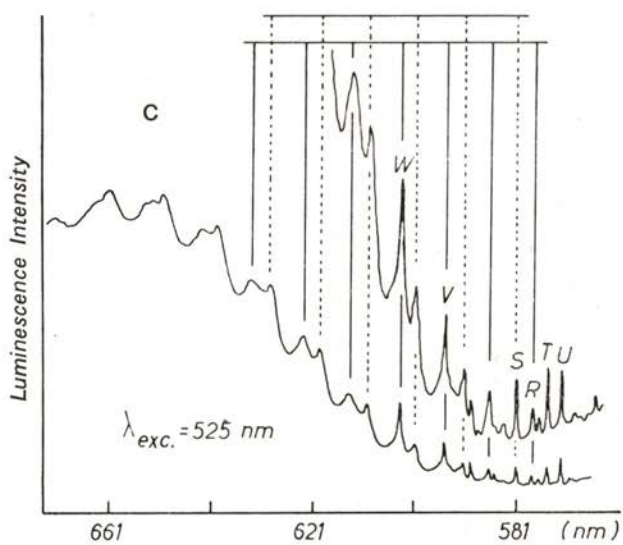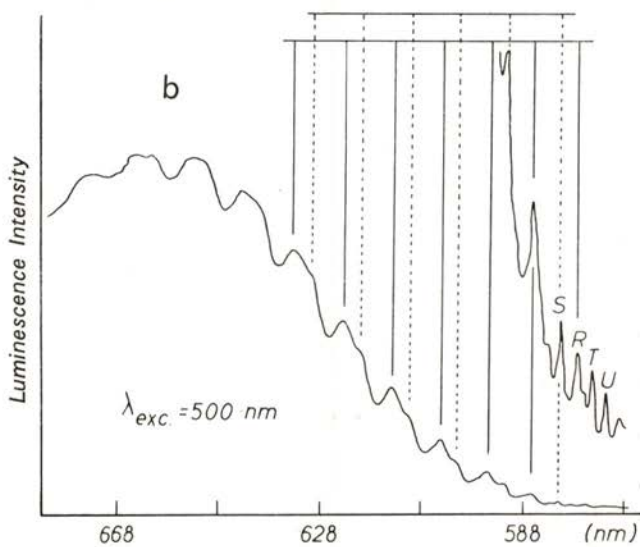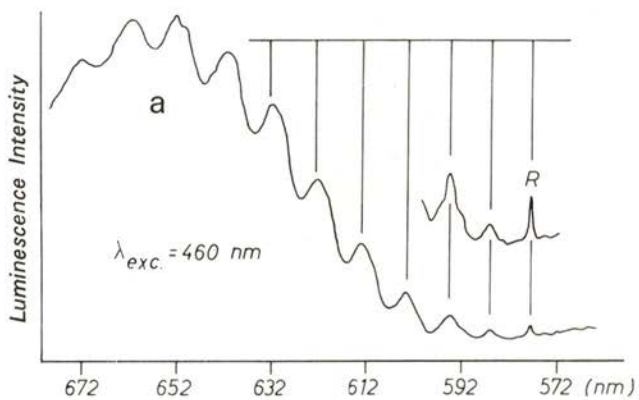
original report of the red luminescence by Collins and Mohammed (1982) who used exciting light of 489 nm (2.53 eV). The energy spacing of the vibronic peaks in figure 4a corresponds to a phonon quantum of 31 meV. When exciting light of a longer wavelength is used, further features appear in the red spectral region (Fig. 4b, c). These features also form vibronic progressions with phonon energies of 31 meV, very similar to the simple spectrum obtained with excitation at 460 nm. The vibronic bands have their origins at the zero-phonon lines R (577.8 nm, 2.146 eV), S (581.0 nm, 2.134 eV), T (574.8 nm, 2.157 eV) and U (572.1 nm, 2.167 eV).
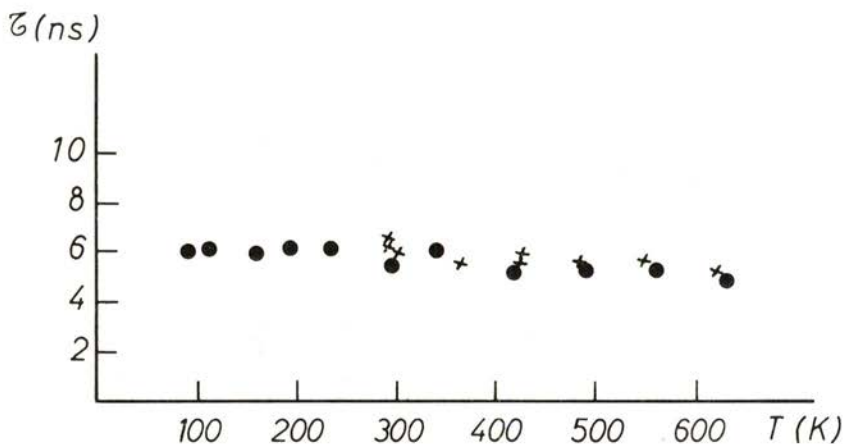
Fig. 5 — Decay times of the red photoluminescence as a function of temperature (• refer to one brown diamond; x refer to another).

Photoluminescence decay time measurements have been made with exciting light of 480 ± 20 nm, (2.58 ± 0.1 eV) chosen to excite predominantly the simple vibronic band with the zero-phonon line R. The luminescence decreased, after spark excitation, with an accurately exponential time dependence. The decay time is 6 ns at room temperature, and changes by less than 1 ns in the temperature range 80 to 600 K (Fig. 5). The same result was obtained when we used exciting light of 500 ± 10 nm

202

Portgal. Phys. — Vol. 14, fasc. 3-4, pp. 195-210, 1983

(2.48 ± 0.05 eV) and between 470 and 530 nm (Corning 5.61 and 3.71 filters on the excitation). The decay time is consequently independent of the wavelength of the exciting light over the wavelength range 460 to 530 nm. The luminescence was detected through a Corning 2.61 filter (cut-off at ~ 600 nm), in all cases.

Luminescence decay times have also been measured for the red luminescence band using cathodoluminescence, with the samples at liquid nitrogen temperature. The cathodoluminescence decay is nonexponential initially with a decay time of about 10 ns. However, about 10 ns after the cessation of excitation, the luminescence decay slows to an approximate decay time of 25 ns.

3.2 — *Yellow luminescence band*

When the yellow luminescence is excited by relatively long-wavelength light (e.g. 425 ± 10 nm, 2.92 ± 0.07 eV) the spectral distribution of the luminescence has the temperature dependence of Fig. 6. The luminescence mainly consists of one
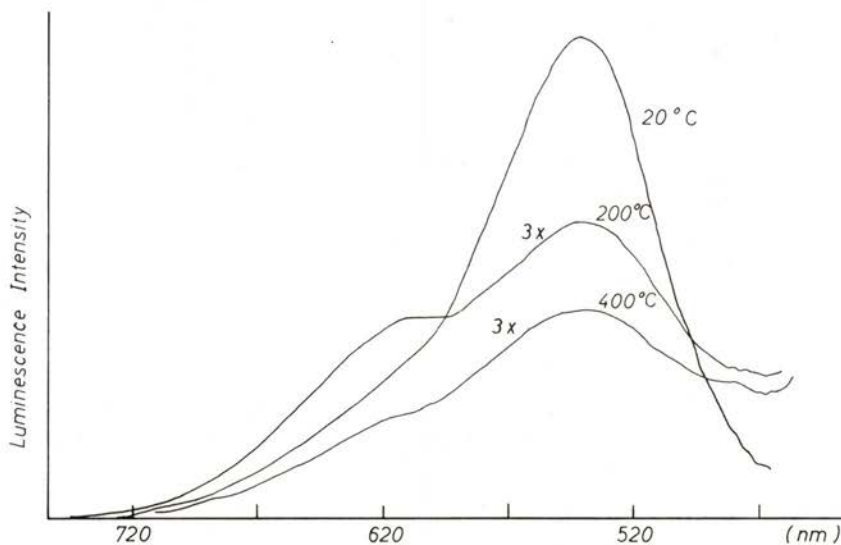
Fig. 6 — Photoluminescence spectra for one brown diamond at three different temperatures and λ_{exc} = 425 nm

band centred on 540 nm (2.30 eV), and the intensity of this band decreases with increasing temperature. When shorter wavelength exciting light is used (e.g. at 325 nm, 3.81 eV) the 540 nm band is seen together with a band near 460 nm, 2.70 eV (Fig. 7). The 460 nm band increases in *absolute* intensity as the temperature increases.
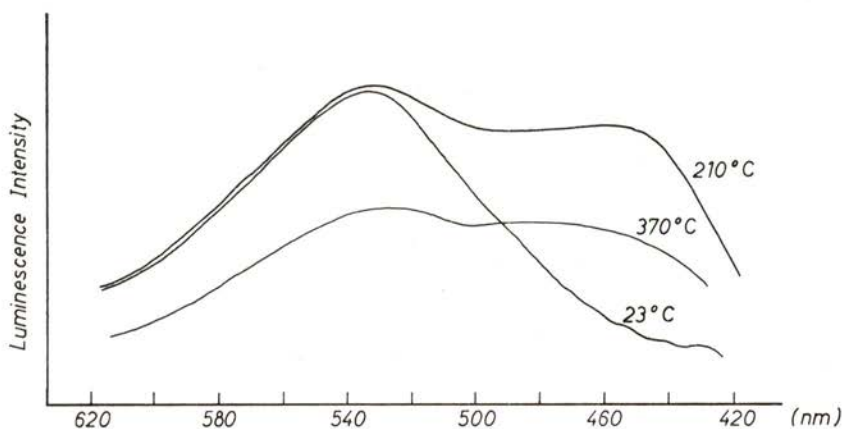
Fig. 7 — Photoluminescence spectra for one brown diamond at three different temperatures and using $\lambda_{exc} = 325$ nm

With 400 ± 20 nm (3.10 ± 0.16 eV) exciting light and a Corning 3.70 filter (cut-off at ~ 500 nm) on the emission side one single exponential decay is obtained with a decay time of 5.8 ± 0.2 ns at room temperature: this presumably is the decay time of the 2.721 eV system. Excitation at 400 nm creates the yellow luminescence most efficiently and the red luminescence is absent.

When shorter wavelength excitation is used (with the exciting light filtered by Chance 0X7 and 0B10 filters to pass light of 330-420 nm) and the luminescence is detected through a Corning 3.70 filter (cut-off at ~ 500 nm) non-exponential decay curves are obtained. These curves were fitted numerically to the sum of two exponentials. One has a decay time of 5.8 ns at room temperature, decreasing with increasing temperature above 350 K

(Fig. 8): this is presumably the decay time of the 2.721 eV system. The second decay time is longer and shows no significant variation with temperature. This component is a weak contributor to the luminescence, giving approximately 15 % of the emission immediately after excitation, and so its decay time is very uncertain (18 ± 4 ns).
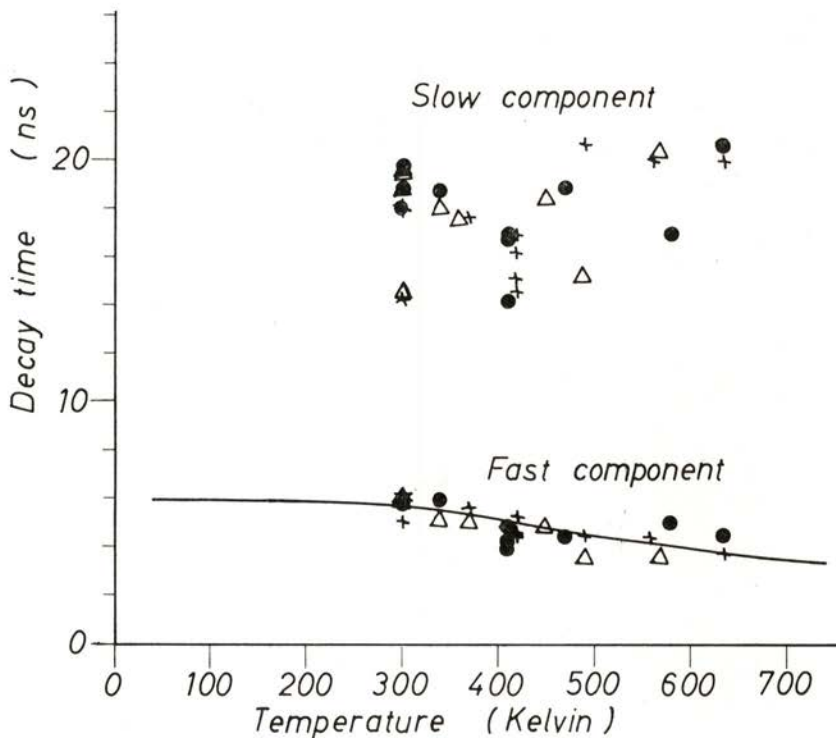
Fig. 8 — Decay times of yellow photoluminescence as a function of temperature. (•, △ and x refer to three different brown diamonds). The curve drawn through the points of the faster component obeys the equation of section 4.

A third much longer-lived component is also observed using the same excitation conditions, confirming the suggestion (Collins and Mohammed 1982) that the yellow luminescence band is complex (several zero-phonon lines are observed over the band as the S1 system, the 440.2 nm, 489 nm, 496.6 nm, 518 nm, 523.2 nm, 524.2 nm

and N3). The intensity of this slow component increases as the specimen temperature increases but is always less than 3 % of the emission immediately after excitation. It corresponds presumably to the 460 nm band whose absolute intensity increases with temperature as shown in Fig. 7.

Measurements have also been made of the decay times of some of the many sharp lines observed in the cathodoluminescence of these brown diamonds (§1). The decay times for lines A (2.403 eV, 515.8 nm), B (2.478 eV, 500.2 nm), F (3.150 eV, 393.5 nm) and another zero-phonon line at 491 nm (2.526 eV) as measured at liquid nitrogen temperature are 32.5, 40, 45 and 70 ns respectively (with an uncertainty of about ± 5 %) as shown in Figs. 9 and 10.
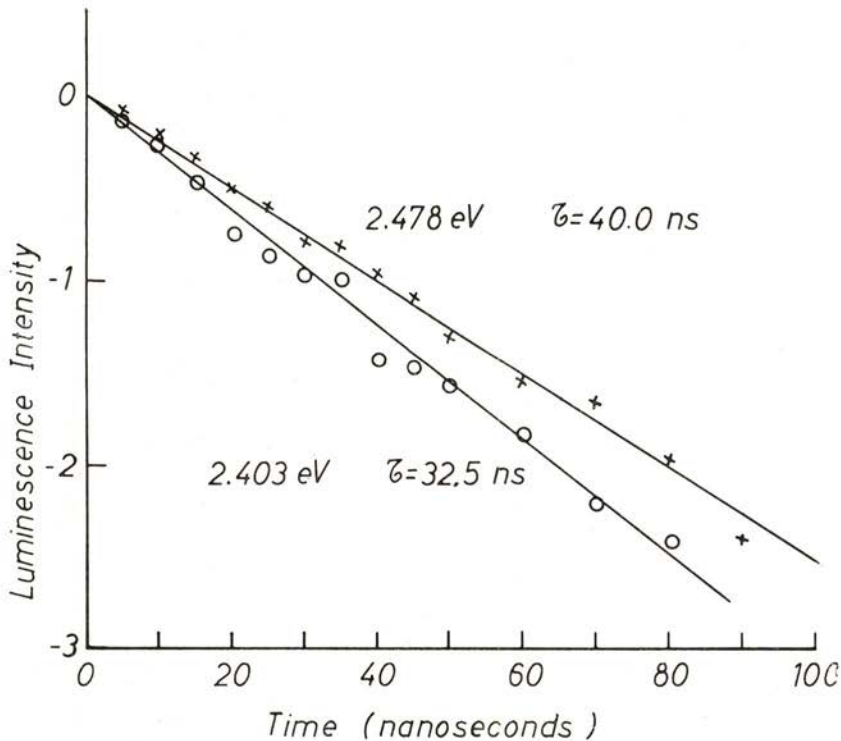
Fig. 9 — Cathodoluminescence decay curves of A line (2.403 eV) and B line (2.478 eV) at liquid nitrogen temperature.
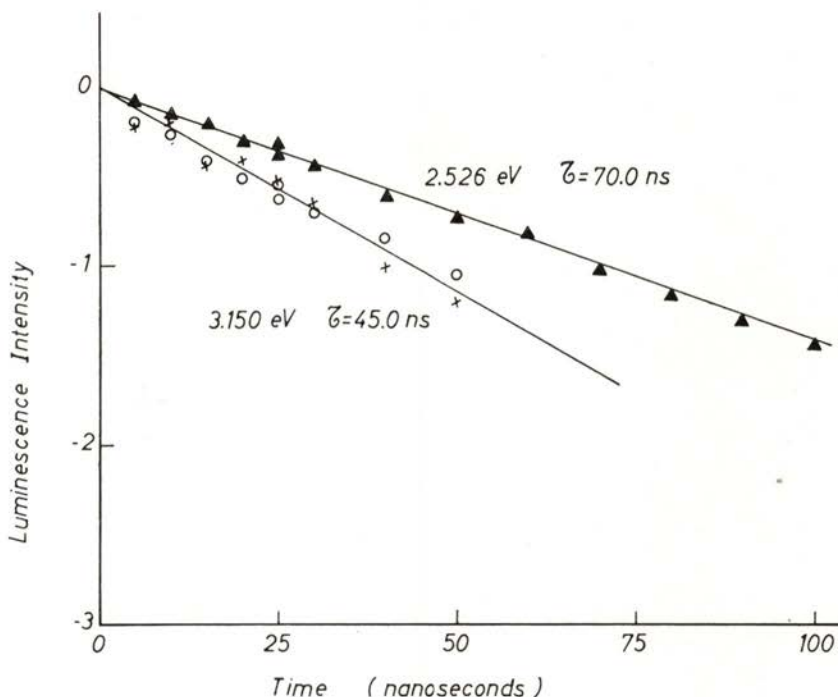
Fig. 10 — Cathodoluminescence decay curves of F line (3.150 eV) and the 491 nm line (2.526 eV) at liquid nitrogen temperature. (Symbols o and x refer to the same brown diamond and ▲ refers to a different diamond).

4 — DISCUSSION

The red luminescence band, excited by 460 nm (2.7 eV) light appears to consist of a single vibronic band with its zero-phonon line at 2.146 eV (R of Fig. 4a). The vibronic progression involves phonons of 31 meV (well away from any critical point in the phonon dispersion curves of diamond (Zdetsis 1979)). The Huang-Rhys factor of the band, at low temperatures, is of the order of 10. (We are currently investigating the electron-phonon coupling of this band in more detail). When the excitation light is changed to 525 nm (2.362 eV) many other transitions are excited (Fig. 4c), with similar phonon energies and Huang-Rhys factors. In particular vibronic bands with zero-phonon lines W (2.051 eV) and V (2.082 eV) are excited (§3.1). As these changes occur, the

luminescence decay times are little changed (§3.1). Evidently the red spectral region contains many similar vibronic bands, derived from another "family" of similar optical centres in these diamonds. Closely related optical centres are common in diamond — in addition to those occurring in brown diamond (§1) there are also several similar radiation damage centres (de Sa and Davies 1977).

In Fig. 8 we showed that the decay time of the photoluminescence band centred on 540 nm (zero-phonon energy 2.721 eV) decreases with increasing temperature. This decrease, and the loss of luminescence intensity with increasing temperature (Figs. 6 and 7), are consistent with a thermally activated non-radiative decay, internally at the optical centre, to another energy level. This process may be described by the well-known single vibrational coordinate model (Freed and Jortner 1970):

$$\tau^{-1} - \tau_0^{-1} = C\,(\,kT^*\,)^{-1/2}\,\coth\,(\,\hbar\omega/2kT\,)\,\exp\,(\,-\,\Delta E/kT^*\,)$$

The line on Fig. 8 shows a fit of this equation to the experimental data with the parameters $\hbar\omega = 34$ meV, $C = 2.0$ ns^{-1} meV$^{1/2}$, and $\Delta E = 127$ meV. T* is the effective temperature defined by

$$kT^* = (\,\hbar\omega/2\,)\,\coth\,(\,\hbar\omega/2kT\,)$$

and τ_0, the decay time at 0 K, was assumed to be 6.0 ns. We note the similarity of the value of $\hbar\omega$ with the quantum observed in the luminescence spectrum.

In §3.2 we reported the decay times of four zero-phonon lines observed in cathodoluminescence in the brown diamonds. The values obtained are several tens of nanoseconds, typical for electric dipole optical transitions in diamond (Crossfield et al. 1974, Thomaz and Davies 1978). The decay times for these zero-phonon lines have not been reported before, except for a measurement of the 491 nm (2.526 eV) line by Crossfield (1981). He reported that the decay was not exponential, in contrast to the result reported here (§3.2). However, the conditions used by Crossfield were inappropriate to determine the decay time of this line. In his diamonds the 491 nm line was a very minor feature superimposed on the blue "band A" donor-acceptor pair recombination. The latter system has a fast decay time (~ 8 ns) and by exciting his samples for 20 μs and looking at the luminescence after a delay of 500 ns

Crossfield was able to obtain a spectrum in which the 491 nm system was the dominant emission. For longer delays (up to 100 μs) the intensity of the 491 nm system decayed in a nonexponential fashion. The behaviour at such long delays is probably determined by other processes in the diamond, rather than by the lifetime of the centre itself. In contrast our measurements have been made on diamonds in which the 491 nm luminescence was the dominant emission and the exponential decay with a time constant of 70 ns is characteristic of the centre itself. Collins and Woods (1982) have shown that the 491 nm emission is associated with a defect which has decorated dislocations in the diamonds.

5 — SUMMARY

Brown diamonds with yellow photoluminescence (under 365 nm Hg excitation) form an appreciable fraction of total natural diamond production. In this paper we have presented the preliminary results of a systematic investigation of the luminescence transitions observed in this class of diamonds. The photoluminescence in broad outline has the form of bands centred at 550 nm (yellow luminescence) and at 650 nm (red luminescence).

The decay time for the red luminescence band is 6.0 ± 0.2 ns at room temperature and does not vary significantly as the temperature is changed in the range $80\,K - 600\,K$. The decay time is also independent of the exciting wavelength, even though different vibronic bands are then excited (§3.1).

The decay curves for the yellow luminescence band can be resolved into a fast component and a slower component. The fast component is shown to be temperature dependent, becoming faster as the temperature is increased. The fast decay time constant (5.8 ± 0.2 ns) is assigned to the 455.5 nm, 2.721 eV luminescence system (§3.2).

We have also measured the decay times of some of the many sharp zero-phonon lines observed in the cathodoluminescence spectra of the brown diamonds, obtaining values of the order of tens of nanoseconds (§3.2) as expected for electric dipole transitions in diamond.

Further work is in progress on the vibronic properties of these bands and on the temperature dependence of the decay times.

REFERENCES

BIRCH, D. J. S. and IMHOF, R. E. 1977, *J. Phys. E: Scientific Instruments*, **10**, 1044-1049.

COLLINS, A. T. and MOHAMMED, K. 1982, *J. Phys. C: Solid State Phys.*, **15**, 147-158.

COLLINS, A. T. and WOODS, G. S. 1982, *Philosophical Magazine B*, **45**, 385-397.

CROSSFIELD, M. D. 1981, PhD. Thesis, University of London, King's College.

CROSSFIELD, M. D., DAVIES, G., COLLINS, A. T. and LIGHTOWLERS, E. C. 1974, *J. Phys. C: Solid State Phys.*, **7**, 1909-1917.

DE SA, E. S. and DAVIES, G. 1977, *Proc. R. Soc. Lond.* **A357**, 231-251.

FREED, K. F. and JORTNER, J. 1970, *J. Chem. Phys.* **52**, 6272-6291.

MOHAMMED, K., DAVIES, GORDON and COLLINS, ALAN T. 1982, *J. Phys. C: Solid State Phys.*, **15**, 2789-2800.

THOMAZ, M. F. and BARRETO, V. J. 1971, *Rev. Fis., Quim. e Engenharia* — vol. III, Serie A, 7-19.

THOMAZ, M. F. and DAVIES, G. 1978, *Proc. R. Soc. Lond.* **A362**, 405-419.

ZDETSIS, A. D. 1979, *Chem. Phys.* **40**, 345-347.

FLUORESCENCE FROM VIBRONIC STATES OF
1-12 - BENZPERYLENE, IN CONDENSED PHASE

Maria Estela Pereira

Departamento e Centro de Física (INIC)
Universidade de Aveiro, 3800 Aveiro, Portugal

ABSTRACT — 1-12 — benzperylene shows fluorescence occurring at energies above the $S_1 \rightarrow S_0$ transition, that is shown to come from four mainly thermally populated vibronic states, being identified the antisymmetrical modes active in the mixing between S_1 and S_2. The rate of vibrational redistribution of the vibronic states energies is shown to be much smaller than the usual rates of pure vibrational states. The intensity of the vibronic bands can be accounted for considering the breakdown of Born — Oppenheimer approximation, using some simplifying assumptions.

1 — INTRODUCTION

Apart from azulene, that shows fluorescence from the second excited state (S_2) due to a rather unusual large energy gap between the first excited state (S_1) and S_2, and has been studied in detail [1], most aromatic hydrocarbon molecules show fluorescence originating only in S_1, irrespective of the state reached in excitation. This fact, known as Kasha's rule [2], is due to a very fast internal conversion between excited states, and is verified both in solution and in the gas phase, even when, in the latter instance, the molecules can be considered as isolated during the lifetime of the excited state.

Using more sensitive spectrometers, it has been possible to see that several other molecules show "anomalous" fluorescence from states with energy above S_1, as pyrene and 3-4 - benzpyrene [3]. This class of molecules has in common a rather small energy gap between S_1 and S_2 (typically 1000-3000 cm^{-1}) and

Portgal. Phys. — Vol. 14, fasc. 3-4, pp. 211-222, 1983

211

also the fact that while the transition from the ground state (S_0) to S_2 is strongly allowed, the transition $S_0 \rightarrow S_1$ is weak, being usually symmetry forbidden. A review of molecules in this class can be found in the literature [4].

Whilst in these molecules absorption to S_2, being allowed, can be considered as a pure electronic transition, with a vibrational progression due to the different equilibrium coordinate of a symmetrical vibrational mode (in aromatic hydrocarbons usually the C-C stretching mode at 1400 cm^{-1}) absorption to S_1 is dominated by vibronic peaks, occurring at energies above the $S_0 \rightarrow S_1$ energy gap equal to the energy of an antisymmetrical vibrational mode ($\hbar\omega_a$). These peaks have been explained by Herzberg and Teller [5] as a departure from the Condon approximation, due to a mixing of S_1 and S_2 with the assistance of that mode. Within this model absorption will take place from S_0 to a state with energy $\hbar\omega_a$ above S_1, while normal fluorescence will occur between S_1 and a state with energy $S_0 + \hbar\omega_a$. Mirror image relationship holds, too. However some molecules do not show this relationship, as pyrene [6], which can be only accounted for by assuming a departure from Born - Oppenheimer approximation [6, 7].

Although "anomalous" fluorescence had been formerly assigned to $S_2 \rightarrow S_0$ transitions as in 1-12 - benzperylene [8], the fact that it is not a mirror image of $S_0 \rightarrow S_2$ absorption, (as might be expected since this is an allowed transition), together with the different behaviour with respect to temperature (shift and intensity) revealed that it indeed occurs from those vibronic states of S_1 where to absorption from S_0 occurs [9, 10]. This fluorescence is therefore known as "hot" fluorescence. When the first absorption band is hidden under the second, "hot" fluorescence can be recognized as it occurs at an energy $\hbar\omega_a$ above the $S_1 \rightarrow S_0$ energy gap exactly equal to the energy below $S_1 \rightarrow S_0$ at which "normal" fluorescence from a vibronic peak occurs.

"Hot" fluorescence gives, therefore, important information regarding radiationless processes in excited molecules and the nature of vibronic states. Using two-photon spectroscopy the mode selectivity in radiationless relaxation has been shown [11]. Most of the work has been carried in the gas phase where the molecule can be considered as isolated during the lifetime of the excited

state; however the condensed phase spectra give information about the mechanism of vibronic mixing.

In the present work a study of the fluorescence of 1-12 - benzperylene in solution is made and the analysis of spectra at 77 K and 293 K provides an estimate of the rates of vibrational redistribution of the energy of the mixing modes, being shown to be rather slower than for pure vibrational states. From the ratio of intensities of "hot" and the corresponding "normal" peaks it can be shown that Herzberg - Teller treatment cannot be used and an alternative model, taking into account the departure from Born - Oppenheimer approximation is used, under some simplifying assumptions that allow numerical estimates.

2 — EXPERIMENTAL RESULTS

A solution of 5×10^{-6} M of 1-12 - benzperylene in 3 - methylpentane was used to study the fluorescence: it was excited at 27.400 cm^{-1} by a Xe lamp whose light was dispersed by a Hilger - Watts monochromator; it was viewed at right angles, through a Hilger - Watts single monochromator, blazed at 500 nm, by an EMI AVP 56 fast rise time photomultiplier. The detection was made by a Brookdeal lock-in amplifier, and corrected for fluctuations in the lamp by sending the signal as numerator in a home built ratiometer, the denominator originating in a small fraction of the light incident on the sample, converted into a fixed wavelength by means of a standard solution of Rhodamine - B. The spectra were further corrected for the wavelength dependent response of the monochromator and photomultiplier.

Corrected fluorescence spectra of 1-12 - benzperylene are shown in Fig. 1 and 2 (77 K and room temperature). It is only on higher gain that at 77 K a very low intensity fluorescence is observed at energies above the $S_1 \rightarrow S_0$ transition. At room temperature it becomes much stronger, in accordance with former results [8].

From the 77 K spectrum an analysis was made assuming a gaussian shape for each peak with a half width of 120 cm^{-1}. As anomalous fluorescence is practically absent, this spectrum gives the structure of the normal fluorescence band.

Besides the $S_1 \rightarrow S_0$ transition (24.700 cm^{-1}) there are four vibronic bands occurring at energies 260 cm^{-1} (B), 530 cm^{-1} (C),

800 cm^{-1} (D) and 1060 cm^{-1} (E) below $S_1 \rightarrow S_0$. The infrared spectrum shows peaks at energies close to the energies of these modes. A 4.2 K spectrum [12], also points to the existence of vibronic bands with energies close to these ones, clearly originating in non-symmetrical modes. All of these peaks show the characteristic 1400 cm^{-1} progression. It can be noted that the relative intensity of the last term of the symmetrical progression to that of the origin is higher for the pure electronic transition than for the vibronic bands, which can be due to a mixing of S_1 with S_3, as the symmetries of these states allow a mixing with the assistance of a symmetrical mode.
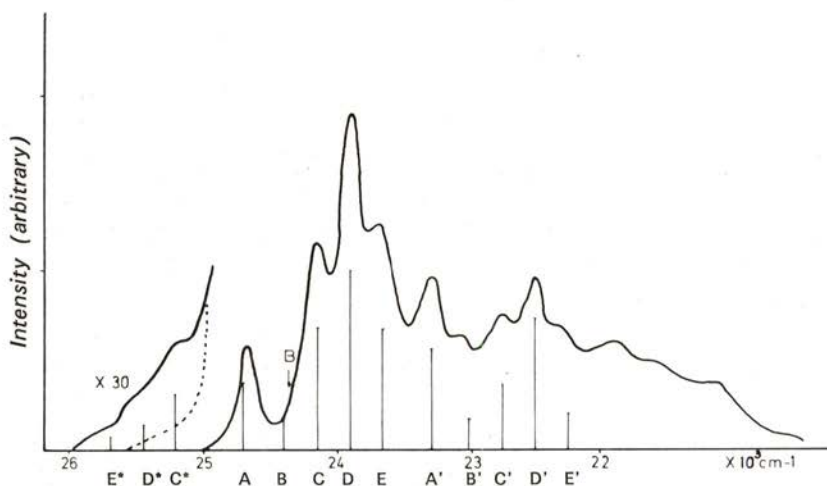
Fig. 1 — Emission spectrum (corrected) of 1-12 Benzperylene at 77 K. The lines show the location and relative intensity of the transitions referred in the text. A', B', C', D', E' are the 1400 cm^{-1} progression of A, B, C, D, E.

A similar analysis of the room temperature spectrum with a gaussian half-width of 240 cm^{-1} shows, together with a very similar behaviour of the "normal" fluorescence, the increase in the "anomalous" fluorescence, peaks being detected at energies 260 cm^{-1} (B*), 530 cm^{-1} (C*), 800 cm^{-1} (D*) and 1060 cm^{-1} (E*) above $S_1 \rightarrow S_0$, each one being origin of 1400 cm^{-1} vibrational
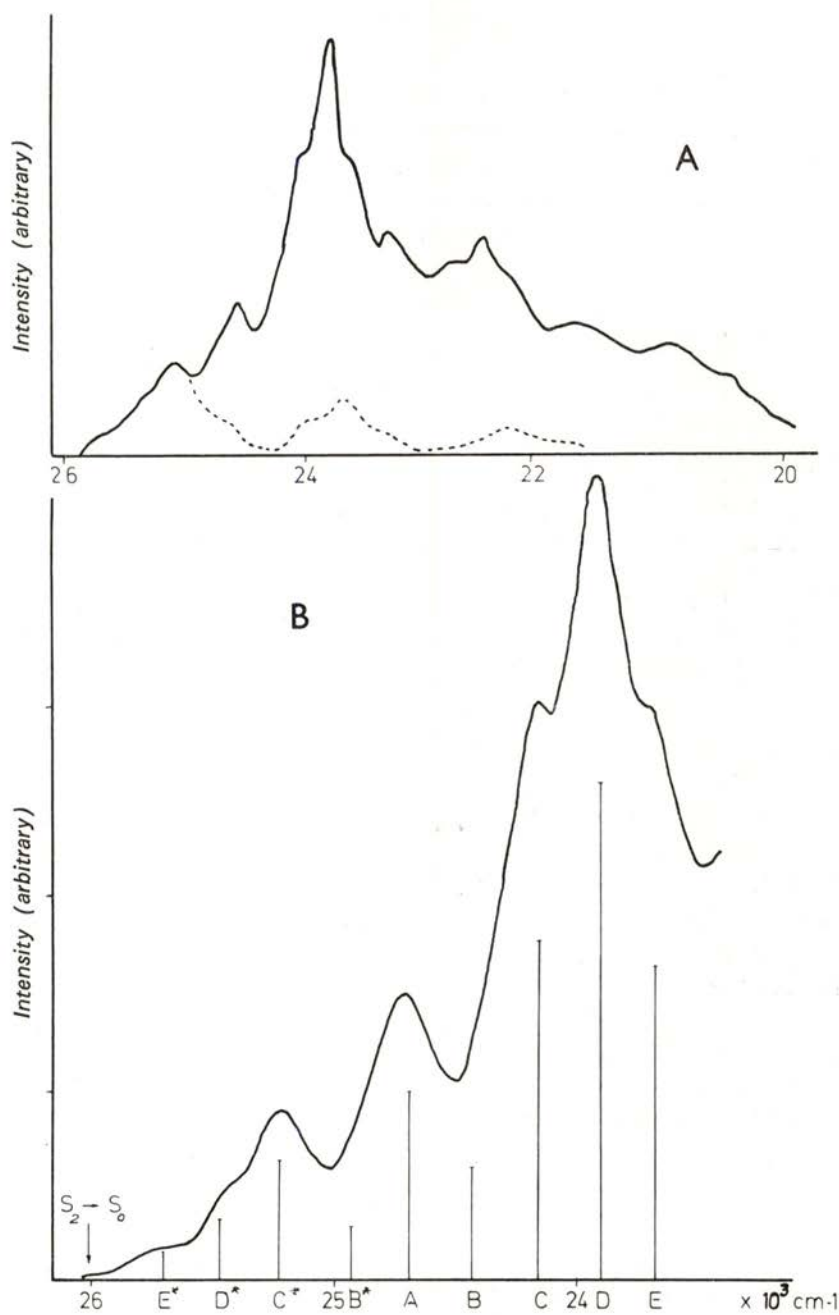
Fig. 2 — Emission spectrum (corrected) of 1-12 Benzperylene at 293 K. A) Dashed curve — "hot" fluorescence spectrum. B) Detail of the higher energy part of the spectrum, with relative intensities of "hot" and normal transitions.

progressions. A summary of the results is shown in Table 1. Assuming also that the vibrational progressions of the "hot" bands are similar to those of the corresponding "normal" bands, an estimate of the whole "hot" fluorescence can be made (Fig. 2A, dashed line).

TABLE 1

		A	B	B*	C	C*	D	D*	E	E*	F
Energy		24.700	24.700	24.700	24.700	24.700	24.700	24.700	24.700	24.700	26.120
(cm^{-1})		(S_1-S_0)	-260	$+260$	-530	$+530$	-800	$+800$	-1060	$+1060$	(S_2-S_0)
Inten -sity	77 K	10.0	5.3	—	18.8	—	26.3	—	18.0	—	—
	293 K	10.0	6.1	2.7	18.7	6.6	26.0	3.5	18.5	2.0	0.5

3 — DISCUSSION

The states B*, C*, D* and E* are mainly thermally populated, the contribution of $S_2 \rightarrow S_0$ emission (F) being weak enough, at all temperatures, to be neglected in our analysis. In a former work [8], an activation energy of 690 cm^{-1} was found, but no attempt was made to distinguish between the behaviour of the different modes.

The 77 K spectrum allows us to estimate the fluorescence originating in states reached directly after excitation, since at this temperature, for instance, only 4.5×10^{-5} of the molecules in S_1 will have an energy 530 cm^{-1} above S_1, by thermal population. On the other hand, the room temperature spectrum shows mainly the contribution of thermally populated states.

3.1 — *Rate of vibrational redistribution of energy of the "hot" states*

The almost absence of $S_2 \rightarrow S_0$ fluorescence clearly shows that the rate of internal conversion from S_2 to S_1 is much faster

than the rate of fluorescence from S_2; therefore internal conversion can be regarded as an irreversible process.

In this instance, after internal conversion a very fast energy loss to the solvent takes place and the molecule ends up in a vibronic state. In Fig. 3 the processes originating in this vibronic
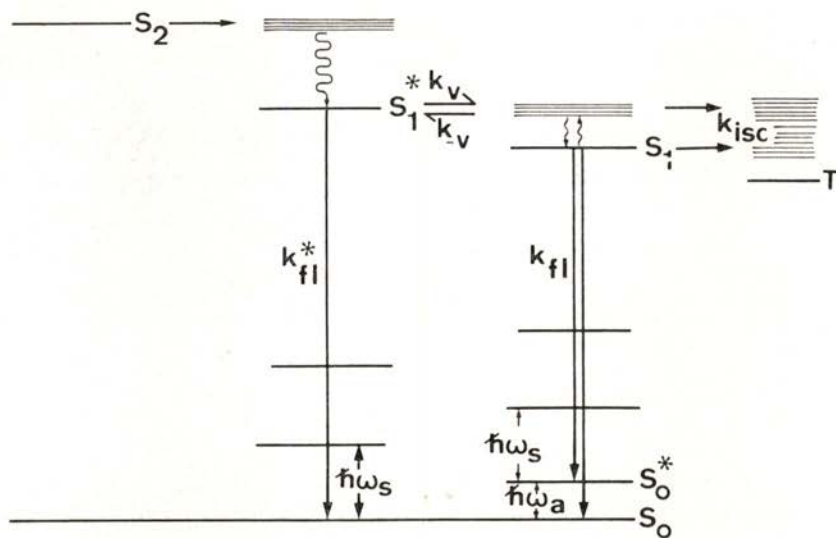
Fig. 3 — Schematic diagram of processes taking place after excitation.
($\hbar \omega_s = 1400$ cm^{-1}).

state are indicated. It is known that the rates of fluorescence from $S_1(k_{fl})$, of intersystem crossing (k_{ISC}) and internal conversion to $S_0(k_{IC})$ are temperature independent [13]. Assuming they are of the same order of magnitude for "hot" and "normal" states, under steady state conditions a relationship between concentrations of S_1 and S_1^* can be found, from which a ratio of "hot" (ϕ^*) and "normal" (ϕ) fluorescence can be obtained:

$$\phi^* / \phi = (k_{fl}^* / k_{fl}) \, k_{-v} / k_v + (k_{fl}^* / k_{fl}) . \, \tau^{-1} \cdot k_v^{-1} \qquad (1)$$

with $\tau = (k_{fl} + k_{ISC} + k_{IC})^{-1}$

From the previous discussion, it can be seen that the first term on the right hand side of (1) dominates at room temperature while the second dominates at 77 K . The rate k_{-v} as thermal activation originates in interaction with the solvent, must be temperature dependent; therefore:

$$k_{-v} / k_v = \exp (- \hbar \omega / k T)$$

Due to the low intensity of fluorescence from the states with energy 260 cm^{-1} and 1060 cm^{-1} above S_1, only the other two will be considered.

The calculated values are presented in Table 2, using $\tau = 1,2 \times 10^{-7}$ s [8].

TABLE 2

Origin of Band	(ϕ^* / ϕ) 293 K	k_{fl}^* / k_{fl}	$\phi^*_{77} / \phi^*_{293}$	k_v (s^{-1})
C *	0.1	1.3	3×10^{-3}	2×10^9
D *	0.03	1.5	1.5×10^{-3}	6.5×10^9

The vibronic character of the "hot" states is clearly apparent from the slow rate of redistribution of the vibrational energy of the active modes, when compared with the same rate of a pure vibrational mode in solution (of the order of 10^{11} s^{-1}).

3.2 — *Comparison between intensity of "hot" and "normal" peaks and theoretical calculations*

It is possible to calculate the ratio of Einstein's B coefficients for "hot" and corresponding "normal" peaks directly from the experimental values of peak intensities at room temperature. As at this temperature the "hot" state is dominantly thermally populated, and under the assumption that the rates of intersystem crossing and internal conversion from the "hot" states are of similar order

of magnitude as from "normal" states, the ratio B* / B ("hot" / "normal") will be:

$$B^* / B = (I^* / I) \left(\frac{E_1 - \hbar\omega}{E_1 + \hbar\omega} \right)^3 \exp (\hbar\omega / kT)$$

The results obtained from the measured intensities are presented in Table 3. They clearly deviate from the Herzberg - Teller model, that predicts a ratio of 1 for the two corresponding peaks.

TABLE 3

$\hbar\omega$	260	530	800	1060
B * / B Exp. results	1.5	4.1	5.5	16.6
B * / B Calculated	2.1	4.8	12.8	46.9

This clearly points to the fact that electrons do not follow instantaneously the nuclear motion, and a breakdown of Born - Oppenheimer approximation has to be taken into account.

In the present calculation, based on previous results [6], a simpler model is used, with the following simplifying assumptions:

I — Interactions occur only between S_1 and S_2, $S_2 \rightarrow S_0$ being symmetry allowed and $S_1 \rightarrow S_0$ symmetry forbidden.

II — The vibrational modes of the molecules behave like harmonic oscillators, with the same frequencies in S_0, S_1 and S_2.

III — Only one symmetrical mode shows transitions from S_0 to S_1 and S_2.

IV — The translation of this mode is the same in S_1 and S_2.

V — The modes active in the mixing are uncoupled, with coordinate Q_a, wave function χ_a and energies $\hbar\omega_a$.

The operator that accounts for the breakdown of the Born - Oppenheimer approximation mixes S_1 and S_2, one state

Portgal. Phys. — Vol. 14, fasc. 3-4, pp. 211-222, 1983

219

with the vibrational active mode in its ground level and the other in the first excited state, due to the term of the breakdown operator $\partial / \partial Q_a$ that acts on χ_a [6].

Labelling the unperturbed wave function (adiabatic Born - Oppenheimer) with two indexes, the first referring to the electronic part and the second to the vibrational part of the wave function, the mixing occurs between $\psi_{1,1}$ and $\psi_{2,0}$ in absorption or "hot" emission, and between $\psi_{1,0}$ and $\psi_{2,1}$ in "normal" fluorescence.

Therefore the mixing states are separated by $E_2 - E_1 - \hbar \omega_a$ and $E_2 - E_1 + \hbar \omega_a$ respectively.

Because it is only the S_2 character of the vibronic states that accounts for the transition dipole moment between those states and S_0, their ratio will be:

$$M_{0 \to 1} / M_{1 \to 0} = (E_2 - E_1 - \hbar \omega_a) / (E_2 - E_1 + \hbar \omega_a)$$

and therefore:

$$B^* / B = [(E_2 - E_1 - \hbar \omega_a) / (E_2 - E_1 + \hbar \omega_a)]^2 \qquad (2)$$

Equation (2) provides a straightforward means of calculating the ratio B^* / B for the different vibronic states. The results are shown in Table 3.

The agreement with experiment is fair in the lower energy states, but deviates for the other two.

Some causes may account for this fact: If hypothesis IV is not satisfied, that is, if the translation of the symmetrical mode is not the same for S_1 and S_2 then a mixing of S_1 with S_2 with the 1400 cm^{-1} mode in its first excited level is possible, as the vibrational wave functions of this mode in the two states will no longer belong to the same orthonormal set. This effect will be larger for the higher energy mixing modes as the ratio will now be given by $(E_2 + 1400) - E_1 \pm \hbar \omega_a$.

However to get agreement with experiment it would have to be assumed a larger contribution of this term than the previously considered one, which is unlikely as the symmetrical progressions do not differ much for $S_0 \to S_2$ absorption and $S_1 \to S_0$ vibronic emission.

Another reason for the experimental ratios being smaller than the theoretical ones can be the fact that $S_1 \to S_0$ is not totally

forbidden as assumed in I. Therefore some of the molecules in a vibronic state (S_i^*) can decay to a ground state with the mixing mode in its first excited level, that is, at an energy corresponding to the A transition. This accounts for a decreased intensity in the "hot" fluorescence from the vibronic states. The weaker the vibronic mixing, the more pronounced is this effect on the measured ratios.

The spectrum however shows that the 800 cm^{-1} mode is the one that gives the higher intensity of fluorescence so the mixing is strong, for this mode. Obviously this effect can not account for the results.

On the other hand the experimental values of the ratios for the B coefficients from spectra in the gas phase [14] are closer to the calculated ratios.

It seems more likely that the ratio of intersystem crossing from the higher vibronic states is larger than for the other states.

This will be possible if there is a triplet state close in energy with $E_1 + 800$ cm^{-1}, to which intersystem crossing is possible, likely T_2 ($E_1 + 800$ cm^{-1} and $E_1 + 1060$ cm^{-1} are 620 cm^{-1} and 360 cm^{-1}, respectively, below S_2). In the gas phase the energy gap between S_1 and S_2 is larger, and so the vibronic levels will be all below T_2; so the rate of intersystem crossing will be again of similar order of magnitude for all states, and so the experimental results are again closer to the theoretical values.

4 — SUMMARY

1-12 benzperylene is a molecule with an electronic structure that renders "hot" fluorescence a likely process. The analysis of the fluorescence spectrum both at room temperature and at 77 K (therefore in condensed phase) makes it possible to estimate the rate of vibrational redistribution of the energy of the vibronic states, that are rather larger than usually found for vibrational modes. Although the first absorption band is hidden under the second it can be shown from the ratio of intensities of "hot" and "normal" corresponding peaks, that the Born - Oppenheimer approximation does not hold. A perturbation method based on the departure from this approximation gives ratios in fair agreement with experiment.

REFERENCES

[1] D. Huppert, J. Jortner, P. M. Rentzepis, *J. Chem. Phys.* **56**, 4826 (1972).

[2] M. Kasha, *Disc. Far. Soc.* **9**, 14 (1950).

[3] F. A. Geldof, R. P. H. Rettschnick and G. J. Hoytink, *Chem. Phys. Lett.* **4**, 59 (1969).

[4] J. B. Birks, *Inorganic Molecular Photophysics* vol. 2, pg. 453 (Wiley, 1975).

[5] G. Herzberg, and I. Teller, *Z. Physik. Chem.* **B21**, 410 (1933).

[6] P. A. Geldof, R. P. H. Rettschnick and G. J. Hoytink, *Chem. Phys. Lett.* **10**, 549 (1971).

[7] G. Orlandi, *Chem. Phys. Lett.* **19**, 459 (1973).

[8] J. G. Carter, L. G. Christophorou and C. E. Easterly, *J. Chem. Soc Farad. Trans.* **69**, 471 (1973).

[9] G. J. Hoytink, *Chem. Phys. Lett.* **26**, 16 (1974).

[10] G. J. Hoytink, *Chem. Phys. Lett.* **22**, 10 (1973).

[11] H. B. Lin, M. R. Topp, *Chem. Phys. Lett.* **67**, 273 (1979).

[12] K. Ohno, *Chem. Phys. Lett.* **70**, 526 (1980).

[13] V. R. Dawson, J. L. Kropp, *J. Chem. Phys.* **73**, 1752 (1969).

[14] M. Estela Pereira, To be published.

NONRADIATIVE RATES OF SINGLE VIBRONIC LEVELS IN BENZENE SINGLET STATE

S. J. Formosinho and A. M. da Silva

Departamento de Química, Universidade de Coimbra, 3000 Coimbra, Portugal

ABSTRACT — A tunnel effect theory is applied to the calculation of the rate constants for internal conversion $S_1 \rightsquigarrow S_0$ and intersystem crossing $S_1 \rightsquigarrow T_1$ of single vibronic singlet levels of C_6H_6. Coupling between the optically excited modes and the accepting CH modes was considered in terms of relative CH bond displacements. Within this model good agreement with experimental data was found. The dependence of the calculated internal conversion rates and the fluorescence lifetimes on the excess vibrational energy of the excited state supports the view that $S_1 \rightsquigarrow S_0$ via direct population of CH modes or of CC modes is responsible for channel 3.

1 — INTRODUCTION

Extensive calculations of the nonradiative rates of single vibronic levels (s. v. l.) of benzene S_1 state have been presented in the literature [1-4], owing to their relevance to the theories of radiationless transitions in large molecules. Freed and coworkers [1, 2] have employed a molecular compound state formalism and have essentially calculated the relative nonradiative rates as a function of vibrational energy. The rate of nonradiative transition between two single vibronic levels, s and l, for a state s in a vibrational level $\{ n_a \}$, is given by

$$k_{sl}(m_a) = (2\pi/\hbar)|C_{sl}^k|^2 \sum_{\{n_a\}} \prod_{a \neq k} |<m_a|n_a>|^2 I[\Delta E_{sl}(\{m_a\})]$$

where $\{ m_a \}$ are the possible sets of final levels, $I(\Delta E)$ is a density of states weighted Franck-Condon factor and C_{sl}^k is the matrix element for the promoting mode k. Since only relative rates for the $S_1 \rightsquigarrow T_1$ transition were calculated the matrix

element C_{sl}^k was not determined [1]. However the experimental results show that intersystem crossing (i.s.c.) is not the only important channel of decay in the isolated molecules, but that there is also an internal conversion (i.c.) to the ground state, $S_1 \rightsquigarrow S_0$, even from the lowest excited vibronic levels [5]. Estimations of the matrix elements for the $S_1 \rightsquigarrow T_1$ and $S_1 \rightsquigarrow S_0$ transitions by Freed et al. [2] gave absolute rates two orders of magnitude smaller for i.s.c. and ten orders of magnitude smaller for the i.c. process. Therefore, although the theory has been able to estimate relative rates in good agreement with experiment, it has not been able to reproduce absolute rates and treat properly i.c. and i.s.c. in benzene S_1 state.

We have employed a tunnelling formalism [3, 4] for such calculations. However only the effect of excess vibrational energy was considered and there was no attempt to treat the nonradiative rates of selected s.v.l. . Here we intend to extend such studies to calculate nonradiative rates of i.c. and i.s.c. in selected s.v.l. in C_6H_6, by employing a tunnel effect theory. Recently Jortner and Ulstrup [6] have shown that for nonradiative transitions of a large electronic energy-gap the molecular compound state theories can be reduced to the tunnel effect formalism for the Franck-Condon factors and the preexponential factor is given by $2\,|\,C_{sl}^k\,|^2 \hbar^{-1} \nu$, where ν is the frequency of an effective vibrational mode. Nevertheless since the multiphonon nonadiabatic transition theories of Jortner and Freed provide underestimates of absolute rates in spite of extensive and difficult calculations of the matrix elements, we will employ the tunnel effect theory in its complete formalism.

2 — TUNNEL EFFECT FORMALISM

The tunnel effect theory for radiationless transitions has been extensively described [3, 7]. Consequently here we will only present the formalism employed in the present calculations. In spite of the fact that benzene S_1 state, at low pressures (~ 0.1 Torr), is in a pseudostatistical situation with respect to i.s.c. [5, 8], theory shows that in a large isolated molecule the average singlet decay is exponential and pressure independent [9]. Therefore the nonradiative rates can be estimated as it were for a statistical case in i.s.c. and i.c. .

Of all the vibrational modes of an aromatic molecule the CH modes are the ones of the smallest reduced mass and consequently are the ones that provide the highest tunnelling rates for weakly displaced oscillators. In a previous study we have considered that the excess of vibrational energy in benzene was redistributed statistically between all the vibrational modes. The effect of vibrational energies in the nonradiative rates was a consequence of the population of the CH modes in high vibrational levels. Such an approach is adequate when intramolecular vibrational relaxation is a process faster than the radiative and nonradiative transitions. However in an isolated molecule such as S_1 benzene such approach is no longer valid. Therefore, except where otherwise stated, we have considered the CH modes with zero point energy, since no direct excitation of the CH modes was experimentally achieved. The effect of the vibrational excitation of other vibrational modes on the CH modes was considered by studying the coupling of these modes with the CC modes. The displacement of the C atom during a CC stretching in the S_1 state leads to a change of equilibrium position of the CH bond in the excited state, with respect to the equilibrium position of the CC and the CH modes in the final state. Such a change of the relative equilibrium position can decrease the barrier width for tunnelling and consequently increase the rates of radiationless transitions. Thus the increase of vibrational energy in a CC mode is translated in a displacement of the potential energy curves of the CH modes.

In the present calculation all the vibrational modes were taken as anharmonic. The potential curves were considered as Morse curves

$$V(x) = D_e (1 - e^{-\beta x})^2 \tag{1}$$

where $V(x)$ is the potential energy for a bond extension or contraction, x. The effective potential energy curve for n identical oscillators [7] is considered for coordinates of a symmetric motion and therefore $\beta = n^{1/4} \, 1.2177 \times 10^7 \, \omega \, \sqrt{\mu/D_e}$ where ω is the frequency of the oscillator, μ its reduced mass and D_e the dissociation energy. The relative displacement for the origin of the effective potential energy for n oscillators is given by [10]

$$R = \left[\sum_i (\Delta r_i)^2 \right]^{1/2} \tag{2}$$

where Δr_i is the change in bond length between the initial and the final electronic states.

The nonradiative transitions are considered to occur via a quantum mechanical tunnelling of oscillators through an energy barrier of the effective potential energy curves in two electronic states. If reflections are ignored and within the WKB approximation, the rate of tunnelling of a particle through a potential energy barrier [3] is given by

$$k_{nr} = 4 f \omega [(D - E_v) E_v / D^2]^{1/2} .$$

(3)

$$\exp \left\{ - \frac{4\pi}{\hbar} \int_{x_1}^{x_2} 2\mu [D_e (1 - e^{-\beta(x-R)})^2 + \Delta E - D_e (1 - e^{-\beta x})^2]^{1/2} dx \right\}$$

f is a forbidden factor which has an electronic (and vibronic) nature and is treated as an empirical parameter. The rates k_{nr} are estimated for the CH stretches which are the ones of highest frequencies and lowest reduced masses, and consequently are the modes which have the largest Franck-Condon factors. In eqn (3) D is the energy of the crossing point of the potential energy curves involved in the transition, E_v the vibrational energy and ΔE the difference in electronic energy between the two states; x_2 is the coordinate of the turning point in the final state, isoenergetic with the initial vibronic state and x_1 is equal to R plus the relative change of origin due the coupling of the CH and CC modes. Such a coupling depends on the nature of the CC modes of vibration. For the C stretch 1 mode the change in the CC bond length at the turning points of vibration is added completely to R (CH) since both stretches are colinear; for the 6 and 16 modes the change in length of the projection along the CH directions was considered.

The relevant parameter for the i.c. $S_1 \rightsquigarrow S_0$ and $S_1 \rightsquigarrow T_1$ transitions are $\Delta r_{CH} = 0.0014$ nm for $S_1 \rightsquigarrow S_0$ [11] and $\Delta r_{CH} = 0.0004$ nm for $S_1 \rightsquigarrow T_1$ [12] and according to eqn (2) for 6 oscillators

$$R_{S_1 \rightsquigarrow S_0} = 0.00343 \text{ nm} , \quad R_{S_1 \rightsquigarrow T_1} = 0.00098 \text{ nm} .$$

The electronic energies are $E_{S_1} = 38200 \text{ cm}^{-1}$ and $E_{T_1} = 29000 \text{ cm}^{-1}$. The characteristics of the potential curves for i.c. and i.s.c. gave higher rates for the transitions on the repulsive part of the potential energy curves.

226

Portgal. Phys. — Vol. 14, fasc. 3-4, pp. 223-233, 1983

As we have previously stated the forbidden factors are treated as empirical parameters. They reflect the role of the promoting modes which are difficult to assess in a quantitative manner [1, 13]. Heller et al. [1] consider that the population of a promoting mode effectively reduces the true energy gap for the nonradiative transition increasing the nonradiative rate and tentatively they consider a reduction of 1500 cm^{-1}. However by the same reasoning the maximum Franck-Condon factor for the accepting modes would have been obtained with a large population of the promoting modes which reduces the effective energy gap to zero. However in their own way the promoting modes have Franck-Condon restrictions. Therefore we will not consider any reduction in the effective energy gap for the electronic transition between the different electronic states since the role of the promoting modes is treated empirically by a forbidden factor. For i.s.c. processes between π, π^* states in aromatic molecules the spin forbidden factor is typically of the order of 10^{-5} - 10^{-6}, as revealed by the phosphorescence and absorption spectra [14]. For i.c. process the forbidden factor can only arise by symmetry considerations and is generally very weak (ca. 10^{-1}). Nevertheless symmetry does not seem to play any significant role in nonradiative internal conversion processes [15]. The forbidden factors were estimated such that the i.s.c. and i.c. rates, together with the radiative rate constant $2.2 \times 10^6 s^{-1}$ [16], reproduce the triplet ($\phi_T = 0.70$) and i.c. ($\phi_{ic} = 0.08$) quantum yields, from the lowest vibrational level in S_1 [5] and its nonradiative rates [16]. The forbidden factors were for the zero level $f_{ic} = 0.57$, $f_{i.s.c} = 0.82 \times 10^{-5}$. A set of data was calculated for all the other s.v.l. with the same value of $f_{i.s.c}$ and for $f_{i.c} = 0.57$ and $f_{i.c} = 1.0$.

3 — RESULTS AND DISCUSSION

Table 1 presents the results of the calculations which reveal that a tunnel effect formalism is able to give a fair account (within ca 20 % error) of the absolute rates of the nonradiative transitions in C_6H_6 in terms of i.c. and i.s.c.. Depending on the nature of the populated modes the best agreement is obtained with $f_{ic} = 0.57$ (modes 6^m and $6^m 1^n$) and with no forbidden factor for the 1^n and $1^n 16^p$ modes. Comparison between this

TABLE 1 — Nonradiative Rates of Single Vibronic Levels in Benzene S_1 State.

Levels	Energy above origin (cm^{-1})	k_{ic} ($10^6 s^{-1}$)		k_{isc} ($10^6 s^{-1}$)	k_{nr} ($10^6 s^{-1}$)		
					Calc.		Obs. [16]
		$f_{ic} = 0.57$	$f_{ic} = 1.0$		$f_{ic} = 0.57$	$f_{ic} = 1.0$	
0	0	0.8	—	7.0	7.8	—	7.8
6^1	521	1.6	2.8	7.7	9.3*	10.5	9.3
6^2	1042	3.2	5.6	8.4	11.6*	14.0	9.9
1^1	923	1.4	2.4	7.7	9.1	10.1*	9.5
1^2	1846	2.2	3.9	8.4	10.6	12.3*	13.5
1^3	2769	3.8	6.6	9.2	13.0	15.8*	18.9
$6^1 1^1$	1444	2.7	4.7	8.4	11.1*	13.1	11.1
$6^2 1^1$	1965	5.4	9.6	9.2	14.6*	18.8	12.8
$6^1 1^2$	2367	4.5	7.9	9.2	13.7*	17.1	15.2
$6^2 1^2$	2888	8.8	15.5	10.2	19.0*	25.7	20.8
$6^1 16^1$	764	1.7	3.1	7.7	9.4	10.7	9.6
$6^1 16^2$	1007	1.9	3.3	7.7	9.6	11.0	11.6
$6^1 1^1 16^1$	1687	2.8	5.0	8.4	11.2	13.4*	13.7
$6^1 1^1 16^2$	1930	3.1	5.5	8.5	11.5	14.0*	16.4
$6^1 1^2 16^1$	2610	4.8	8.5	9.2	14.0	17.7*	21.7
$6^1 1^3$	3290	16.6	29.0	11.0	27.6	40.0	—

* Values closer to experimental data.

calculation and previous approaches [1, 2] is not valid, because the other models were adjusted to reproduce relative rates in terms only of $S_1 \leadsto T_1$ i.s.c.. However we can compare our range of discrepancy with respect to the experimental data (1.23) to the ones of Heller et al. [1] (1.66); for the $6^m 1^n$ progression the highest discrepancy is 1.14 and 1.18 respectively.

The present calculations can be employed to discuss the controversial problem of the nature of channel 3 in C_6H_6 [2, 4, 15, 17-22]. Upon excitation at 240 nm the rates of nonraditive decay in benzene increase so much that fluorescence emission becomes very weak. Due to the very fast rates the initial lifetime data was obtained by measurement of linewidths [17]. Based on such data several explanations were proposed such as radiationless transitions to another state [4, 21] or simply an enhanced i.c. [18],

although strong doubts were raised about the possibility of i.c. being able to interpret channel 3. However since factors other than population relaxation could contribute to line broadening such as internal vibrational randomization, the need for direct fluorescence measurements was necessary. Such experiments were carried out recently by employing very fast laser pulses [15, 20]. The lifetime measurements confirm the very fast rates of nonradiative decays in this region, but are not identical to the linewidth measurements of Callomon et al. [17].

Theories of radiationless transitions predict an exponential dependence of nonradiative rates with an increase on the vibrational energy, E_v, of the excited state [3, 6, 13] as Fig. 1 reveals. The
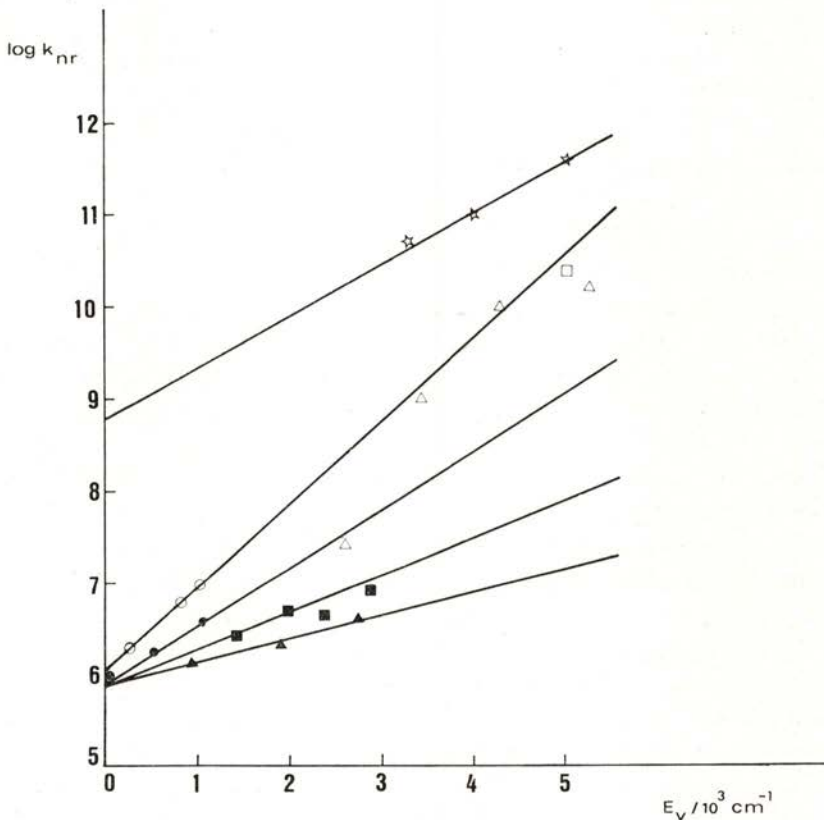
Fig. 1 — Vibrational energy dependence of the calculated i.c. rates ($f_{i.c.} = 0.57$) and channel 3 data: (●) 6^m, (■) $6^m 1^n$, (▲) 1^n, (o) $7^p 1^n$; Callomon's data [17] (☆), Takagi's [20] (□) and Wunsch's [15] (△).

Portgal. Phys. — Vol. 14, fasc. 3-4, pp. 223-233, 1983

229

interesting point is that although this behaviour was also present in Callomon's data, the rates extrapolate to rates ca. $6 \times 10^8 \text{ s}^{-1}$, at zero vibrational energy. Since much lower rates ($\sim 10^6 \text{ s}^{-1}$) were observed from this levels such a behaviour suggests the onset of another process at 3000 cm^{-1} excess energy above S_1. However this is not the situation with the more recent data based on fluorescence lifetime studies. In particular the most accurate data which was based on one photon absorption and was pressure independent up to 20 torr (C_6H_6) allowed an estimation of a lifetime of 42 ps for the $7^1 1^2$ level. This level involves the direct population of a CH mode (7 mode). We have performed calculations for the i.c. rates with the population of a CH mode which has a faster E_v dependence than the 6^m or $6^m 1^n$ modes (Fig. 1). The data extrapolate well to the experimental value of Takagi et al. [20] at $E_v \simeq 4950 \text{ cm}^{-1}$. For other levels which do not involve the population of the CH modes, the data of Wunsch et al. [15] for the $14^q 1^n$ levels can also be interpreted reasonably well in terms of an i.c. process. At high excitation energies the data fits better the curve for the population of CH modes. However this data was not determined directly from lifetime measurements owing to the time resolution of the experimental system, but was estimated from the fluorescence intensities. The present results support the view that in C_6H_6 S_1 isolated state, in the current region of excitation ($E_v = 0$ to 5000 cm^{-1}), there are only two channels of nonradiative decay: the internal conversion $S_1 \rightsquigarrow S_0$ and the intersystem crossing $S_1 \rightsquigarrow T_1$. Channel 3 would be simply the result of a fast increase of internal conversion with the excess vibrational energy in S_1.

A final word should be said on the triplet yields in C_6H_6 as a function of vibrational energy. Since $S_1 \rightsquigarrow S_0$ increases faster than $S_1 \rightsquigarrow T_1$ the triplet yield decreases with an increase in excitation energy. Only recently the experimental techniques of supersonic free jets allowed some measurement of the triplet yields in isolated molecules as a function of vibrational energy. Otis et al. [22] have employed a supersonic molecular beam of C_6H_6 to ensure isolated molecule conditions. The singlet S_1 state is populated by a laser pulse and allowed to evolve in time. Following this, excited molecules are pumped by a second pulse which photoionizes the molecules in S_1 and T_1. The decays are analyzed in terms of a biexponential attributed to S_1, the fast

component, and to T_1, the slow component. The ratio of the two components allows the estimation of the triplet yields. However such analysis is based on the statistical behaviour for the nonradiative transition in isolated excited C_6H_6. Fig. 2 reveals
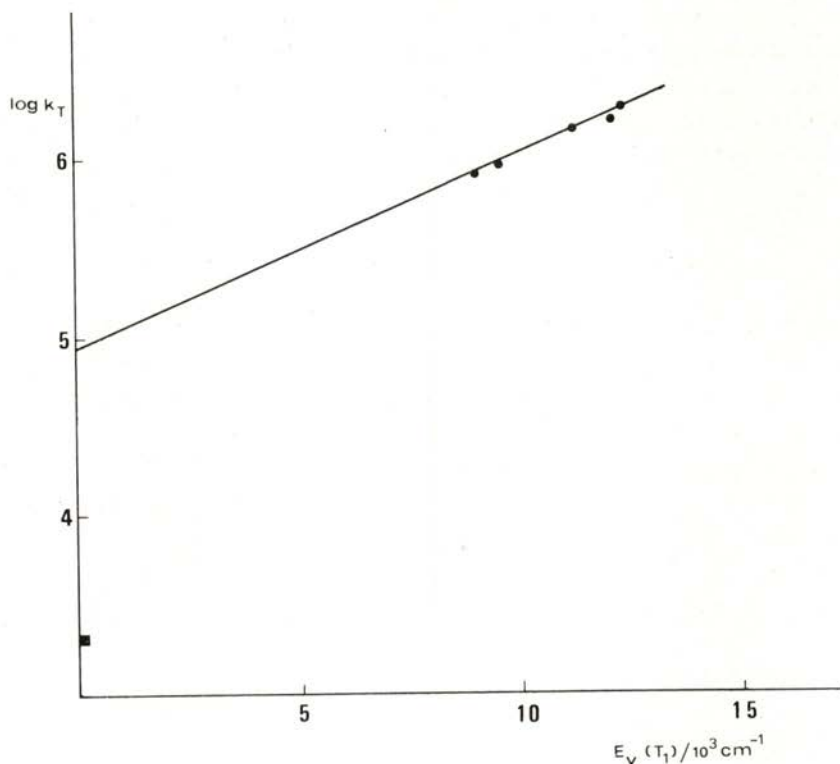
Fig. 2 — Logarithmic plot of the triplet decay rates k_T [22] as a function of triplet vibrational energy; triplet decay rate (■) from the thermally equilibrated T_1 state.

that benzene T_1 state is not on a statistical case. In fact the decay rates [22] of the vibrationally excited T_1 levels do not extrapolate to the T_1 decay rate in vapour phase at high pressures, $2 \times 10^3 \text{ s}^{-1}$ [23]; the extrapolated value is almost two orders of magnitude higher, $9 \times 10^4 \text{ s}^{-1}$, revealing that the hot triplet levels, T_1^v, have a different channel of decay than T_1^o. The decays are considered to

be $T_1^v \rightsquigarrow S_1 \, (E_v \, (T_1) \geqslant E_{S_1} - E_{T_1})$ and $T_1^o \rightsquigarrow S_o \, (E_v \, (T_1) < E_{S_1} - E_{T_1})$. Consequently the biexponential decay observed in the photoionization experiments may have some contribution of S_1 in the slow component and of T_1 in the fast component. Nevertheless in relative terms the analysis of Otis et al. [22] reveals a decrease in ϕ_T with an increase in E_v. Such a decrease is in reasonable agreement with the yields estimated from the calculated nonradiative transitions, as shown in Table 2. The best agreement is apparently with $f_{i.c} = 1.0$ but no conclusion can be made, because the absolute values of Otis et al. [22] may be subjected to some error owing to the assumption of a statistical behaviour.

TABLE 2 — Triplet Quantum Yields from Singlet Levels

Levels	E_v (cm^{-1})	Experimental Values		Calculated	
		a	b	$f_{ic} = 0.57$	$f_{ic} = 1.0$
6^0	0	0.62	0.70	—	—
6^1	521	0.58	0.65	0.67	0.61
$6^1 1^2$	2367	0.57	0.64	0.63	0.49
$6^1 1^3$	3290	0.29	0.33	0.40	0.28

a Values of ref [22].
b Values of ref [22] corrected for the yield 0.7 at zero level.

The yield for all the triplet vibronic levels from the zero singlet level calculated by Otis et al. [22] is smaller than the yield from the thermally equilibrated molecule (0.70). This difference cannot be due to the thermal population of higher singlet vibronic levels, because this would decrease ϕ_T even further. The discrepancy may be due to the assumption of the statistical behaviour for T_1. When the yields are corrected for $\phi_T = 0.70$ a better agreement is found with the calculated yields for $f_{i.c} = 0.57$ (Table 2).

REFERENCES

[1] D. F. HELLER, K. F. FREED and W. M. GELBART — *J. Chem. Phys.*, 56, 2309 (1072).
M. PAGITSAS and K. F. FREED — *Chem. Phys.*, 23, 387 (1977).

[2] M. G. PRAIS, D. F. HELLER and K. F. FREED — *Chem. Phys.*, 6, 331 (1974).

[3] S. J. FORMOSINHO — *J. C. S. Faraday II*, 70, 605 (1974).

[4] S. J. FORMOSINHO and J. DIAS DA SILVA — *Mol. Photochem.*, 6, 409 (1974).

[5] S. J. FORMOSINHO and A. M. DA SILVA — *J. C. S. Faraday II*, 72, 2044 (1976).

[6] J. JORTNER and J. ULSTRUP — *Chem. Phys. Letters*, 63, 236 (1979).

[7] S. J. FORMOSINHO — *Mol. Photochem.*, 7, 41 (1976).

[8] S. J. FORMOSINHO, and A. M. DA SILVA — *J. Chem. Phys.*, submited for publication.

[9] S. J. FORMOSINHO and A. M. DA SILVA — *Mol. Photochem.*, 9, 257 (1979).

[10] E. F. McCOY and I. G. ROSS — *Austral. J. Chem.*, 15, 591 (1962).

[11] G. HERZBERG — *Molecular Spectra and Molecular Structure* (III Electronic Spectra and Electronic Structure of Polyatomic Molecules) D. van Nostrand, London (1966), p. 666.

[12] D. P. GRAIG — *J. Chem. Soc.*, 2146 (1950).

[13] M. D. MORSE, A. C. PUIU and R. E. SMALLEY — *J. Chem. Phys.*, 78, 3435 (1983).

[14] J. B. BIRKS — *Photophysics of Aromatic Molecules* (Interscience, London, 1970).

[15] L. WUNSCH, H. J. NEUSSER and E. W. SCHLAG — *Z. Natürforsch Teil A*, 36, 1340 (1981).

[16] K. G. SPEARS and S. A. RICE — *J. Chem. Phys.*, 55, 5561 (1971).

[17] J. H. CALLOMON, J. E. PARKIN and R. LOPEZ-DELGADO — *Chem. Phys. Letters*, 13, 125 (1972).

[18] M. JACON — *Chem. Phys. Letters*, 47, 466 (1977).

[19] P. AVOURIS, W. M. GELBART and M. A. EL-SAYED — *Chem. Rev.*, 77, 793 (1977).

[20] Y. TAKAGI, M. SUMITANI, N. NAKASHIMA, D. V. O'CONNOR and K. YOSHIHARA — *J. Chem. Phys.*, 77, 6337 (1982).

[21] C. FISCHER and R. NAAMAN — *Chem. Phys. Letters*, 42, 581 (1976).

[22] C. E. OTIS, J. L. KNEE, P. M. JOHNSON — *J. Chem .Phys.*, 78, 2091 (1983); *J. Phys. Chem.*, 87, 2232 (1983).

[23] T. F. HUNTER and M. G. STOCK, *J. C. S. Faraday II*, 70, 1028 (1974).

EVEN MAGNETOOPTICAL EFFECT IN COBALT THIN FILMS

Francisco Carmona González

Instituto de Física de Materiales. Serrano 144. Madrid-6. Spain

ABSTRACT — In a study of cobalt thin films, hysteresis loops, magne-tooptically determined, were displaced along the magnetization axis. This can be explained by assuming that an even magnetooptical effect is present. Use is made of observed displacements to evaluate this effect for different film thicknesses and deposition angles; it amounts to 30 % of Kerr effect for films of 150 Å obtained by normal incidence.

1 — EXPERIMENTAL

Cobalt thin films were vacuum deposited on Corning "7059" glass slides. Evaporation was achieved by electron bombardment, and vacuum during deposition was better than 10^{-6} Torr.

Several sets of films were obtained, with thicknesses ranging from 150 to 1000 Å, placing the substrates in such a way that, within each set, thickness was the same (± 25 Å) for all films, whilst θ , angle of incidence of the flux on the substrate (deposition angle), was different for each one.

Placing substrates at 50 cm, or nearer, to the emitting focus, gave as a result, especially for those films obtained under high incidence, non-uniformity in thickness. However magnetooptical measurements were made of areas uniform within 5 % or less.

Hysteresis loops were traced with the device sketched in Fig. 1. The film, located between the pole pieces of an electromagnet, with which fields up to ± 5000 Oersted are applied, is parallel to the applied field and can be rotated around an axis perpendicular to it; it is thus possible to determine hysteresis loops along different directions in the plane of the films. This was necessary

. because, due to oblique incidence, anisotropic properties were expected [1], [2], [3].

Reflectivity was measured at H = 5000 Oe and H = — 5000 Oe by noting voltage drop across resistance R of Fig. 1.

Some samples were also measured by means of a vibrating sample magnetometer.
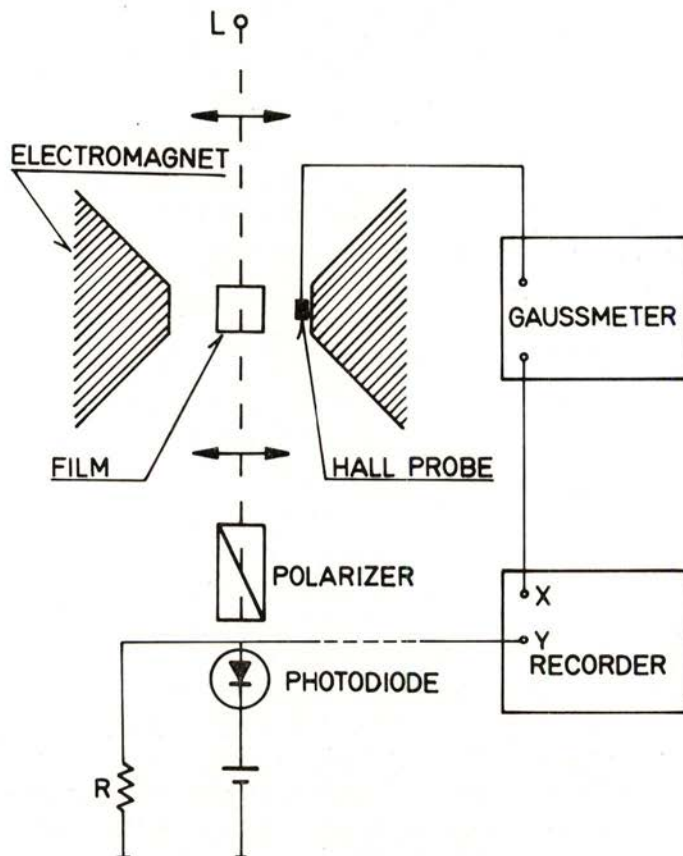
Fig. 1 — Kerr effect device for the measurement of thin films

White light from lamp L, reflected in the film under an angle of 60°, passes through calcite polarizer in P position and finally reaches a photodiode. Voltage across resistance R is thus proportional to the reflectivity of the film, and because of the equatorial Kerr affect, proportional to its magnetization. This voltage is adequately processed and applied to the vertical axis of an XY recorder.

2 — RESULTS AND DISCUSSION

Magnetooptic measurements gave hysteresis loops displaced along the magnetization axis. The magnitude of these displacements is direction dependent, and shows a variation with angle of measurement with the same periodicity as coercive force, remanence and reflectivity.

Hysteresis loops traced with a vibrating sample magnetometer were *not* displaced. Observed displacements would thus have to be ascribed to the magnetooptic method that was used.

The simplest explanation of these displacements is to assume that we have, superposed on the equatorial Kerr effect, an even magnetooptical effect; that is, to assume that the *apparent*, or as measured, magnetization, μ, is given by

$$\mu = A m^2 + B m + C \tag{1}$$

where m is the *actual* magnetization.

A, B and C are easily determined: Let $\mu = \pm 1$ for $m = \pm 1$ and $\mu = (\mu_r)_\pm$ for $m = \pm m_r$, where $(\mu_r)_+$ and $(\mu_r)_-$ are (reduced) apparent remanences and m_r is the actual (reduced) remanence. It follows that

$$A = -C = -[(\mu_r)_+ + (\mu_r)_-] / 2(1 - m_r^2) \quad , \quad B = 1 \tag{2}$$

$$m_r = [(\mu_r)_+ - (\mu_r)_-] / 2$$

It is thus possible to correct displaced hysteresis loops. But the point is that the first of eqs. (2) allows us to evaluate the magnitude of the even magnetooptical effect that causes the displacement.

In Fig. 2 we have mean values of A against deposition angle for different thicknesses. Straight lines are least squares fits in order to show tendencies: an increase of A with θ, except for the thinner films group (125-175 Å).

It is to be noted that A values are relative, and that B is, as the second of eqs. (2) shows, arbitrarily made equal to unity. In order to arrive at "absolute" values, let us recall that Bm, the second term of eq. (1), is the equatorial Kerr effect. Values for

this are given in Fig. 3, in which δ , reduced reflectivity difference, is represented against thickness with θ as a parameter. Curves are best fit approximations to experimental values. Orders of
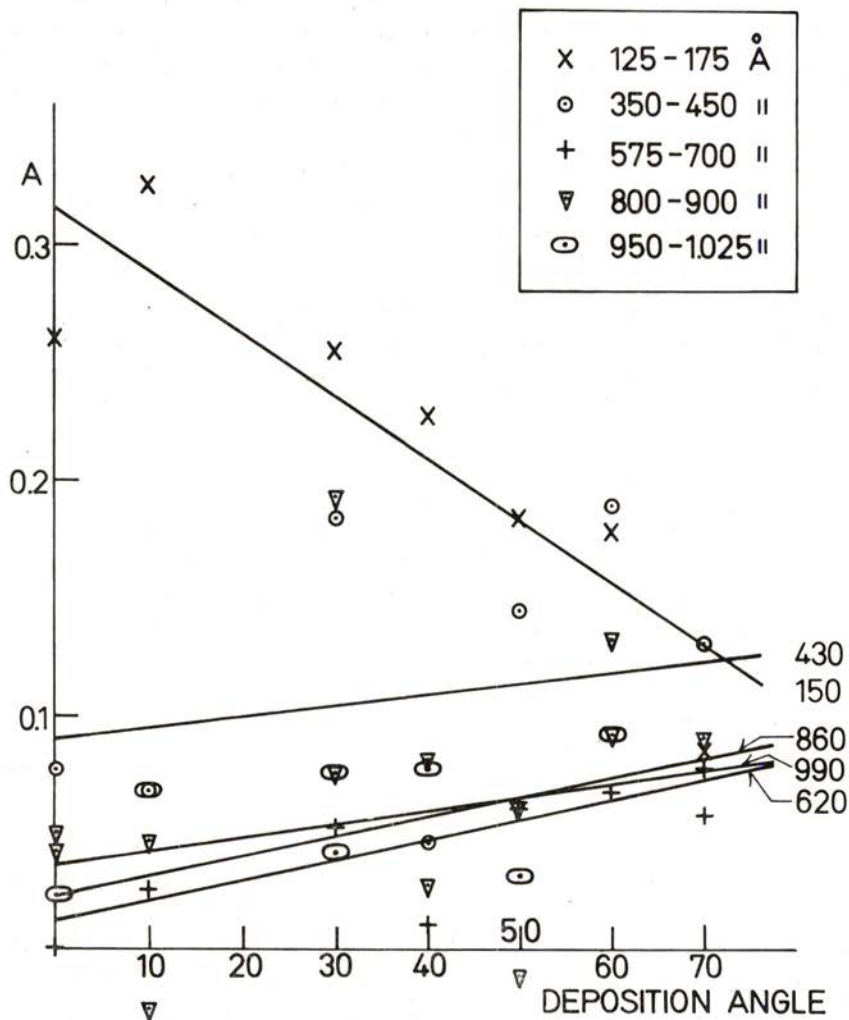
Fig. 2 — Mean values of A vs. deposition angle for different thicknesses

A is the magnitude of the even magnetooptical effect relative to the equatorial Kerr effect taken as unity. Films were measured along twelve different directions in their plane. The average over the twelve directions is here given for each film vs. deposition angle. Straight lines are least squares fits showing tendencies for groups of films of similar thickness.
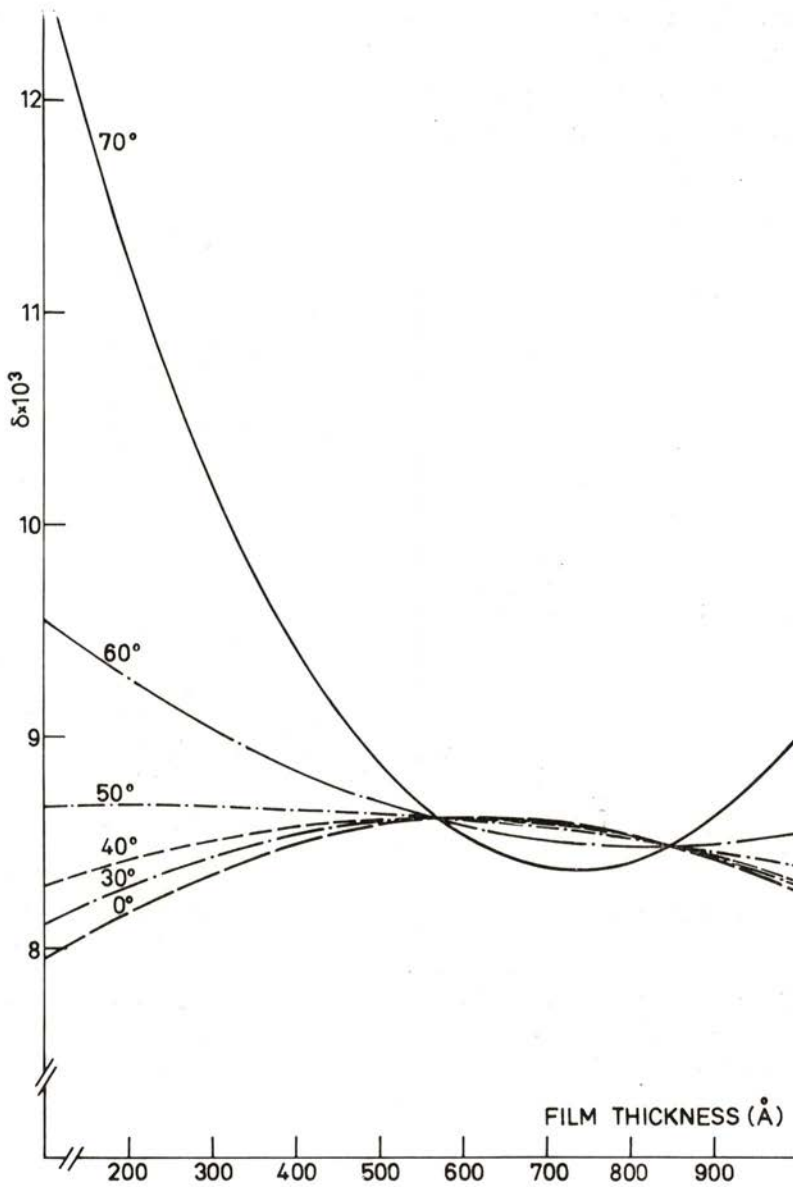
Fig. 3 — Reduced reflectivity difference vs. thickness for different values of θ.

Reduced reflectivity difference is defined as $\delta = (I_1 - I_2)/I_0$, where I_1 and I_2 are reflected light intensities corresponding to saturation states, and I_0 reflected light intensity for zero magnetization [4]. Curves are best fit approximations to mean values of δ over 12 directions in the plane of the film.

magnitude and shape of curves are in agreement with the work or Carey et al. [4].

A should be multiplied by the corresponding value of δ in order to have a measure of the even magnetooptical effect allowing comparison between samples. In Fig. 4 we have δ · A
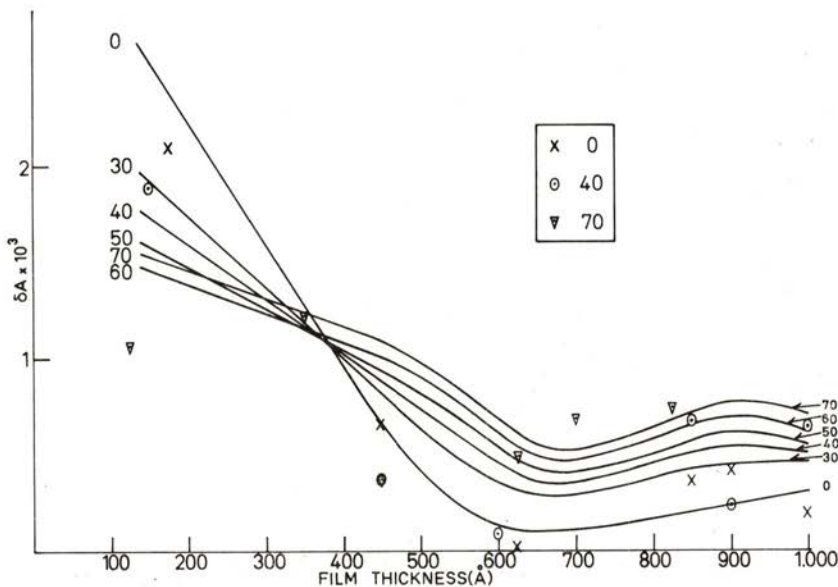
Fig. 4 — Even magnetooptical effect vs. thickness for different values of θ

A is just a measure of the even magnetooptical effect relative to the equatorial Kerr effect taken as unity. If each value of A is multiplied by the corresponding value of δ, we have a measure of the effect that allows comparison between samples. A · δ is represented vs. film thickness for different deposition angles. Curves are best fit approximations.

against thickness for different θ's. Experimental results can be seen to be somewhat dispersed, but the overall picture for the magnetooptical effect under consideration is clear: a) it is bigger for thinner films; b) it depends on the deposition angle under which the film was formed (higher for normal incidence for small

thicknesses, in the range 100-300 Å, and higher for oblique incidence in the range 500-1000 Å).

The nature of even magnetooptical effects has been thoroughly studied by Krinchik et al. [5], [6], [7] and by Afonso [8]. A striking feature of these effects, pointed out as a "paradox" in Ref. [6], is that their maximum value should correspond to zero magnetization, whilst their minimum value (zero) corresponds to saturation. There is no such paradox. A term proportional to the magnetization squared has the same value for $m = m_s$ and for $m = -m_s$; which amounts to no relative effect at all. On the other hand, it is necessary to add a constant to the term in m^2 (otherwise, it would not be possible to have symmetry for $m = \pm m_s$ unless $A = B = 0$). The effect is thus given by $Am^2 + C = A[(M/M_s)^2 - 1]$ with its maximum (absolute) value for $M = 0$.

REFERENCES

[1] D. O. Smith, M. S. Cohen, G. P. Weiss, *J. Appl. Phys.*, **31**, 1755-1762 (1960).
[2] D. E. Speliotis, G. Bate, J. K. Alstad, J. R. Morrison, *J. Appl. Phys.*, **36**, 972-974 (1965).
[3] E. Münster, *IEEE Trans. Mag.*, **7**, 263-267 (1971).
[4] R. Carey, D. M. Newman, B. W. J. Thomas, *J. Phys. D: Appl. Phys.* **10**, L131-L134 (1977).
[5] G. S. Krinchik, V. S. Gushchin, *JETP Letters*, **10**, 24-26 (1969).
[6] G. S. Krinchik, E. E. Chepurova, *JETP Letters*, **11**, 64-66 (1970).
[7] G. S. Krinchik, E. A. Gan'shina, *Sov. Phys. JETP*, **38**, 983-987 (1974).
[8] C. N. Afonso, «*Efectos magnetoópticos de simetría par en metales ferro-magnéticos*», Tesis, Universidad Complutense de Madrid, 1979.
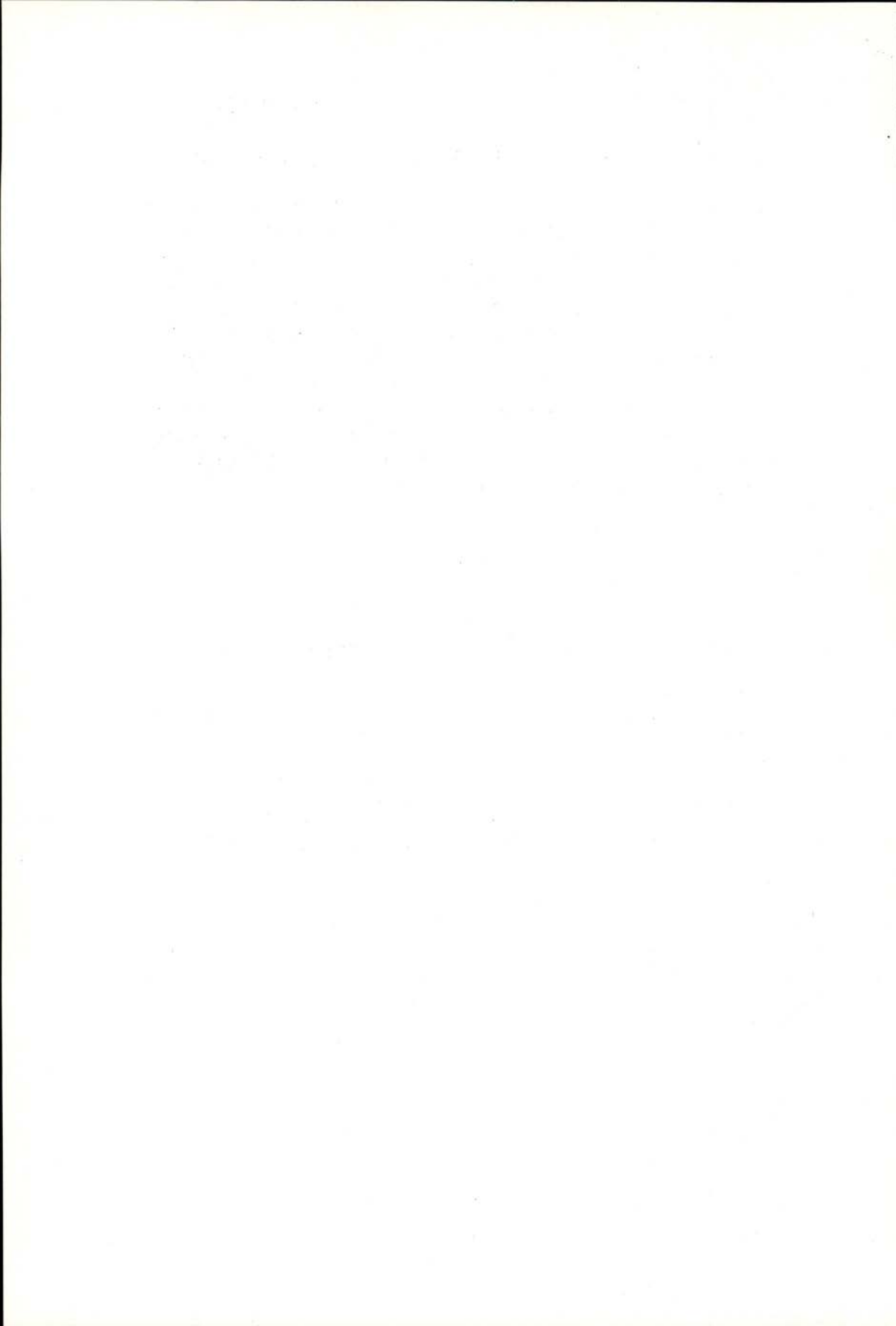
INSTABILITY SATURATION BY NONLINEAR MODE COUPLING IN A PLASMA

A. M. Martins and J. T. Mendonça

Centro de Electrodinâmica
Instituto Superior Técnico, 1000 Lisboa, Portugal

ABSTRACT — We study the instability saturation by the process of resonant three-wave coupling, comparing the results obtained in the fixed and random phase approximations. We show that the transition to chaos occurring in the fixed phase equations does not exist in the random phase equations. In quite general conditions the random phase leads to a well defined saturation level of the unstable mode.

1 — INTRODUCTION

It is now commonly accepted in Plasma Physics that the turbulent state arises from some instability which eventually saturates and breaks into a number of different modes. In this context, an important problem is the determination of the nonlinear state resulting from a linearly unstable wave.

One of the elementary processes leading to the instability saturation is the resonant three-wave coupling. The equations describing the interaction of three waves have been already studied, assuming that the two linearly damped modes into which the unstable mode decays are equal and further assuming that the unstable wave is strictly monochromatic [1], [2]. It has been shown numerically that in this case a strange atractor occurs and the wave amplitudes can behave chaotically. This fixed phase approximation is only valid when the frequency width of the unstable wave packet, Δ, is less than $1/\tau_c$, where τ_c is the characteristic time for the instability saturation.

In the present work we discuss the instability saturation from a more general point of view. In Section 2 we state the nonlinear equation for the wave field amplitude in its general form. In Section 3 we discuss the fixed phase approximation which can be used in order to solve the nonlinear equation. Section 4 is devoted to the analysis of the random phase approximation, which is valid when $\Delta \gg 1/\tau_c$. Finally in Section 5 we state the conclusions, and compare the results obtained in the fixed and random phase approximations.

2 — NONLINEAR EQUATION

Let us assume the general situation of an infinite, homogeneous and nonlinear dielectric medium, which can be a plasma. Using Maxwell equations and making space and time Fourier transforms we can get the equation of propagation for the electric field $E(k)$ in the following form:

$$D(k, \omega) \, E(k) = -(i/\omega \varepsilon_0) \, \hat{a}_k^* \cdot J_{NL}(k) \qquad (1)$$

where

$$D(k, \omega) = \frac{c^2}{\omega^2} \, | \, k \cdot \hat{a}_k \, |^2 - \frac{k^2 c^2}{\omega^2} + \hat{a}_k^* \cdot \overline{\overline{\varepsilon}}(k, \omega) \cdot \hat{a}_k \qquad (2)$$

In these equations $\overline{\overline{\varepsilon}}(k, \omega)$ is the dielectric tensor describing the medium, ω and k are the frequency and wavevector associated to the field $E(k)$ and $\hat{a}_k$ is the unit polarization vector. The nonlinear current appearing in equation (1) is given by:

$$J_{NL}(k) = \int \overline{\overline{\sigma}}(k, k') \cdot E(k') \, E(k'') \, e^{i\Omega t} \frac{dk'}{(2\pi)^3} \qquad (3)$$

where $\overline{\overline{\sigma}}(k, k')$ is the 'second order conductivity' tensor, $k'' = k - k'$ and Ω is the frequency mismatch

$$\Omega = \omega(k) - \omega'(k') - \omega''(k'') \qquad (4)$$

We see from equation (1) that when the nonlinear current is neglected, $J_{NL}(k) = 0$, a nontrivial solution for the electric wave field $E(k)$ implies that:

$$D(k, \omega) = 0 \qquad (5)$$

This is the linear dispersion relation which specifies ω as a function of k, $\omega = \omega(k)$. Equation (4) shows that, in the expression for the nonlinear current (3) we assume that each Fourier component of the electric field in the medium $E(k)$ obeys the linear dispersion equation (5). However, if the nonlinear current is taken into account, $J_{NL}(k) \neq 0$, equation (5) is no longer valid. Developping $D(k, \omega)$ around the linear dispersion relation we get [3]:

$$D(k, \omega) \simeq i \left(\frac{\partial D}{\partial \omega} \right)_k \left[\frac{\partial}{\partial t} + \mathbf{v}_k \cdot \frac{\partial}{\partial \mathbf{r}} + \gamma_k \right] \qquad (6)$$

where $\mathbf{v}_k = \partial \omega / \partial k$ is the linear group velocity and γ_k is the linear damping coefficient for the wave field $E(k)$. Replacing (6) in equation (1) we get the nonlinear equation in its final form:

$$(2\pi)^3 (d/dt + \gamma_k) E(k)$$
$$= - \int H(k, k') E(k') E(k-k') e^{i\Omega t} dk' \qquad (7)$$

where the total time derivative means:

$$\frac{d}{dt} = \frac{\partial}{\partial t} + \mathbf{v}_k \cdot \frac{\partial}{\partial \mathbf{r}} \qquad (8)$$

and the nonlinear coupling coefficient $H(k, k')$ is given by:

$$H(k, k') = \frac{\hat{a}_k^* \cdot \overset{=}{\sigma}(k, k') \cdot \hat{a}_{k'} \hat{a}_{k''}}{\varepsilon_0 \omega (\partial D / \partial \omega)_k} \qquad (9)$$

Equation (7) gives the rate of change of the Fourier component $E(k)$ of the electric field in the medium due to the nonlinear three-wave interaction of $E(k)$ with each of the pairs $E(k')$ and $E(k'')$ of the spectrum which satisfy the selection rule: $k = k' + k''$. The solution of this equation would give the turbulent

Portgal. Phys. — Vol. 14, fasc. 3-4, pp. 243-254, 1983

245

spectrum in a plasma if the three-wave interaction was the only process of energy exchange between the Fourier components of the spectrum. Actually, in a turbulent plasma, not only the four-wave or the higher order wave interaction processes are present but also are the wave-particle processes which cannot be described in the frame of the dielectric theory used here.

3 — FIXED PHASE APPROXIMATION

Let us apply the general nonlinear equation (7) to the case of instability saturation. The physical picture is the following: A given region of the spectrum around $k = k_1$ becomes unstable, due to the linear properties of the plasma. In this case we have $\gamma_1 = \gamma_{k_1} < 0$. If the unstable wave field attains a significant level, the nonlinear effect described by the right hand side of equation (7) is able to transfer a significant amount of energy from the unstable region of the spectrum to the stable regions where dissipation occurs. Instability saturation can then be achieved.

In order to discuss this process in detail it is useful to assume that the unstable spectrum reduces to a single wave $k = k_1$ and is described by a Dirac δ function. In this case, only two other waves defined by $k = k_2$ and $k = k_3$, such that $k_1 = k_2 + k_3$ can take energy from the unstable one and eventually saturate its growth. It is the so called fixed phase approximation. We can then wite:

$$E(k) = (2\pi)^3 \sum_{i=1}^{3} E_i \delta(k - k_i) \qquad (10)$$

Using this expression in equation (7) we get three coupled evolution equations:

$$(d/dt + \gamma_1) \, E_1 = -H \, E_2 E_3 \, e^{i\Omega t}$$

$$(d/dt + \gamma_2) \, E_2^* = -H' \, E_1^* E_3 \, e^{-i\Omega t} \qquad (11)$$

$$(d/dt + \gamma_3) \, E_3^* = -H'' \, E_1^* E_2 \, e^{-i\Omega t}$$

where $H = H(k_1, k_2)$, $H' = H(-k_2, k_3)$, $H'' = H(-k_3, k_2)$ and $\Omega = \omega(k_1) - \omega(k_2) - \omega(k_3)$. Using normalized amplitudes for the wave fields:

$$C_j = 1/2 \ (\partial D / \partial \omega)^{1/2}_{k_j} \ E_j \tag{12}$$

and defining real amplitudes a_j and phases ϕ_j such that

$$C_j = a_j \ e^{i \phi_j} \tag{13}$$

we can give to the system of equations (11) a symmetric form:

$$(d/dt + \gamma_1) \ a_1 = - V a_2 a_3 \sin \Theta$$

$$(d/dt + \gamma_2) \ a_2 = + V a_1 a_3 \sin \Theta \tag{14}$$

$$(d/dt + \gamma_3) \ a_3 = + V a_1 a_2 \sin \Theta$$

where the evolution of the phase mismatch $\Theta = \phi_1 - \phi_2 - \phi_3$ is described by the equation:

$$\frac{d\Theta}{dt} = \Omega + V \left(\frac{a_1 a_3}{a_2} + \frac{a_1 a_2}{a_3} - \frac{a_2 a_3}{a_1} \right) \cos \Theta \tag{15}$$

and the nonlinear coupling coefficient V is given by

$$V = 2H \left[\left(\frac{\partial D}{\partial \omega} \right)_{k_1} \left(\frac{\partial D}{\partial \omega} \right)_{k_2} \left(\frac{\partial D}{\partial \omega} \right)_{k_3} \right]^{-1/2} \tag{16}$$

Consider now the particular case of an unstable mode $\omega_1 = \omega(k_1)$, k_1 which saturates by subharmonic generation. In this case we have $\omega_2 = \omega_3 \simeq \omega_1/2$. And we also have $a_2 = a_3$ and $\gamma_2 = \gamma_3 > 0$. Equations (14) and (15) then reduce to:

$$(d/dt + \gamma_1) \ a_1 = - V a_2^2 \sin \Theta$$

$$(d/dt + \gamma_2) \ a_2 = V a_1 a_2 \sin \Theta \tag{17}$$

$$d\Theta/dt = \Omega + V a_1 [2 - (a_2/a_1)^2] \cos \Theta$$

Portgal. Phys. — Vol. 14, fasc. 3-4, pp. 243-254, 1983

247

It has already been shown that such a system contains chaos [1], [2]. This quite remarkable result however has a limited range of application. In the first place, the unstable spectrum always has a finite bandwidth Δ and the ideal situation of a monochromatic wave ($\Delta \to o$) never occurs. In the second place, the two linearly stable waves a_2 and a_3 are, in general, different waves, as in the Brillouin or in the Raman scattering processes. We can avoid the first difficulty if we add to the evolution equations (11) a random term R, which phenomenologically describes the contribution of the spectrum components not entering in (10), say, the neglected nonlinear term

$$\int_{k \neq k_2} H(k, k') \; E(k') \; E(k - k') \; e^{i\Omega t} \; \frac{dk'}{(2\pi)^3}$$

The influence of this random term on the transition to chaos and its justification will be discussed elsewhere. Here we only want to stress that if the phases are assumed to be random the three equations (17) reduce to two and chaos is no longer observed. This quite obvious conclusion will be stated more clearly in the next Section. The second difficulty noted above can also be avoided if we keep the four equations (14) and (15). In the next Section we show that the two great limitations of the fixed phase approximation can be avoided if we study the nonlinear wave saturation using the random phase approximation.

4 — RANDOM PHASE APPROXIMATION

Let us return to equation (7). If we multiply this equation by $E^*(k)$ and its complex conjugate by $E(k)$ and sum the results, we get:

$$(2\pi)^3 \; (d / dt + 2\gamma_k) \; |E(k)|^2$$
$$= -2 \int Re \; [H(k, k') \; E^*(k) \; E(k') \; E(k'') \; e^{i\Omega t}] \; dk' \tag{18}$$

If we write the field amplitude as $E(k) = |E(k)| \exp(i\phi_k)$ and if we assume that the phase behaves randomly we can make a statistical average of equation (18) over the phase. It is easy

to see that a statistical average over a random phase leads to $<E(k)> = o$ and $<E^*(k) E(k')> = |E(k)|^2 \delta(k-k')$. In order to calculate the mean of product $E^*(k) E(k') E(k'')$ entering in equation (18) we take an approximate solution of equation (7), assuming that $d/dt \simeq i\Delta$ where $\Delta \gg \gamma_k$ is the wave frequency width. We get then:

$$i\Delta (2\pi)^3 E(k) \simeq -\int H(k,k') E(k') E(k'') e^{i\Omega t} dk' \quad (19)$$

Using this result we can write:

$$i\Delta (2\pi)^3 <E^*(k) E(k') E(k'')>$$

$$\simeq \int H^*(k,s) <E^*(s') E^*(k-s') E(k') E(k-k')> e^{-i\Omega' t} ds'$$

$$\quad (20)$$

$$-\int H(k',s'') <E^*(k) E(s'') E(k'-s'') E(k-k')> e^{-i\Omega'' t} ds''$$

$$-\int H(k-k',s''') <E^*(k) E(k') E(s''') E(k-k'-s''')> e^{-i\Omega''' t} ds'''$$

where $\Omega' = \Omega(k' \to s', k'' \to k-s')$ and Ω'' and Ω''' are defined in a similar way. Now, in the random phase approximation it is easy to see that:

$$<E^*(s') E^*(k-s') E(k') E(k-k')>$$

$$\simeq <E^*(s') E(k')> <E^*(k-s') E(k-k')> \quad (21)$$

$$\simeq |E(s')|^2 |E(k-k')|^2 \delta(s'-k')$$

Using (20) and (21) we can write the statistical average of equation (18) in the form.

$$(2\pi)^3 (d/dt + 2\gamma_k) N_k$$

$$\quad (22)$$

$$= \int w(k,k') [N_{k'} N_{k''} - N_k N_{k''} - N_k N_{k'}] dk'$$

where $N_k = C_k^2$ are the number of photons of wavevector k and C_k is defined by equation (12). The nonlinear coupling coefficient $w(k, k')$ is now given by:

$$w(k, k') = -(4\pi/\varepsilon_0) \frac{|H(k, k')|^2 \delta(\Omega)}{\left(\frac{\partial D}{\partial \omega}\right)_k \left(\frac{\partial D}{\partial \omega}\right)_{k'} \left(\frac{\partial D}{\partial \omega}\right)_{k''}} \qquad (23)$$

Assuming further that the main components of the wave spectrum lie in the region of wavevectors around $k = k_i$ (with $i = 1, 2, 3$) we can use the properties of the δ function $\delta(\Delta)$ and get, after integration in k',

$$(d/dt + \gamma_1) \, N_1 = a_1 (N_2 N_3 - N_1 N_3 - N_1 N_2) \qquad (24)$$

where $N_i = N_{k_i}$ (for $i = 1,2,3$), $\gamma_1 = 2\gamma_{k_1}$ and

$$a_1 = w(k, k') \, [2\pi (\partial\Omega/\partial k')_{k_2}]^{-1} \qquad (25)$$

For positive energy waves, we always have $a_1 > 0$ [3]. Coupled with this evolution equation for N_1 we have two similar equations for N_2 and N_3. If we normalize the time with respect to the growth rate of the unstable mode N_1, with the aid of a new time variable $\tau = |\gamma_1| t$, it is easily seen that we can write the three coupled equations in the form:

$$dN_1/d\tau = N_1 + A_1 (N_2 N_3 - N_1 N_3 - N_1 N_2)$$

$$dN_{2,3}/d\tau = -\Gamma_{2,3} N_{2,3} - A_{2,3} (N_2 N_3 - N_1 N_3 - N_1 N_2) \qquad (26)$$

where $A_i = a_i / |\gamma_1| > 0$ and $\Gamma_{2,3} = \gamma_{2,3}/|\gamma_1| > 0$ are the linear damping rates of the stable modes N_2 and N_3. These equations are quite similar to the Lotka-Volterra equations for three populations in competition, but we will see that the behaviour of their solution is quite different.

Equations (26) have two singular points defined by:

$$P_0: \quad N_1 = N_2 = N_3 = 0$$

$$P_1: \quad N_1 = A_2\Gamma_2\Gamma_3/B, \quad N_2 = A_2\Gamma_3/B, \quad N_3 = A_3\Gamma_2/B \qquad (27)$$

where

$$B = A_1 (A_2 \Gamma_3 + A_3 \Gamma_2) - A_2 A_3 \tag{28}$$

The origin P_0 is always unstable and is of the node-saddle type. Its stable manifold is the plane $P_0 N_2 N_3$ and the unstable manifold is the axis $P_0 N_1$. The second singular point P_1 exists in the first octant of the phase space only if $B > o$. Equation (26) has a physical meaning only when the point representing the system in phase space belongs to the first octant, because the numbers of photons are positive quantities, $N_i > o$. Then, in order to get an instability saturation the singular point P_1 must be accessible to the system. The necessary condition for the instability saturation is then $B > o$.

Furthermore, if we use the Hurwitz criterion we can easily show that P_1 is always stable and shows a focus behaviour, provided that $B > o$. We can then say that the configuration in phase space is always the same and no bifurcation parameter can be defined. The conclusion is that, unlike the three dimensional Lotka-Volterra equations, no chaos can be generated in this system, because it would have to exist even for very small values of N_i when the nonlinear terms are negligible.

These results are confirmed by the numerical integration of equations (26). When $B = o$ the unstable mode boes to infinity, as well as the linearly stable modes. When $B > 0$ the unstable mode attains a maximum at a time τ_c and then slowly decays to the saturation level, as shown in Fig. 1. This maximum of N_1 grows with Γ, as well as the saturation time τ_c. For high enough values of Γ a series of oscillations around P_1 are observed with decreasing amplitudes (Fig. 2), revealing the focus nature of P_1. The behaviour is essentially of the same nature for $\Gamma_2 \neq \Gamma_3$.

5 — CONCLUSIONS

We have studied the instability saturation by nonlinear mode coupling and we have discussed the behaviour of the saturation wave amplitude levels in two extreme approximations. The first one corresponds to a nearly monochromatic unstable spectrum and it is the fixed phase approximation ($\Delta \tau_c \ll 1$) . In this case the
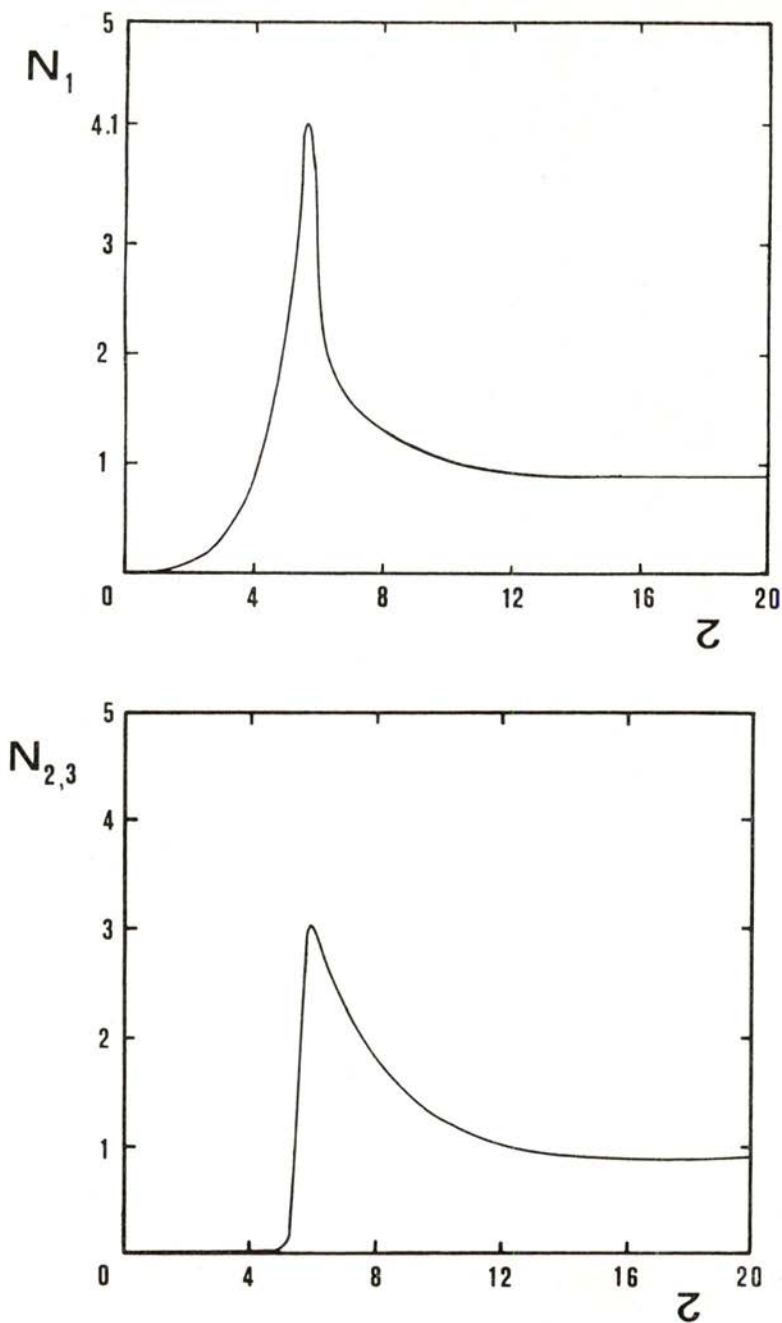
Fig. 1 — Instability saturation in the random phase approximation, for $A_1 = A_2 = A_3 = 1$ and $\Gamma_2 = \Gamma_3 = 1$. (a) Intensity of the first mode; (b) Intensity of the second and third modes (arbitrary units).
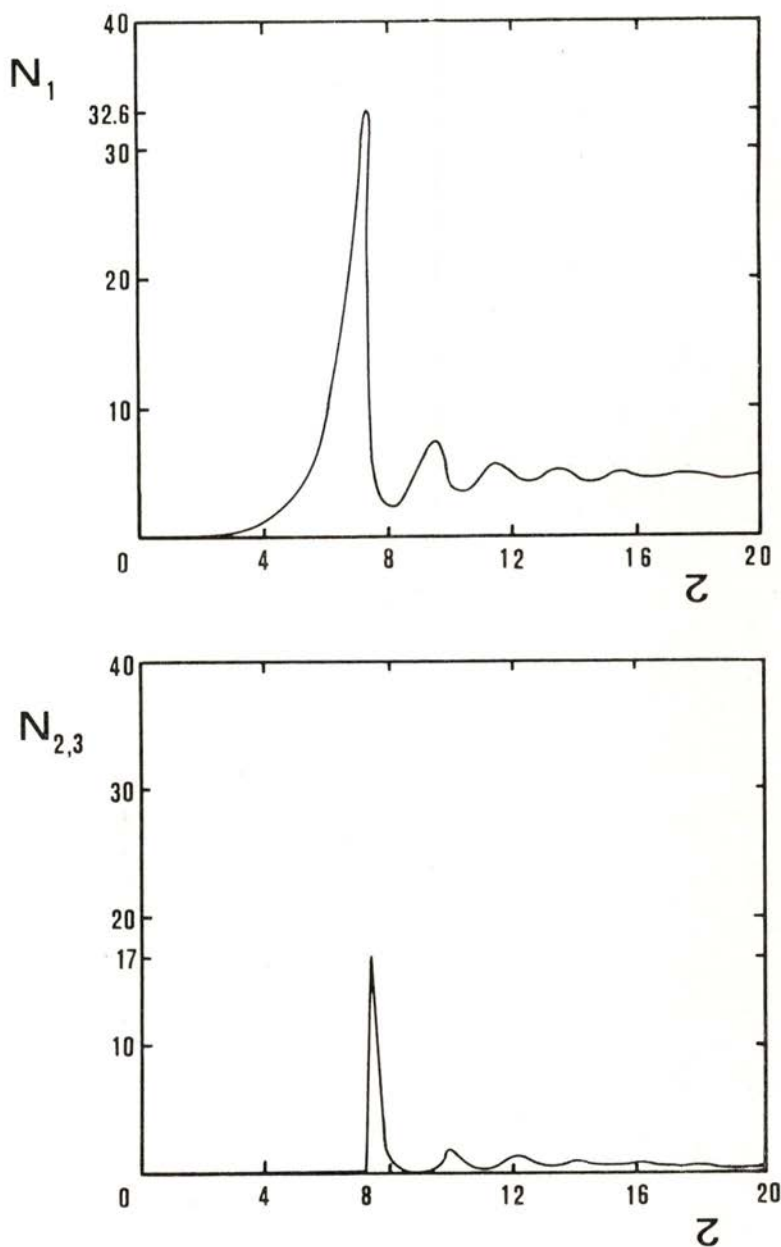
Fig. 2 — The same as in Fig. 1, but for $\Gamma_2 = \Gamma_3 = 100$.

wave amplitudes starting from zero can asymptotically attain a limit cycle regime which eventually bifurcates to chaos. This was shown by numerical calculations, assuming that the two stable waves are equal ($k_2 = k_3$, $a_2 = a_3$) , which means that we have sub-harmonic generation ($\omega_2 = \omega_3 \simeq 2\omega_0$) . Of course, if chaos is attained, the unstable spectrum broadens and the waves can no more be considered as monochromatic.

The second extreme case is that of a broad-band unstable spectrum, described by the random phase approximation ($\Delta \tau_c \gg 1$). Making no restriction on the character of the stable waves ($k_2 \neq k_3$, $N_2 \neq N_3$) we have shown that in this case the system tends to a stable focus and no bifurcation to chaos is observed.

It is our intuition that the random phase approximation is more appropriate to describe the physical phenomena because, even if the unstable spectrum is nearly monochromatic it becomes broader when the chaotic behaviour is observed. But only a detailed study of the intermediate case described by the fixed phase equations with a noise term can eventually give a qualified answer to this intuition.

REFERENCES

[1]   J. M. Wersinger, J. M. Finn and E. Ott, *Phys. Fluids* **23**, 1142 (1980).

[2]   M. N. Bussac, *Physica Scripta* T2/1, 110 (1982).

[3]   R. C. Davidson, *Methods in Nonlinear Plasma Theory*, Academic Press, N. Y. (1972).

CONTENTS

FASCÍCULO 1-2

CONTENTS

FASCÍCULO 3-4

AUTHOR INDEX

PORTUGALIAE PHYSICA publishes articles or research notes with original results in theoretical, experimental or applied physics; invited review articles may also be included.

Manuscripts, with an abstract, may be written in English or French; they should be typewritten with two spaces and in duplicate. Fi~ures or photographs must be presented in separate sheets and be suitable fo. reproduction with eventual reduction in size; captions should make the figures intelligible without reference to the text. Authors are requested to comply with the accepted codes concerning references.

There is no page charge. Author(s) will get 50 free reprints (without covers); these are to be shared among all the authors of the article. Authors interested in more reprints should say so when sending their manuscripts; quotations shall be sent with the proofs.

Subscription rates for volume 14:

> 2,400 Escudos (US$24) — individuals
> 6,000 Escudos (US$60) — libraries

PORTUGALIAE PHYSICA may also be sent on an exchange basis; we wellcome all suggestions to such effect.

All mail to be addressed to

PORTUGALIAE PHYSICA

VOL. 14 · NUMB 3/4 · 1983

CONTENTS